CHALLENGES IN LOW-TEMPERATURE FUEL CELLS

A Dissertation
Presented to
The Academic Faculty

By

Kevin Gregory Gallagher

In Partial Fulfillment
Of the Requirements for the Degree
Doctor of Philosophy in
Chemical & Biomolecular Engineering

Georgia Institute of Technology
December 2009

CHALLENGES IN LOW-TEMPERATURE FUEL CELLS

Approved by:

Dr. Thomas F. Fuller, Advisor
School of Chemical & Biomolecular Engineering
Georgia Institute of Technology

Dr. Meilin Liu
School of Materials Science & Engineering
Georgia Institute of Technology

Dr. William J. Koros
School of Chemical & Biomolecular Engineering
Georgia Institute of Technology

Mr. Michael L. Perry
United Technologies Research Center
United Technologies Corporation

Dr. Paul A. Kohl
School of Chemical & Biomolecular Engineering
Georgia Institute of Technology

Date Approved: August 11, 2009

ACKNOWLEDGEMENTS

The completion of this dissertation was only possible through the efforts and support of many people. First and foremost, my family has been an unwavering basis of understanding, encouragement, and motivation. Without the love and guidance of my parents Terry and Gloria, I surely would not have obtained the accomplishments or experiences that make up the life I currently enjoy. My siblings and best friends, Sean and Megan, have provided daily support for my decision to pursue a PhD that has led me away from home. Loved ones and friends, too numerous to list, have made these four years bearable and at times quite enjoyable. Whether they lived in Atlanta or elsewhere, our shared relationships have truly shaped this experience. Special recognition must be made of my labmates Raji, Wu, Cheng, Erin, Eric, and Norm for their support and tolerance over the past four years.

My application to Georgia Tech, five years ago, was in response to the biographical summary of Professor Tom Fuller. In his stated research interests, Tom expressed a clear desire to apply his efforts to help overcoming the energy challenge faced by our world in the 21st century. My decision to attend Georgia Tech to work with Tom has proved to be an excellent one. Tom has been an outstanding mentor for both my intellectual and personal growth. His objectivity, strong ethics, and humble manner are all aspects that I will try to carry forward. Georgia Tech also has a number of faculty members that have profoundly affected my academic development. Professors Bill Koros and Chris Jones have been sources of great advice and support throughout. My committee

members Professors Paul Kohl and Meilin Liu are thanked for their guidance through this process.

My one year term at UTC Power in South Windsor, CT was an invaluable experience that I would recommend to any student. However, without the presence of Rob Darling, Tim Patterson, and Mike Perry, this time would not have been so fruitful. Rob, Tim, and Mike are fantastic mentors and guided my education in science, engineering, and product development. Perhaps more importantly, their friendships made my time at UTC perhaps the most rewarding of my PhD. Tim has an unparalleled ability to explain complicated concepts while Mike always has a clear view of how technology fits into the larger picture. Rob's technical advisement was irreplaceable and accelerated my understanding of electrochemical engineering. During my time at UTC Power, I initiated a collaborative effort with Bryan Pivovar of the National Renewable Energy Laboratory. Though our physical contacts were limited to a brief visit to Los Alamos, my understanding of the physics of polymer electrolytes is attributed entirely to his guidance during our telephone conversations. It is through his great mentorship that Chapter 8 of this dissertation was achieved.

The research presented throughout this dissertation is the result of the combined efforts from the following people. David Wong produced some of the most important data composing Chapter 4. He is also thanked for his many hours in the lab as we worked together to develop fabrication techniques. Galit Levatin assisted with the XPS measurements made in Chapter 4. Rob Darling is a contributing author for Chapters 2

and 9 and is thanked for the opportunity to work together on the article for the "Handbook of Fuel Cells." Professor Gleb Yushin is a contributing author of Chapter 5 and the source of some of the more interesting materials tested. T.T. Aindows from UTC Power and Lichun Zhang, at the University of Connecticut, are responsible for the TEM imaging in Chapters 3 and 5. SEMs in Chapter 9 were provided by Bob Brown and Dave Condit at the United Technologies Research Center. The McGrath research group, The Dupont Company, Cabot Corporation, NanoBlox, and Arkema are thanked for the supplying the materials used in this dissertation.

UTC Power funded the last two years of my graduate research. The majority of work presented in this dissertation was made possible through this funding. My sincere gratitude is expressed to Tom Jarvi and the rest of UTC Power that made this possible.

TABLE OF CONTENTS

LIST OF TABLES

LIST OF FIGURES

LIST OF ABBREVIATIONS

AR	As-received
BET	Brunauer-Emmett-Teller
BPSH	Sulfonated poly(arylene ether sulfone) based membrane
CNON	Carbon onion
COR	Carbon oxidation reaction
CP	Constant potential
CPSR	Capillary pressure saturation relation
CV	Cyclic voltammogram
DSC	Differential scanning calorimetry
ENMR	Electrophoretic nuclear magnetic resonance
GDL	Gas diffusion layer
GHG	Green house gas
HOR	Hydrogen oxidation reaction
HT	Heat treated
HTT	Heat treatment temperature
IPA	Isopropyl alcohol
LTFC	Low-temperature fuel cell
MEA	Membrane electrode assembly
MIP	Mercury intrusion porosimetry
MRC	Mitsubishi Rayon Corporation
MWCNT	Multi-walled carbon nanotubes

NDIR	Nondispersive infrared detector
NMR	Nuclear magnetic resonance
ORR	Oxygen reduction reaction
PAFC	Phosphoric acid fuel cell
PAN	Polyacrylonitrile
PEMFC	Proton exchange membrane fuel cell
PFSA	Per(fluorosulfonic acid)
PTFE	Poly(tetrafluoroethylene)
QENS	Quasielastic neutron scattering measurements
Q/HQ	Quinone/Hydroquinone
RDS	Rate determining step
RH	Relative humidity
RHE	Reversible hydrogen electrode
SEM	Scanning electron micrographs
SHE	Standard hydrogen electrode
SQWV	Square wave potential cycle
TEM	Transmission electron microscopy
TPD	Temperature programmed desorption
WT	Wet treated
WTP	Water transport plate
XPS	X-ray photoelectron spectroscopy
XRD	X-ray diffraction
Y–LE	Young–Laplace equation

LIST OF SYMBOLS

CHAPTER 2

i	mass specific current, A g^{-1}
i_j	current density of species j, A cm^{-2}
$i_{0,j}$	exchange current density of species j, A cm^{-2}
k	rate parameter, A g^{-1} s^{m}
k'	pre-exponential rate constant, mol g^{-1} s^{m-1}
m	time decay exponent
n	number of electrons
p_j	partial pressure of species j, kPa
t	time, s
E_a	Activation energy, kJ mol^{-1}
F	Faradays constant, 96487.5 C mol^{-1}
R	Universal gas constant, 8.3144 kJ mol^{-1} K^{-1}
T	Temperature, K
U^{θ}	Standard potential, V
V_{cell}	Cell potential, $\Phi_{1,+} - \Phi_{1,-}$, V
$\alpha_{a,j}$	Anodic transfer coefficient of species j
$\alpha_{c,j}$	Cathodic transfer coefficient of species j
Φ_1	Metal potential, V
Φ_2	Solution potential, V
γ	Reactant order

CHAPTER 4

a	relative activity
A	active surface area, cm^2
C	capacitance, F/cm^2
i	current, A
k	rate constant, $A\ s^n$
Q	charge, C
t	time, s
U	potential, V
v	sweep rate, V/s

superscript

n	time decay constant
θ	standard or equilibrium

subscript

w	water
cv	cyclic voltammogram
dl	double layer
red	reduction

CHAPTER 6

A'	Lumped rate parameter, mol s^{n-1} /cm^2
A''	Lumped rate parameter, mol s^{n-1} /cm^2
C_{dl}	Double capacitance, μF/cm^2
C_o	Double capacitance prefactor, μF/cm^2
E_a	Activation energy, J/mol K
EW	Equivalent weight, g polymer / mol $–SO_3^-$
F	Faraday's constant, 96485.3 C
K_l	Equilibrium constant of species l
N_c	Moles of carbon, mol/cm^2-geometric
$N_{c,o}$	Initial moles of carbon, mol/cm^2-geometric
M	Molecular weight of carbon, 12.01 g/mol
R	Universal gas constant, 8.3144 J/mol K
S	Specific surface area as measured by the BET method, cm^2/g
T	Temperature, K
U_j	Equilibrium potential of reaction j versus a standard hydrogen electrode, V
V	Electrode voltage versus a standard hydrogen electrode, V
c_+	Concentration of protons, mol/L
g	Frumkin factor, unitless
i_j	Current from reaction j, A/cm^2-geometric
k_j	Rate constant j, mol/cm^2 s
k_j^o	Pre-exponential rate constant j, mol/cm^2 s
l	Species

n	Time decay exponent in power law expression, unitless
n_j	Number of electrons transferred in reaction j, unitless
p_{H2}	Partial pressure of hydrogen gas, kPa
p_o	Partial pressure of water vapor, kPa
r_j	Reaction j, mol/cm^2 s
s	Site
t	Time, s

Greek

$\alpha_{a,j}$	Anodic transfer coefficient of reaction j, unitless
$\alpha_{c,j}$	Cathodic transfer coefficient of reaction j, unitless
θ_l^s	Coverage of species l on site s, unitless

subscript

ads	adsorbed
cov	covered
vac	vacant

CHAPTER 8

a	relative activity
C_i	constant i, mol H_2O / mol $–SO_3H$
c_i	concentration of species i, mol/cm^3
$D_{\mu 0}$	diffusion coefficient of water, cm^2/s
F	Faraday's constant, 96,485.3 C/mol
f	water volume fraction
K_{ij}	frictional coefficient between species i and j, Js/cm^5
M	molecular weight, g/mol
m	molality, mol solute / kg solvent
N	molar flux, mol/cm^2 s
n	number of species
p	pressure, kPa
R	universal gas constant, 8.3144 J/mol K
T	temperature, K
t	transference
U	cell potential, V
V_i	molar volume of species i, mol/cm^3
v_i	velocity of species i, cm/s
x_i	mole fraction of species i
z	charge

Greek

α	transport coefficient, $mol^2/J\ cm\ s$
κ	conductivity, S/cm
λ	lambda, mol H_2O / mol $–SO_3H$
μ	chemical potential, J/mol
υ	number of moles electrolyte dissociates
ξ	electro-osmotic drag coefficient
ρ	density, g/cm^3
Φ_1	solid potential, V
Φ_2	solution potential, V
ϕ	osmotic coefficient

subscript

e^-	electron
l	liquid water
max	maximum value at temperature T
o	water
s	solid water, ice
+	proton
*	reference state
0	prefactor

superscript

m membrane phase

α hydrogen electrode on right side of activity-gradient cell

β membrane phase on right side of activity-gradient cell

γ membrane phase on left side of activity-gradient cell

δ hydrogen electrode on left side of activity-gradient cell

CHAPTER 9

A parameter for CPSR fit, kPa^{-1}

B parameter for CPSR fit, kPa

d characteristic time, s

D_i diffusion coefficient of species I, cm^2/s

f_i fraction of S_w attributed to S_i

I_{lim} limiting current, A/cm^2

k absolute permeability, cm^2

K relative permeability

L characteristic length, cm

m mass, g

n constant

N_i flux of species I, mol/cm^2 s

P pressure, kPa

r pore or capillary radius, cm

R universal gas constant, 8.3144 J/mol K

S	saturation
t	time, s
T	absolute temperature, K
v_0	volumetric flux, cm^3/cm^2 s
V	volume, cm^3
X	dimensionless length
y_i	mole fraction of species i

γ	surface tension of wetting fluid, dynes/cm
Δ	residual, measured value – fitted value
ε	porosity
θ	contact angle, degrees
Θ	dimensionless time
μ	viscosity, centipoise
ρ	density, g/cm^3
τ	tortuosity

subscript

a	advancing
c	capillary
f	fluid
nw	non-wetting
o	bulk

p	pore
s	sample
sk	skeleton
w	wetting

superscript

0	residual
*	characteristic

SUMMARY

Low-temperature fuel cells (LTFC) are a promising electrochemical energy system for the conversion of hydrogen to electricity. LTFCs are a zero emission source of energy when the hydrogen is produced from a source free of green house gases. LTFCs are being developed for use in stationary and transportation applications. Many challenges must be overcome before commercialization is possible. This dissertation focuses on the degradation of carbon catalyst supports and transport properties related to water management.

The electrochemical oxidation of carbon black catalyst supports is recognized as a durability challenge to the commercialization of LTFCs. LTFCs include phosphoric acid fuel cells (PAFC) and proton exchange membrane fuel cells (PEMFC). A review of the electrochemical oxidation of carbon is presented with a specific focus on corrosion during abnormal conditions (*e.g.* start or stop of a fuel cell). Kinetic studies of structure-reactivity relationships are presented in an in-depth study of commercially available and model carbons. The electrochemical oxidation of ten seemingly disparate carbon materials is separated into two distinct mechanisms. Iron and sulfur impurities are shown to not be a significant controlling factor. The difference between the two mechanisms is tentatively attributed to the degree of interlayer interaction between graphene sheets.

A mechanism and numerical model of the electrochemical oxidation of graphene-based carbon is proposed to explain longstanding questions. The model predicts carbon

weight loss and surface oxide growth as a function of time, temperature, and potential. Three mechanisms are concluded to contribute to the current decay commonly observed during electrochemical oxidation: mass loss, reversible passive oxide formation, and irreversible oxide formation.

Material and transport parameters are investigated to improve the understanding of water management in PEMFCs. Measurements of water sorption isotherms show a significant reduction in the water capacity of polymer electrolytes below 0 °C. Measurements of the electro-osmotic drag coefficient for Nafion® and both random and multi-block co-polymer sulfonated poly(arylene ether sulfone) (BPSH) chemistries are reported for vapor equilibrated samples below 0 °C. The electro-osmotic drag coefficient of BPSH chemistries is found to be ~0.4 , and that of Nafion® is ~1. The implication of an electro-osmotic drag coefficient less than unity is discussed in terms of proton transport mechanisms. Simulations of the ohmically limited current below 0 °C show a significant decreases in PEMFC performance. Capillary pressure saturation relations (CPSRs) are presented for Toray TGP-H-060 and Mitsubishi Rayon carbon fiber paper which can both be used as gas-diffusion layers in PEMFCs. Boundary and scanning curves for imbibition and drainage are measured to further understanding of the hysteresis observed during PEMFC operation.

The work presented in this dissertation is significant, but many challenges remain within the same areas of research. Recommendations are presented for future experiments and possible approaches for overcoming catalyst support degradation in LTFCs.

CHAPTER 1

INTRODUCTION

Arguably the most significant challenge facing society in the 21st century is the development of new energy sources, for current industrialized nations and emerging economies, while reducing or stabilizing atmospheric concentrations of greenhouse gases (GHGs) [1]. Such new energy supplies must be safe, sustainable, and cost competitive with conventional technologies [2]. Renewable sources of energy free from GHGs, such as electricity from wind or solar power, are inherently variable in their output (the sun does not shine at night) and demand a step change in energy storage compared with the requirements of current electricity generating technologies [3, 4]. Indeed the storage of electrical energy will be far more important in the future than at any time in history. Using electricity from renewable energy sources to produce hydrogen is an alternative to storing electricity in a battery, mechanical device, or water reservoir [5]. The fuel cell technology platform provides a possible solution to not only the aforementioned issues, but can also improve national security and geopolitical concerns by utilizing a locally available energy source.

The transportation sector produces as much as 30 % of all carbon dioxide emissions [6]. Low-temperature fuel cells (LTFC) are being considered as a possible replacement for the internal combustion engine in automobiles. LTFCs are an attractive option as they are an efficient means of converting hydrogen to electricity with water as the only byproduct [5, 7]. Furthermore, LTFCs have a larger energy density than lithium-

ion batteries and would provide for a longer vehicle range between refueling compared to an all electric vehicle [4, 7]. Improvements made through intensive research must be realized to reduce the system cost and to extend the functional life of the cell before fuel cell technology can compete with existing technologies [8].

Sir William Grove invented the fuel cell in 1839 [9, 10]. This device would be considered a LTFC and used platinum catalyst, similarly to technologies discussed here-in. LTFCs are generally considered to be those which operate below 230 °C. This encompasses, but not limited to, phosphoric acid and proton exchange membrane fuel cell technologies. Currently, phosphoric acid fuel cells (PAFCs) are available for commercial combined heat and power application [11]. The PAFC units typically operate on hydrogen from reformed natural gas. The power system can be used as the primary source of electricity or as a reliable, clean source of back-up power. Proton exchange membrane fuel cells (PEMFCs) have been touted as a possible replacement for the internal combustion engine in automobiles [7, 8, 12].

A fuel cell is typically constructed in a stack configuration to raise the voltage of the energy device [13]. A schematic of a PEMFC stack and a single repeat unit is found in Figure 1.1. A fuel-cell stack may contain 300 cells depending on the configuration and system design. A single cell is considered two gas diffusion layers (GDL), a membrane electrode assembly (MEA), and one half of two bipolar plates.

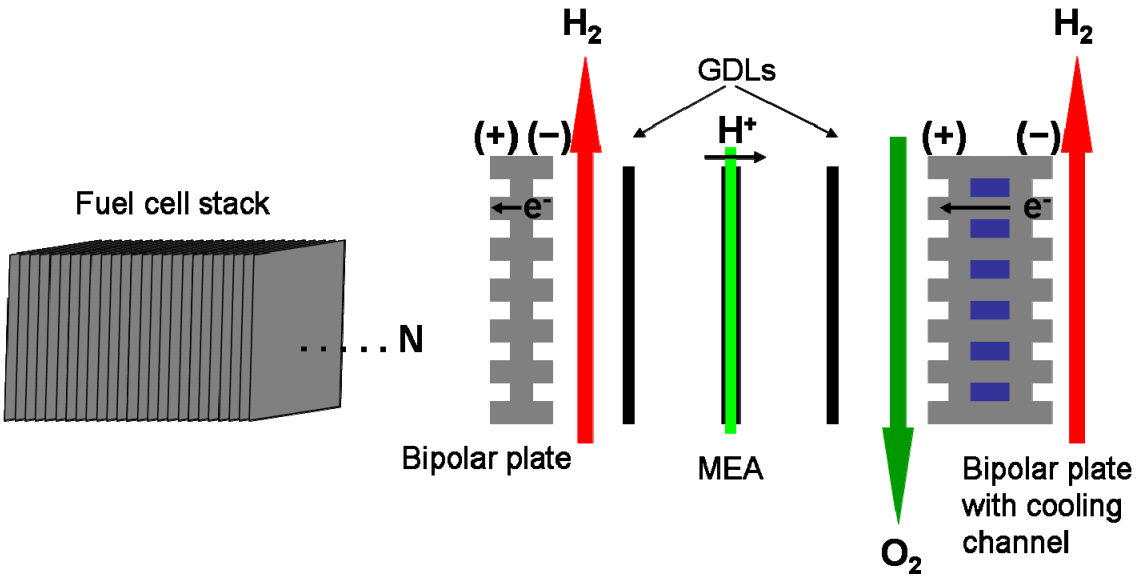

Figure 1.1. Repeating unit in PEMFC stack

The MEA is the heart of the fuel cell [14]. The MEA is composed of a thin ion conducting membrane (18-50 μm), typically a per(fluorosulfonic acid) (PFSA) copolymer with a polytetrafluoroethylene (PTFE) backbone, sandwiched between two thin catalyst layers (10-20 μm each). The membrane not only conducts ions, but also separates the reactant gases and prevents electrical shorts. The catalyst layers are a porous electrode composed of a precious metal catalyst, typically platinum, on a carbon support. This supported catalyst is mixed with a recast ionomer, also of PFSA chemistry. This layer is further sandwiched by GDLs (100-400 μm each) and then sealed with gasket material. Although the MEA may be symmetric, the cathode typically has a higher catalyst loading due to the sluggish oxygen reduction reaction (ORR). Alloying of the catalyst or GDL differences may also exist between the anode and cathode sides of a cell. The reactants are introduced by the so-called bipolar plates, which may also contain cooling channels. The plates are called bipolar because the electrons flow from the

negative to the positive electrode within the same bipolar plate. The positive electrode or cathode is the location of the ORR, Equation 1.1. The negative electrode or anode is where the hydrogen oxidation reaction occurs, Equation 1.2. The standard potentials at 25 °C for these two reactions are also shown versus the standard hydrogen electrode (SHE) [15]. The thermodynamic cell voltage for a hydrogen-oxygen fuel cell is thus 1.23 V vs SHE at 25 °C. In practice, voltages below 1 V are obtained due to mixed potentials, reactant crossover, and various sources of overpotential [13].

$$O_2 + 4H^+ + 4e^- \leftrightarrow 2H_2O \qquad U^\theta = 1.23 \text{ V vs SHE} \quad (1.1)$$

$$H_2 \leftrightarrow 2H^+ + 2e^- \qquad U^\theta = 0.00 \text{ V vs SHE} \quad (1.2)$$

A number of significant challenges must be overcome before the widespread implementation of LTFCs is realized. The challenges are best separated into the production, storage, and conversion of the fuel with the recognition that the inability to overcome any of these challenge prevents widespread entry into the marketplace [12]. Hydrogen is generally considered the fuel of choice for LTFC operation; however, significant efforts are being made to research and commercialize methanol fuel cells for portable power applications [16, 17]. The high volume production of hydrogen in an efficient manner without the creation of GHGs has yet to be realized. Reformed natural gas has been suggested to be the best source of hydrogen until sustainable production, free of GHGs, is made more efficient [12]. The storage of hydrogen is perhaps the most significant challenge preventing LTFC use in personal automobiles. Being a lightweight

and disperse gas, the economical and efficient storage of hydrogen in the volumes and weights required by automotive applications is extremely challenging. Recently, the United States Department of Energy dramatically reduced funding for hydrogen storage research after concluding the widespread adoption of LTFCs in transportation applications is at least 20 years [18]. The slow progress achieved in the storage of hydrogen was likely the deciding factor.

The challenges to the conversion of energy in LTFCs are the focus of this dissertation. LTFC operability, cost, and durability are the three largest obstacles to creating a successful LTFC absent other challenges with fuel production and storage [8, 12, 19, 20]. These three challenges are interrelated as optimization of one typically affects another. Improving operability requires enhanced LTFC performance under a range of operating conditions. LTFC for personal transportation must start independently from below 0 °C temperatures and remove heat successfully during normal operation. The need for better heat rejection has motivated an increase in the operating temperatures of PEMFCs for automotive applications. While higher temperatures will reduce the size and complexity of a heat exchanger, high temperatures will also exponentially increase degradation of the current materials. Cost issues are associated most famously with the use of precious metal catalysts, such as platinum, but also relates to other repeat materials such as the electrolyte and bipolar plates. Furthermore, the overall cost of the system that delivers the fuel, moderates operating temperature, and manages water must be lowered by reducing complexity. Cleary, the cost of the system is related to both performance

(operability) and durability. The longevity of the LTFC is directly related to the components used and system that controls the operating conditions.

This dissertation presents research specifically in the areas of durability and operability. Part 1 focuses on the durability challenges presented by the electrochemical oxidation of carbon black catalyst supports used in LTFCs. The material characteristics, its role in LTFCs, and degradation studies are presented. Part 2 focuses on the challenges related to water management in LTFCs with a particular focus on PEMFC. Transport parameters related to water management are measured and then discussed in terms of consequences in fuel cell operation.

Although PEMFC are at best 20 years away from widespread implementation in the transportation sector [18], other sectors of the economy may provide a suitable point of entry to the marketplace. Forklifts and back-up power may be for fuel cells what portable electronics are to the battery for hybrid electric vehicles [21]. Current fuel cell developer Ballard Power Systems has signed an agreement with ACME Tele Power for 10,000 back-up power units [22]. The advantage of increased scale of production and the knowledge gained by in-the-field operation must not be understated. Other fuel cell developers are focusing on the design of PEMFCs for buses [22, 23]. PEMFC development for buses is less challenging than personal automotive transport as more space is available for hydrogen storage, centralized hydrogen fueling stations could be utilized, and other advantages. The compilation of work in this dissertation represents a significant contribution to the effort to overcome the challenges faced by LTFCs. The

development of the technology required to move to a GHG free energy paradigm will only occur through continued fundamental research to develop new materials and systems. Perhaps the necessary motivation to conduct this research on the scale needed is only possible by imposing a substantial price on emitted carbon [2].

REFERNCES

[1] Smalley RE. Future global energy prosperity: The terawatt challenge. MRS Bulletin. 2005; **30**(6), 412-7.

[2] Lewis NS, Nocera DG. Powering the planet: Chemical challenges in solar energy utilization. Proceedings of the National Academy of Sciences of the United States of America. 2006; **103**(43), 15729-35.

[3] Basic Research Needs for Electrical Energy Storage. Washington, D. C.: United States Department of Energy; 2007.

[4] Armand M, Tarascon JM. Building better batteries. Nature. 2008; **451**(7179), 652-7.

[5] Turner JA. A realizable renewable energy future (vol 285, pg 687, 1999). Science. 1999; **285**(5433), 1493-.

[6] Inventory of U.S. Greenhouse Gas Emissions and Sinks 1990-2006. Washington, D.C.: United States Environmental Protection Agency; 2008.

[7] Demirdoven N, Deutch J. Hybrid cars now, fuel cell cars later. Science. 2004; **305**(5686), 974-6.

[8] Chalk SG, Miller JE. Key challenges and recent progress in batteries, fuel cells, and hydrogen storage for clean energy systems. Journal of Power Sources. 2006; **159**(1), 73-80.

[9] Liebhafsky HA, Cairns EJ. Fuel Cells and Batteries. New York: John Wiley & Sons 1968.

[10] Appleby AJ. From Sir William Grove to today: fuel cells and the future. Journal of Power Sources. 1990; **29**, 3-11.

[11] Fuller TF, Gallagher KG. Phosphoric Acid Fuel Cells (PAFC). In: Gasik M, ed. *Materials for Fuel Cells*. Cambridge, UK: Woodhead Publishing Limited 2008:209-47

[12] Basic Research Needs for the Hydrogen Economy. Washington, D.C.: United States Department of Energy; 2003.

[13] Larminie J, Dicks A. Fuel Cell Systems Explained. 2nd ed. Hoboken, New Jersey: John Wiley & Sons 2003.

[14] Kocha SS. Principles of MEA Preparation. In: Vielstich W, Yokokawa H, Gasteiger HA, eds. *Handbook of Fuel Cells: Fuel Cell Technology and Applications, Volumes 3 & 4*. Chichester, UK: John Wiley & Sons, Ltd 2003.

[15] Newman J, Thomas-Alyea KE. Electrochemical Systems. 3rd ed. Hoboken, New Jersey: John Wiley & Sons, Inc. 2004.

[16] Kamarudin SK, Daud WRW, Ho SL, Hasran UA. Overview on the challenges and developments of micro-direct methanol fuel cells (DMFC). Journal of Power Sources. 2007; **163**(2), 743-54.

[17] Wee JH. A feasibility study on direct methanol fuel cells for laptop computers based on a cost comparison with lithium-ion batteries. Journal of Power Sources. 2007; **173**(1), 424-36.

[18] FY 2010 Congressional Budget Request: Budget Highlights. Washington, D.C.: United States Department of Energy; 2009.

[19] Borup R, Meyers J, Pivovar B, Kim YS, Mukundan R, Garland N, et al. Scientific aspects of polymer electrolyte fuel cell durability and degradation. Chemical Reviews. 2007; **107**(10), 3904-51.

[20] Mathias MF, R. M, H.A. G, Conley JJ, Fuller TJ, Gittleman CJ, et al. Two Fuel Cells In Every Garage? The Electrochemical Society Interface. 2005; **14**(3), 24-35.

[21] Perry ML, Darling RM, Kandoi S, Patterson TW, Reiser C. Operating Requirements for Durable Polymer-Electrolyte Fuel Cell Stacks. *Polymer Electrolyte Fuel Cell Durability* 2009:399-417.

[22] Ballard Power Systems: Building a Clean Energy Growth Company. 2009 [cited 2009 June 2009]; Available from: ballard.com

[23] UTC Power. 2009 [cited 2009 June 2009]; Available from: utcpower.com

PART 1

CHAPTER 2

THE ELECTROCHEMICAL OXIDATION OF CARBON IN FUEL CELLS

2.1. INTRODUCTION

Graphene based carbon materials are ubiquitous in electrochemical devices. Carbons of various levels of graphitization, ranging from amorphous to crystalline to novel nanostructures, are found both in commercially available devices and in fundamental research laboratories [1-3]. The success of carbon in electrochemical systems may be attributed to its natural abundance, stability, relatively low cost, and diverse morphologies. High surface area carbons are often used for their large double layer capacities or their ability to support nanoparticles catalysts. Low surface area carbons generally have a more significant crystalline nature and are used for their high conductivity and resistance to oxidation. Commercially available carbons used in the porous electrodes of low temperature fuel cells (LTFC), redox-flow batteries and supercapacitors generally consist of a high surface area carbon that has a complex, poorly defined morphology.

Carbon is used in various forms and locations in a LTFC stack [2, 4]. An LTFC is defined as a fuel cell that operates below 200 °C such as proton exchange membrane fuel cells (PEMFCs) and phosphoric acid fuel cells (PAFCs). In a catalyst layer, a carbon with a surface area of 100 to 700 m^2/g is chosen (~12 to 84 m^2/cell or ~4000 C/cell). Graphitized carbon fiber with poly(tetrafluorethylene) (PTFE) is typically used in the gas

diffusion layer to help manage reactant and water transport between the catalyst layer and the flow field [5]. Carbon black, 30 to 250 m^2/g (~24 to 200 m^2/cell), may also be combined with PTFE and applied on the gas diffusion layer adjacent to the catalyst layer forming a microporous layer to aid mass transport, particularly when liquid water is present. Graphitized carbon or graphite may also be used in the bipolar plate instead of metals such as stainless steel [6]. Corrosion resistant coatings are under development to enable the use of metal plates [7]. Carbon is advantageous for water management relying on porous bipolar plates [8]. In general, the stability of the carbon increases as we move outwards from the catalyst layer to the bipolar plate.

The durability of high surface area carbons in LTFCs is the focus of Part 1 of this dissertation. The purpose of this chapter is to provide an introduction to the present understanding. First, a description of the role of carbon and the challenges faced in a LTFC is presented. Next, the fundamentals of electrochemical oxidation and known mechanistic details are discussed. Finally, the chapter focuses on an in-depth review of the reverse current decay mechanism (e.g. start/stop) and mitigation. The reverse decay mechanism is presented in detail because this high potential environment is the greatest challenge to the use of high surface area carbon in PEMFCs.

2.2. CARBON AS A CATALYST SUPPORT

Acidic LTFCs require precious metal catalysts to accelerate the heterogeneous electrochemical reactions happening at the anode and cathode. In order to reduce the cost of the fuel-cell power plant, the mass of precious metal must be minimized. Order of magnitude reductions in catalyst loadings have been achieved by dispersing the metal on a support with high surface area [9]. Carbon black is the preferred support material in acidic LTFCs. A drawing of a carbon black particle supporting platinum nanoparticles in an ionomer bonded electrode is displayed in Figure 2.1. The catalyst support is the backbone of the electrode. The support conducts electrons, enables the use of nanoparticles, and creates open porosity in the electrode for water and gas transport.

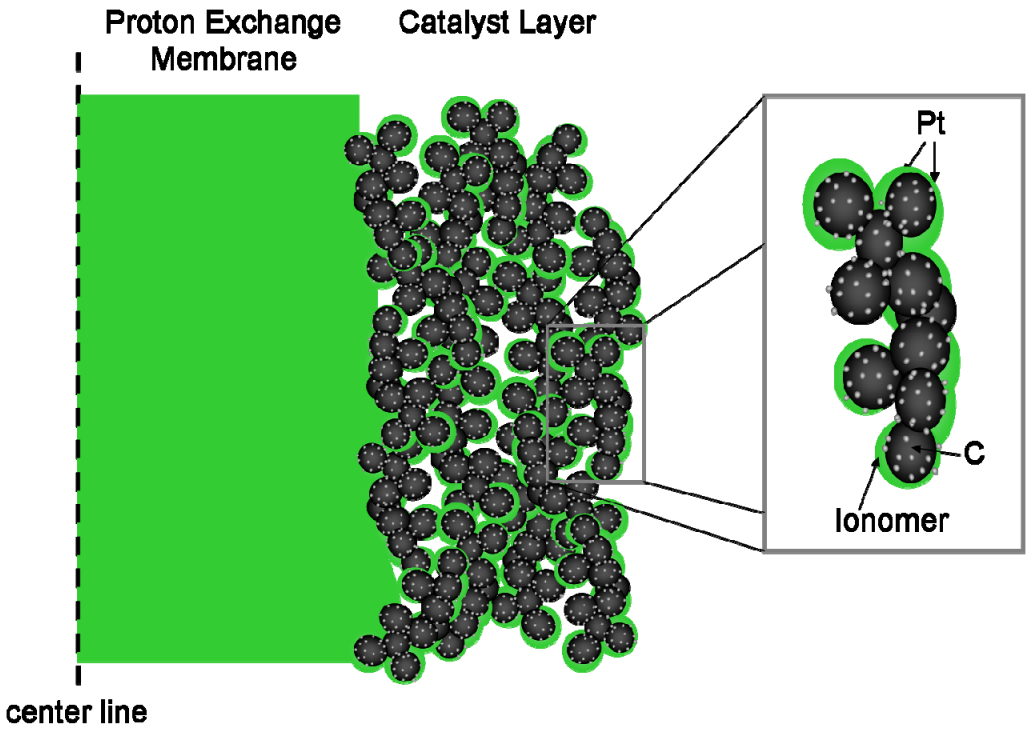

Figure 2.1. Depiction of carbon black particle (black) supporting platinum nanoparticles (grey) and surrounded by proton conducting ionomer (green).

The success of carbon black as a catalyst support is due to its high specific surface area, sufficient electrical conductivity, low cost, high abundance, and relative stability. This stability is challenged by oxidants (water and oxygen), temperature, catalysts, and high potential environments. The Pourbaix diagram for carbon is displayed in Figure 2.2. The area of concern for acidic LTFC operation is highlighted within the hatched box. Clearly, carbon is only thermodynamically favored over a small portion of potentials experienced. The widespread use of carbon is solely due to the sluggish kinetics for electrochemical oxidation.

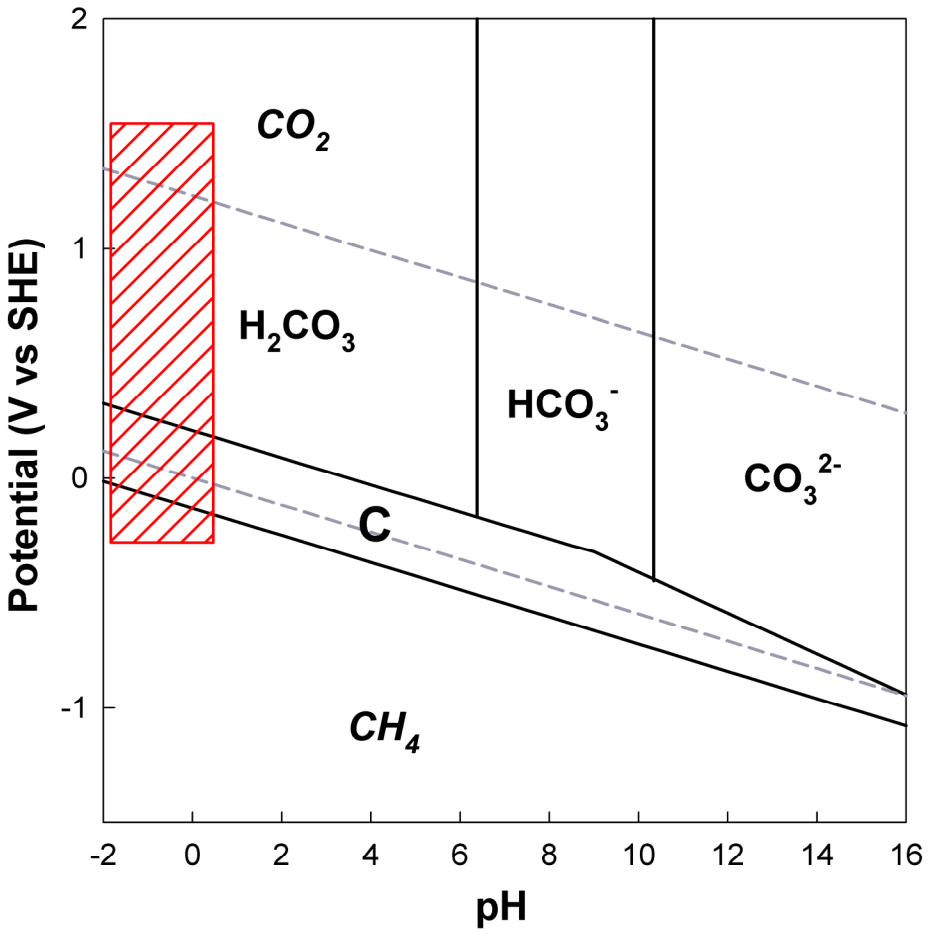

Figure 2.2. Pourbaix diagram for carbon. Hatched box (red lines) is the region of potentials experienced in a LTFC cathode without systems-based mitigation strategies.

LTFC materials may be exposed to a range of electric potentials during operation (see hatched box in Figure 2.2). Cathode components are exposed to high potentials, > 0.9 V vs. the reversible hydrogen electrode (RHE), during open circuit, stop, start, and local fuel starvation. PEMFCs are a possible alternative to the internal combustion engine in the transportation sector. In order to meet the demands of this market, PEMFCs will undergo more than 30,000 start/stop cycles [10]. The start/stop decay mechanism results in high interfacial potentials at the normal air electrode, resulting in severe carbon oxidation and mass loss. Dramatic performance loss will occur without proper mitigation techniques and robust materials [11].

PEMFCs and PAFCs may both be subjected to localized fuel starvation, which is caused by an inadequately distributed supply of hydrogen to the negative or fuel electrode. The fuel electrode is the anode during normal operation. This partial hydrogen coverage may be caused by deficiencies in gas delivery, transient operation, or poor water management. Localized fuel starvation results in the reverse-current mechanism akin to the start or stop of a fuel cell; however, this decay mechanism occurs during normal operation.

Prolonged electrochemical oxidation changes the physico-chemical characteristics of the carbon material. Surface oxide species of various chemistries are formed increasing the electronic resistance and hydrophilicity [12-14]. The larger resistance results in increased ohmic losses while the decreased hydrophobicity complicates PEMFC water transport and PAFC electrolyte transport. The gasification of the support

to CO_2 weakens the electrode and leads to collapse of the porous structure under severe oxidation [15-17]. A weight loss of 5-10 % has been correlated with unacceptable performance loss [5, 17-19]. This weight loss likely occurs before the collapse of the electrode structure.

The remainder of this chapter is organized to enable a deeper understanding of the electrochemical oxidation of carbon with a focus on the reverse-current mechanism. Following a discussion on the state of fundamental electrochemical oxidation research, the details of the reverse-current mechanism are presented including a review of published literature. Finally, material and system mitigation strategies are discussed in the context of published models and experimental data with a focus on the catalyst layer.

2.3. FUNDAMENTALS OF ELECTROCHEMIAL OXIDATION OF CARBON

A significant amount of research was published on the electrochemical oxidation of carbon black during the development of PAFCs, which began in the 1960's. Due to the high operating temperatures, 160 to 220 °C, carbon supports quickly oxidize at open-circuit voltages [9]. Systems and materials improvement were necessary to mitigate catastrophic corrosion on the cathode. Commercially available PAFC designs overcame this issue by avoiding the high potentials of open circuit by letting current flow through a resistor [9]. Materials were improved by heat treating or graphitizing the carbon black, which reduces surface heterogeneities, decreases surface area, and increases

crystallographic order [20, 21]. Individual PAFC power plants employing these strategies have operated in excess of 60,000 hours [22, 23].

2.3.1 Microstructure

Carbon black may be idealized as porous spherical particles 10 to 50 nm in diameter that fuses with other particles to form aggregates [3, 24]. The spherical carbon structure is of turbostratic nature with the nanocrystilline graphene sheets ordered to the curved outer surface of the particle. Graphene sheets are the basic building block of graphite and are essential a single layer of continuously bonded hexagonal aromatic rings. In graphite or nanocrystalline graphitic regions, the graphene sheets are stacked and held together by π-π noncovalent bonding [25]. Donnet's *Carbon Black* describes the production and resulting structure of carbon black [24]. The edges of the graphene sheets are rationalized to be susceptible to oxidation. Edges are anywhere the basal plane terminates such as dislocations, vacancies, defects and the edge of a graphene sheet. The π-bonded basal plane is considered stable to oxidation [3]. Vulcan XC-72 (Cabot Corporation) and Ketjen Black (Ketjen Black International Company) are typical carbon blacks used as catalyst supports for fuel cells. The exact structure of carbon black is still under much debate in the literature [26]. A more complete discussion of carbon black and graphene based carbon materials is found in Chapter 3 of this Dissertation.

2.3.2 Reaction mechanism

The exact mechanism of the electrochemical oxidation of carbon is poorly understood and without widespread agreement. The overall reaction may be represented

by Equation 2.1. The stability of carbon black is due to the poor kinetics of carbon oxidation as typical cathode potentials are well above the standard potential, U^{θ}. The standard potential depends on temperature and is reported at 25 °C in Equations 2.1-2.3. As a reference, the standard potential for Equation 2.1 lowers from 0.207 to 0.161 V vs. the standard hydrogen electrode (SHE) at 80 °C. Carbon monoxide (CO) may also be formed at high potentials according to Equation 2.2. However, when CO is detected it is usually an order of magnitude lower in concentration than carbon dioxide (CO_2) [27-30]. This low CO concentration is most likely a result of the favorable equilibrium for CO_2 formation at cathodic voltages as shown in Equation 2.3.

$$C_{(s)} + 2H_2O_{(l)} \rightarrow CO_{2(g)} + 4H^+_{(l)} + 4e^-_{(s)} \qquad U^{\theta} = 0.207 \text{ V } vs. \text{ SHE} \qquad (2.1)$$

$$C_{(s)} + \ H_2O_{(l)} \rightarrow CO_{(g)} \ + 2H^+_{(l)} + 2e^-_{(s)} \qquad U^{\theta} = 0.518 \text{ V } vs. \text{ SHE} \qquad (2.2)$$

$$CO_{(g)} + H_2O_{(l)} \rightarrow CO_{2(g)} \ + 2H^+_{(l)} + 2e^-_{(s)} \qquad U^{\theta} = -0.103 \text{ V } vs. \text{ SHE} \qquad (2.3)$$

For PAFCs, carbon oxidation is typically studied with a PTFE bonded electrode similar to those used in the fuel cell. The electrode is flooded with phosphoric acid and held at a constant potential as the current is monitored. The resulting carbon oxidation current follows the empirical rate law found in Equation 2.4 [28]. Here i is the mass specific current density, k is a temperature and potential dependent rate parameter, t is the time elapsed, and m is a potential dependent parameter.

$$i = kt^{-m} \tag{2.4}$$

The resulting linear plot of the logarithm of current against the logarithm of time is common to corrosion systems; however, the origin of this behavior remains elusive. The decay has been suggested to result from the growth of surface oxides which may either protect corrosion sites or serve as a barrier through which the reactants must diffuse [28]. Other researchers have proposed elaborate surface oxide intermediates [31]. Perhaps the most useful model is based on that originally suggested by Donnet for chemical oxidation by ozone [32], Equations 2.5 and 2.6. These equations were introduced by Kinoshita as analogous to the electrochemical oxidation of carbon black in fuel cells [20].

$$C \rightarrow CO_2 \tag{2.5}$$

$$C \rightarrow CO_{surf} \rightarrow CO_2 \tag{2.6}$$

The simplicity of the proposed mechanism is an attractive aspect: CO_2 is formed in two independent and parallel paths, both exhibiting separate logarithmic time decay. The oxidation of the surface carbon oxides, CO_{surf} to CO_2, is much slower than the direct formation. The total current, *i*, is the sum of the partial currents for Equations 2.5 and 2.6. For a more complete review of the development of carbon for fuel cells during the PAFC era, the reader is referred to Kinoshita's contribution *Carbon*: *Electrochemical and*

Physicochemical Properties [3] and the *Proceedings of the Workshop on the Electrochemistry of Carbon*, held at Case Western Reserve University in 1983 [20].

In contemporary times, the attention of low-temperature fuel cell developers has focused to a greater extent on PEMFCs. Although the mechanism of electrochemical oxidation has been shown to change in different electrolytes [33-35], the lessons learned from research on carbon corrosion during PAFC development are largely applicable to PEMFCs [23]. Until recently, the corrosion of carbon black was believed to be minimal due to the much lower operating temperatures 60 to 90 °C [10]. However, the reverse-current mechanism has highlighted the unfavorable thermodynamics of carbon.

In PEMFC research, a version of Equation 2.4 with a rate constant following Tafel kinetics has been published for the electrochemical oxidation of the carbon black supporting platinum (Pt/C) in a catalyst layer at 100 % relative humidity [10, 17, 18]. A slightly modified version of this equation is given below.

$$i = nFk'\left(\frac{p_w}{p_w^{ref}}\right)^{\gamma} \exp\left[\frac{-E_a}{RT}\left(1-\frac{T}{T_{ref}}\right)\right]\exp\left[\frac{\alpha_{a,C}F}{RT}\left(\Phi_1-\Phi_2\right)\right]t^{-m} \qquad (2.7)$$

Here k' is the pre-exponential rate constant, n is the number of electrons transferred, p_w is the partial pressure of water and γ is the order dependence of the reactant. The reference partial pressure of water, p_w^{ref}, is 101.325 kPa as defined by the calculation of the standard potential. F is Faraday's constant, R is the universal gas

constant, and T is the temperature. The electrode potential is defined as the difference between the metal potential, Φ_1, and the solution potential, Φ_2. Mathias *et al.* report a Tafel slope of 150 mV decade^{-1} and a time decay exponent of m = 0.3 to fit carbon dioxide measurements collected during potentiostatic oxidation experiments [10, 17, 18]. The Tafel slope may be expressed as an anodic transfer coefficient, $\alpha_{a,C}$, of 0.47 at 80 °C. The authors did not provide a rate constant although this can be estimated from their data. Mathias *et al.* did not present the dependence of the rate on reactant concentrations. We have amended Equation 2.7 to include the partial pressure of water. The authors report an activation energy of E_a = 67 kJ mol^{-1}, which probably overstates the Arrhenius dependence after one considers the effect of the partial pressure of water which depends exponentially on temperature.

Other workers have focused on cyclic voltammetry coupled with in-line gas analysis. Willsau and Heitbaum first analyzed the role of platinum nanoparticles on carbon corrosion in sulfuric acid [30]. Both Roen *et al.* and Maass *et al.* extended this work to PEMFC testing [29, 36]. All researchers concluded that platinum catalyzes the carbon oxidation reaction. However, during longer potential exposures this effect diminishes [37, 38]. This time dependent effect of platinum on carbon oxidation suggests that the growth of an anodic oxide film on platinum may pacify the catalytic effect of the noble metal. The activation energy for carbon dioxide formation at 1.2 V vs. RHE for Pt/C was found to be 58 kJ mol^{-1} by Maass *et al*. [29]. Compared to carbon alone, Roen *et al*. found a lower activation energy for Pt/C [36]. More subtle oxidation reactions

involving the platinum carbon couple were also discovered within the operating potential window of PEMFCs, but they will not be discussed further in this work.

The partial pressure of the water in the electrode may have direct consequences on the rate of electrochemical oxidation of carbon. PAFCs and PEMFCs operate at disparate temperature and relative humidity: PAFCs utilize concentrated acid while PEMFCs require a hydrated solid electrolyte. To illustrate the different environments, consider the relative humidity (RH) at a fixed air utilization of 60 % for dry feeds of a PAFC and a PEMFC. Here we assume that all product water exits in the air stream at atmospheric pressure. Material balance determines the mole fraction, thus the partial pressure of water is the same in each system. For a PAFC operating at 160 °C, the air would exit at a RH of 4 %, while air from a PEMFC operating at 65 °C would leave at a RH over 90 %. However, conventional PEMFCs require high RH to hydrate the polymer electrolyte and thus additional water to humidify the reactant streams is necessary at higher temperatures. If a PEMFC were operated near PAFC temperatures, the PEMFC would be subjected to higher rates of carbon oxidation because of the high water concentration. The lack of a RH requirement in phosphoric acid is probably a key reason why carbon has been successfully used in PAFC at high temperatures. As summarized by Appleby, the rate dependence of carbon oxidation on water partial pressure in phosphoric acid is first order when acid concentration is less than 95 % and near zero order in more concentrated acid [39]. In PEMFCs, Maass *et al.* have shown the oxidation rate to be proportional to water vapor partial pressure [29].

Experimental characterization of carbon corrosion is essential to understanding the mechanism. Electrochemical current measurements such as chronoamperometry and cyclic voltammetry are indispensable to probing the oxidation process. In-line gas analysis is a convenient approach to measure corrosion rates with non-dispersive infrared, gas chromatography and mass spectroscopy. CO_2 is the compound typically monitored; however, CO and other gases have also been analyzed [27]. *Ex situ* techniques are greater in number. The growth of surface oxides has been measured with titration, thermal gravimetric analysis coupled with mass spectrometry, X-Ray photoelectron spectroscopy, and Fourier-transform infrared spectroscopy [3, 40]. This growth in oxides has been shown to change the wetting characteristics of the carbon using the sessile drop method to measure contact angle [14, 41]. Thinning of the PEMFC electrode is commonly shown with scanning electron micrographs.

A complete description of carbon corrosion remains elusive as kinetic models that accurately predict the electrochemical oxidation are absent from the open literature. Furthermore, the repeated potential cycles occurring in transportation applications have been shown to result in a different corrosion path than constant potential exposures [29, 42]. Continued fundamental research to understand the corrosion mechanism is required to enable predictions of longevity and determine material requirements for PEMFCs.

2.4. REVERSE-CURRENT DECAY MECHANISM

2.4.1 Mechanism Overview

Reiser *et al*. were the first to introduce and explain the reverse-current mechanism in PEMFCs [15]. They demonstrated catastrophic carbon loss when the negative electrode was partially covered with hydrogen, particularly when a fuel cell was started or stopped. Using a simple mathematical model, the authors showed how a large interfacial potential difference, >1.4 V *vs.* RHE, could drive carbon oxidation and oxygen evolution on the air electrode (positive electrode) adjacent to the hydrogen poor portion of the fuel electrode. This high potential environment drastically reduces the life of the fuel cell in transportation applications where tens of thousands of start/stop cycles are required. This phenomenon appears to have been first published by researchers in the PAFC field in 1990 [43-45]. The authors demonstrated the large interfacial potential difference using multiple reference electrodes.

Figure 2.3 shows electron-microprobe images from the four corner locations of the same single cell subjected to repeated start/stop cycles without mitigation. Start is the replacement of air by hydrogen on the fuel electrode; stop is the replacement of hydrogen with air. The cell has a rectangular active region with an area of approximately 400 cm^2. The membrane-electrode assembly consists of platinum supported on carbon in the cathode and anode catalyst layers and a reinforced membrane. The cathode is on the bottom in each image. For reference, the membrane is approximately 20 μm thick. Fuel enters at the bottom left and exits at the top left after executing two passes over the active

area. Air is arranged in cross flow, and executes two passes over the cell. The visual appearance of the cell worsens as distance from the fuel inlet increases. The cathode catalyst layer appears thinner and brighter near the exit, because of loss of carbon. Furthermore, a bright band of platinum is visible in the membrane adjacent to the cathode catalyst layer. Both of these observations are consistent with exposure to high potentials.

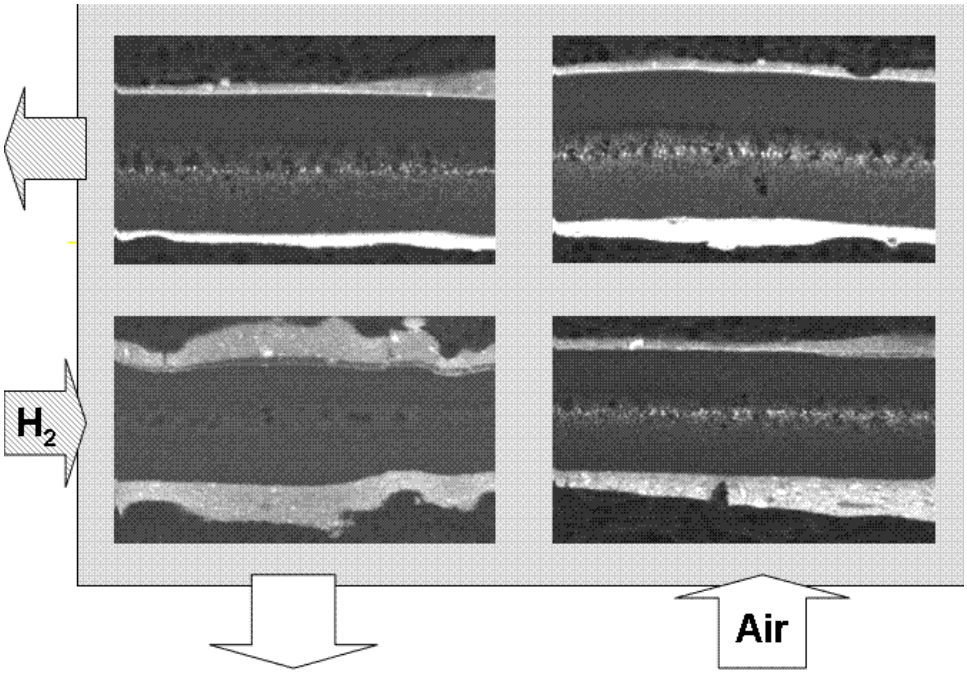

Figure 2.3. Electron-microprobe images of a PEMFC after repeated stop/start cycles. Cathode is on the bottom in all images. Damage increases with distance from the fuel inlet.

The observed pattern in catalyst layer thickness is consistent with increasing time at high potential with increasing distance from the inlet. When the cell is started, hydrogen moves from inlet to exit. The interfacial potential at the cathode catalyst layer in the hydrogen rich region is slightly below the normal open-circuit potential of a hydrogen/air cell. Ionic current moves from anode to cathode as it would in a normal fuel

cell. In the hydrogen deficient region ahead of the fuel front, the interfacial potential in the cathode catalyst layer is above that of the reversible potential for oxygen reduction (> 1.18 V *vs*. RHE at 80 °C). The ionic current in this region moves in the opposite direction of a normal fuel cell.

The presence of the reverse-current decay mechanism is not readily apparent in the current-potential behavior monitored by the observer, and thus several demonstrations and graphical aids have proven invaluable in the communication of the mechanism. Reiser *et al.* explained the mechanism by making a distinction between the portions of the negative electrode with and without fuel by drawing a cartoon similar to Figure 2.4 [15]. The illustration demonstrates to the observer that although both negative and positive electrodes are electrically connected, two different interfacial potential zones may exist.

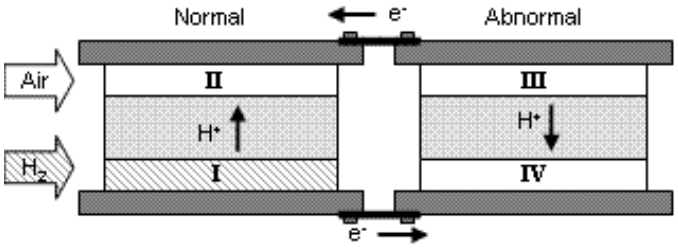

Figure 2.4. Illustration of partial hydrogen coverage as occurs during the start/stop of a cell or during localized fuel starvation. The ionic current in the abnormal cell flows in reverse of normal operation.

The left cell is named normal because hydrogen is present on the fuel electrode and right cell is referred to as abnormal because air is present on both electrodes. The carbon oxidation reaction (COR), the oxygen reaction, and the hydrogen reaction are

possible in each of the four regions (I-IV), Equations 2.1, 2.8, and 2.9. Platinum oxidation and dissolution, Equation 2.10 and 2.11, may also occur as shown in Figure 2.3.

$$2H_2O \leftrightarrow O_2 + 4H^+ + 4e^- \tag{2.8}$$

$$H_2 \leftrightarrow 2H^+ + 2e^- \tag{2.9}$$

$$Pt + H_2O \leftrightarrow PtO + 2H^+ + 2e^- \tag{2.10}$$

$$Pt \leftrightarrow Pt^{2+} + 2e^- \tag{2.11}$$

In the fuel distribution shown in the cartoon, some simplifying assumptions can be made in each region. In the normal cell, the hydrogen oxidation reaction (HOR) dominates in region I while the oxygen reduction reaction (ORR) occurs in region II. In the abnormal cell, the oxygen evolution reaction (OER) and the COR occur in region III and the ORR in region IV. The platinum reactions are not discussed beyond this point, because they are expected to be less important.

The cell potential is determined by measuring the difference between the metal potentials of the positive and negative electrodes. The metal potential of the positive electrode is set by the mixed potential of the ORR, OER, COR and HOR. The metal (mixed) potential of the negative electrode is set by the ORR and the HOR. The potential

difference between the positive and negative electrodes defines the drop in solution potential in the hydrogen starved portion of the cell, abnormal cell in Figure 2.4, as only one potential exists that will result in local anode and cathode currents being equal and opposite. In the hydrogen deficient region, the oxidation reactions of carbon and water occur on what is normally the cathode while the oxygen reduction reaction occurs on the fuel electrode. Hence, the current is flowing in reverse of normal operation.

2.4.2 Literature Review

A large portion of the published work concerning the reverse-current mechanism exists in the non-peer reviewed literature of patents, conference presentations, and transactions, particularly those of the Electrochemical Society. A detailed review of all of these works is beyond the scope of this chapter; however, important contributions will be recognized along with published journal articles.

Tang *et al.* cycled fuel and air on the anode of a PEMFC accelerating the frequency of start/stop to measure the resulting performance loss [46]. Patterson and Darling demonstrated the reverse current mechanism during partial fuel starvation by plugging the pores of the gas diffusion layer to impede hydrogen access to a small area of the fuel electrode [47]. In this area, the only available reactant gas is the oxygen that permeates through the membrane. The absence of hydrogen locally results in high interfacial potentials at the cathode. This experiment simulates a possible water droplet or other obstruction during stack operation. Their results suggest that damage does not occur until 2 mm inside of the occlusion. A more drastic form of this experiment is provided by

Reiser *et al*. [15]. They fed hydrogen to the top half of the fuel electrode and starved the bottom half of hydrogen by sending only nitrogen. The result is a rapid oxidation of the cathode opposite of the hydrogen starved region.

Meyers and Darling developed a transient pseudo-2D model [48] to elaborate upon the presentation by Reiser *et al*. [15]. The authors provide a discussion of the theory of the reverse-current mechanism as well as different mitigation strategies. Fuller *et al*. presented a one dimensional analytical model and a two dimensional numerical solution that included the reversal of the solution potential gradient at the air-fuel front [49]. A sensitivity analysis is given explaining how different kinetic and material properties may exacerbate or ameliorate decay. Yu *et al*. developed a simplified kinetic model to compare against their experiments [19]. To account for the greater severity of corrosion during the introduction of fuel (start), compared to the introduction of air (stop), Gu *et al*. updated their model to include a pseudo-capacitive effect [50]. This empirical approximation accounted for both the charging of the porous electrode double layer and the platinum oxidation reaction. The modified model resulted in a more accurate fit of the accelerated testing results.

Siroma *et al*. validated the reverse-current mechanism using a 97-fold segmented cell to measure currents and three voltages along the length of the anode [51]. Others used a segmented cell to show a dramatic decrease in oxygen reduction limiting current in the portion of an electrode subjected to reverse-current decay [50]. Dross and Maynard validated the mechanism with an external reference electrode [52]. The authors were able

to measure the interfacial potential differences during reverse-current decay, hence removing the need for CO_2 measurements or time consuming accelerated testing when material and/or system changes are implemented.

2.4.3 Simple Models and Governing Equations

Modeling of the reverse-current mechanism has provided insight into the physics of the process and aided in the exploration of methods to mitigate decay. The models discussed in the previous section are of various levels of complexity. However, all models are founded on the requirement that the sum of partial currents on the negative and positive electrodes must be the same. Five reactions are considered on each electrode involving carbon, oxygen, hydrogen, and platinum, Equations 2.1 and 2.8-2.11. The capacitance may also be treated, although this process and the platinum reactions are usually neglected. Furthermore, carbon black in the microporous layer may also react [13].

The kinetics for oxygen reduction [53] and hydrogen oxidation [54] have been published. The mechanism of the oxygen reaction is reviewed by Kinoshita [55] and this handbook [56]. However, carbon oxidation and to a lesser extent oxygen evolution lack robust published kinetic parameters. Kinetic models of carbon oxidation suffer from the need to describe the logarithmic decay and parallel reactions of CO_2 evolution and surface oxide formation as described in section 3.2. Because gas entry during the start or stop of a fuel cell is generally a quick process, ~0.5-5 seconds, the time decay of carbon corrosion has been neglected almost universally. For carbon corrosion caused by local

fuel starvation this may be a poor assumption. Oxygen evolution kinetics for Pt/C catalyst systems is nearly absent in published literature due to lack of prior need for this information. However, a much larger body of work exists on oxygen evolution occurring on platinum black electrodes, which should prove to be a suitable replacement [55]. Butler-Volmer or Tafel equations are often adequate models of electrode kinetics. The oxygen and hydrogen reactions are typically modeled with kinetics similar to Equations 2.12 and 2.13. The dependence on proton concentration has been neglected. Carbon oxidation is generally accepted as irreversible, and thus Equation 2.7 or 2.14 is used.

$$i_{O_2} = i_{0,O_2}\left\{\begin{array}{l}\left(\frac{p_w}{p_{w_{ref}}}\right)^{\gamma}\exp\left[\frac{\alpha_{a,O_2}F}{RT}\left(\Phi_1-\Phi_2-U_{O_2}^{\theta}\right)\right] \\ -\frac{p_{O_2}}{p_{O_{2,ref}}}\exp\left[-\frac{\alpha_{c,O_2}F}{RT}\left(\Phi_1-\Phi_2-U_{O_2}^{\theta}\right)\right]\end{array}\right\} \tag{2.12}$$

$$i_{H_2} = i_{0,H_2}\left\{\left(\frac{p_{H_2}}{p_{H_{2,ref}}}\right)\exp\left[\frac{\alpha_{a,H_2}F}{RT}\left(\Phi_1-\Phi_2-U_{H_2}^{\theta}\right)\right]-\exp\left[-\frac{\alpha_{c,H_2}F}{RT}\left(\Phi_1-\Phi_2-U_{H_2}^{\theta}\right)\right]\right\} \tag{2.13}$$

$$i_C = i_{0,C}\left(\frac{p_w}{p_{w_{ref}}}\right)\exp\left[\frac{\alpha_{a,C}F}{RT}\left(\Phi_1-\Phi_2-U_C^{\theta}\right)\right] \tag{2.14}$$

Fuller provides an analytical solution for the situation illustrated in Figure 2.4 [49]. To reach an analytical solution, carbon oxidation transient decay, oxygen evolution, and the potential drop across the electrolyte are neglected. The solution potential is then found to be a function of the cell potential and the kinetics of equal and opposite

reactions: oxygen reduction on the negative electrode and carbon oxidation on the positive electrode, Equation 2.15. Alternatively, this equation may be rearranged to express the carbon oxidation current as shown in Equation 2.16.

$$\Phi_2 = \frac{RT}{F(\alpha_{a,C} + \alpha_{c,O_2})} \ln\left[\frac{i_{0,C}}{i_{0,O_2}}\right] - \frac{(\alpha_{a,C} U_C^{\theta} + \alpha_{c,O_2} U_{O_2}^{\theta})}{(\alpha_{a,C} + \alpha_{c,O_2})} + \frac{\alpha_{a,C}}{(\alpha_{a,C} + \alpha_{c,O_2})} V_{cell} \tag{2.15}$$

$$\begin{aligned} i_C = {} & i_{0,C} \left(\frac{i_{0,O_2}}{i_{0,C}}\right)^{\frac{\alpha_{a,C}}{(\alpha_{a,C}+\alpha_{c,O_2})}} \\ & \times \exp\left\{\frac{\alpha_{a,C} F}{RT}\left[\left(1 - \frac{\alpha_{a,C}}{\alpha_{a,C} + \alpha_{c,O_2}}\right) V_{cell} + \frac{\alpha_{c,O_2}\left(U_{O_2}^{\theta} - U_C^{\theta}\right)}{\alpha_{a,C} + \alpha_{c,O_2}}\right]\right\} \end{aligned} \tag{2.16}$$

According to this analytical solution, the carbon oxidation current may be decreased by reducing the cell voltage or by decreasing the exchange currents for oxygen reduction and carbon oxidation. One shortcoming of the model is the omission of oxygen evolution on the cathode, which Fuller goes on to describe in the numerical 2-D solution [49]. The extended model shows that oxygen evolution raises the solution potential, lowering the overpotential, by providing a portion of the anodic current at a fixed cell potential. Fuller and co-workers also demonstrate that a higher ionic conductivity allows for current redistribution, lowering the overpotential for corrosion during localized fuel starvation.

2.4.4 Mitigation: Materials and Systems

New robust materials would provide the simplest solution to reverse-current decay; however, these usually result in increased cost and insufficient mitigation. Therefore a strategy that combines systems and materials improvements is necessary to overcome this degradation mechanism [11, 49, 50].

2.4.4.1 Material Development

Because the electrochemical oxidation of carbon results in performance decay, an obvious approach to solving the reverse-current decay mechanism is to search for a more stable carbon support. Graphitization, heat-treating carbon above 1600 °C, is commonly used to improve stability, but this lowers the specific surface area, which limits the ability to adequately disperse platinum. Carbon supports may need surface areas greater than 100 m^2/g to meet automotive platinum loading requirements [5]. Furthermore, researchers have shown three-fold reductions in decay with graphitized supports [19], which is much less than the order magnitude reduction needed to meet automotive durability requirements. Novel supports such as carbon nanotubes have shown some success, but are still in the early stages of development [57]. Other attempts include the development of ceramic based supports [58, 59]. The solubility of these non-carbon supports may be the durability challenge rather than electrochemical oxidation. Moreover, the dispersion of platinum on these supports is poor and requires low loadings. The degradation of carbon results in CO_2 that is harmless to the rest of the fuel cell system. Conversely, the dissolution of metal oxide catalyst supports may poison the electrocatalyst or exchange with protons in the membrane.

Catalyst system development is another approach to minimizing the electrochemical oxidation of carbon. The rate of carbon corrosion may be lowered by minimizing the ORR exchange current on the fuel electrode and raising the OER exchange current on the cathode. Gains can be made on the fuel electrode by lowering the amount of platinum on the anode to that required for automotive applications, 0.05 mg/cm^2, or with the development of a catalyst which is fast for the HOR, but not for the ORR. Adding catalysts that improve OER in the air electrode catalyst layer will shift current demand from carbon to water lowering the rate of carbon oxidation.

Changes in the properties of the polymer-electrolyte may prove advantageous for mitigating decay, especially localized fuel starvation. By increasing the conductivity, the current is allowed to redistribute during localized fuel starvation. Lowering the oxygen permeability through membrane reduces the limiting current for ORR on the anode, raising the solution potential.

2.4.4.2 Voltage Control

The cell potential may be reduced by connecting the fuel and air electrodes with a resistor, which allows current to flow externally. The flow of current results in a reduction in cell potential as the normally operated portion of the cell (H_2/Air) follows an approximation of the normal polarization curve. The deviation from typical polarization response is a result of the anode being shifted from the reversible hydrogen potential by the presence of oxygen. Starting with a large resistance, little current flows and the cell

potential is near the open-circuit value, ~ 0.85 V *vs*. RHE. As smaller resistances are used, the cell voltage decreases until the limiting current for oxygen reduction is reached. At the limiting current, the cathode potential falls to a value near the anode potential as hydrogen reduction has begun to take place on the air electrode. Orders of magnitude reduction in corrosion are possible by this simple approach to preventing the degradation typically endured during the start of the fuel cell.

It is important to note that even if the cell potential is near zero and oxygen is present, carbon oxidation may still be occurring. The best scenario is the interfacial potential at the cathode across from the portion of the anode which is locally fuel starved is near the reversible potential of the oxygen electrode, 1.18 V *vs.* RHE at 80 °C. Although this driving force is much lower than that experienced during an unmitigated start, corrosion of carbon still occurs.

Discharging a stack through a resistor when hydrogen is introduced generates a net current through all of the cells. This could damage the anode catalyst layers of cells without sufficient hydrogen to support the net current. Carbon on the anode would oxidize to support the current. The fuel manifold should be designed to introduce the fuel to all cells at the same time to prevent this. The simultaneous delivery of fuel to each cell is not a trivial task and may require the use of an external fuel manifold. The engagement of the resistor should be delayed until fuel has reached all of the cells [11]. The disengagement of the resistor during start should be reliant upon potential or columbic

measurements. After introducing hydrogen first on the fuel electrode, the introduction of fresh air should be delayed until residual oxygen on the air electrode is consumed.

2.4.4.3 Hydrogen On

Unless a fuel cell is pressurized with hydrogen during shutdown, air will eventually be present on both electrodes. The effect of this air intrusion may be minimized by leaving fuel on the electrodes long enough for the stack to cool to ambient temperature. The corrosion rate is lowered by a factor of six when the stack is cooled from 80 to 25 °C, using the kinetic parameters of Mathias *et al*. [10]. If hydrogen were maintained on both electrodes until start, the reverse-current mechanism would not occur [11]. The presence of oxygen is a requirement for this mechanism. Consider a fuel cell stack that is in the stop condition. The state of platinum, oxidized (ox) or reduced (red), and the gas present at each electrode is considered. The result of introducing hydrogen on the negative electrode is considered to simulate the start transition as described in Table 1. Oxidized platinum may be reduced allowing for the reverse-current mechanism even in the absence of oxygen gas.

Table 2.1. Effect of introducing hydrogen on the negative electrode on different states of the fuel cell due to different stop conditions.

Negative Electrode		**Positive Electrode**		**Result From**
Pt	**Gas**	**Pt**	**Gas**	**H_2 Introduction**
Red	N_2	Ox or Red	N_2	Safe
Ox	N_2	Ox	N_2	Moderate loss
Ox	N_2	Ox	Air	Significant loss
Ox	Air	Ox	Air	Significant loss

2.4.4.4 Fuel Utilization and Delivery

The hydrogen utilization in practical fuel-cell systems must approach 100 %. The risk that reverse-current decay will occur near the fuel exit is significant. A typical automotive fuel cell may contain 300 cells, each of which contains perhaps 30 fuel channels. The flow of hydrogen at the exit of each of these channels must be sufficient to prevent carbon corrosion. Clearly, the tolerance on channel dimensions must be tight and the gas manifolds must be designed to distribute fuel evenly between cells. One common approach is to have fewer channels exiting than entering a cell. When simple parallel channels are used, the fuel velocity drops dramatically with increasing utilization when the fuel is pure hydrogen. Reducing the number of channels tends to increase the fuel velocity while reducing the number of parallel paths should decrease the sensitivity to fabrication tolerance.

Recirculation of fuel with a blower or ejectors is often done to reduce the risk of carbon corrosion associated with insufficient hydrogen delivery at the exit of the stack. To a good approximation, this does not change the partial pressure of hydrogen exiting the stack, assuming the same overall fuel utilization. Recirculation increases the velocity of the gas exiting the stack. This ensures that portions of the active area with relatively poor access to fuel will not corrode. The higher velocity may also assist in the removal of liquid water from the channels [60]. Obstruction of the hydrogen path to the anodic catalyst layer by water is another potential cause of corrosion [47]. Recirculation of hydrogen may increase the dew point of the fuel entering the stack. Darling and Jayne demonstrated that condensing water in the fuel inlet manifold may result in carbon

corrosion [61]. Condensation at the inlet may also be a concern when using hydrogen made from a hydrocarbon in a reformer. Recirculation of the fuel is undesirable due to decreases in the net efficiency of the system and added equipment.

The speed of fuel delivery or residence time during the start or stop of a fuel cell has important implications. The more time hydrogen and air are spatially separated on the fuel electrode, the greater the extent of carbon corrosion. By increasing the rate of fuel entry by an order of magnitude, a proportional decrease in cumulative carbon loss is achieved [50]. However, the benefit from increasing fuel entry velocity is limited by the diffusion of the reactants from the gas channel to the catalyst layer [62].

2.5. CONCLUSIONS

The reverse-current mechanism will result in catastrophic degradation if left unmitigated. However, the use of material and system solutions results in manageable decay rates. Further development in mitigation strategies will extend the life of carbon in both PEMFCs and PAFCs. As research into the mechanism of the electrochemical oxidation of carbon progresses, a better understanding of the thermodynamic and kinetic requirements of catalyst supports will be reached. As carbon black is one of the few materials currently utilized in low-temperature fuel cells that meet the stringent cost targets of commercialization, its continued use as a catalyst support is likely for the foreseeable future.

REFERENCES

[1] Conway BE. Electrochemical Supercapacitors: Scientific Fundamentals and Technological Applications: Springer 1999.

[2] Dicks AL. The role of carbon in fuel cells. Journal of Power Sources. 2006; **156**(2), 128-41.

[3] Kinoshita K. Carbon: Electrochemical and Physicochemical Properties. New York: Wiley 1988.

[4] Kocha SS. Principles of MEA Preparation. In: Vielstich W, Yokokawa H, Gasteiger HA, eds. *Handbook of Fuel Cells: Fuel Cell Technology and Applications, Volumes 3 & 4*. Chichester, UK: John Wiley & Sons, Ltd 2003.

[5] Mathias M, Roth J, Fleming J, Lehnert W. Diffusion Media Materials and Characteristics. In: Vielstich W, Yokokawa H, Gasteiger HA, eds. *Handbook of Fuel Cells: Fuel Cell Technology and Applications, Volumes 3 & 4*. Chichester, UK: John Wiley & Sons, Ltd 2003.

[6] Roßberg K, Trapp V. Graphite-Based Bipolar Plates. In: Vielstich W, Yokokawa H, Gasteiger HA, eds. *Handbook of Fuel Cells: Fuel Cell Technology and Applications, Volumes 3 & 4*. Chichester, UK: John Wiley & Sons, Ltd 2003:308-14.

[7] Wind J, LaCroix A, Braeuninger S, Hedrich P, Heller C, Schudy M. Metal Bipolar Plates and Coatings. In: Vielstich W, Yokokawa H, Gasteiger HA, eds. *Handbook of Fuel Cells: Fuel Cell Technology and Applications, Volumes 3 & 4*. Chichester, UK: John Wiley & Sons, Ltd 2003:295-307.

[8] Weber AZ, Darling RM. Understanding porous water-transport plates in polymer-electrolyte fuel cells. Journal of Power Sources. 2007; **168**(1), 191-9.

[9] Landsman DA, Luczac FJ. Catalyst Studies and Coating Technologies. In: Vielstich W, Yokokawa H, Gasteiger HA, eds. *Handbook of Fuel Cells: Fuel Cell Technology and Applications, Volumes 3 & 4*. Chichester, UK: John Wiley & Sons, Ltd 2003.

[10] Mathias MF, R. M, H.A. G, Conley JJ, Fuller TJ, Gittleman CJ, et al. Two Fuel Cells In Every Garage? The Electrochemical Society Interface. 2005; **14**(3), 24-35.

[11] Perry ML, Patterson TW, Reiser C. Systems Strategies to Mitigate Carbon Corrosion in Fuel Cells. ECS Transactions. 2006; **3**(1), 783.

[12] Bi W, Fuller TF. Temperature effects on PEM fuel cells Pt/C catalyst degradation. Journal of the Electrochemical Society. 2008; **155**(2), B215-B21.

[13] Owejan JE, Yu PT, Makharia R. Mitigation of Carbon Corrosion in Microporous Layers in PEM Fuel Cells ECS Transactions. 2007; **11**(1), 1049.

[14] Paik CH, Saloka GS, Graham GW. Influence of cyclic operation on PEM fuel cell catalyst stability. Electrochem Solid State Lett. 2007; **10**(2), B39-B42.

[15] Reiser CA, Bregoli L, Patterson TW, Yi JS, Yang JDL, Perry ML, et al. A reverse-current decay mechanism for fuel cells. Electrochem Solid State Lett. 2005; **8**(6), A273-A6.

[16] Liu ZY, Brady BK, Carter RN, Litteer B, Budinski M, Hyun JK, et al. Characterization of carbon corrosion-induced structural damage of PEM fuel cell cathode electrodes caused by local fuel starvation. Journal of the Electrochemical Society. 2008; **155**(10), B979-B84.

[17] Yu PT, Gu W, Zhang J, Makharia R, Wagner FT, Gasteiger HA. Carbon-Support Requirements for Highly Durable Fuel Cell Operation. *Polymer Electrolyte Fuel Cell Durability* 2009:29-53.

[18] Makharia R, Kocha SS, Yu PT, Sweikart MA, Gu W, Wagner FT, et al. Durable PEM Fuel Cell Electrode Materials: Requirements and Benchmarking Methodologies. ECS Transaction. 2006; **1**(8), 3-18.

[19] Yu PT, Gu W, Makharia R, Wagner FT, Gasteiger HA. The Impact of Carbon Stability on PEM Fuel Cell Startup and Shutdown Voltage Degradation. ECS Transaction. 2006; **3**(1), 797-809.

[20] Kinoshita K. Influence of Heat-Treatment and Physicochemical Properties on the Electrochemical Oxidation of Carbon Blacks In Phosphoric Acid. In: Sarangapani S, Akridge JR, Schumm B, editors. The Electrochemistry of Carbon; 1983 August 17-19; Cleveland, OH: The Electrochemical Society, Inc; 1983. p. 273-90.

[21] Stonehart P. Carbon Substrates for Phosphoric-Acid Fuel-Cell Cathodes. Carbon. 1984; **22**(4-5), 423-31.

[22] Fuller TF, Gallagher KG. Phosphoric Acid Fuel Cells (PAFC). In: Gasik M, ed. *Materials for Fuel Cells*. Cambridge, UK: Woodhead Publishing Limited 2008:209-47

[23] Fuller TF, Perry ML, Reiser C. Applying Lessons Learned from PAFC to PEM Fuel Cells. ECS Transactions. 2006; **1**(8), 337.

[24] Donnet J-B, Bansal RC, Wang M-J. Carbon Black. 2nd ed. New York: Marcel Dekker 1993.

[25] Grimme S. Do special noncovalent pi-pi stacking interactions really exist? Angewandte Chemie-International Edition. 2008; **47**(18), 3430-4.

[26] Harris PJF. New perspectives on the structure of graphitic carbons. Critical Reviews in Solid State and Materials Sciences. 2005; **30**(4), 235-53.

[27] Chaparro AM, Mueller N, Atienza C, Daza L. Study of electrochemical instabilities of PEMFC electrodes in aqueous solution by means of membrane inlet mass spectrometry. Journal of Electroanalytical Chemistry. 2006; **591**(1), 69-73.

[28] Kinoshita K, Bett J. Electrochemical Oxidation of Carbon-Black in Concentrated Phosphoric-Acid at 135 Degrees C. Carbon. 1973; **11**(3), 237-47.

[29] Maass S, Finsterwalder F, Frank G, Hartmann R, Merten C. Carbon support oxidation in PEM fuel cell cathodes. Journal of Power Sources. 2008; **176**(2), 444-51.

[30] Willsau J, Heitbaum J. The Influence of Pt-Activation on the Corrosion of Carbon in Gas-Diffusion Electrodes - a Dems Study. Journal of Electroanalytical Chemistry. 1984; **161**(1), 93-101.

[31] Sihvonen V. The influence of keto- and ketene groups, adsorbed molecules and ions on the mechanism of carbon oxidation. Transactions of the Faraday Society. 1938; **34**(2), 1062-72.

[32] Donnet JB, Ehrburge.P, Voet A. Study on Oxidation Mechanism of Carbon-Blacks by Ozone in Aqueous-Medium. Carbon. 1972; **10**(6), 737-&.

[33] Binder H, Kohling A, Richter K, Sandstede G. Ueber Die Anodische Oxydation Von Aktivkohlen In Wässrigen Elektrolyten. Electrochimica Acta. 1964; **9**, 255-74.

[34] Nystrom WA. Electrolytic Degradation and Electrode Structure. Journal of the Electrochemical Society. 1969; **116**(1), 17-&.

[35] Thiele H. The oxidation of carbon in electrolytes at normal temperature. Transactions of the Faraday Society. 1938; **34**(2), 1033-9.

[36] Roen LM, Paik CH, Jarvic TD. Electrocatalytic corrosion of carbon support in PEMFC cathodes. Electrochem Solid State Lett. 2004; **7**(1), A19-A22.

[37] Ball SC, Hudson SL, Thompsett D, Theobald B. An investigation into factors affecting the stability of carbons and carbon supported platinum and platinum/cobalt alloy catalysts during 1.2 V potentiostatic hold regimes at a range of temperatures. Journal of Power Sources. 2007; **171**(1), 18-25.

[38] Passalacqua E, Antonucci PL, Vivaldi M, Patti A, Antonucci V, Giordano N, et al. The Influence of Pt on the Electrooxidation Behavior of Carbon in Phosphoric-Acid. Electrochimica Acta. 1992; **37**(15), 2725-30.

[39] Appleby AJ. Corrosion in Low and High Temperature Fuel Cells - An Overview. Corrosion. 1987; **43**(7), 398-408.

[40] Burg P, Cagniant D. Characterization of Carbon Surface Chemistry. *Chemistry and Physics of Carbon, Vol 30* 2008:129-75.

[41] Kangasniemi KH, Condit DA, Jarvi TD. Characterization of vulcan electrochemically oxidized under simulated PEM fuel cell conditions. Journal of the Electrochemical Society. 2004; **151**(4), E125-E32.

[42] Gallagher KG, Wong DT, Fuller TF. The effect of transient potential exposure on the electrochemical oxidation of carbon black in low-temperature fuel cells. Journal of the Electrochemical Society. 2008; **155**(5), B488-B93.

[43] Mitsuda K, Murahashi T. Polarization Study of a Fuel-Cell with 4 Reference Electrodes. Journal of the Electrochemical Society. 1990; **137**(10), 3079-85.

[44] Mitsuda K, Murahashi T. Air and Fuel Starvation of Phosphoric-Acid Fuel-Cells - a Study Using a Single Cell with Multireference Electrodes. Journal of Applied Electrochemistry. 1991; **21**(6), 524-30.

[45] Mitsuda K, Murahashi T, Matsumoto M, Usami K. Estimation of Corrosion Conditions of a Phosphoric-Acid Fuel-Cell. Journal of Applied Electrochemistry. 1993; **23**(1), 19-25.

[46] Tang H, Qi ZG, Ramani M, Elter JF. PEM fuel cell cathode carbon corrosion due to the formation of air/fuel boundary at the anode. Journal of Power Sources. 2006; **158**(2), 1306-12.

[47] Patterson TW, Darling RM. Damage to the cathode catalyst of a PEM fuel cell caused by localized fuel starvation. Electrochem Solid State Lett. 2006; **9**(4), A183-A5.

[48] Meyers JP, Darling RM. Model of carbon corrosion in PEM fuel cells. Journal of the Electrochemical Society. 2006; **153**(8), A1432-A42.

[49] Takeuchi N, Fuller TF. Modeling and investigation of design factors and their impact on carbon corrosion of PEMFC electrodes. Journal of the Electrochemical Society. 2008; **155**(7), B770-B5.

[50] Gu W, Carter RN, Yu PT, Gasteiger HA. Start/Stop and Local H2 Starvation Mechanisms of Carbon Corrosion: Model vs. Experiment ECS Transactions. 2007; **11**(1), 963.

[51] Siroma Z, Fujiwara N, Loroi T, Yamazaki S, Senoh H, Yasuda K, et al. Transient phenomena in a PEMFC during the start-up of gas feeding observed with a 97-fold segmented cell. Journal of Power Sources. 2007; **172**(1), 155-62.

[52] Dross R, Maynard B. In-Situ Reference Electrode Testing for Cathode Carbon Corrosion ECS Transactions. 2007; **11**(1), 1059.

[53] Gasteiger HA, Kocha SS, Sompalli B, Wagner FT. Activity benchmarks and requirements for Pt, Pt-alloy, and non-Pt oxygen reduction catalysts for PEMFCs. Appl Catal B-Environ. 2005; **56**(1-2), 9-35.

[54] Neyerlin KC, Gu WB, Jorne J, Gasteiger HA. Study of the exchange current density for the hydrogen oxidation and evolution reactions. Journal of the Electrochemical Society. 2007; **154**(7), B631-B5.

[55] Kinoshita K. Electrochemical Oxygen Technology. New York: Wiley-Interscience 1992.

[56] Gattrell M, MacDougall B. Reaction mechanisms of the O2 reduction/evolution reaction. In: Vielstich W, Yokokawa H, Gasteiger HA, eds. *Handbook of Fuel Cells, Fundamentals Technology and Applications*. Chichester, UK: John Wiley & Sons, Ltd 2003.

[57] Lee K, Zhang JJ, Wang HJ, Wilkinson DP. Progress in the synthesis of carbon nanotube- and nanofiber-supported Pt electrocatalysts for PEM fuel cell catalysis. Journal of Applied Electrochemistry. 2006; **36**(5), 507-22.

[58] Antolini E, Gonzalez ER. Ceramic materials as supports for low-temperature fuel cell catalysts. Solid State Ionics. 2009; **180**(9-10), 746-63.

[59] Wang Y, Song SQ, Maragou V, Shen PK, Tsiakaras P. High surface area tungsten carbide microspheres as effective Pt catalyst support for oxygen reduction reaction. Appl Catal B-Environ. 2009; **89**(1-2), 223-8.

[60] Kumbur EC, Sharp KV, Mench MM. Liquid droplet behavior and instability in a polymer electrolyte fuel cell flow channel. Journal of Power Sources. 2006; **161**(1), 333-45.

[61] Darling RM, Jayne D. ECS Transactions. 2007; **11**(1), 975.

[62] Takeuchi N, Fuller TF. The Influence of Gas Permeation through Membrane on Carbon Corrosion in PEMFC 213th Meeting of The Electrochemical Society; 2008; Phoenix, AZ; 2008.

CHAPTER 3

GRAPHENE BASED CARBON MATERIALS

3.1. INTRODUCTION

Carbon black is the material of choice for catalyst supports in low temperature fuel cells (LTFC) such as proton exchange membrane fuel cells (PEMFC) and phosphoric acid fuel cells (PAFC). Carbon black is heterogeneous in nature being composed of nanocrystalline domains, buckled graphene sections, and possibly amorphous regions [1, 2]. The precise nature or structure of carbon black is still being debated [1, 2]. Fundamentally, carbon black may be considered a graphene based carbon; thus, the properties of carbon black are best understood through a discussion of the graphene sheet, graphite, and other related carbons. The purpose of this chapter is not to review all literature on the structure and properties of graphene based carbons – multiple monographs exist for that purpose (see for example [3, 4]). Instead, the goal of this chapter is to provide the reader with a basis to understand the scientific investigation of the electrochemical oxidation of graphene based carbons presented in Chapters 4 – 6.

3.2. PRODUCTION, CHARACTERISTICS, AND USE OF CARBON BLACK

Carbon blacks are generally formed by the partial combustion of hydrocarbons [3]. The exact method of production leads to a more specific naming methodology and a

range of material properties. *Furnace*, *channel*, *thermal*, and *acetylene blacks* are all commonly available materials. The differences in production method (e.g. temperature, atmosphere, phase of precursor, etc) controls the particle size, 10 – 500 nm, specific surface areas, 10 – 1000 m^2/g, and underlying material structure [3]. During production spherical, porous carbon particles are produced that join together to form larger aggregates. The size of the aggregates is typically an order of magnitude larger than the particles. The sphericity of the particles is thought to arise from the condensable or liquid nature of the hydrocarbon precursor [3]. The carbon black particles contain micro and mesopores while the agglomerates may form macropores 50 nm or larger (IUPAC terminology) [4]. The pores play an important role in how the support interacts with the surrounding polymer, liquid, or gas.

The main uses of carbon black is for composite polymer materials, pigments, and general-purpose adsorbents [3, 4]. An important, secondary use is that of carbon catalyst supports. These supports may be for electrochemical or heterogeneous chemical reactions. What is more, carbon black is an irreplaceable electrode component of supercapacitors, Li-ion batteries, and redox-flow batteries [4, 5].

3.3. MATERIAL SCIENCE OF GRAPHENE

A graphene sheet is composed of a single layer of hexagonally bonded carbon atoms, Figure 3.1. The sp^2 hybridized carbon atoms form a stable structure terminated by

the edge and basal planes. The basal plane refers to a top-down view of the honeycomb structure or flat portion in common parlance. The edge may have either arm-chair or zig-zag bonding when observed viewing through plane. Graphite is formed when the graphene sheets are layered on top of one another. Noncovalent bonding in the form of π-π electron interactions hold the graphene sheets in place [6]. The structure of the graphene sheet leads to the anisotropic physico-chemical characteristic of graphite. The electronic conductivity of the graphite is considered a semi-metal parallel to the basal plane [7, 8]. However, the electrical conductivity perpendicular to the basal plane is lower by an order of magnitude. The two most common graphite crystals include ABABAB stacked *hexagonal graphite* and ABCABC stacked *rhombohedral graphite* [4, 7, 9]. Hexagonal graphite is most common and depicted in Figure 3.2 .

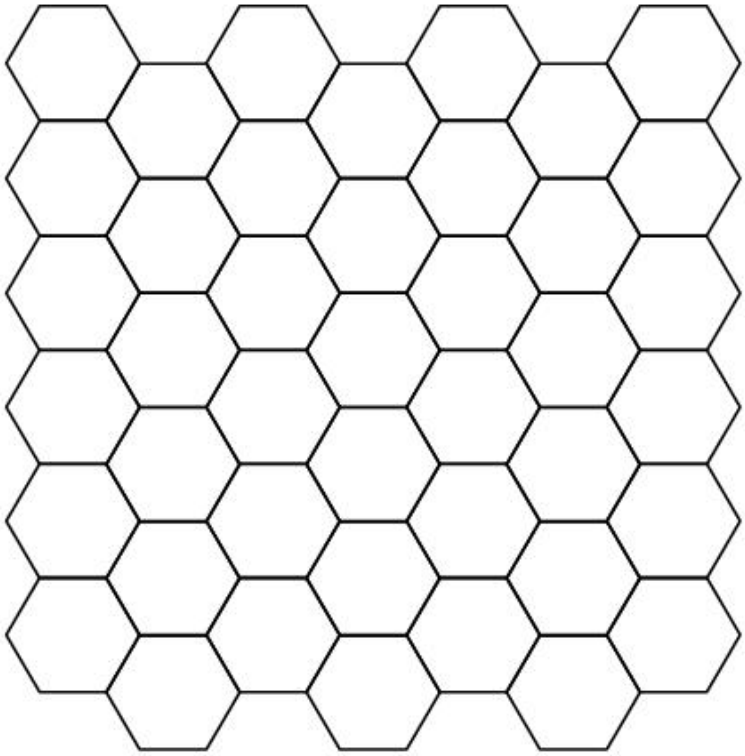

Figure 3.1. Graphene sheet with the left and right edges in the zig-zag configuration and the top and bottom edges in the arm-chair conformation.

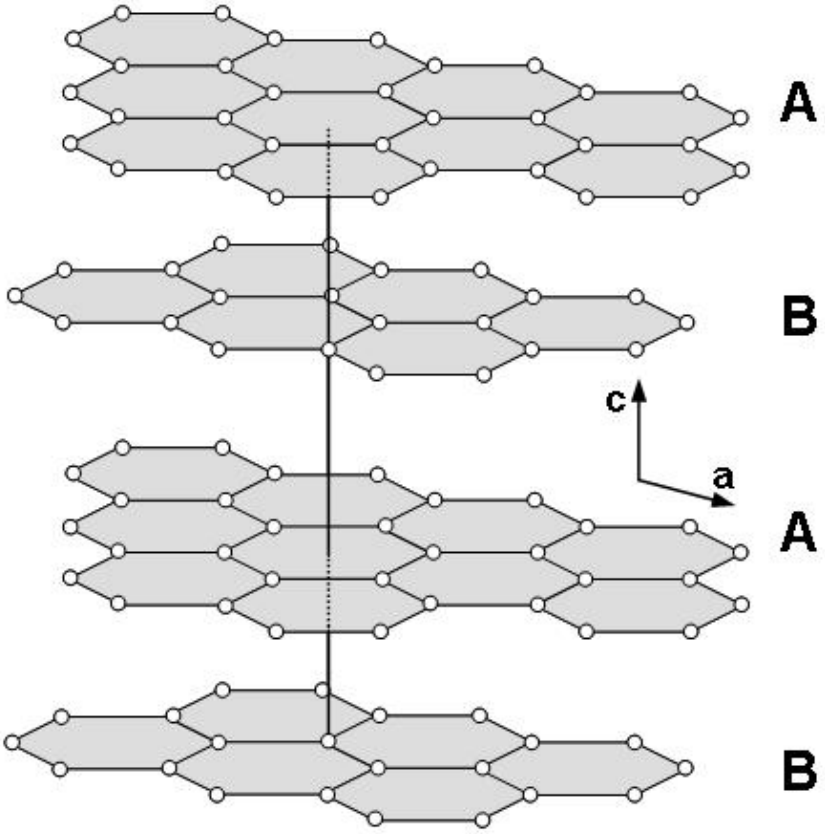

Figure 3.2. Hexagonal graphite layered in an ABABAB sequence.

The dimensions of the graphene sheet and the spacing between consecutive layers are important characteristics for comparison to less ordered systems such as carbon black. The interlayer spacing, sometimes referred to as the d-spacing, is 0.3354 nm in a perfect graphite crystal [4, 7]. The length of uninterrupted stacking in the c-direction is referred to as L_c. The continuous length of graphene in the a-direction is referred to as L_a. These values may be measured utilizing a number of different experimental techniques such as X-ray diffraction (XRD), Raman spectroscopy, and high resolution transmission electron microscopy (TEM) [4, 7]. L_a and L_c refer to average values for various crystals present when measured with spectroscopic and diffraction techniques.

3.4. STRUCTURE OF LESS ORDERD CARBONS

Less ordered, high surface area carbons are composed of an imperfect structure without a clear understanding of the inter-atomic bonding and higher level ordering [1, 2]. Carbon blacks have no or little long range graphitic structure. Typical L_a and L_c parameters are around 1 – 5 nm, two orders of magnitude less than graphite [4, 9]. A TEM image of a carbon black, Vulcan XC-72 produced by the Cabot Corporation, is shown in Figure 3.3. The spherical nature of an individual particle composing the agglomerate is evident. The individual graphene sheets are observed as dark lines in the TEM image. The structure appears turbostratic, with the sheets ordered to the outer layer of the particle. No ABABAB stacking is observed most likely due to minimal interlayer interaction. XRD analysis provides evidence for some degree of crystalline nature. The XRD technique and method of analysis is discussed in more detail in Chapter 6.

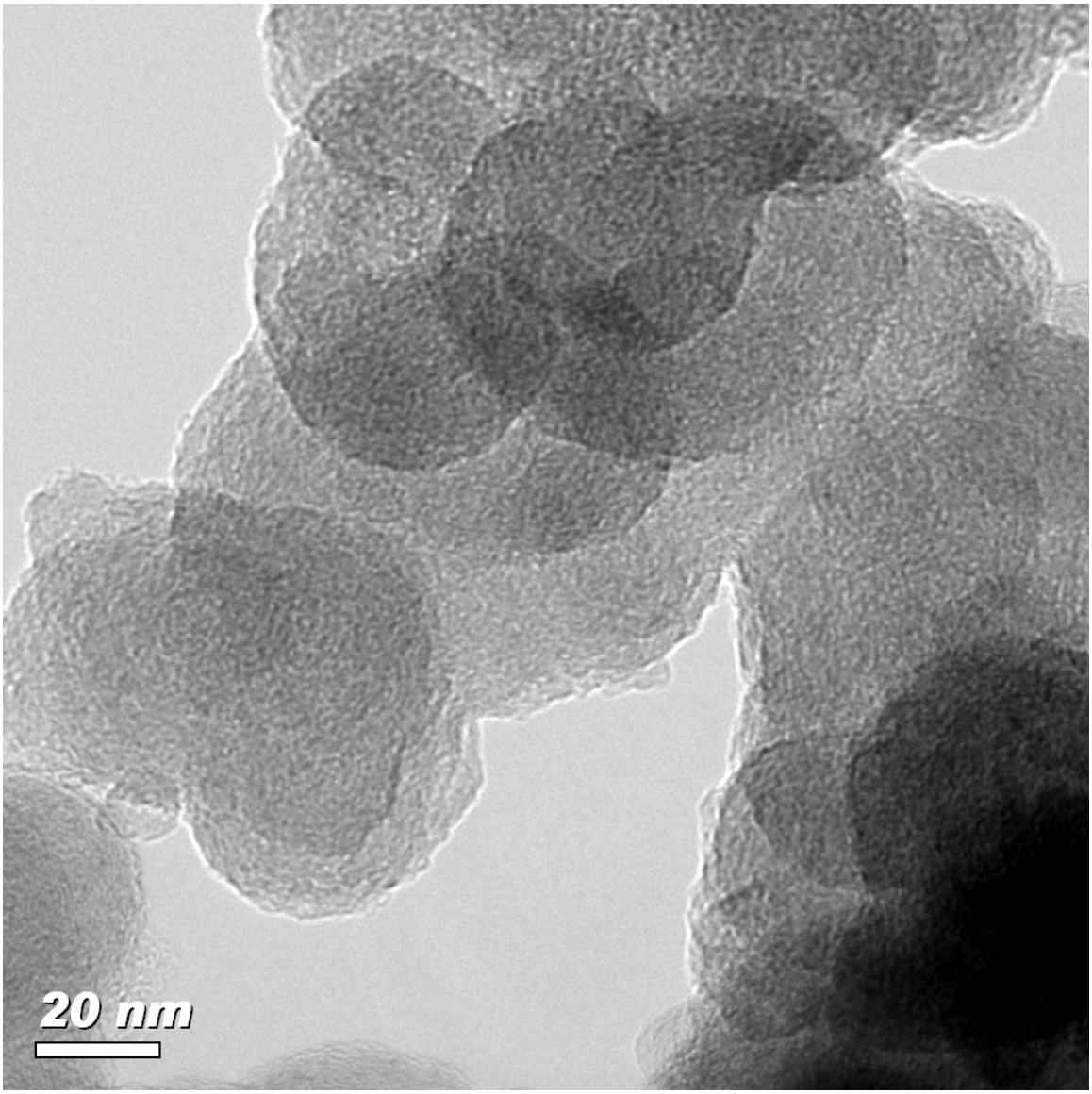

Figure 3.3. TEM image of Vulcan XC-72 carbon black particle.

Many descriptions have been given to carbon black and the nature of intra- and interlayer bonding over the years [1, 2, 10, 11]. Some suggest regions of high strain between well–ordered, low strain nanocrystalline graphene sections [10]. Pentagon and heptagon bonding arrangements have been invoked to explain the high strain carbon sheets or non-crystalline regions. Indeed these bonding arrangements have recently been observed directly in activated carbon [12]. The observation of these bonding configurations have led to a discussion of the relationship between fullerenes, hexagonal graphite, and disordered carbons [1, 2]. Much work remains before a final conclusion is reached, but fullerene fragments, rather than graphene sheets, may prove to be a more accurate representation of the basic structural unit of carbon blacks.

The relationship between graphite and carbon black is perhaps best displayed through TEM images of carbon blacks that have been heat treated. Figure 3.4 compares XC-72 as-received to samples exposed to heat treatment temperatures (HTT) of 1600 °C and 2200 °C under Argon. Heat treating the carbon black promotes graphitization. The high temperatures allow the graphene sheets to begin stacking in the arrangement expected in graphite. Existing strain and defects are removed as sheets begin to overcome the energy barrier for rearrangement. The carbon heat treated to 1600 °C maintains the turbostratic nature of the original material while transforming to a more ordered system. The 2200 °C is clearly more graphitic with nanocrystalline regions dominating the structure. This material is still far from graphite since no long range ordering exists. The graphitization process and the resulting effect on electrochemical oxidation are detailed in Chapter 5.

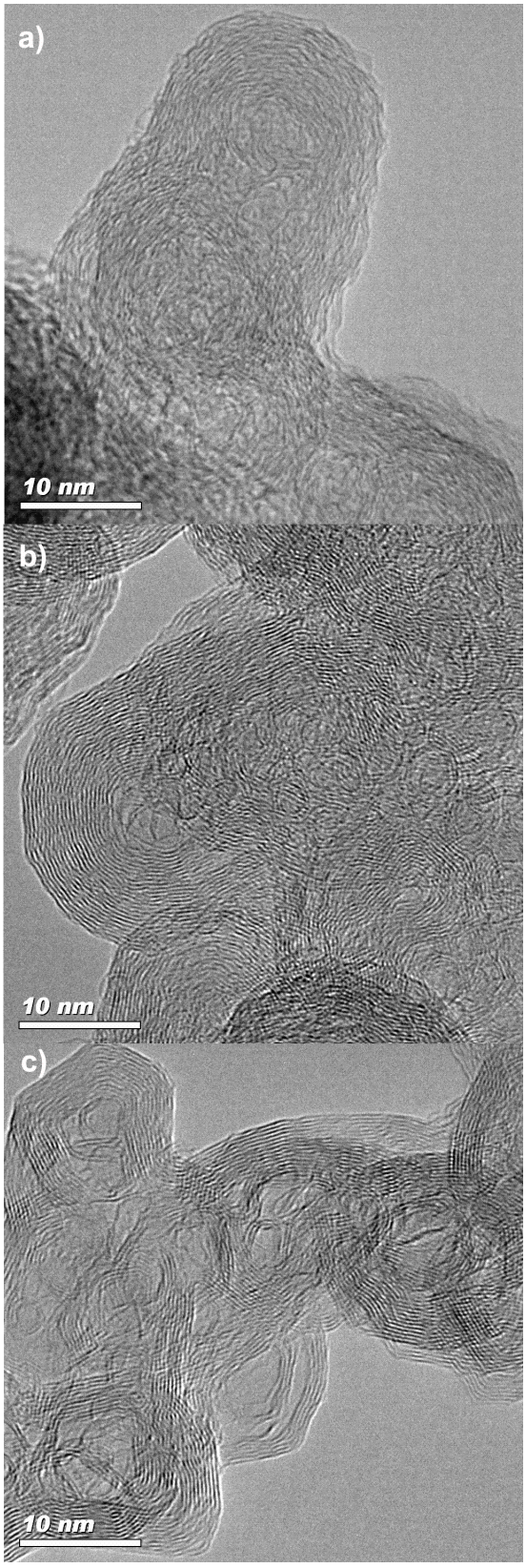

Figure 3.4. TEM image of Vulcan XC-72 a) as-received b) 1600 °C and c) 2200 °C HTT

3.5. SURFACE CHEMISTRY AND REACTIVITY OF CARBON BLACK

Carbon black is known to contain hydrogen, oxygen, sulfur, and other contaminants depending on the method of production [4]. Oxygen may also be introduced through chemisorption, chemical oxidation, or electrochemical oxidation [13]. Chemisorption may occur naturally from the earth's atmosphere principally after production, heat treatment, or other modification of the carbon black. Chemical oxidation refers to any chemical attack promoted by increased temperature or by acid treatment. Common oxidation techniques include gas phase attack with O_2, CO_2, or H_2O [4, 14]. Acid treatment is also common using chemicals such as HNO_3 [4]. Electrochemical oxidation is the focus of Part 1 of this dissertation and is discussed more completely in Chapters 2 and 4-6.

A variety of oxygen surface chemistries exist in carbon and have been the subject of review [13]. Interestingly, carbon contains amphoteric character with both acidic and basic functional groups on the same surface. The quantity and speciation of surface oxides on graphene based carbons has been investigated with a large number of experimental techniques. These techniques include, but are not limited to, X-ray photoelectron spectroscopy, temperature programmed desorption (TPD), Boehm titration, and Fourier Transform Infrared spectroscopy. Due to the well documented limitations of each technique, only a qualitative understanding of the chemistry exists. In general, multiple techniques are required, but still leave the researcher with only a modest understanding of the quantity of a specific chemistry. Lactone, anhydride, carboxylic,

quinone, and phenol functional groups have been detected as well as others. TPD involves the controlled heating of the carbon under an inert atmosphere with the simultaneous monitoring of the off-gas, preferably with mass spectroscopy. This technique is similar to heat treating but typically only reaches temperatures of 1000 °C. The vast majorities of surface oxides are desorbed from the surface by this temperature revealing the total quantity of oxides. Furthermore, a great amount of literature has attempted to correlated desorption temperature with oxide chemistry [13]. These conclusions are usually based on a chemistry leaving as either CO_2 or CO.

The edges of the graphene sheets are considered to be the location of oxide formation and reaction [4, 13]. This conclusion is reached in large part by gas phase oxidation studies of highly orientated pyrolytic graphite (HOPG) and graphitized carbons, materials with well defined basal and edge orientations [15-21]. The edge sites are theorized to be more reactive due to unsaturated bonds and a high electron density compared to the basal plane [13]. The high surface area and thus high edge site concentration of disordered carbons leads them to be more susceptible to oxidation by both chemical and electrochemical conditions. The exact reaction sites are unknown but are postulated to occur at the edges in the form of vacancies, dislocations, surface oxides, or unpaired electrons. Graphitization is a known method to decrease the concentration of all of these sites by increasing the dimensions L_a and L_c. Unfortunately, the increase in graphitic nature almost always reduces the specific surface and likely the desired property of the disordered carbon that was selected for in the initial product or process design.

3.6. SUMMARY

A material science basis for understanding the structure, chemistry, and reactivity of carbon black has been presented. Carbon black may be idealized as containing hexagonally bonded carbon sheets that could also include some pentagon and heptagon arrangements. The interlayer interaction of these sheets is governed by the method of production and post-production heat treatment. High temperature heat treatments in an inert environment promote the graphitization of carbon black by reducing strain, removing defects, desorbing surface oxides, and stacking graphene sheets. This heat treated carbon has a lower concentration of reaction sites as oxides, unpaired electrons, and dislocations are replaced by the stable basal plane.

REFERENCES

[1] Harris PJF. Impact of the Discovery of the Fullernees on Carbon Science. In: Radovic LR, ed. *Chemistry and Physics of Carbon, Vol 28* 2003:1-39.

[2] Harris PJF. New perspectives on the structure of graphitic carbons. Critical Reviews in Solid State and Materials Sciences. 2005; **30**(4), 235-53.

[3] Donnet J-B, Bansal RC, Wang M-J. Carbon Black. 2nd ed. New York: Marcel Dekker 1993.

[4] Kinoshita K. Carbon: Electrochemical and Physicochemical Properties. New York: Wiley 1988.

[5] Conway BE. Electrochemical Supercapacitors: Scientific Fundamentals and Technological Applications: Springer 1999.

[6] Grimme S. Do special noncovalent pi-pi stacking interactions really exist? Angewandte Chemie-International Edition. 2008; **47**(18), 3430-4.

[7] Dresselhaus MS, Avouris P. Introduction to carbon materials research. *Carbon Nanotubes* 2001:1-9.

[8] Kinoshita K. Electrochemical Oxygen Technology. New York: Wiley-Interscience 1992.

[9] Bandosz TJ, Biggs MJ, Gubbins KE, Hattori Y, Iiyama T, Kaneko K, et al. Molecular Models of Porous Carbon. In: Radovic LR, ed. *Chemistry and Physics of Carbon, Vol 28* 2003:41-213.

[10] Dahn JR, Sleigh AK, Shi H, Reimers JN, Zhong Q, Way BM. Dependence of the Electrochemical Intercalation of Lithium in Carbons on the Crystal-Structure of the Carbon. Electrochimica Acta. 1993; **38**(9), 1179-91.

[11] Heindenrich RD, Hess WM, Ban LL. A Test Object and Criteria for High Resolution Electron Microscopy. Journal of Applied Crystallography. 1968; **1**, 1-&.

[12] Harris PJF, Liu Z, Suenaga K. Imaging the atomic structure of activated carbon. Journal of Physics-Condensed Matter. 2008; **20**(36).

[13] Burg P, Cagniant D. Characterization of Carbon Surface Chemistry. *Chemistry and Physics of Carbon, Vol 30* 2008:129-75.

[14] Stanmore BR, Brilhac JF, Gilot P. The oxidation of soot: a review of experiments, mechanisms and models. Carbon. 2001; **39**(15), 2247-68.

[15] Rodrigue.F, Thrower PA. Microscopic Studies of Oxidized Highly Oriented Pyrolytic Graphites. Carbon. 1974; **12**(3), 269-79.

[16] Bansal RC, Vastola FJ, Walker PL. Studies on Ultra-Clean Carbon Surfaces .4. Decompostion of Carbon-Oxygen Surface Complexes. Carbon. 1970; **8**(4), 443-&.

[17] Hart PJ, Vastola FJ, Walker PL. Oxygen Chemisorption on Well Cleaned Carbon Surfaces. Carbon. 1967; **5**(4), 363-&.

[18] Lussow RO, Vastola FJ, Walker PL. Kinetics of Oxygen Interaction with Graphon between 450 and 675 Degrees C. Carbon. 1967; **5**(6), 591-&.

[19] Laine NR, Vastola FJ, Walker PL. Importance of Active Surface Area in Carbon-Oxygen Reaction. Journal of Physical Chemistry. 1963; **67**(10), 2030-&.

[20] Smith WR, Polley MH. The Oxidation of Graphitized Carbon Black. Journal of Physical Chemistry. 1956; **60**(5), 689-91.

[21] Grisdale RO. The Properties of Carbon Contacts. Journal of Applied Physics. 1953; **24**(10), 1288-96.

CHAPTER 4

THE EFFECT OF TRANSIENT POTENTIAL EXPOSURE ON THE ELECTROCHEMICAL OXIDATION OF CARBON BLACK IN LOW TEMPERATURE FUEL CELLS

4.1. INTRODUCTION

Carbon black is commonly used as a catalyst support in low-temperature fuel cells, including polymer electrolyte and phosphoric acid electrolyte fuel cells. Whereas the electrochemical oxidation (corrosion) of carbon in phosphoric acid fuel cells (PAFCs) has long been a known issue, it has only recently received attention by developers of proton exchange membrane fuel cells (PEMFCs). The lower operating temperature of PEMFCs was thought to mitigate the stability challenges; however, a push towards higher operating temperatures [1] and newly recognized decay mechanisms [2, 3] that result in excursions to high overpotentials have motivated an improved understanding of the corrosion of carbon catalyst supports.

In the history of the electrochemical oxidation of carbon in low-temperature fuel cells, the mechanism has primarily been investigated by the use of constant potential holds. The current response under these experimental conditions follows the linear log-log relation [4, 5] as described by Equation 4.1, where i is the current, k is a temperature and potential dependent rate constant, n is a potential dependent constant, and t is the time elapsed.

$$i = kt^{-n} \tag{4.1}$$

This approach of modeling the corrosion current is appropriate for long potential exposures seen in systems such as PAFCs. In contrast, PEMFCs, which are targeted for transportation applications, are more likely to experience carbon corrosion conditions for brief periods but over thousands of cycles. The inadequacy of Equation 4.1 to accurately represent this transient potential exposure is becoming apparent [6]. Hysteresis is exhibited during carbon oxidation tests, but this has been explored to only a minor extent in open literature [4, 7]. The purpose of this work is to explore the electrochemical oxidation of carbon black catalyst supports under transient potential exposures.

The effect of platinum in accelerating the electrochemical oxidation of carbon catalyst supports has been studied [8-10]. Although the exact mechanism is still unclear, evidence suggests that platinum serves to catalyze the carbon oxidation reaction. Understanding of this coupling is complicated by both the poorly understood carbon corrosion mechanism and the instability of platinum under high potentials [11-13]. The surface area of the platinum constantly changes due to particle growth and loss from sintering and dissolution. Before the role of platinum can be elucidated, a consensus on the mechanism of carbon corrosion must be realized.

4.2. EXPERIMENTAL

4.2.1 Material

All results reported here-in are based on Vulcan XC-72R provided by the Cabot Corporation. The ability of this material to meet the durability demands of automotive applications remains uncertain; nevertheless, this carbon black is considered the standard for experimental work.

4.2.2 Liquid Half-Cell

A three-electrode setup was used to evaluate the effect of dynamic potential exposures on PTFE bonded carbon in ½ M H_2SO_4. The working electrode, 90 % carbon and 10 % PTFE, was controlled against a reversible hydrogen electrode (RHE) and a platinum gauze counter electrode. The working electrode consisted of a wet-proofed Toray^{TM} (TGPH-060, 8 mil thickness, standard wet proofing, purchased from E-TEK) carbon paper support on which an isopropyl alcohol solution containing the appropriate proportions of carbon and PTFE was applied. The resulting sample was sintered in air at 330 °C for fifteen minutes. Electrical contact was made by threading a platinum wire through the carbon paper above the point of electrolyte contact to minimize background currents. The pores of the electrode were filled using the solvent switch procedure of Kangasniemi *et al*. [14]. The electrolyte was continuously purged with nitrogen gas that was saturated with water at the same temperature as that of the cell. The loss of electrolyte over the length of the experiments conducted was deemed negligible due to

the low vapor pressure of sulfuric acid. The electric potential was controlled using a PAR 263 potentiostat with CorrWare™ software.

4.2.3 Single-Cell Membrane Electrode Assemblies

Membrane electrode assemblies (MEAs) were fabricated by airbrushing the catalyst layer ink onto a Nafion® 117 membrane provided by the DuPont Company. On the cathode side, the ink consisted of carbon black and Nafion® ionomer solution (Electrochem, Inc.) mixed to maintain a mass ratio of 1.0:0.8 grams of carbon to ionomer with a typically carbon coating of 0.9 mg/cm^2. On the anode side, 40 % Pt/C ETEK catalyst was mixed with the same ratio of ionomer with a typical platinum loading of 0.3 mg/cm^2. The resulting MEA was sandwiched between two wet-proofed Toray carbon paper gas diffusion layers and assembled in single cell hardware (Fuel Cell Technologies, Inc.). This unit was tested in a fuel-cell test stand that provided accurate control of reactant flow, humidity bottle temperature and cell temperature (Teledyne Energy System Inc. Model 890CL). The electric potential was controlled using a PAR 263 potentiostat with CorrWare™ software. The anode served as both the reference and counter electrodes. The anode and cathode were fed hydrogen and nitrogen respectively at 0.3 dm^3/min. The MEA was cycled from 0.35 to 0.85 V vs. RHE (V_{RHE}) at the cell temperature of 80 °C until a constant voltammogram was obtained. The gas streams were humidified at 60 °C, a_w = 0.42, minimizing required water removal capacity and thus minimizing downstream mixing of the gas stream.

4.2.4 On-line Gas Analysis

The cathode exhaust was continuously monitored for CO_2 with a model 600 series non-dispersive infrared detector (NDIR) from California Analytical Instruments, Inc. Typical values of measured CO_2 concentrations varied from 10-150 ppm. The humidified stream was chilled to 5 °C to condense the water before sending the dry gas to the instrument.

4.2.5 X-ray Photoelectron Spectroscopy

The XPS spectra were collected using a Physical Electronics (PHI) Model 1600 XPS system equipped with a monochromator and an Al Kα source ($h\nu$ = 1486.8 eV) operating at 350 W beam power. Corroded samples were repeatedly rinsed in deionized water to remove any acid residue. Samples were aligned in the beam by maximizing photoelectron counts corresponding to the primary C1s peak in C-C bonds located at a binding energy of 284.6 eV. A neutralizer beam was used during XPS measurements to compensate for peak shifting that occurs due to charging of samples during X-ray exposure. The XPS chamber was maintained below 5×10^{-9} Torr. All high resolution spectra were collected using a pass energy of 46.95 eV. The step size and time per step were chosen to be 0.025 eV and 100 ms, respectively.

4.3. RESULTS

Hysteresis is observed during potentiostatic oxidation experiments, depending upon the range of deviation from the original potential. If a constant potential carbon

corrosion test is interrupted, held at the open-circuit potential briefly, and then restarted, only a small deviation from the typical current response results. If during the interruption, the potential is cycled in a typical procedure for a cyclic voltammogram (CV) between 0.04 and 1.30 V_{RHE}, the current response appears to restart, Figure 4.1. In other words, the current follows Equation 4.1 if the time variable, t, is replaced by $(t-t_{cv})$ where t_{cv} is the time the last CV was measured. The difference in the two current responses may be explained by the reduction of the surface oxides, which grow during the constant potential hold, by the low potentials of the CV sweep. When the hold is re-initiated, the surface of the carbon is once again electrochemically oxidized.

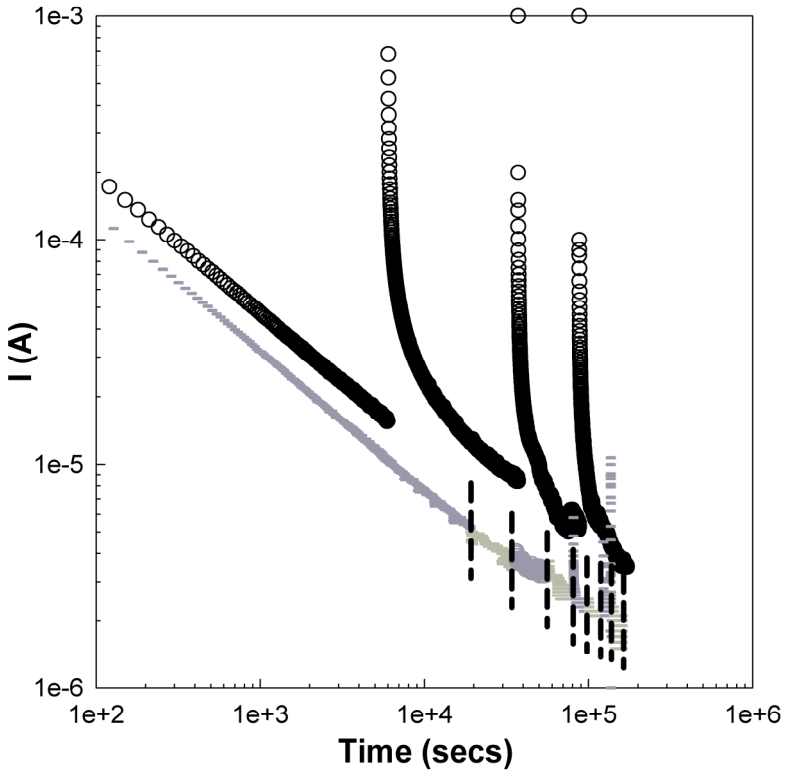

Figure 4.1. Comparison of constant potential holds interrupted by CVs (13600 cm^2 active carbon; circles) or open circuit holds (8775 cm^2 active carbon; solid lines separated by vertical dashed lines for every start). Total current is not normalized to mass of sample to prevent overlay of data. Sample tested at 1.2 V_{RHE} in ½ M H_2SO_4 at 22 °C.

To further investigate the effect of potential exposure on oxidation, square wave cycling was compared to constant potential holds in the liquid half cell. In the cycling, the sample is held for the same total amount of time at the high potential as experienced by the sample in the constant potential experiment, 1.2 V_{RHE}. The lower potential, 0.6 V_{RHE}, was chosen to be relevant to fuel cell operation. CVs were measured at room temperature with a sweep rate of 10 mV/s after 50 hours at the high potential in 60 °C ½ M H_2SO_4 (100 total hours for the square wave cycled sample), Figure 4.2a. These characteristic voltammograms occur at all temperature conditions tested from 22 to 80 °C.

The most interesting result is that at potentials greater than 1.0 V_{RHE} the current for carbon oxidation is 50 % lower for the case where the potential is cycled. At 22 °C, this change in the SQWV cycled CV is found to happen within the first six hours of the corrosion process whereas little change has occurred in the constant potential hold CV, Figure 4.2b. Shorter potential scan CVs, 0.35 to 0.85 V_{RHE}, reveal the current of the quinine/hydroquinone group (Q/HQ) found at the redox potential of ~0.55 V_{RHE} [15] to be similar for the two different oxidation tests, see inset in Figure 4.2a. The two short potential scan CVs are nearly identical.

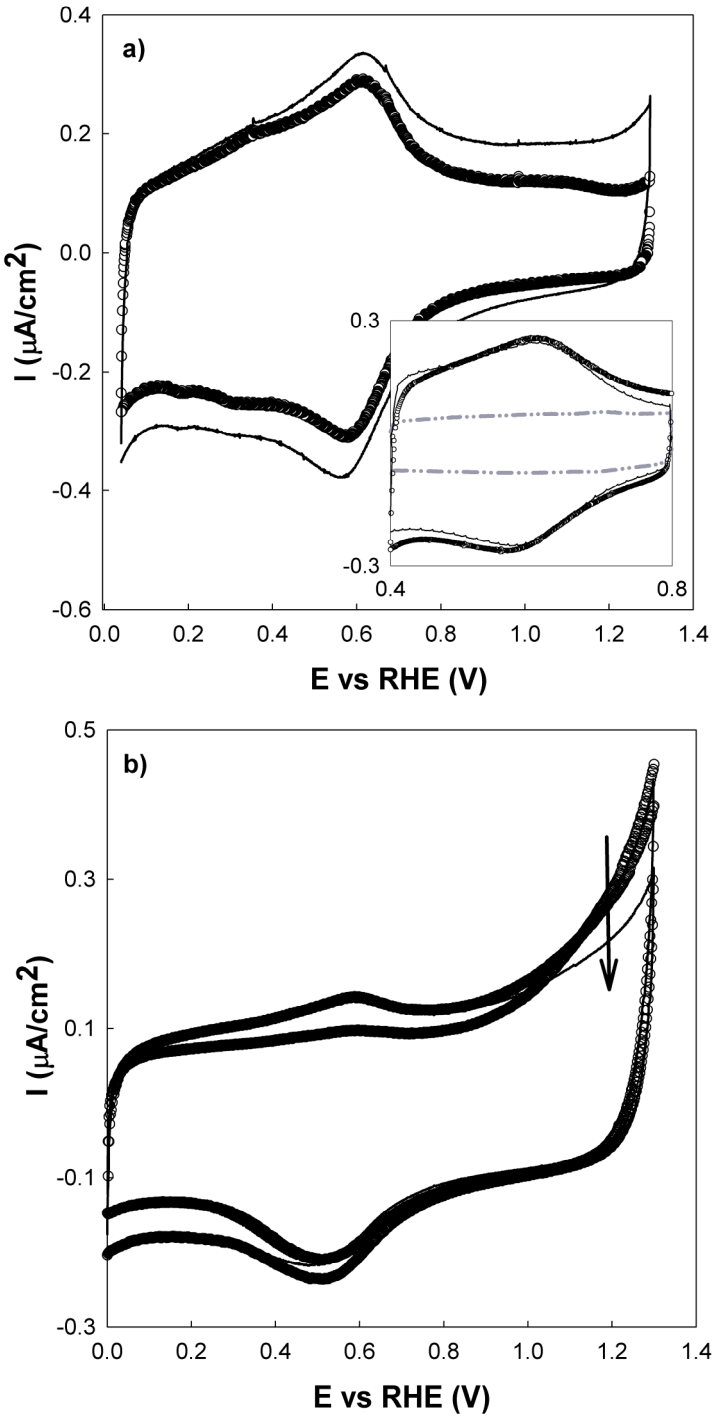

Figure 4.2. a) Comparison of square wave cycling (circles) to constant potential hold (line) at 60°C. Inset: Measure of Q/HQ activity over short potential range scan. Dashed line is before anodic treatment. b) Evolution of CV during different corrosion testing at 22 °C: SQWV (circles) and constant potential hold (line). All CVs conducted with a sweep rate of 10 mV/s.

On-line gas analysis was employed to quantify the differences in CO_2 production between these two potential exposures. These experiments were performed in the PEMFC single cell to allow for the higher gas flows required by the NDIR and to avoid solubility issues with a liquid electrolyte. Previous unpublished work by the authors of this paper has found the solubility of CO_2 in dilute sulfuric acid is high enough to preclude its use for transient analyses. The upper potential was raised from 1.2 to 1.3 $V_{RHE,}$ and the cell temperature was raised to 80 °C to increase the level of CO_2 and thereby enhance detection. CVs were performed after each corrosion test to monitor the activity of the surface oxides and carbon oxidation. The CVs and CO_2 values are normalized to the active area of the carbon determined during an initial short scan CV, 0.35 to 0.85 V_{RHE}, where the current is largely due to the charging of the double layer. Using Equation 4.2, with a capacitance of $8x10^{-6}$ F/cm^2 [15] we have found ~95 % of the electrode is available during the test. This is based upon in-house gas adsorption measurements of Vulcan XC-72R that find a BET specific surface area of 250 m^2/g in good agreement with literature. In Equation 4.2, v is the potential sweep rate, A is the active surface area and C is the capacitance. All reported current and rate of carbon loss values are normalized to carbon surface area unless otherwise stated.

$$i_{dl} = Vac \tag{4.2}$$

The CO_2 response comparing the SQWV cycling to a constant potential hold is shown in Figure 4.3a. The two different exposures produce similar CO_2 values in the beginning of the tests, albeit against different units of time. Around 60 minutes, the

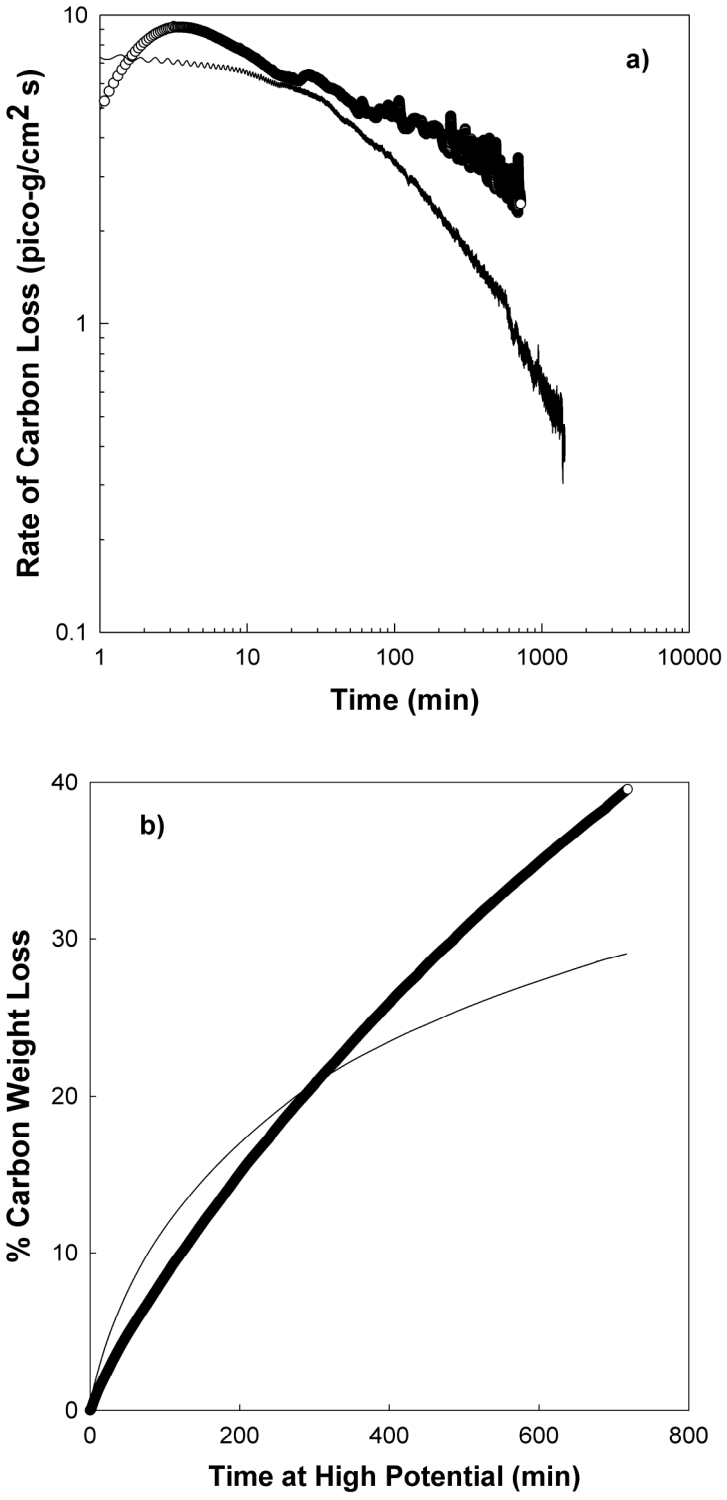

Figure 4.3. a) Comparison of area normalized CO_2 production by SQWV (0.6 to 1.3 V_{RHE}, thick line) to constant potential hold (1.3 V_{RHE}, thin line) at 80 °C in PEMFC. b) Comparison of percent weight loss between SQWV (thick line) and constant potential (thin line) versus time at high potential.

SQWV cycling rate of CO_2 production begins to decrease quickly. As previously stated, less severe testing in the liquid half cell (22 °C and 0.6 to 1.2 V_{RHE}) showed substantial changes in the CV near 360 minutes. In an attempt to compare the two potential exposures on a similar time scale, the percent weight loss calculated from measured CO_2 is plotted in Figure 4.3b against the time at high potential, 1.3 V_{RHE}. The early weight loss is larger for the SQWV cycled sample due to an initial higher electrochemical oxidation rate. This production rate begins to slow down and eventually becomes smaller than the constant potential hold suggesting the growth of a protective oxide or inhibition of the corrosion process. The large weight loss, ~30 %, may affect the CO_2 production rate; however, the characteristic voltammograms are observed under significantly less severe potential and temperature exposures supporting the validity of the presented results.

The differences between the two potential exposures are further realized by monitoring the CO_2 produced during a CV at 80 °C after the corrosion test. In Figure 4.4, results are presented for both a pristine sample and a sample that underwent SQWV cycling. For the SQWV cycled sample each full potential scan, 0.04 and 1.30 V_{RHE}, has two separate areas where CO_2 is evolved. The second burst of CO_2 occurs at the apex of the potential scan due to the high overpotential for the electrochemical oxidation as is also seen for the pristine sample. The first peak is only present after the sample is exposed to high potential and is barely detectable in the CVs of the pristine sample. The first burst of CO_2 is unexpected since it occurs at a much lower potential, below the standard potential for carbon, $U^{\theta} = 0.207$ V vs. SHE.

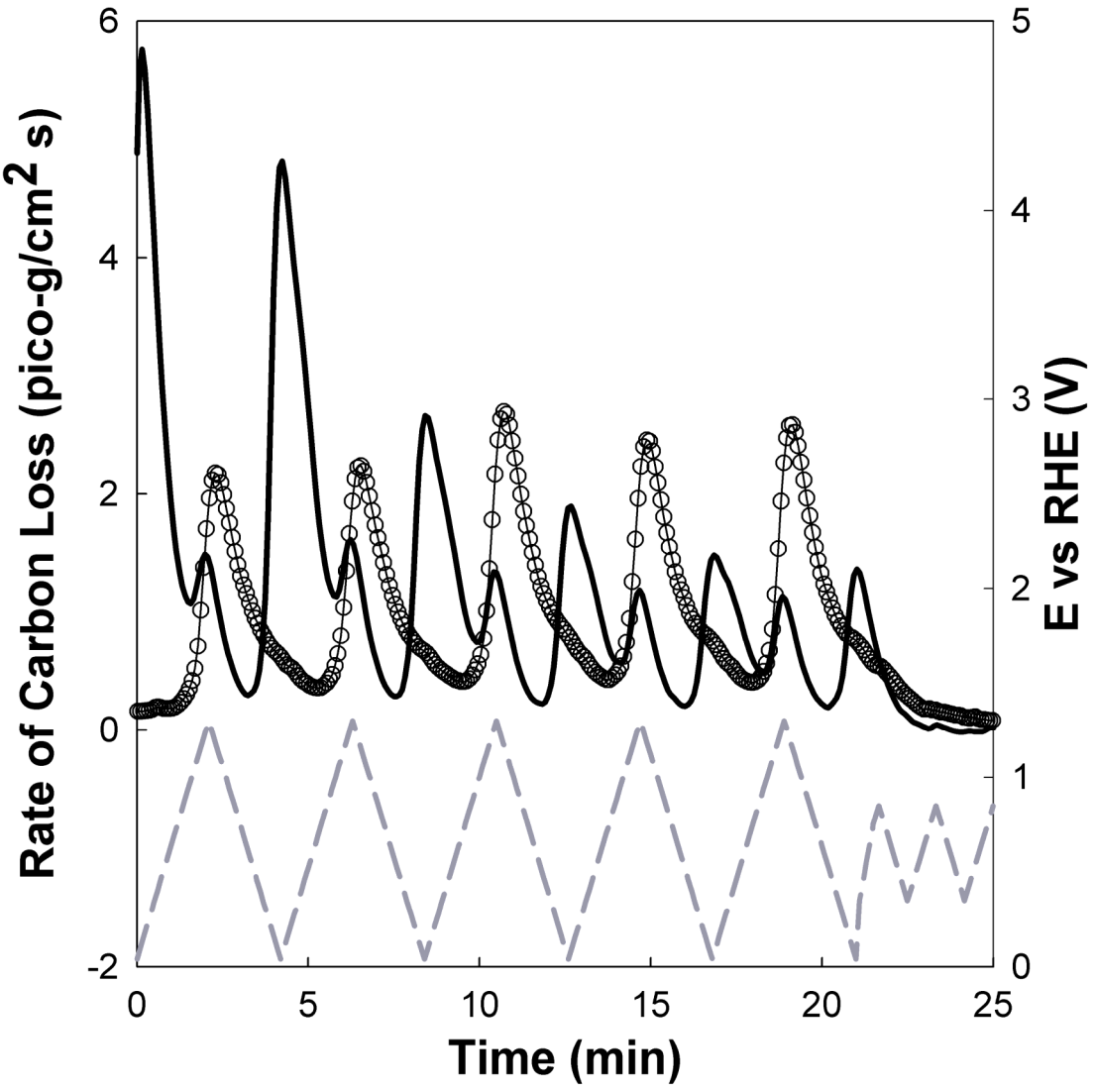

Figure 4.4. CO_2 produced during a diagnostic CV for a pristine sample (circles) and after SQWV cycling (solid line). Dashed line represents potential wave-form, ν = 10 mV/s.

After five full scale potential scan CVs, we immediately conducted three small scale potential scan CVs, 0.35 to 0.85 V_{RHE}, which evolve no further CO_2. In Figure 4.5, potential scans of different ranges were investigated to probe the CO_2 formation. Figure 4.5a shows that only the CO_2 peak corresponding to low potentials is seen when the CV scans over 0.04 to 0.85 V_{RHE}. Figure 4.5b presents the alternate result of CO_2 being measured only at the high potential of a 0.35 to 1.30 V_{RHE} scan. This evidence coupled with the lack of an obvious oxidation current peak at low potentials suggests that the CO_2 found at low potentials relies upon an electrochemical reduction before the gas is formed and/or expelled from the carbon. Indeed the reduction peak below 0.14 V_{RHE} qualitatively matches the decrease in the size of the first peak of CO_2 with each repeated CV, Figure 4.6a. The cumulative CO_2 and reduction current below 0.14 V_{RHE} on the negative sweep of the CV is compared in Figure 4.6b. The CO_2 is converted into a current assuming four electrons and Faraday's Law. The ratio of charge, Q_{CO2}/Q_{red}, decreases with each successive voltammogram. When an oxidized sample is held at 0.040 V_{RHE} for ten minutes, the current attributed to CO_2 decreases to an order of magnitude less than the total reduction current (data not shown here). Since the first presentation of this material, Colmenares *et al*. have presented a more robust treatment of this phenomenon [16] that is discussed further in section 4.2. The CV should have been initiated at the open circuit potential. The SQWV cycled sample has a lower concentration of reversible oxides than the sample oxidized at potentiostatic conditions. However the work presented later in Chapter 6 suggests the lower concentration of reversible oxides is not responsible for the behavior observed here.

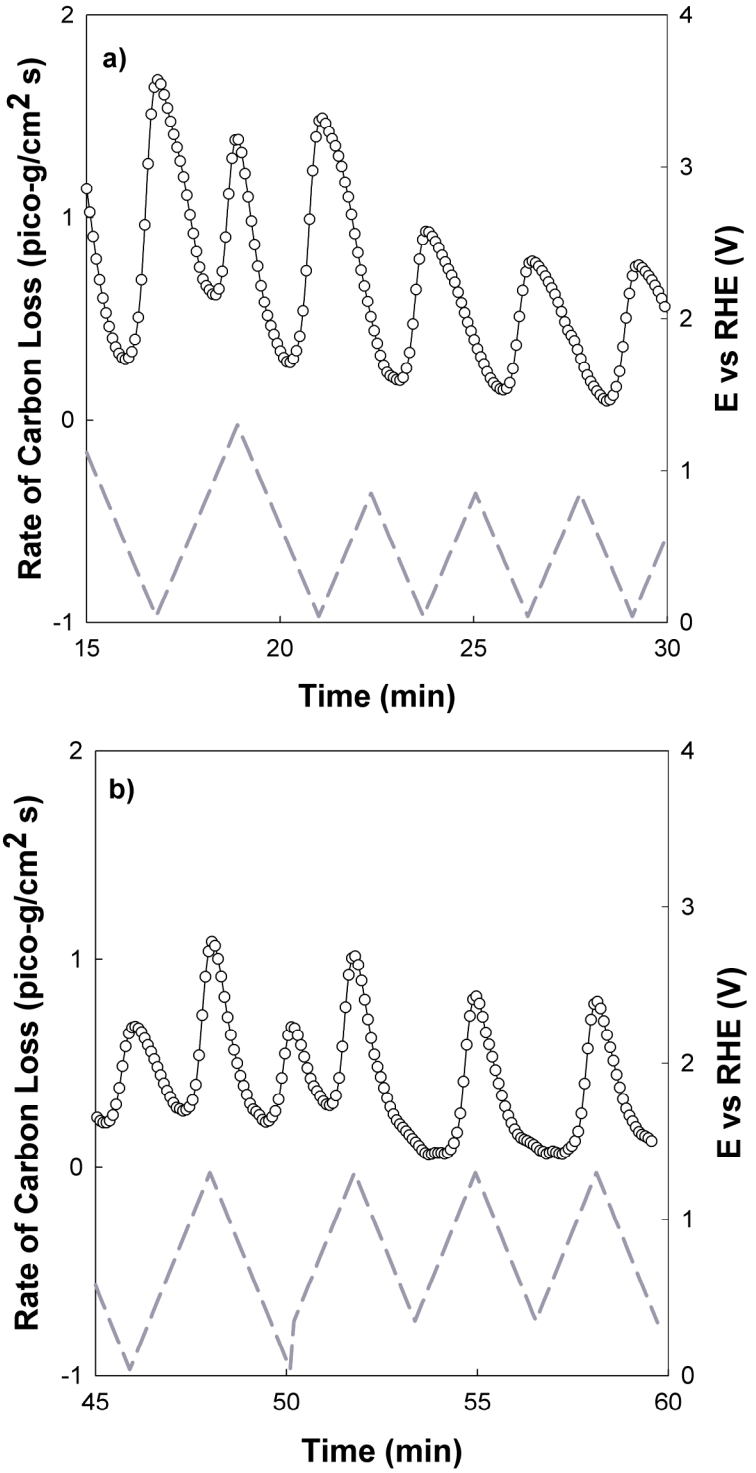

Figure 4.5. CO_2 produced during a diagnostic CV after SQWV cycling. Dashed line represents potential wave-form, v = 10 mV/s. a) CV sweeps 0.04 to 1.30 V_{RHE} then 0.04 to 0.85 V_{RHE} b) CV sweeps 0.04 to 1.30 V_{RHE} then 0.35 to 1.30 V_{RHE}.

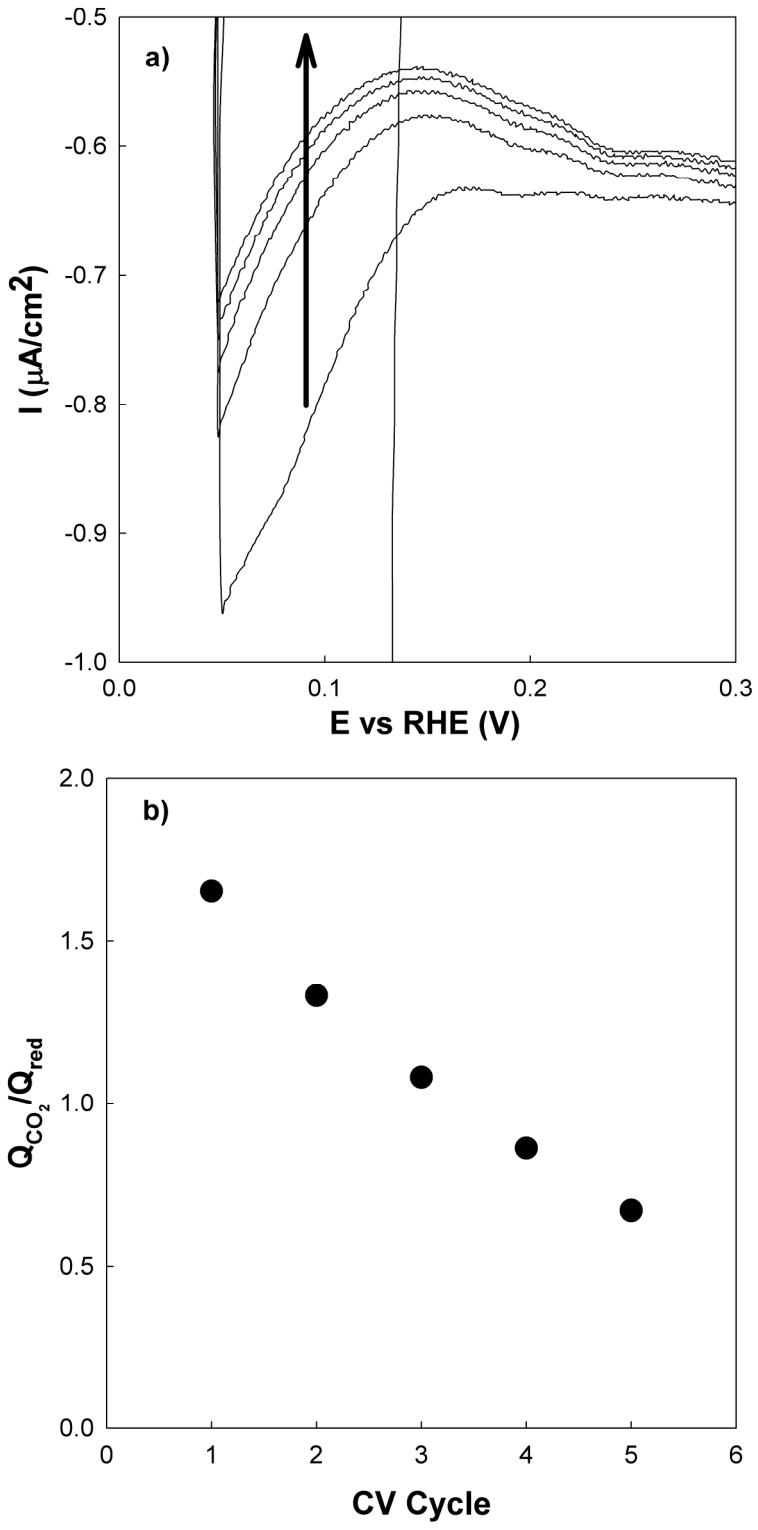

Figure 4.6. a) Portion of a full scale potential sweep over five CVs. b) Ratio of charge Q_{CO2}/Q_{red} from on-line CO_2 measurements and measured currents collected during a diagnostic CV.

The different corrosion tests result in different quantities of CO_2 to be produced during the post-diagnostic CV. Figure 4.7 displays the CV CO_2 measurements for SQWV cycling followed by a constant potential hold and finally a SQWV cycling series all on the same MEA. The CO_2 produced from a CV taken after a constant potential exposure is higher than after square wave cycling. This is most apparent on the CO_2 peak that occurs at high potential. The two CO_2 peaks decay at different rates for the CV taken after a constant potential hold. The second CO_2 peak seems relatively constant for the CV taken after square wave cycling though the first peak shows a similar decay rate to the constant potential hold case. The difference between the first and third test, both SQWV, is most likely due to the loss of carbon over the course of the experiment. Thus, the higher quantity of CO_2 during the CV after a constant potential hold is surprising since it had experienced more overall CO_2 loss than when the previous CV had been measured, 12 hours earlier. However, this matches the relative magnitude of the carbon oxidation current in the voltammogram at potentials greater than 1.0 V_{RHE}, see Figure 4.2 for comparison. These data considered with the CO_2 response during the corrosion tests strongly suggest a surface chemistry of a protective nature (i.e. passivity) is forming during square wave cycling.

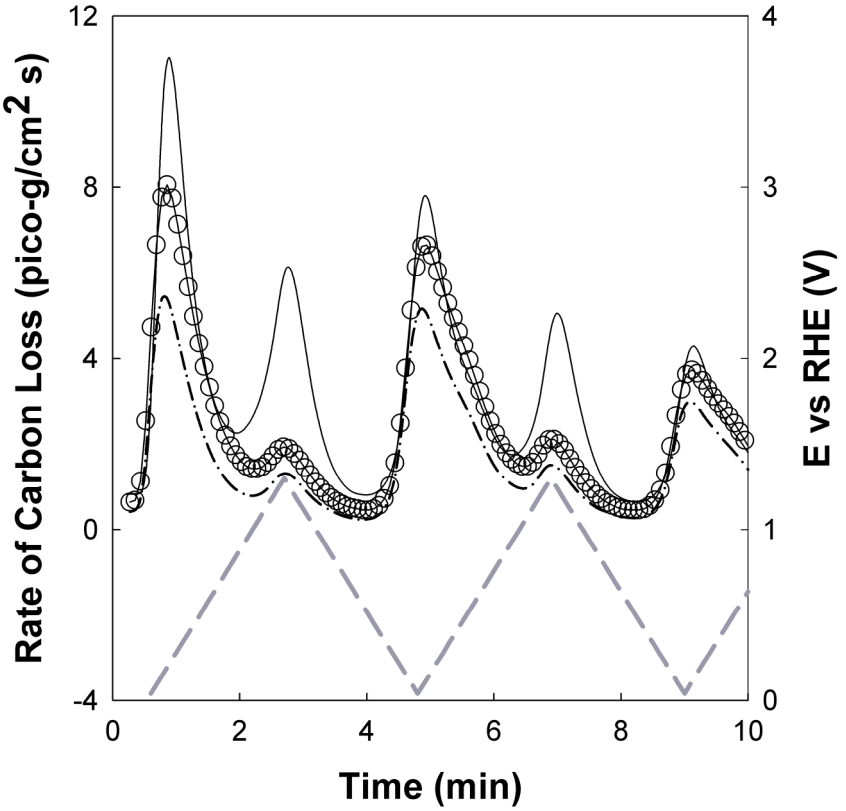

Figure 4.7. CO_2 produced during a diagnostic CV for the same sample after SQWV cycling (circles), constant potential hold (solid line) and a repeat SQWV cycling (dash dot line). Dashed line represents potential wave-form, v = 10 mV/s.

The full scan CV and corresponding CO_2 production imply that the surface chemistries of the two different corrosion processes are different. XPS was employed in attempt to distinguish speciation and concentration. Three samples were tested at 60 °C in the liquid half cell. One sample was held at 1.2 V_{RHE} for 50 hours while another was square wave cycled between 0.6 and 1.2 V_{RHE} for 50 hours at the high potential (100 hours total). The pristine sample underwent the initial CV diagnostic and no further testing. Three XPS scans were taken at different locations on each sample.

The C1s (carbon 1s orbital) spectrum of carbon requires peak fitting to deconvolute the overlapping peaks. Our experience along with that of other researchers in the field [17] lead to a caveat: the fitting of an XPS spectrum must be undertaken with caution. Without even considering the surface oxides, the C1s spectrum of carbon black is complex. Three overlapping peaks resulting from the carbon structure dominate the electron emission. The first peak at 284.6 eV is attributed to the graphitic portion of carbon black and is well documented. Only recently, strong evidence has been published supporting the division of this peak into another defect peak 0.5 to 1.0 eV higher in binding energy [17, 18]. The defect peak is a result of the nanocrystalline nature of graphite in carbon black. The third peak is the so called carbon shake up peak, $\pi \rightarrow \pi^*$, related to the excitation of the delocalized electrons in the graphene sheets located near 291 eV. Accurate curve fitting requires maintaining the physical relationships between these three peaks. In this analysis, the separation distances between the main carbon peak and the defect and shake-up peaks are held constant. Also, the ratio of the main carbon peak area to the shake-up peak area is held constant. These values are taken from the pristine sample. In a more rigorous analysis, these values would be derived from the spectra of the sample after heat treatment, which will reduce complications due to oxides and the large defect peak.

Although the degree of specific chemistry is arguable, agreement exists on the binding energies of two general carbon oxygen bonds, C-O and C=O. The single and double bonded oxygen groups are found at a binding energy of 286.7 and 288.9 eV respectively [14, 17, 18]. The CF_2 peak is located at 293 eV and only overlaps with the

shake-up peak of carbon [19]. Examples of the measured spectrum may be found in Figure 4.8. No attempt to deconvolute the O1s (oxygen 1s orbital) spectrum was made due to the lack of distinct characteristics. Only a direct comparison of total atomic oxygen in the O1s to total carbon in the C1s is considered. Oxygen due to quantified residual sulfate anions detected in the sulfur S2p spectra was removed from the O1s total.

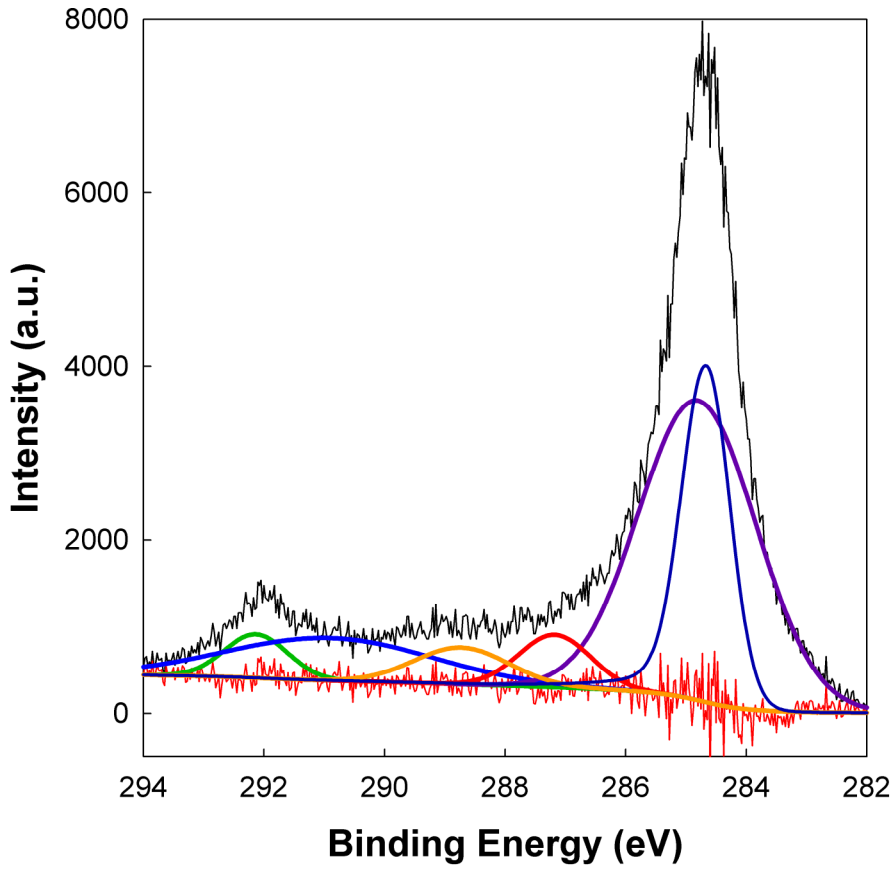

Figure 4.8. XPS C1s measurements curve fit to determine oxygen speciation and concentration for a SQWV cycled sample.

No statistically significant concentration differences between corrosion tested samples were found using this method, Table 4.1. A typical standard deviation was found to be 15 % of the mean value. XPS is limited by a number of factors such as its inability

to probe deeper than ~5 nm of the carbon black particle and the inaccurate nature of curve fitting a carbon 1s orbital spectrum [17].

Table 4.1. XPS results for different potential exposures at 60 °C in ½ M H_2SO_4.

Sample	%CF	%C-O	%C=O	Total %CO	%O1s/%C1s
1.2 V 50hrs	4.7	6.6	4.7	11.3	0.12
0.6-1.2V 100hrs	4.9	5.6	5.6	11.2	0.11
Pristine	4.9	5.3	2.2	7.5	0.09

4.4. DISCUSSION

4.4.1 Square Wave Potential Cycling

The corrosion response of carbon black under square wave cycling is different from that which occurs under a constant potential hold. Based upon cyclic voltammetry and on-line CO_2 measurements, the square wave cycling appears to undergo less corrosion after an initial accelerated period. No significant difference in surface oxide concentration or speciation was found within the limitations of the XPS analysis. Nonetheless, the short potential scan CV (0.35 to 0.85 V_{RHE}) shows a comparable activity in the Q/HQ species suggesting similarities between the two different potential exposures. Previous works have shown the Q/HQ species, measurable in short potential scan CVs, are a fraction of the total surface oxide coverage [14, 15]. Greater understanding of the corrosion response under transient potential exposures is necessary to enable the prediction of long term performance decay in PEMFCs.

4.4.2 Carbon Dioxide at Low Potentials

The appearance of the CO_2 peak at low potentials was not shown in two previously published works [9, 10] and only briefly considered in another analyzing gas evolution off of porous carbon electrodes under a potential sweep [20]. This is most likely a result of the previous works analyzing the sample prior to significant anodic treatment. As is shown in Figure 4.4, the low potential CO_2 peak only results after electrochemical oxidation of the carbon has taken place. Since the public presentation of the work contained in this chapter, two other papers have investigated this phenomenon [16, 21]. Their results will be discussed after the origin discussion of the source of CO_2 is presented.

The origin of the CO_2 emitted at potentials below the standard potential for carbon oxidation is in question. The correlation with an electrochemical reduction is apparent although the exact relation is unclear. In order for this CO_2 to be released, another species must be reduced. Two possible mechanisms are suggested by the authors of this work. First, the reduced species could be an oxidant that chemically attacks the carbon and produces CO_2. This pathway is commonly referred to as an EC mechanism for an electrochemical reaction followed by a chemical reaction [22]. The other possible mechanism requires a reduction of the surface oxide species to release previously produced CO_2. Each of these possible scenarios will be expounded upon below.

The EC mechanism requires a species that oxidizes the carbon black chemically, and this species must be the product of an electrochemical reduction below 0.35 V_{RHE}.

Hydrogen peroxide is a known product of the reduction of oxygen on carbon black, U^{θ} = 0.695 V vs. SHE. Hydrogen peroxide is also a known oxidant. A proposed mechanism could be based off the work of Chaparro *et al*. as shown in Equations 4.3-4.5 [20]. This mechanism requires the transfer of four electrons to result in one molecule of CO_2. Willsau and Heitbaum also briefly suggest this mechanism [10].

$$2O_2 + 4e^- + 4H^+ \rightarrow 2H_2O_2 \quad (4.3)$$

$$C + H_2O_2 \rightarrow CO + H_2O \quad (4.4)$$

$$CO + H_2O_2 \rightarrow CO_2 + H_2O \quad (4.5)$$

Although these experiments were conducted under the flow of nitrogen, only a trace amount of oxygen, ~35 ppm based upon Equation 4.3 and Faraday's Law, is required to sustain the observed reduction currents at low potentials. This oxygen could enter through the water in the fuel cell test station saturators or perhaps across an imperfect seal. A reason for the absence of the CO_2 at low potentials in the pristine cyclic voltammogram is also required. Other published works suggest that an oxidized or activated carbon surface is required for oxygen reduction on carbon black [23, 24]. This would explain why anodic treatment of the electrode is necessary before this phenomenon is observed.

The EC mechanism is less likely when one considers the changing ratio of CO_2 and charge passed over time. As shown in Figure 4.6b, the CO_2 production decreases at a faster rate than the electrochemical reduction current. A constant ratio would be expected if the proposed reactions, Equations 4.3-4.5, were indeed taking place. Not only does the ratio of CO_2 to reduction current decrease, but the reduction current is independently decreasing with each cycle. An initial explanation may rationalize that oxygen adsorbed during anodic treatment is reduced over time until the concentration reaches a steady state. However, all of the adsorbed O_2 would most likely be reduced in the first scan. The second mechanism addresses these concerns.

The release of adsorbed or trapped CO_2 might be possible if surface oxide species are reduced. This line of reasoning coincides with the potential region being below that of the standard potential for carbon oxidation. A constant ratio of CO_2 to reduction current would not be expected and indeed the measured CO_2 quantity should approach a lower value as only a limited amount of CO_2 is produced at the high potentials in the voltammogram. The decrease of reduction current with each cycle is explained as the surface oxides are approaching a steady state between the oxidation at high potentials and the reduction at low potentials of the voltammogram. Determining the origin of the reduction current is necessary to understanding the source of CO_2 at low potentials and the mechanism of carbon corrosion.

The recent contributions of Maass *et al*. and Colmenares *et al*. present discussions and evidence favoring both of the mechanisms discussed above [16, 21]. Maass *et al*.

measure the production of H-F from membrane degradation suggested by H_2O_2 attacking the membrane. This H-F formation is largest at low potentials. They conclude that the CO_2 peak must result from Equations 4.3-4.5 above. However, this conclusion is based on correlation and is not a direct measure of the mechanism. Conversely, Colmenares *et a*l. conducted a potential dependent CO_2 adsorption study measuring the mechanism directly. They found that CO_2 did adsorb on the carbon surface at high potentials and was released at low potentials. Thus, at least some fraction of the CO_2, if not all, released at low potentials is due to desorption of CO_2 formed at high potentials. Recent experiments in our laboratory suggest ~ 5 % of CO_2 formed is adsorbed on the surface during anodic polarization.

4.5. CONCLUSIONS

Clearly, surface oxide species play a complex role in the corrosion of carbon and may act as both an intermediate or protective layer and even perhaps a site for catalytic reduction. The nature of the potential exposure may alter the corrosion pathway. Understanding the chemistry and kinetics of these processes may lead to a universally accepted mechanism for the electrochemical oxidation of carbon. From that point, further understanding of the role of carbon microstructure or catalyst interactions may be obtained.

REFERENCES

[1] Chalk SG, Miller JE. Key challenges and recent progress in batteries, fuel cells, and hydrogen storage for clean energy systems. Journal of Power Sources. 2006; **159**(1), 73-80.

[2] Patterson TW, Darling RM. Damage to the cathode catalyst of a PEM fuel cell caused by localized fuel starvation. Electrochem Solid State Lett. 2006; **9**(4), A183-A5.

[3] Reiser CA, Bregoli L, Patterson TW, Yi JS, Yang JDL, Perry ML, et al. A reverse-current decay mechanism for fuel cells. Electrochem Solid State Lett. 2005; **8**(6), A273-A6.

[4] Kinoshita K, Bett J. Electrochemical Oxidation of Carbon-Black in Concentrated Phosphoric-Acid at 135 Degrees C. Carbon. 1973; **11**(3), 237-47.

[5] Mathias MF, R. M, H.A. G, Conley JJ, Fuller TJ, Gittleman CJ, et al. Two Fuel Cells In Every Garage? The Electrochemical Society Interface. 2005; **14**(3), 24-35.

[6] Meyers JP, Darling RM. Model of carbon corrosion in PEM fuel cells. Journal of the Electrochemical Society. 2006; **153**(8), A1432-A42.

[7] Siroma Z, Tanaka M, Yasuda K, Tanimoto K, Inaba M, Tasaka A. Electrochemical corrosion of carbon materials in an aqueous acid solution. Electrochemistry. 2007; **75**(2), 258-60.

[8] Passalacqua E, Antonucci PL, Vivaldi M, Patti A, Antonucci V, Giordano N, et al. The Influence of Pt on the Electrooxidation Behavior of Carbon in Phosphoric-Acid. Electrochimica Acta. 1992; **37**(15), 2725-30.

[9] Roen LM, Paik CH, Jarvic TD. Electrocatalytic corrosion of carbon support in PEMFC cathodes. Electrochem Solid State Lett. 2004; **7**(1), A19-A22.

[10] Willsau J, Heitbaum J. The Influence of Pt-Activation on the Corrosion of Carbon in Gas-Diffusion Electrodes - a Dems Study. Journal of Electroanalytical Chemistry. 1984; **161**(1), 93-101.

[11] Bi W, Gray GE, Fuller TF. PEM fuel cell Pt/C dissolution and deposition in nafion electrolyte. Electrochem Solid State Lett. 2007; **10**(5), B101-B4.

[12] Darling RM, Meyers JP. Kinetic model of platinum dissolution in PEMFCs. Journal of the Electrochemical Society. 2003; **150**(11), A1523-A7.

[13] Ferreira PJ, la O GJ, Shao-Horn Y, Morgan D, Makharia R, Kocha S, et al. Instability of Pt/C electrocatalysts in proton exchange membrane fuel cells - A mechanistic investigation. Journal of the Electrochemical Society. 2005; **152**(11), A2256-A71.

[14] Kangasniemi KH, Condit DA, Jarvi TD. Characterization of vulcan electrochemically oxidized under simulated PEM fuel cell conditions. Journal of the Electrochemical Society. 2004; **151**(4), E125-E32.

[15] Kinoshita K, Bett JAS. Potentiodynamic Analysis of Surface Oxides on Carbon-Blacks. Carbon. 1973; **11**(4), 403-11.

[16] Colmenares LC, Wurth A, Jusys Z, Behm RJ. Model study on the stability of carbon support materials under polymer electrolyte fuel cell cathode operation conditions. Journal of Power Sources. 2009; **190**(1), 14-24.

[17] Estrade-Szwarckopf H. XPS photoemission in carbonaceous materials: A "defect" peak beside the graphitic asymmetric peak. Carbon. 2004; **42**(8-9), 1713-21.

[18] Yang DQ, Sacher E. Carbon 1s X-ray photoemission line shape analysis of highly oriented pyrolytic graphite: The influence of structural damage on peak asymmetry. Langmuir. 2006; **22**(3), 860-2.

[19] Langley LA, Villanueva DE, Fairbrother DH. Quantification of surface oxides on carbonaceous materials. Chemistry of Materials. 2006; **18**(1), 169-78.

[20] Chaparro AM, Mueller N, Atienza C, Daza L. Study of electrochemical instabilities of PEMFC electrodes in aqueous solution by means of membrane inlet mass spectrometry. Journal of Electroanalytical Chemistry. 2006; **591**(1), 69-73.

[21] Maass S, Finsterwalder F, Frank G, Hartmann R, Merten C. Carbon support oxidation in PEM fuel cell cathodes. Journal of Power Sources. 2008; **176**(2), 444-51.

[22] Bard AJ, Faulkner LR. Electrochemical Methods: Fundamentals and Applicaitons. New York: John Wiley & Sons 2001.

[23] Antoine O, Durand R. RRDE study of oxygen reduction on Pt nanoparticles inside Nafion (R): H2O2 production in PEMFC cathode conditions. Journal of Applied Electrochemistry. 2000; **30**(7), 839-44.

[24] Horita K, Nishibori Y, Ohshima T. Surface modification of carbon black by anodic oxidation and electrochemical characterization. Carbon. 1996; **34**(2), 217-22.

CHAPTER 5

THE ROLE OF NANOSTRUCTURE IN THE ELECTROCHEMICAL OXIDATION OF MODEL-CARBON MATERIALS IN ACIDIC ENVIRONMENTS

5.1. INTRODUCTION

Carbon black is the material of choice for catalyst supports in low temperature fuel cells (LTFC) such as proton exchange membrane fuel cells (PEMFC) and phosphoric acid fuel cells (PAFC) [1]. Carbon black is heterogeneous in nature being composed of nanocrystalline domains, buckled graphene sections, and possibly amorphous regions [2]. Thermodynamically, carbon is unfavored under almost all conditions experienced during abnormal and normal LTFC operation, Equation 5.1. The slow kinetics of this oxidation reaction allows carbon's use as catalyst support, diffusion media, and bipolar plate. Indeed without this sluggish mechanism of the electrochemical oxidation of carbon, the progress achieved in LTFC development since the 1960s would be very unlikely [3, 4].

$$C + 2H_2O \rightarrow CO_2 + 4H^+ + 4e^- \qquad U = 0.207 \text{ V vs SHE} \qquad (5.1)$$

The apparent stability of carbon is challenged during exposures to high potential, high temperature and cyclic conditions [5-7]. However, little is known regarding the mechanism for electrochemical oxidation. The oxidation reaction exhibits transient behavior and most likely parallel and possibly competing reactions [6, 8]. Due to the aforementioned confounded nature of the carbon black nanostructure, attributing

oxidation mechanisms to specific surface species or even domains is suspect. Here we present the electrochemical behavior of multiple model carbon materials in an attempt to decouple the complex behavior observed.

Various published studies have compared the electrochemical oxidation behavior of different carbon materials [8-16]. However, little to no broad conclusion has been reached connecting the underlying material structure of the carbon materials and oxidation mechanism. Early electrochemical oxidation kinetic studies often incorrectly assumed the entire process to be irreversible and the total current to be dominated by CO_2 formation. Other studies were conducting in concentrated acid with low water activity. The published effect of heat treatment or degree of graphitization on carbon stability may be summarized as follows. The oxidation current normalized to the material mass decreases with increasing heat treatment temperature and graphitic nature [8]. The reduction in oxidation is attributed to the decrease in active sites such as the edges of the graphene sheets, dislocations, and disordered carbon. The oxidation response normalized to a surface area, usually the Brunauer-Emmett-Teller (BET) surface area [17], is less understood. Furthermore, the elementary or even stoichiometric steps of the electrochemical oxidation mechanism continue to elude the scientific community.

Some general behavior of the electrochemical oxidation of carbon is reviewed. The reaction increases with temperature, potential, and water partial pressure [8, 18, 19]. A lower water concentration limit of below 5% has been suggested to shift kinetics from a first order dependence on water partial pressure to zero order [20]. Under an oxidative

potentiostatic hold, the total current measured decays with time. For a large number of materials and conditions, the current decay is adequately represented by a simple power law expression [21], Equation 5.2. Here i is the specific current, k is the rate parameter and n is the time decay exponent. The parameter k is a function of temperature and potential and n has been suggested to be a function of potential only [8]. Researchers have postulated multiple physical reasons for the logarithmic decay of current with time [16, 21]. Perhaps the most compelling is a mechanism involving competing parallel reactions: one to passivate the surface and another to evolve CO_2 [8, 21]. An alternate suggested mechanism resembles those of typical corrosion systems [21]. Here, an oxide film is formed and the carbon dioxide formation is controlled by either diffusion or migration of the reactants through this film [22-24]. This mechanism is unlikely due to carbon's anisotropic nature, low measured surface oxide coverage [14, 25], and reaction rate not following the logarithmic, inverse logarithmic or parabolic rate law. CO evolution has also been reported but typically a factor of ten less than CO_2 [18, 26, 27].

$$i = kt^{-n} \tag{5.2}$$

The purpose of this work is to improve the understanding of the role of carbon nanostructure in the electrochemical oxidation reaction. Through the evaluation of well characterized model materials, the controlling factors of electrochemical oxidation related to the underlying material properties may be elucidated. These materials also allow for a greater understanding of the general oxidation process resulting from the analysis of their diverse characteristics.

5.2. EXPERIMENTAL

5.2.1 Electrochemical Oxidation Characterization

Electrochemical measurements were performed with a PAR 263 potentiostat with CorrWare software or an Autolab potentiostat with General Purpose Electrochemical System software. The I/E filter on the PAR 263 and the Autolab current integration settings were used to measure comparable cyclic voltammograms. All potentials are referred to the reversible hydrogen electrode (RHE). We define RHE as a platinum electrode, preferably platinized, exposed to hydrogen gas and the same electrolyte as the working electrode (carbon). Wet-proofed Toray TGPH-060 carbon paper purchased from ETEK was used as a working electrode current collector and contributes negligible background current.

5.2.1.1 Liquid Half Cell Measurements

Both poly(tetrafluoroethylene) (PTFE) and Nafion bonded carbon electrodes were fabricated for liquid half cell measurements. The 1100 g/mol equivalent weight (EW) Nafion ionomer was purchased as 20 wt% alcohol based solution from Ion-power, Inc. The binder and carbon were dispersed in isopropanol by sonication and then painted onto the carbon paper while on a 70 °C hot plate. The PTFE bonded carbon electrodes were sintered at 315 °C in air while no heat treatment was applied to the Nafion based samples. Typical loadings were 3-20 mg/cm^2. The PTFE bonded carbon electrodes are 10 wt% PTFE and the Nafion bonded carbon electrodes are 44 wt% Nafion. The PTFE bonded carbon electrodes were fully wetted by soaking in isopropanol and then removed and

boiled for two minutes in 18 M-ohm water [25]. The Nafion bonded carbon electrodes were boiled in water for two minutes. Nafion bonded electrodes that were directly immersed into the ½ M H_2SO_4 electrolyte showed slightly less active carbon than those that were boiled in water before immersion.

The liquid half cell consisted of a three electrode setup with ½ M H_2SO_4 as the electrolyte. 18 M-ohm water was used in the dilution of the certified ACS plus grade sulfuric acid. A RHE was connected to the cell via a Luggin capillary and platinum gauze was used as the counter electrode. Electrical contact was made to the sample by threading a platinum wire through the carbon paper above the electrolyte. Ultrahigh purity nitrogen gas was slowly bubbled through the electrolyte to eliminate the presence of oxygen. Temperature was controlled and both the hydrogen and nitrogen gases were humidified to the cell dew point before entering the electrolyte.

5.2.1.2 Single Fuel Cell Measurements

Membrane electrode assemblies (MEAs) of 25 cm^2 active geometric area were fabricated inhouse to enable the use of the model carbons being investigated. The reference and counter electrode was made from a carbon supported platinum catalyst (Pt/C) purchased from ETEK (40 wt% Pt). A weight ratio of 0.8/1.0 ionomer/carbon was maintained for both the counter and working electrodes. 1100 EW Nafion was used as the proton exchange membrane and as ionomer in the electrodes. Nafion 117, provided by the DuPont Co., was chosen to minimize H_2 crossover currents. The 1100 EW Nafion ionomer was purchased as 20 wt% alcohol based solution from Ion-power, Inc. The

ionomer and carbon, or Pt/C, were sonicated in an equal mixture of 18 M-ohm water and isopropanol. The working electrode (carbon and ionomer) was airbrushed onto the pretreated N117 membranes over a 70 °C hotplate. Typical carbon loadings were 1-1.5 mg C/cm^2. After drying at room temperature overnight, the reference/counter electrode (Pt/C and ionomer) was applied in the same manner to the other side but with a target coat weight of 0.1-0.2 mg Pt/cm^2.

The MEAs were tested in a Scribner Associates 850e test station using serpentine graphite flow fields. The conditioning of the cell involved repeated cycling in the double layer charging region (0.1 to 0.7 V) at 80 °C and 100 % relative humidity (RH) for 12 hours. The cell was allowed to cool to 30 °C before an initial full scale cyclic voltammogram is measured (0.04 to 1.30 V). All potentiostatic holds were conducted at 100 % RH and 80 °C to increase the concentration of CO_2 in the working electrode exhaust.

5.2.2 Inline Gas Analysis

During single fuel cell tests, the concentration of CO_2 in the working electrode exhaust was continuously monitored with a model 600 series nondispersive infrared detector (NDIR) from California Analytical Instruments, Inc. with Labview interface. The NDIR requires dry gas flow at a rate to be greater than or equal to 0.3 dm^3/min. After the working electrode exhaust left the fuel cell, it passed through a 50 mL container to collect condensing water before passing through a Perma Pure tube dryer. Typical

concentrations of CO_2 measured varied between 5 and 150 ppm. More oxidation resistant materials were difficult to characterize as progressively lower levels of CO_2 were present.

5.2.3 Materials

Within this work, we evaluate a broad selection of graphene-based carbon material to elucidate structure-reactivity relationships that will help to explain the electrochemical oxidation mechanism. The materials chosen range from industrially produced carbons, heat-treated varieties of these available products, and model carbon materials that provide a well defined structure. The pertinent structural characteristics of these materials are presented in this section. Elemental analysis was performed by Columbia Analytical Services (Tucson, AZ). X-ray diffraction (XRD) patterns were obtained from a PANalytical X-ray diffractometer with a Cu Kα radiation (λ = 1.54187 Å). A monochromator was not used. Background levels were measured using a blank sample and subtracted from the carbon material's spectrum. Specific surface areas were determined using N_2 adsorption at –196 °C with the BET method. The morphologies of the catalyst supports were characterized by high-resolution transmission electron microscopy (TEM). Specimens for TEM examination were prepared by suspending the support powders in a solvent and ultrasonicating to obtain a uniform suspension. One or two drops of this suspension were deposited onto a copper mesh grid coated with a holey carbon film (Quantifoil Micro Tools GmbH). The TEM specimens were allowed to dry completely before examination in a JEOL 2010 FasTEM operating at 200 kV. The accelerating voltage used was higher than the irradiation damage threshold in carbon (80-

140 kV) [28, 29]. However, it is accepted in literature and is our view that a qualitative evaluation of the material appearance is reasonable.

5.2.1.1 Commercial Carbon Black

Vulcan XC72 was purchased from the Cabot Corporation. The as-received material will be denoted here-in as XC-AR. Portions of this material were held at different heat treatment temperatures (HTT) under Argon for two hours. These carbons will be referred to as the material origin followed by the HTT in degrees Celsius (e.g. XC-1900).

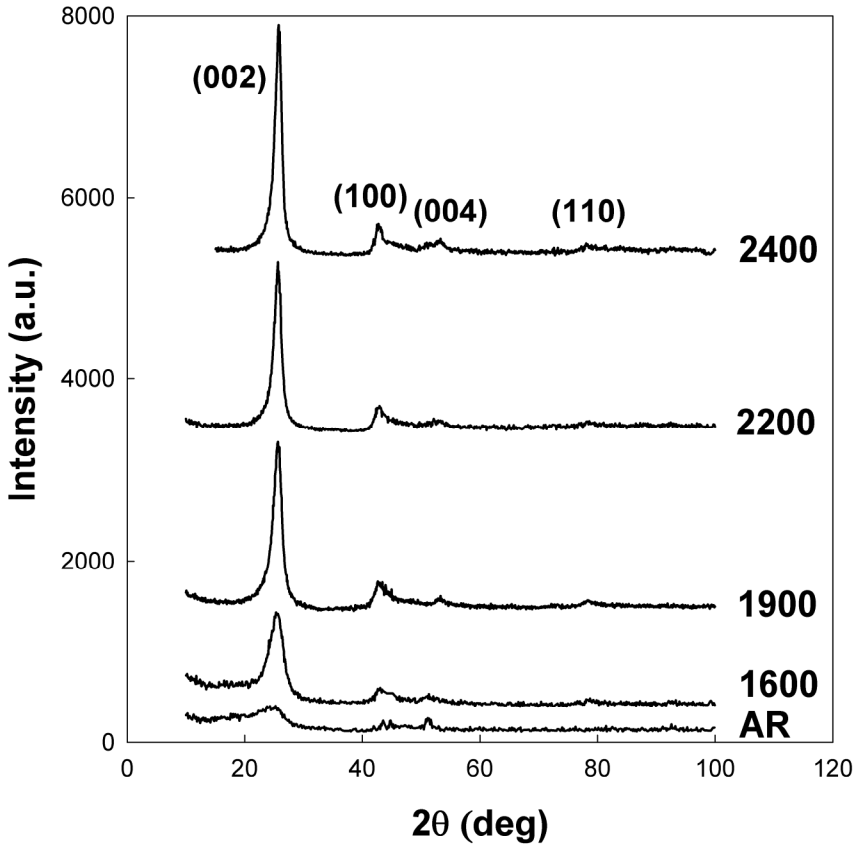

Figure 5.1. XRD line spectrums of XC72 as received and after various heat treatments. The carbon increases in crystallographic order as the heat treatment temperature is increased. Temperatures labeled in degrees Celsius.

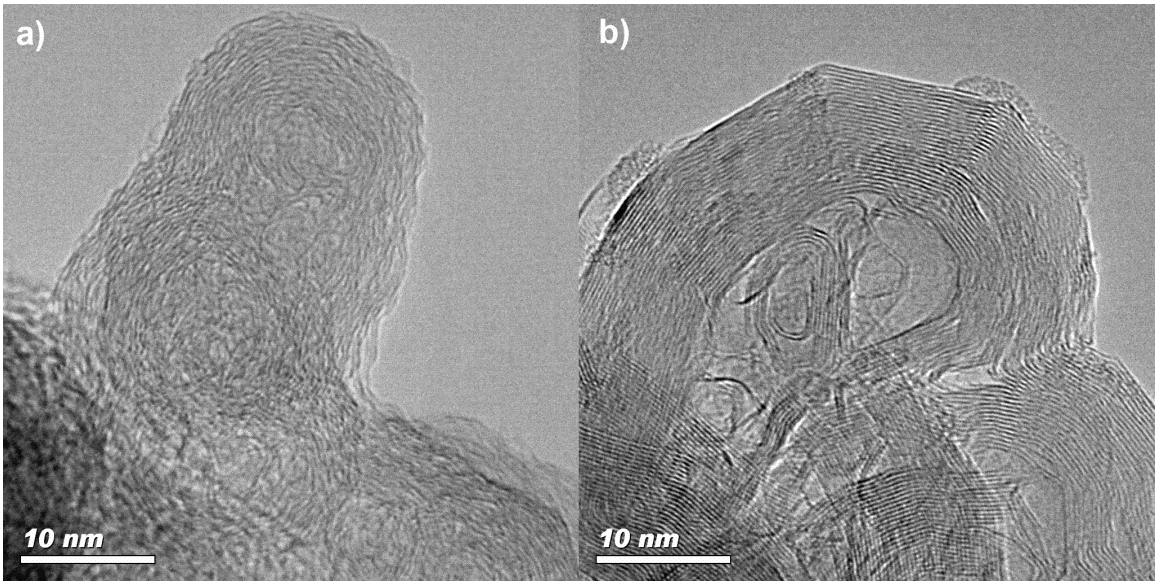

Figure 5.2. a) XC-AR shows turbostratic ordering with little to no interlayer interaction. b) XC-2200 shows a stacking of graphene sheets and crystallites on the order of 10 nm in size.

XC-AR is one of the standard carbon materials used as a catalyst support in LTFCs. In PAFC use, XC-AR is commonly heat treated to achieve reasonable oxidation resistance in the elevated operating temperatures, 165-220 °C versus 65-90 °C for PEFCs. Heat treatment improves the carbon stability by increasing the degree of crystallinity by promoting graphene sheet stacking and reducing defects such as crumpled sheets, heteroatoms, and vacancies. This process may be summarized by comparison of the specific surface area measurements found in Table 5.1, XRD line spectrums in Figure 5.1, and the TEM images of XC-AR and XC-2200 in Figure 5.2.A and 5.2.B. In general, a higher HTT results in a lower specific surface area as the graphene sheets align and stack in an ABAB sequence, Table 5.1. Figure 5.2 clearly shows the increased graphitic nature resulting from heat treatment. In XC-2200, the stacked graphene sheets begin to facet to lower the free energy of the crystallite. The heat treated XC72 materials still

contain some disorder with little long-range crystallinity. However, the order is greatly increased when compared to the XC-AR. The CarbonXS structure refinement program from Dahn *et al*. [30, 31] was used to analyze the XRD line profiles of the XC72 materials. Figure 5.3 displays the CarbonXS calculated fraction of high strain or disordered carbon as a function of the continuous in-plane distance, L_a. As the HTT is increased, the fraction of high strain material decreases and L_a increases. The increase in the L_a dimension demonstrates the decreasing ratio of edge site carbon atoms to those within the basal plane. A HTT of 1600 °C, the lowest used here, results in a dramatic increase in graphitic order. 1900 °C also results in a significant decrease in disordered carbon and increase in L_a. Raising the HTT to 2200 °C continues to increase the in-plane dimension while 2400 °C provides only minimal changes in the fitted parameters. The refinement program calculates little change in the interlayer spacing, commonly referred to as d-spacing, from that expected from a turbostratic carbon, 3.45 to 3.55 Å. To summarize, the heat treatment process reduces the fraction of disorganized carbon and number of edge sites while promoting the lengthening and alignment of graphene sheets. We will show this graphitization process significantly increases the carbon stability on both a specific mass and area basis for a specific carbon.

Table 5.1. Materials tested in this study and their relevant measured properties.

Sample	Carbon	HTT	m^2/g	C (%)	H (%)	O (%)	S (%)	Fe (%)	X Factor	Ox Group
XC-AR	XC72	AR	250	97.42	0.85	0.44	0.586	< 0.001	1	*erstens*
XC-1600	XC72	1600	121	98.58	0.77	0.13	0.266	< 0.001	N/A	*zweitens*
XC-1900	XC72	1900	99	98.3	0.71	0.12	0.025	< 0.001	N/A	*zweitens*
XC-2200	XC72	2200	79	98.12	0.69	0.1	< 0.005	< 0.001	N/A	*zweitens*
XC-2400	XC72	2400	72	97.73	0.64	0.13	< 0.005	< 0.001	N/A	*zweitens*
UD50	UD50	AR	380	85.88	0.61	4.56	< 0.005	1.3	1.3	*erstens*
CNON	UD50	1900	500	96.88	0.65	0.14	< 0.005	< 0.001	N/A	*zweitens*
xGnP	xGnP	AR	150	94.21	0.62	1.74	0.064	0.008	1.1	*erstens*
CNT-AR	MWCNT	AR	200	92.12	0.53	0.38	< 0.005	1.1	1.5	*erstens*
CNT-1900	MWCNT	1900	200	98.28	0.55	0.15	< 0.005	< 0.001	3.8	*erstens*

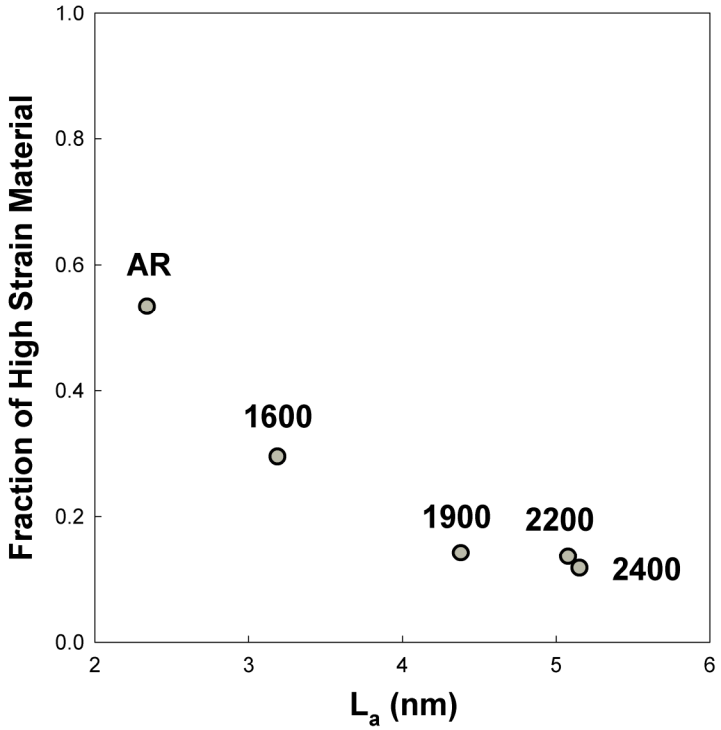

Figure 5.3. Structure refinement parameters for the XRD analysis of XC72 carbons. The increase in heat treatment temperature lowers the fraction of high strain material and increases the in-plane dimension of the graphene sheets.

5.2.1.2 Diamond Nanoparticles and Carbon Onions

UD50 diamond nanoparticles were supplied by NanoBlox, Inc (Boca Raton, FL). This material will be referred to as UD50. Soft X-ray absorption near-edge structure (XANES) spectroscopy and TEM have shown UD50 to consist of diamond nanoparticles surrounded by amorphous and disordered sp^2 bonded carbon [32]. Upon annealing at a HTT of 1900 °C in vacuum, UD50 transforms into a carbon onion structure [32-34], Figure 5.4. The particles remain spherical and 5-10 nm in diameter. Interestingly, the diamond structure transforms into concentric spheres of highly ordered graphene sheets. This material was first communicated by Ugarte [35]. The annealed UD50 will be

referred to as CNON for carbon onion. CNON is of interest here since it possesses the particle curvature of XC-AR but with a high degree of order and low defect density similar to heat treated XC72 (XC-HT). The curvature of the CNON material requires pentagonal carbon rings in addition to the typical hexagonal bonding in graphite. Pentagonal bonding has also been postulated to be the source of the wrinkled or crumpled graphene sheets in disordered carbons such as XC-AR [2, 30, 36]. Both UD50 and CNON materials have a high specific surface area, Table 5.1, of 380 and 500 m^2/g respectively. The difference in nanostructure is further evident by comparison of the XRD line spectrums in Figure 5.5. UD50 shows almost no crystallinity, particularly in the (002) plane of graphite. In comparison, CNON displays well-defined and strong (002) and (l00) peaks. The initial high iron concentration in the UD50 is dramatically reduced during the annealing process, Table 5.1.

Hyperfullerenes or nested fullerenes have been used to describe the structure of carbon onions [35, 37]. Here the TEM images support a less perfect structure, inset of Figure 5.4. The particles are not perfect spheres that would result from fullerenes (C_{60}, C_{240}, etc) being the sole building block. Instead, the CNONs appear to have a bonding somewhere between a fullerene and XC-HT. The stacking of layers similar to XC-HT is evident but the CNONs also have strong curvature, most likely from the inclusion of five member rings. If these onions were composed only of true fullerenes, the reactivity would be greatly reduced as only the basal plane of the structure would be exposed. In the CNONs used in this study, edges and defects are present with the appearance of faceting and discontinuous sheets.

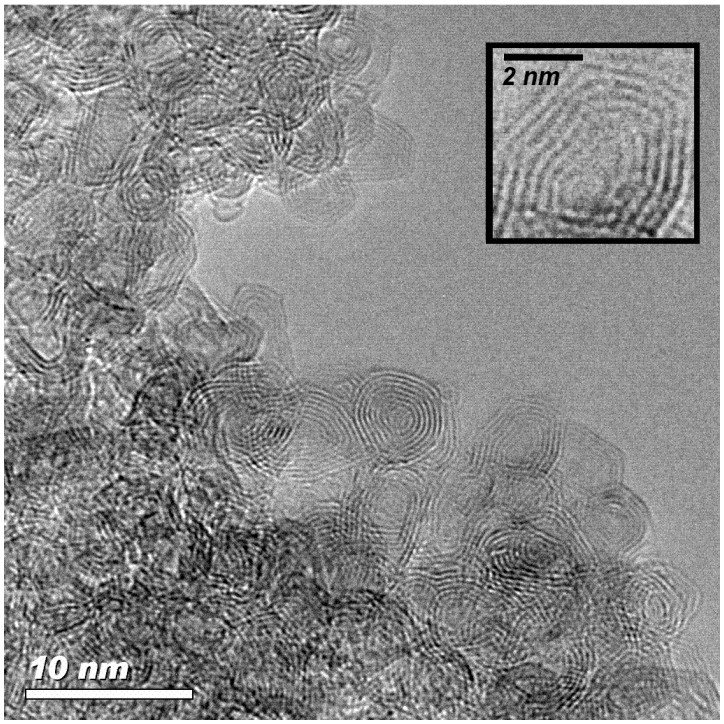

Figure 5.4. CNON material is UD50 annealed at 1900 °C for two hours under vacuum. Inset reveals polygonal features and faceting of some particles.

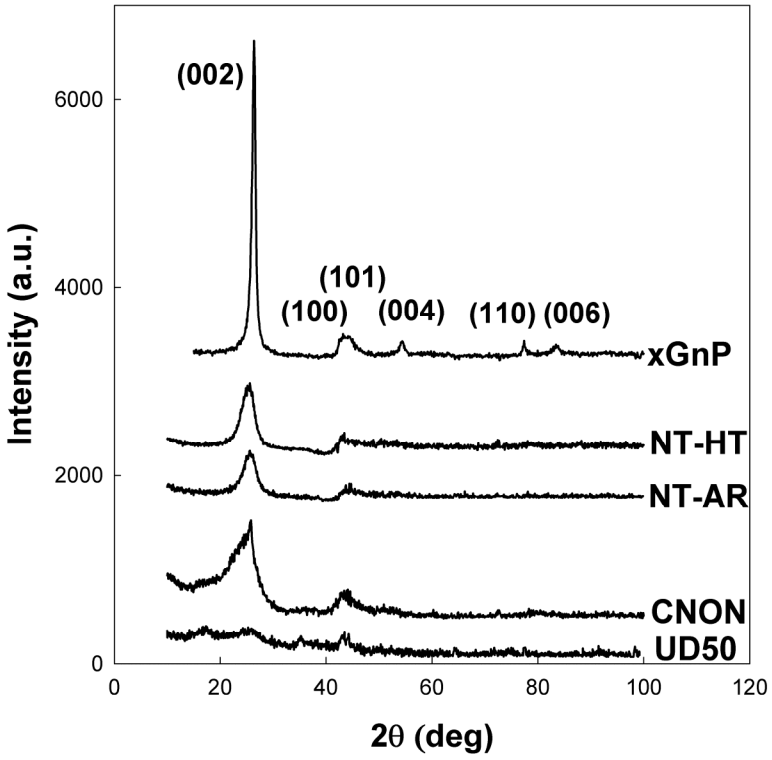

Figure 5.5. XRD line spectrums of model-carbon materials.

5.2.1.3 Multi-walled Carbon Nanotubes (MWCNT)

MWCNTs, 5-10 nm in diameter, were obtained from Arkema (France) under their brand name, U100. A portion of this material (CNT-AR) was also heat treated for two hours under vacuum at 1900 °C (CNT-1900). The heat treatment process reduces the iron concentration although not completely [38, 39], Table 5.1. Figure 5.6.A and 5.6.B compare TEM images of the material before and after heat treatment. The effect of heat treatment here is less dramatic than the XC72 and UD50 materials as evidenced by the imaging and lack of difference in BET area. The defect concentration appears to have decreased and continuous length of graphene sections appears to have increased. XRD shows modest increases in intensity of the (002) and the full width at half maximum (FWHM) of the (100) peak. Behler *et al.* conducted an in-depth characterization of Arkema MWCNT heat treated at 1800 and 2000 °C [38]. Raman spectroscopy showed an increase in ordering and more uniform structure after heat treatment. They reported significant polygonalization of the tubes annealed at 2000 °C for three hours. The TEM images of the CNT-1900 contain no evidence of faceting or polygonal structure. However, the CNT-1900 shows some capping of the end of tubes that is expected to reduce reactivity.

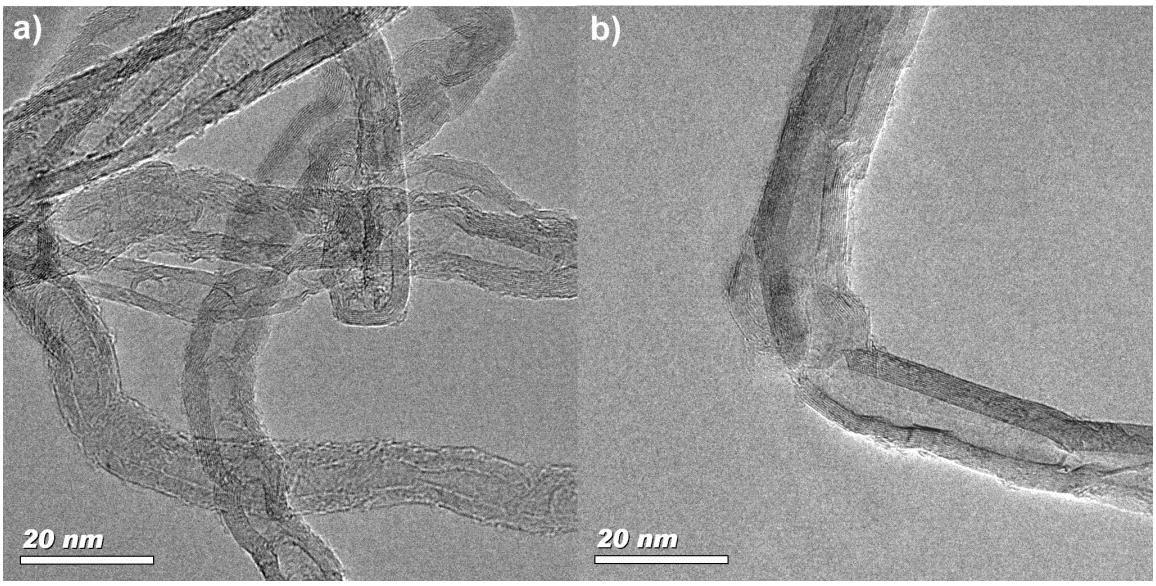

Figure 5.6. a) CNT-AR show a great degree of inter and intra-layer disorder than b) CNT-1900.

5.2.1.4 Exfoliated Graphite Nanoplatelets

xGnP was generously provided by Lawrence Drzal of Michigan State University through XG Sciences, Inc (East Lansing, MI) [40, 41]. xGnP is formed in two steps. First, natural graphite is exfoliated by the vaporization of an intercalate. Second the feature size of the platelets is reduced by ball milling until a BET specific surface area of 150 m^2/g is obtained. The size of the platelets used in this study is approximately 10 nm x 1 μm x 1 μm. The XRD line spectrum is typical of a well ordered graphitic material. However, TEM images reveal disordered graphene sheets on the surfaces of these platelets, Figure 5.7. This characterization reveals the nature of xGnP. Internally, a high degree of graphitic order exists originating from natural graphite starting material. After exfoliation and ball-milling the outer regions of the platelets are damaged and contain disordered carbon similar to XC-AR and UD50. Milling has been shown to destroy the graphitic order of carbons over time [42, 43].

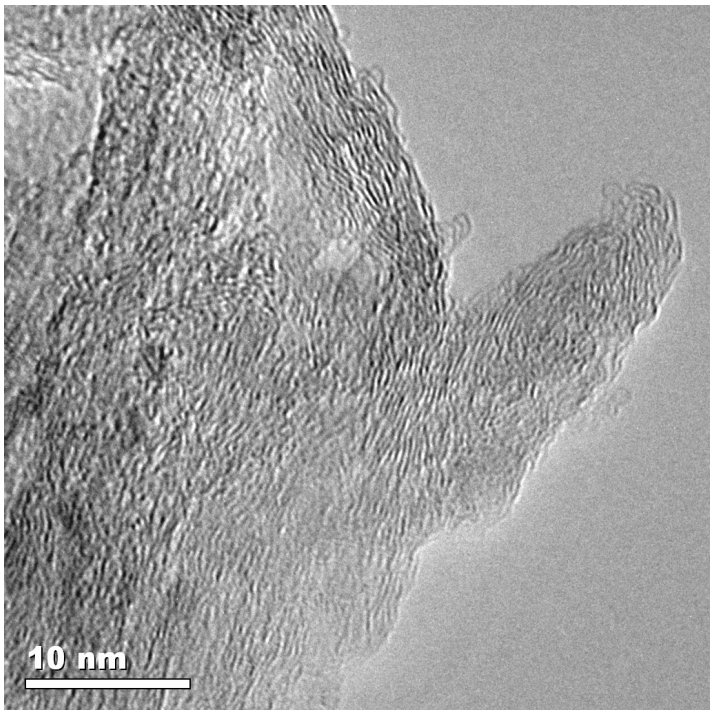

Figure 5.7. xGnP generally consists of 10 nm x 1 μm x 1 μm platelets. The external regions appear to have greater disorder from exfoliation and ball-milling.

5.3. RESULTS

5.3.1 Electrochemical Oxidation

The current resulting from potentiostatic holds in the range of 1.0 to 1.4 V provides a means of evaluating the stability of the carbon materials [8, 19]. The magnitude of the current, normalized to the carbon mass or surface area, is a measure of the specific resistance of the material (of a certain history) to further electrochemical oxidation. The slope of the current decay with time is representative of the surface oxide growth, carbon weight loss, and possibly the underlying nanostructure. For the first time,

we present evidence for two distinct mechanistic pathways and assign the materials tested to one of two groups. To avoid attributing the mechanistic differences to a material property, we name the groups *erstens* and *zweitens* or first and second.

Figure 5.8 displays the potentiostatic behavior of carbons in the *ersten* group at 1.2 V in 60 °C ½ M H_2SO_4 normalized to their BET specific surface areas. The similarity in the current decay between previously believed disparate materials is striking. The inset in Figure 5.8 shows that the carbons within the *ersten* group may be normalized to XC-AR so that all currents are nearly identical. In the inset, a constant was multiplied to the experimental data to normalize the materials to BET area specific current of XC-AR The *ersten* materials and their normalization factor are listed in Table 5.1 (X Factor). Although normalization of the current to the BET specific surface area collapses the data to a great extent, clearly the active site density is not based solely on this factor. This result is expected as the basal plane of graphene sheets also contributes to the BET surface area but is unlikely to react under the conditions tested [8, 14]. The magnitude of the CNT-1900 oxidation current falls well below the rest of the materials within the *ersten* group (3.8 times less than XC-AR) but the slope is remarkably the same. The reason for this substantial decrease is most likely the result of a small edge to basal plane ratio in the heat treated nanotubes. Between the time of 1 and 10 minutes, the time decay of exponent of Equation 5.2 for the *ersten* group at this condition is $n = 0.6$. For times between 30 and 100 minutes, $n = 0.4$.

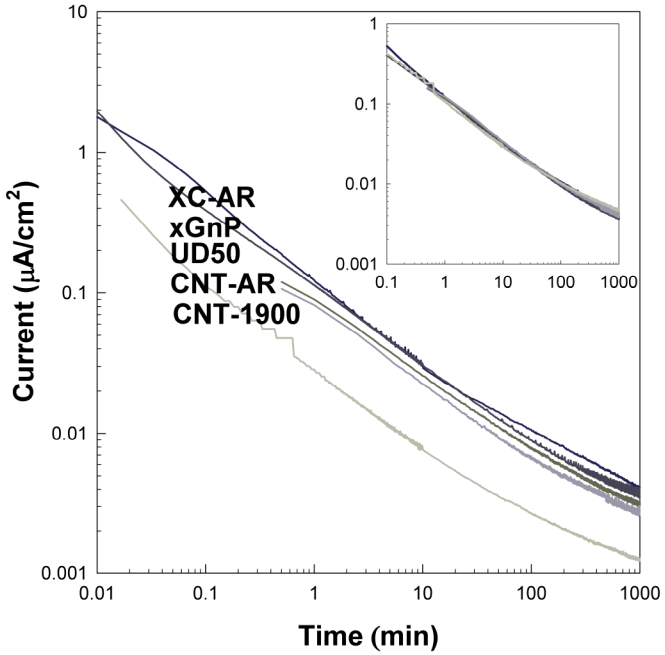

Figure 5.8. Current response of *ersten* group carbons held at potentiostatic condition of 1.2 V in 60 °C ½ M H_2SO_4. Inset: Carbons normalized to the current from XC-AR.

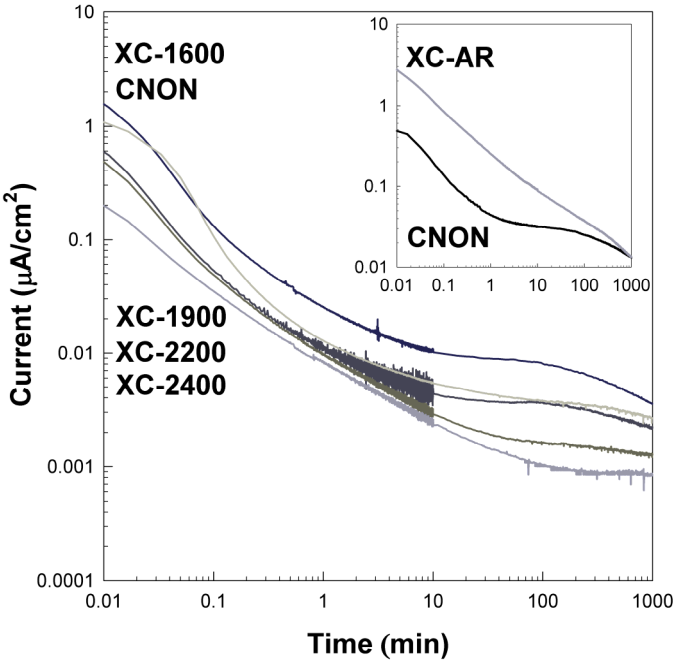

Figure 5.9. Current response of *zweiten* group carbons held at potentiostatic condition of 1.2 V in 60 °C ½ M H_2SO_4. Inset: Comparison of *erstens* to *zweitens* at 1.2 V in 80 °C ½ M H_2SO_4.

Figure 5.9 displays the potentiostatic behavior of carbons in the *zweiten* group at 1.2 V in 60 °C ½ M H_2SO_4 normalized to specific surface area. The *zweiten* group contains all XC-HT samples and the CNON material. Once again, all of these materials exhibit a similar current decay with time. We suggest the shape of this decay is indicative of a mechanism of electrochemical oxidation. The specific oxidation current for XC-HT decreases as the HTT increases. This is attributed to a decreasing number of edge or defect sites in ratio to basal plane growth. The steep initial decline of current could be attributed to the growth of surface oxides and possibly ion electrosorption. As we later demonstrate in section 3.3.2, the plateau and subsequent decay of current is related to the peak in the current at 10-100 min corresponding to CO_2 formation. The XC-1900 and CNON carbons exhibit nearly identical behavior in both magnitude and shape when normalized to BET surface area. Here the HTT appears to control the active site concentration as both materials were exposed to a high temperature of 1900 °C.

The inset in Figure 5.9 compares characteristic currents of the two groups: XC-AR of the *ersten* group and CNON of the *zweiten* group. Clearly the oxidation process is occurring in a different manner for these two materials. Although the total current is greater on a surface area basis for XC-AR, the CNON material has a higher oxidation current when normalized by mass. A discussion of the appropriate evaluation of oxidation resistance is postponed to a later point in the paper.

5.3.2 Cyclic Voltammetry

The current-potential behavior of porous carbon electrodes contains a wealth of information. Here again, the *ersten* and *zweiten* groups of carbon materials exhibit distinctive behavior. However, the heat treated MWCNT, CNT-1900, displays behavior of both groups. For PTFE bonded porous electrodes in ½ M H_2SO_4, the representative cyclic voltammograms (CV) for the two groups are presented in Fig 10. The capacitance of CNON, representative of the *zweiten* group, is much less than that for the XC-AR, which is representative of the *ersten* group. The reduction in capacitance for heat treated carbons has been attributed to desorption of surface oxide groups during the heat treatment under vacuum or inert gas environment. When present, surface oxide groups increase capacitance values by interacting with the electrolyte solvation structure, exhibiting redox behavior, or reducing the electrolyte-carbon contact angle allowing the wetting of previously inaccessible pores [44, 45]. As previously reported, carbons exposed to high temperature heat treatment have double layer capacitances 4 fold lower even in non-aqueous electrolytes which do not exhibit redox reactions [33].

Both carbon groups exhibit oxidation currents at the apex potential of 1.4 V and a single reduction peak near 0.5 V when the potential sweep rate is 10 mV/s. The CNON material and all other heat treated carbons exhibit an oxidation peak near 1.2 V at this sweep rate. The observation of this peak clearly depends on the potential range scanned but just as importantly the potential sweep rate employed. The oxidation peak is found at higher potentials as the potential sweep rate is increased.

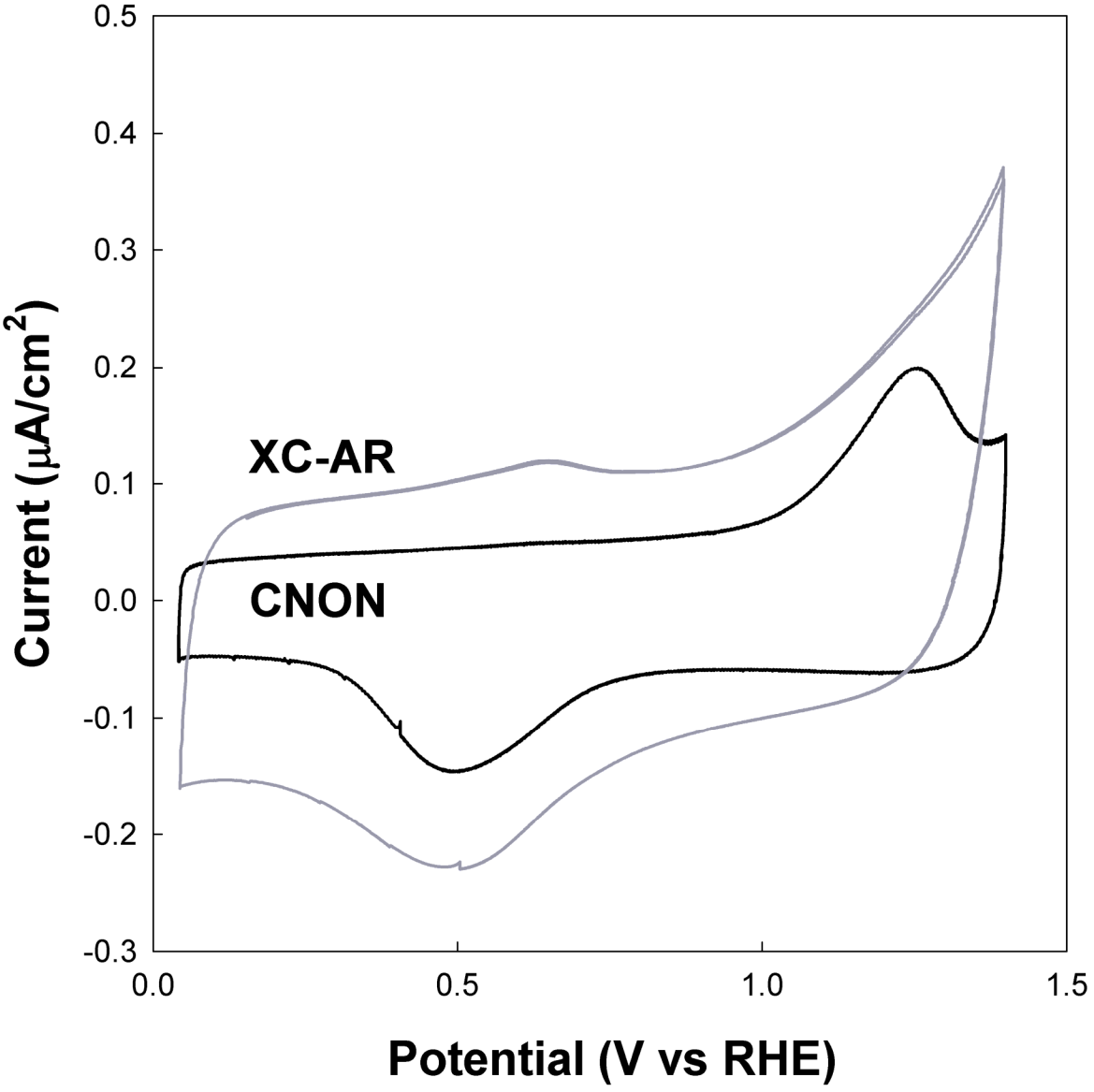

Figure 5.10. Cyclic voltammograms of XC-AR and CNON recorded at 10 mV/s in 22 °C ½ M H_2SO_4.

Figures 5.11 and 5.12 present the current-potential behavior of XC-AR and CNON respectively by progressively sweeping to higher vertex potentials at 1 mV/s. The current response of XC-AR is dominated by the charging of the double layer up to vertex potentials of 0.8 V. Above this potential, an oxidation reaction is observed being more prominent at higher potentials. This oxidation current is believed to consist of current from surface oxide formation and CO_2 formation. The surface oxide functionalities formed include both electrochemically reversible and irreversible species [46]. The reduction peak near 0.6 V is the partial and/or complete reduction of the reversible oxides. However, the irreversible oxide formation is responsible for the measurable increase in pseudo-capacitance. Here, we define irreversible as an oxide group that can not be removed by electrochemical reduction in ½ M H_2SO_4. However, this oxide may be partially reducible and thus display pseudo-capacitance. As larger apex potentials are reached, both the subsequent reduction peak current and capacitance responses increase. A redox couple is also observed near 0.6 V as the concentration of irreversible oxides increases due to exposure to potentials > 1.2 V. This redox couple has been attributed to the quinone/hydroquinone oxide group (Q/HQ) [8, 47]. During the positive potential scan the hydroquinone (>–OH) is oxidized to the quinone (>=O) with the reverse reaction taking place during the reduction. The majority of charge passed in the reduction peak near 0.6 V at 1 mV/s is from reversible oxides. We suggest the complete reduction of reversible oxides resulting in desorption of oxygen from the carbon surface as water, Equation 5.3. At this time the exact surface chemistry is unknown.

$$C_sO + 2H^+ + 2e^- \leftrightarrow sC + H_2O \qquad (5.3)$$

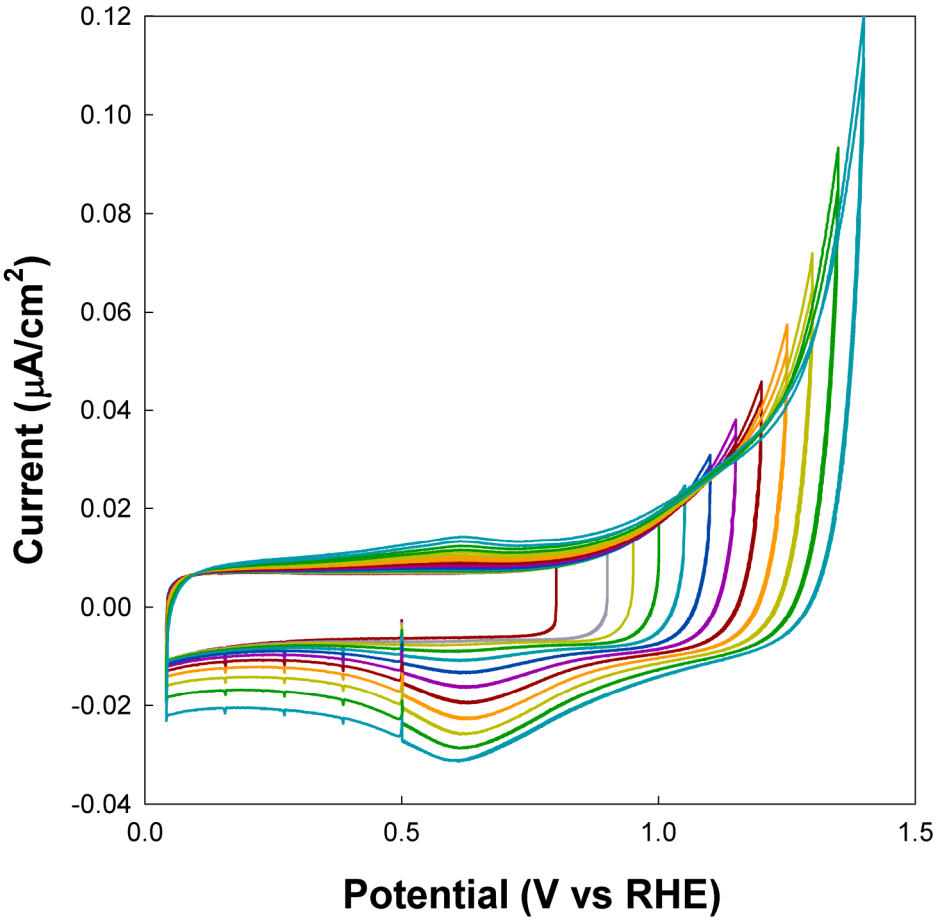

Figure 5.11. Cyclic voltammograms of XC-AR with increasing apex potentials recorded at 1 mV/s in 22 °C ½ M H_2SO_4.

The *zweiten* group member, CNON, progressive vertex CVs in Figure 5.12 clearly demonstrate the reversible nature of a redox couple with an oxidation peak near 1.15 V and reduction peak near 0.6 V at a sweep rate of 1 mV/s. The standard potential for this couple is ~1.0 V determined from sweep rate studies (not shown). As potentials >1.25 V are reached, the following reduction peak at 0.6 V contains additional contributions from surface oxide reduction resulting from electrochemical oxidation and not solely the redox couple centered around 1.0 V.

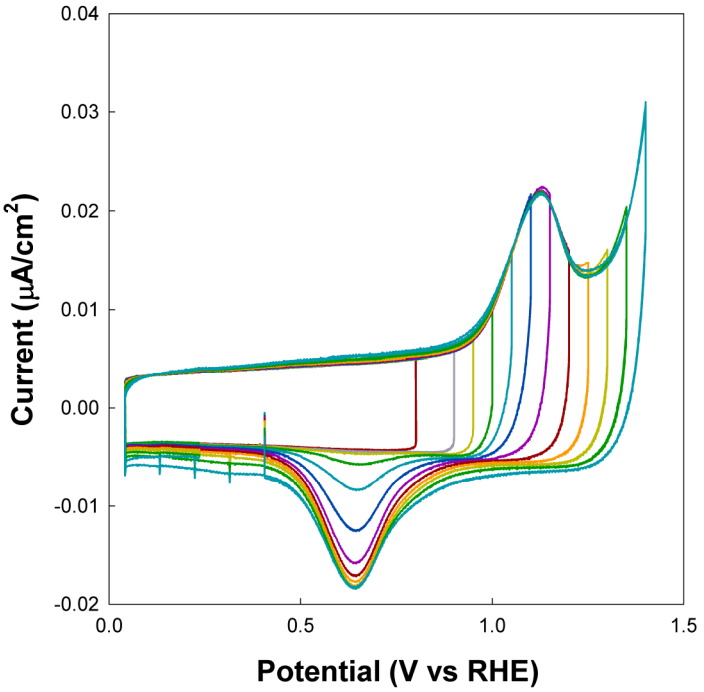

Figure 5.12. Cyclic voltammograms of CNON with increasing apex potentials recorded at 1 mV/s in 22 °C ½ M H_2SO_4.

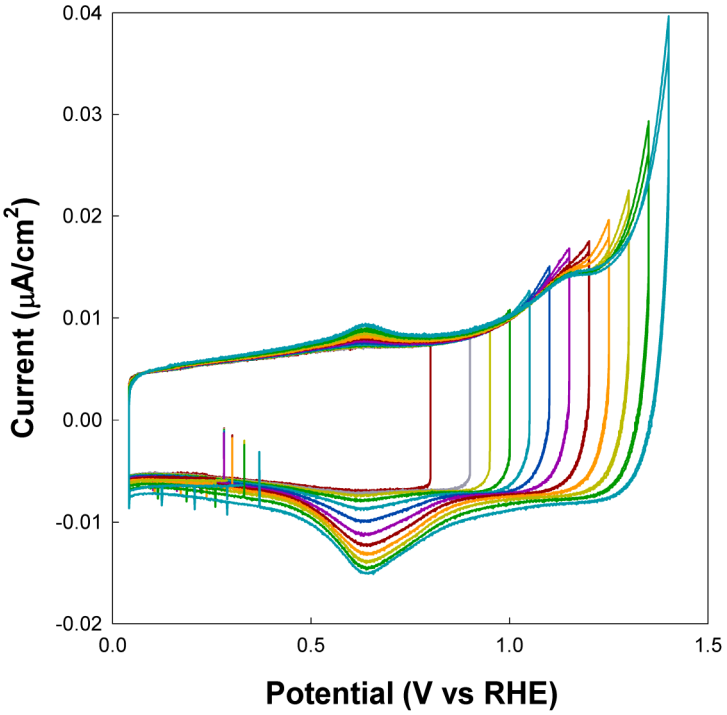

Figure 5.13. Cyclic voltammograms of CNT-1900 with increasing apex potentials recorded at 1 mV/s in 22 °C ½ M H_2SO_4.

The CV for CNT-1900 is the only model material characterized that exhibits electrochemical behavior of both groups. The CV with increasing apex potentials for CNT-1900 is displayed in Figure 5.13. For apex potentials less than 1.2 V at 1 mV/s, the CV is similar to the heat treated carbon group, Figure 5.12. The specific capacitance and presence of an oxidation peak at 1.0 V both resemble the other heat treated carbons. As the electrode is exposed to greater potentials, the CV begins to exhibit qualities of the carbons without heat treatment. The CNT-1900 oxidation current at 1.4 V is 40% higher than that for the CNON at a sweep rate of 1 mV/s. Similar to the behavior of XC-AR, the redox couple at 0.6 V is present in the CNT-1900 CV after exposures to potentials greater than 1.2 V.

The CNT-1900 carbon provides clues to what characteristics might govern the electrochemical behavior. The capacitive and pseudo-capacitive behavior of a carbon is a function of the HTT. We are not able to distinguish between individual contributions by the underlying nanostructure, defect density or oxide content. However, as shown by the classification of CNT-1900 in the *ersten* group, heat-treatment alone does not solely control the electrochemical oxidation mechanism. This is also apparent from the similarity between XC-AR and CNT-1900 for CV cycles reaching peak potentials above 1.2 V.

The CVs for the rest of the individual carbons all have some level of unique features when compared to each other. In general, a greater surface oxide presence results

in larger (pseudo-) capacitance and the presence of a redox couple ~0.55 V. This couple is generally attributed to the Q/HQ couple. Researchers have shown this group tends to be directly proportional to the total oxide concentration as measured by temperature programmed desorption and to a lesser degree X-ray photoelectron spectroscopy [25].

The CVs after prolonged oxidation are also informative. The CVs are shown in Figure 5.14 for XC-AR, CNON, and CNT-1900 after a 1000 minute 1.2 V hold in 60 °C ½ M H_2SO_4. The sweep rate is 10 mV/s and initially towards lower potentials. In the first sweep, the reduction current observed is larger than for each subsequent cycle. The difference between the initial reduction sweep and subsequent reduction sweeps is attributed to a complete reduction and removal of reversible species formed during the potentiostatic hold. A more correct quantification of this would be to measure the reduction current and compare this to the current passed during a short scan CV (0.04-0.80) where no oxidation is occurring. XC-AR appears to have a greater amount of reversible surface oxide formation during this oxidative treatment. Interesting, the CVs of the heat treated materials, CNON and CNT-1900, are similar to the XC-AR as they all have the presence of the Q/HQ redox couple. Furthermore, the oxidation peak near 1.2 V is no longer present. From these observations, we conclude that the surface chemistry controls the current response during cyclic voltammetry. However, the electrochemical oxidation mechanism appears to depend on the underlying nanostructure of the carbon material.

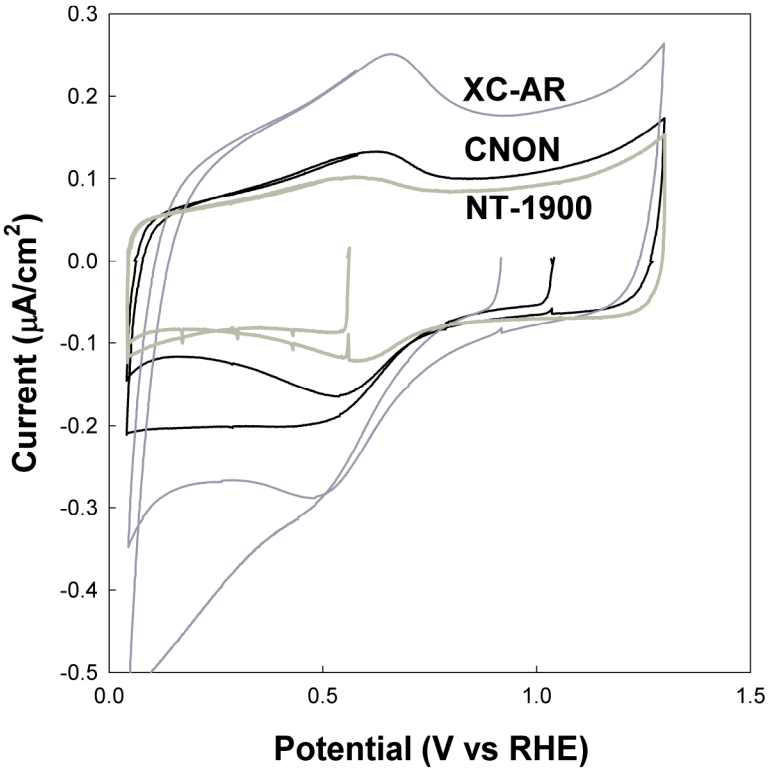

Figure 5.14. Cyclic voltammograms of XC72-AR, CNON and CNT-1900 after holding at 1.2 V and 60 °C for 1000 minutes recorded at 10 mV/s in 22 °C ½ M H_2SO_4.

5.3.2 Inline CO_2 Measurements

5.3.2.1 Effect of Electrolyte

Before comparing results of single fuel cell tests to liquid half cells, we must establish any differences that result from using a solid-polymer-electrolyte, Nafion, in the place of dilute sulfuric acid. Figure 5.15 compares the CV response for PTFE bonded electrodes in ½ M H_2SO_4, Nafion bonded electrodes in single fuel cell tests, and Nafion bonded carbon in ½ M H_2SO_4. Although not identical, the CVs display very similar behavior. This is further reflected in the current response from a 1.2 V potentiostatic hold

at 80 °C (not shown). The differences observed appear to be minor and not a controlling factor for the mechanism of electrochemical oxidation.

A significant difference is seen in the CVs of the heat treated carbons, *zweitens* and CNT-1900. The redox couple observed in the PTFE bonded electrodes with a standard potential near 1.0 V is absent from the CVs for all MEAs and the Nafion bonded carbon in ½ M H_2SO_4. It is not clear how the structure of Nafion changes the redox behavior observed for the heat treated carbons. One possible source for the difference is the drying conditions during sample preparations. PTFE bonded samples are dried at 315 °C in air for fifteen minutes while all Nafion bonded samples never reach temperatures greater 100 °C. However, a PTFE bonded carbon sample that was not sintered displayed the redox couple. We believe the absence of the redox peak to be from the non-adsorption of the fixed anion in Nafion. Nonetheless, the currents measured during potentiostatic operation in different electrolytes are similar enough to neglect any effect of the different electrolytes tested.

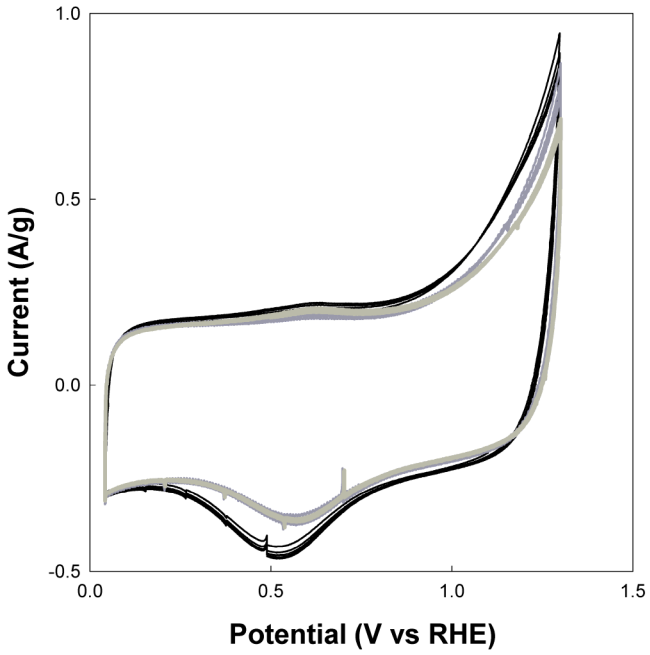

Figure 5.15. Cyclic voltammograms of XC-AR in different electrolyte environments at 10 mV/s in 30 °C ½ M H_2SO_4: PTFE bonded (black), Nafion bonded (dark grey), MEA (light grey).

5.3.2.2 CO_2 Evolution Rates

As might be expected, the two electrochemical oxidation groups follow different CO_2 evolution rates with time. The *zweiten* group starts at low CO_2 evolution rates and reaches a maximum at 10 to 100 minutes before decaying at the same rate as the total measured current, Figure 5.16. At this point, the current efficiency for CO_2 formation approaches 80 %. The initially low value of CO_2 production is attributed to a need of an oxide intermediate in the oxidation mechanism. This oxide intermediate is suggested to grow quickly during the beginning of the potentiostatic hold, thus increasing the CO_2 evolution with time. This was also observed for a graphitized carbon that was chemically oxidized prior to electrochemical testing [11]. The current decay at long times is suggested to result from the continued growth of a passive surface oxide.

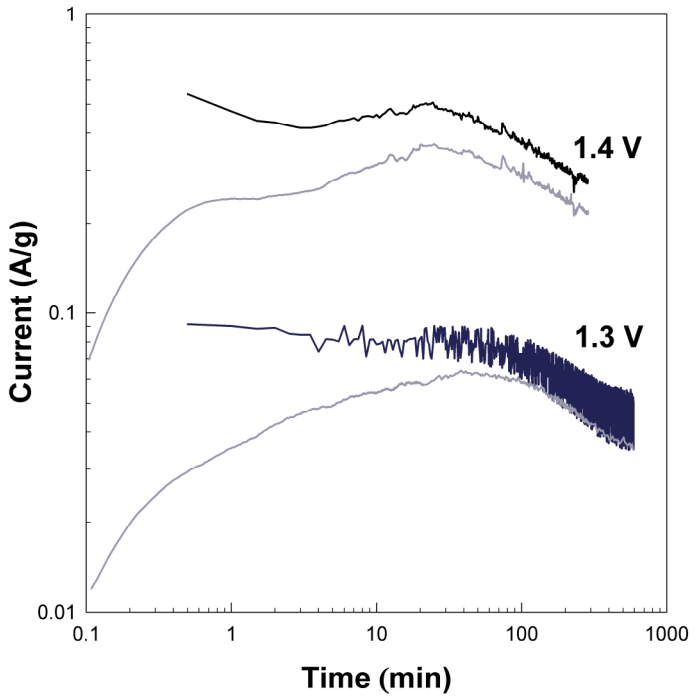

Figure 5.16. CO_2 gas evolution current (grey curves) and the value of the total current (black curves) for XC-1900 MEAs at 1.3 V and 1.4 V, 80 °C and 100% RH.

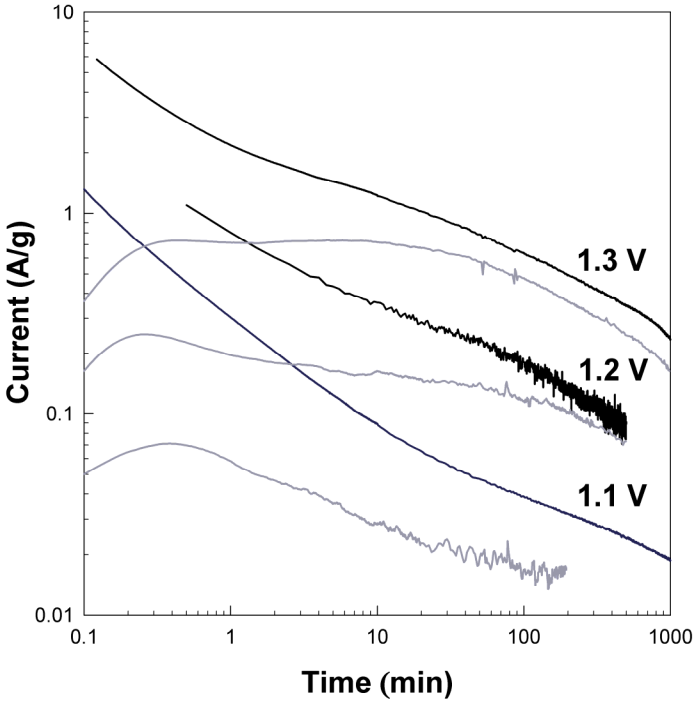

Figure 5.17. CO_2 gas evolution current (grey curves) and the value of the total current (black curves) for XC-AR MEAs at 1.1, 1.2, 1.3 V, 80 °C and 100% RH.

Under potentiostatic exposure, the *ersten* group has a much higher initial rate of CO_2 evolution than the *zweiten* group, Figure 5.17. The current efficiency for CO_2 formation reaches 80 % at long times. These findings are in agreement with Kinoshita who reported the non-graphitized carbons having higher CO_2 current efficiencies at short times than graphitized carbons [8, 13, 14]. However, Kinoshita also found no differences in the slope of the current decay under a potentiostatic hold for different carbons. This may be a result of using a concentrated acid where reaction kinetics are believed to have no dependence on water concentration and thus different mechanistically [20] .

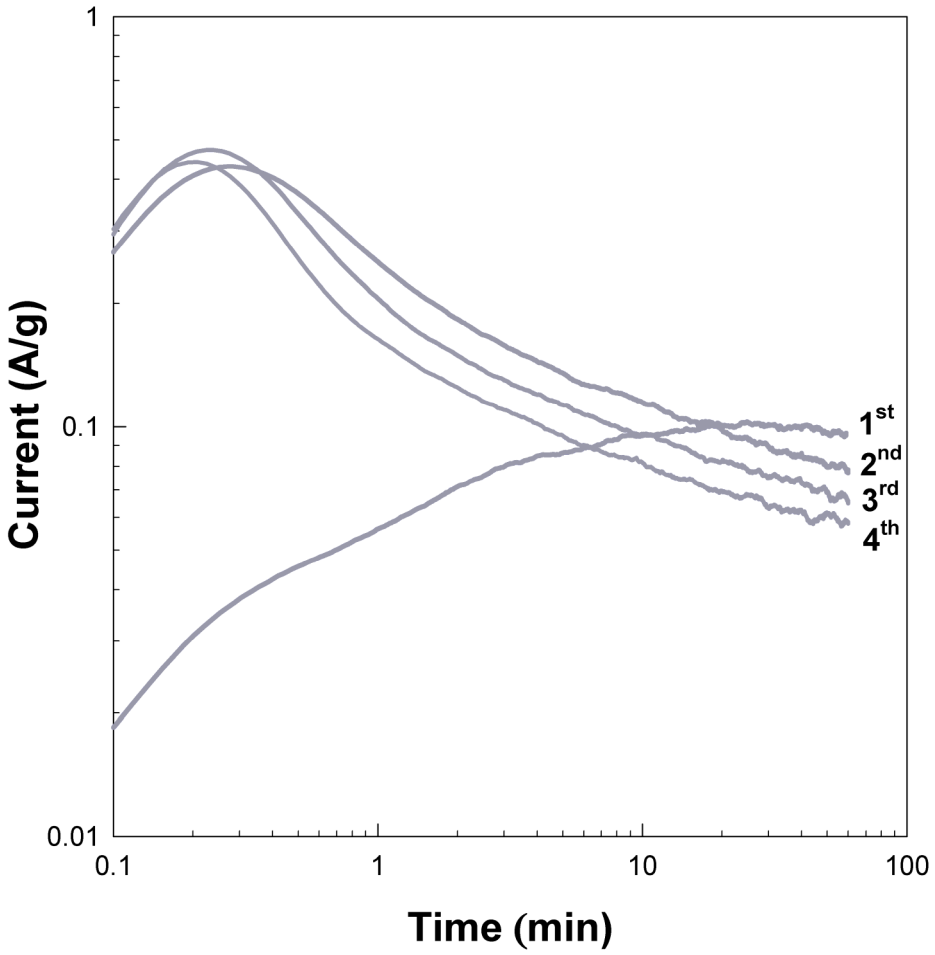

Figure 5.18: CO_2 current for XC-1600 MEAs at 1.3 V, 80 °C and 100 % RH after repeated reduction at 0.04 V.

As some reversibility has been demonstrated for the electrochemical oxidation of carbon, a transient potential exposure is used to analyze the CO_2 response. The carbon electrode is held at 1.3 V for 60 minutes and then reduced at 0.04 V for 5 minutes. This exposure is repeated for a total of four cycles. The CO_2 response for the repeated high potential exposures is shown in Figure 5.18 for XC-1600, a member of the *zweiten* group. The initial CO_2 response increases with time, similarly to that depicted in Figure 5.16. However, the subsequent oxidation exposures all show the characteristic power law behavior of Equation 5.2. It appears the required surface oxide intermediate is irreversibly built up in the first high potential hold. The total CO_2 evolved decreases from exposure 2 to 4. This is most likely a result of carbon mass loss lowering the amount of carbon available to oxidize. The calculated mass loss for each exposure is 1.1 %, 1.2 %, 1.0 %, and 0.9 %. The decreasing weight loss with exposure may also be the result of further passive oxide growth. Figure 5.19 displays the CO_2 response for xGnP under the same potential exposure cycle. As this carbon is a member of the *ersten* group, the CO_2 evolution is large from the start and reaches 80 % current efficiency repeatedly. The slopes of the CO_2 currents during the second high potential exposure may be compared to analyze any differences in the electrochemical oxidation mechanism after both samples have electrochemically formed oxides. Between 5 and 60 minutes, the *ersten* group has an $n = 0.3$ and the *zweiten* group has an $n = 0.2$. Even after both materials are oxidized, the oxidation mechanism remains different.

A current efficiency of 80% for CO_2 requires the contributions of an additional process to the measured current. The literature instructs that CO formation is never

greater than 1/10th of the rate of CO_2 evolution. CO requires two electron transfers and thus the contribution to the total current is far less, perhaps 5 %. The 80 % current efficiency at long times is observed for many different carbons and both 1.2 and 1.3 V exposures at 80 °C. This observation along with a continually decreasing measured current allows us to neglect the effects of molecular hydrogen oxidation and oxygen evolution. We suggest the formation of a surface oxide species as part of the CO_2 evolution mechanism. Increasing the oxidation process to a five electron transfer provides for an excellent fit of the experimental data. Binder *et al*. reached this same conclusion in one of the first in-depth studies of the electrochemical oxidation of carbon in acids.[48] An example of such a reaction is suggested in Equation 5.4.

$$C^* + C_sOH + 2H_2O \rightarrow C_sO + * + CO_2 + 5H^+ + 5e^- \quad (5.4)$$

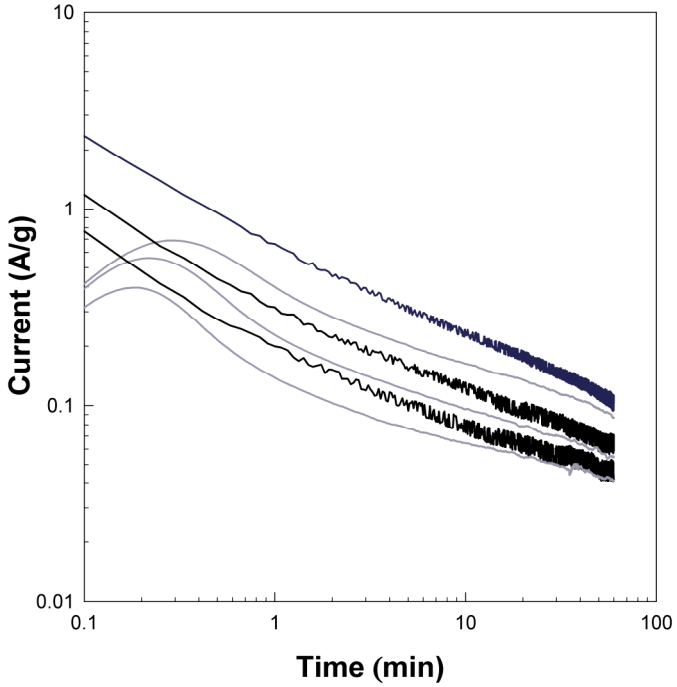

Figure 5.19. Total (black) and CO_2 (grey) currents for xGnP MEAs at 1.3 V, 80 °C and 100 % RH after repeated reduction at 0.04 V.

5.4. DISCUSSION

5.4.1 The Presence and Role of Contaminant Species

Iron and sulfur are common residual species in commercial carbon blacks, diamond nanoparticles, and MWCNTs that result from the feedstock and method of production. Researchers have long been suspicious of the role these species may play in the oxidation of carbon [12, 49]. Indeed, iron is a catalyst for many chemical reactions and evidence does exist to support its role in gas phase oxidation of carbons [8]. We are able to state some conclusions on the role of these contaminant species having evaluated a wide range of materials and being able to separate the materials into two groups. UD50 and CNT-AR have the largest iron content of ~1 wt% while the heat treated materials have the lowest contents, Table 5.1. Materials in the *ersten* group range in concentration from 1 wt% to levels below the detection limit of the elemental analysis. One effect we are unable to control, is the mechanism of iron removal in the MWCNTs. Iron is commonly encapsulated within the tube and then removed during heat treatment. The UD50 material contains high levels of iron but none was observed or expected to be encapsulated. The effect of the iron removal on the MWCNT and its subsequent reactivity is unknown. However, we take this effect as secondary and most likely not controlling. Since we have materials that oxidize in a comparable manner with varying levels of concentration, we conclude that iron and sulfur do not play a significant role in the electrochemical oxidation of carbons under the conditions evaluated in this work.

5.4.2 The Role of Nanostructure in the Oxidation Mechanism

We may hypothesize the controlling factor that separates the electrochemical oxidation of the tested carbon materials. The interaction between stacked graphene sheets, mostly in the form of dispersion or van der Waals forces, may be the significant factor separating these carbon groups. This non-covalent bonding, referred to as π - π interactions, is present in varying amounts in all carbon materials tested. However when heat treatment is imposed on these carbons, the ordering of the graphene sheets provides for a greater interaction between adjacent layers. So why does CNT-1900 behave in the same manner as the more disordered carbons in the *ersten* group? Two reasons preclude MWCNT from obtaining strong interlayer interactions even though TEM images present long continuous, defect free lengths of graphene. First, various tubes within a single MWCNT are of different crystallographic orientation. Without direct control, perhaps through the introduction of dopants (B, N), each successive tube is likely to have a different lattice vector (u, v) [50]. The different lattice vectors preclude the carbon atoms from aligning in the energetically favorable manner observed in graphite. Due to geometric constraints of having multiple concentric cylindrical tubes, the interlayer spacing is typical ~3.44 nm [50, 51]. For these two reasons, interlayer interactions are minimal as no ABAB ordering is present. Indeed Dresselhaus *et al.* has suggested MWCNTs should behave more like turbostratic carbon than graphite [51]. Our observations support this statement. So why then does the CNON material, which also has small size, behave similarly to the heat treated XC72 carbons? Based upon TEM images, we conclude that our CNON particles are far from the nested-fullerene structure that is often used to describe carbon onions and have rather polygonal shape. We do

observe small, highly curved and ordered graphene sheets, but faceting and straight runs of layered graphene are very prominent (see inset of Figure 5.4). If the CNON were in fact hyper-fullerenes, very low reactivity would be predicted since these structures are without the edges of graphene sheets where the postulated reactions occur. Oxidation for hyper-fullerenes would likely take place at vacancies in the outer layer. We may also rule out the role of graphitized amorphous carbon. TEM images show no evidence for large amounts of graphitized soot which may be a side product of the nanodiamond synthesis and subsequent heat treatment. This is further evidenced by the high specific surface area measured. Graphitized soot would have a lower specific surface area, ~5 times less than the CNON.

The behavior of xGnP also warrants discussion. The XRD pattern is indicative of a material with large graphitic character. The TEM images also support this as large particle sizes of 1 μm x 1 μm are seen. However, these slabs are only 10-20 nm in thickness. Within the large slab we suggest the presence of well ordered ABAB graphene sections that remain from the original graphite starting material. After exfoliation and then ball-milling, the outer portions of this slab are no longer composed of well ordered material [42, 43]. However, under the moderate weight losses investigated here, < 10 %, the underlying graphitic structure is never isolated.

The electrochemical oxidation behavior of commercial carbon blacks, such as XC-AR, is no different than a wide range of graphene-based carbon materials. TEM images of severely degraded carbon blacks have shown a somewhat hollow center of the

particle although no images have been published for moderate levels of oxidation [52, 53]. This void is suggested to arise from the preferential oxidation of less ordered carbon material. While it is not certain whether this hypothesis is correct, a few questions may be addressed. What is the catastrophic result from the removal of internal disorganized carbon? Certainly pathways for electronic conduction are available through the outer nanocrystalline domains. Furthermore, the wetting properties of the carbons are most likely controlled by surface oxides on the outer surface. Finally, weight loss has been shown to correlate well with performance loss of PEMFC air cathodes regardless the degree of graphitization the support has experienced [16, 54]. This would suggest internal loss of carbon does not control performance loss. One can conclude the important mechanistic details falls within the $\pi - \pi$ interactions elucidated here and not concerns about mass transport to the internal domains of the carbon particles.

5.4.3. Surface Oxides

The edges of the graphene sheets in carbon are decorated with oxides of various chemistries. The exact determination of these oxides is very challenging [55]. The low weight percent of oxides, complex carbon structure, and chemisorption of atmospheric oxygen confound many experimental approaches. Good work has been presented and has significantly increased the community's understanding mostly through the use of temperature programmed desorption [8, 25, 46, 55-57]. However, our view is that the accuracy of oxide quantification is far below that of electric current and CO_2 measurements [6]. Thus these two techniques have been the focus of this study. The difference between the measured current and calculated CO_2 current should be the current

passed for surface oxide formation. This approach requires proper corrections for the small but existent activity for hydrogen oxidation and oxygen evolution or the use of conditions to mitigate this issue (i.e. low H_2 crossover, potentials below O_2 evolution, etc).

The complex behavior observed in a large study of the electrochemical oxidation of carbon in our laboratory requires at least three oxide species. The phenomenological oxides are suggested to be:

1) Reversible passivating oxide "X" responsible for time decay

2) Irreversible passivating oxide "Y"

3) Catalytic or intermediate oxide "Z" involved in CO_2 formation

The X oxide is needed to explain the reversibility and restarting of time decay current after reduction of the carbon [6, 11, 18, 58]. The Y oxide is needed to explain the transition to passivation under square wave cycling and most likely interacts with oxides X or Z to explain the breakdown of passivity [6]. The Z oxide is necessary to explain the carbon dioxide behavior of graphitized carbons [11]. A numerical model is proposed in the next section, Chapter 6, to provide a tool for predicting the oxide concentrations, time decay and carbon dioxide production as a function of time, potential, and temperature.

5.4.4 Performance Decay in Electrochemical Systems

The electrochemical oxidation of carbon catalyst supports results in a general performance loss in the porous electrodes of electrochemical systems. The growth of surface oxides on the carbon material increases the electronic resistivity and decreases the water-carbon contact angle. Under severe oxidation, the gasification of the support to CO_2 results in a collapse of the electrode structure impeding mass transport. Carbon systems used as catalyst supports are also postulated to lose contact to the catalyst particles as a result of catalyst-carbon oxidation interactions. In LTFCs such as PEMFCs, the performance loss may be correlated with the fraction of carbon mass lost irrespective of the surface area of the material [16, 54]. This provides a means to compare the oxidative resistance of one carbon material to another. Clearly, heat treated materials such as XC-2400 and CNT-1900 provide the lowest specific mass oxidation. However, these support materials are also the poorest materials to achieve well dispersed catalyst particles of 2 to 6 nm. The same sites on the carbon surface which are most likely to be active for electrochemical oxidation also serve as bonding sites for the catalyst particle. An optimization between average life-time catalyst particle size and carbon oxidation resistance is necessary for the product design of electrochemical systems. Prediction of this tradeoff is difficult and meaningful conclusions will most likely require testing of a proposed catalyzed support in the fuel cell electrode.

5.5. CONCLUSIONS

The electrochemical oxidation of graphene based carbon materials appears to proceed by two separate pathways dependent upon the degree of interlayer $\pi - \pi$ interactions. This finding groups commercially available carbons with model materials that possess the same interlayer interactions. The differences in the two reaction mechanisms were presented in terms of carbon dioxide evolution and current-potential behavior. Iron and sulfur impurities, common in commercially available and laboratory produced carbons, do not control the electrochemical oxidation mechanism. Surface oxides are found to control the behavior observed in cyclic voltammetry while the interlayer interactions controls oxidation. By using a large number of diverse but well-characterized carbon materials, the role of nanostructure and other material properties has been deconvoluted and used to increase our understanding of structure-reactivity behavior.

REFERENCES

[1] Dicks AL. The role of carbon in fuel cells. Journal of Power Sources. 2006; **156**(2), 128-41.

[2] Harris PJF. New perspectives on the structure of graphitic carbons. Critical Reviews in Solid State and Materials Sciences. 2005; **30**(4), 235-53.

[3] Appleby AJ. Carbon Components in the Phosphoric Acid Fuel Cell - An Overview. In: Sarangapani S, Akridge JR, Schumm B, editors. The Electrochemistry of Carbon; 1983 August 17-19; Cleveland, Ohio: The Electrochemical Society, Inc; 1983. p. 251-72.

[4] Perry ML, Fuller TF. A historical perspective of fuel cell technology in the 20th century. Journal of the Electrochemical Society. 2002; **149**(7), S59-S67.

[5] Gallagher KG, Darling RM, Fuller TF. Carbon-support corrosion mechanisms and models. In: Vielstich W, Yokokawa H, Gasteiger HA, eds. *Handbook of Fuel Cells: Advances in Electrocatalysis, Materials, Diagnostics and Durability, Volumes 5 & 6*. Chichester, UK: John Wiley & Sons, Ltd 2009:819-282.

[6] Gallagher KG, Wong DT, Fuller TF. The effect of transient potential exposure on the electrochemical oxidation of carbon black in low-temperature fuel cells. Journal of the Electrochemical Society. 2008; **155**(5), B488-B93.

[7] Perry ML, Darling RM, Kandoi S, Patterson TW, Reiser C. Operating Requirements for Durable Polymer-Electrolyte Fuel Cell Stacks. *Polymer Electrolyte Fuel Cell Durability* 2009:399-417.

[8] Kinoshita K. Carbon: Electrochemical and Physicochemical Properties. New York: Wiley 1988.

[9] Antonucci PL, Pino L, Giordano N, Pinna G. A Comparative-Analysis of Structural and Surface Effects in the Electrochemical Corrosion of Carbons. Materials Chemistry and Physics. 1989; **21**(5), 495-506.

[10] Ball SC, Hudson SL, Thompsett D, Theobald B. An investigation into factors affecting the stability of carbons and carbon supported platinum and platinum/cobalt alloy catalysts during 1.2 V potentiostatic hold regimes at a range of temperatures. Journal of Power Sources. 2007; **171**(1), 18-25.

[11] Colmenares LC, Wurth A, Jusys Z, Behm RJ. Model study on the stability of carbon support materials under polymer electrolyte fuel cell cathode operation conditions. Journal of Power Sources. 2009; **190**(1), 14-24.

[12] Giordano N, Antonucci PL, Passalacqua E, Pino L, Arico AS, Kinoshita K. Relationship between Physicochemical Properties and Electrooxidation Behavior of Carbon Materials. Electrochimica Acta. 1991; **36**(13), 1931-5.

[13] Kinoshita K. Influence of Heat-Treatment and Physicochemical Properties on the Electrochemical Oxidation of Carbon Blacks In Phosphoric Acid. In: Sarangapani S, Akridge JR, Schumm B, editors. The Electrochemistry of Carbon; 1983 August 17-19; Cleveland, OH: The Electrochemical Society, Inc; 1983. p. 273-90.

[14] Kinoshita K, Bett JAS. Effects of Graphitization on the Corrosion of Carbon Blacks. In: Tedmon CS, editor. Proceedings of the Symposium on Corrosion Problems in Energy Conversion and Generation; 1974; 1974. p. 43-55.

[15] Shao YY, Yin GP, Zhang J, Gao YZ. Comparative investigation of the resistance to electrochemical oxidation of carbon black and carbon nanotubes in aqueous sulfuric acid solution. Electrochimica Acta. 2006; **51**(26), 5853-7.

[16] Yu PT, Gu W, Makharia R, Wagner FT, Gasteiger HA. The Impact of Carbon Stability on PEM Fuel Cell Startup and Shutdown Voltage Degradation. ECS Transaction. 2006; **3**(1), 797-809.

[17] Brunauer S, Emmett PH, Teller E. Adsorption of gases in multimolecular layers. Journal of the American Chemical Society. 1938; **60**, 309-19.

[18] Maass S, Finsterwalder F, Frank G, Hartmann R, Merten C. Carbon support oxidation in PEM fuel cell cathodes. Journal of Power Sources. 2008; **176**(2), 444-51.

[19] Makharia R, Kocha SS, Yu PT, Sweikart MA, Gu W, Wagner FT, et al. Durable PEM Fuel Cell Electrode Materials: Requirements and Benchmarking Methodologies. ECS Transaction. 2006; **1**(8), 3-18.

[20] Appleby AJ. Corrosion in Low and High Temperature Fuel Cells - An Overview. Corrosion. 1987; **43**(7), 398-408.

[21] Kinoshita K, Bett J. Electrochemical Oxidation of Carbon-Black in Concentrated Phosphoric-Acid at 135 Degrees C. Carbon. 1973; **11**(3), 237-47.

[22] Cabrera N, Mott NF. Theory of the Oxidation of Metals. Reports on Progress in Physics. 1948; **12**, 163-84.

[23] Schmuki P. From Bacon to barriers: a review on the passivity of metals and alloys. Journal of Solid State Electrochemistry. 2002; **6**(3), 145-64.

[24] Uhlig HH. Initial Oxidation Rate of Metals and the Logarithmic Equation. Acta Metallurgica. 1956; **4**(5), 541-54.

[25] Kangasniemi KH, Condit DA, Jarvi TD. Characterization of vulcan electrochemically oxidized under simulated PEM fuel cell conditions. Journal of the Electrochemical Society. 2004; **151**(4), E125-E32.

[26] Chaparro AM, Mueller N, Atienza C, Daza L. Study of electrochemical instabilities of PEMFC electrodes in aqueous solution by means of membrane inlet mass spectrometry. Journal of Electroanalytical Chemistry. 2006; **591**(1), 69-73.

[27] Willsau J, Heitbaum J. The Influence of Pt-Activation on the Corrosion of Carbon in Gas-Diffusion Electrodes - a Dems Study. Journal of Electroanalytical Chemistry. 1984; **161**(1), 93-101.

[28] Hashimoto A, Suenaga K, Gloter A, Urita K, Iijima S. Direct evidence for atomic defects in graphene layers. Nature. 2004; **430**(7002), 870-3.

[29] Banhart F. Irradiation effects in carbon nanostructures. Reports on Progress in Physics. 1999; **62**(8), 1181-221.

[30] Dahn JR, Sleigh AK, Shi H, Reimers JN, Zhong Q, Way BM. Dependence of the Electrochemical Intercalation of Lithium in Carbons on the Crystal-Structure of the Carbon. Electrochimica Acta. 1993; **38**(9), 1179-91.

[31] Shi H, Reimers JN, Dahn JR. Structure-Refinement Program for Disordered Carbons. Journal of Applied Crystallography. 1993; **26**, 827-36.

[32] Osswald S, Yushin G, Mochalin V, Kucheyev SO, Gogotsi Y. Control of sp(2)/sp(3) carbon ratio and surface chemistry of nanodiamond powders by selective oxidation in air. Journal of the American Chemical Society. 2006; **128**(35), 11635-42.

[33] Portet C, Yushin G, Gogotsi Y. Electrochemical performance of carbon onions, nanodiamonds, carbon black and multiwalled nanotubes in electrical double layer capacitors. Carbon. 2007; **45**(13), 2511-8.

[34] Tomita S, Burian A, Dore JC, LeBolloch D, Fujii M, Hayashi S. Diamond nanoparticles to carbon onions transformation: X-ray diffraction studies. Carbon. 2002; **40**(9), 1469-74.

[35] Ugarte D. Onion-Like Graphitic Particles. Carbon. 1995; **33**(7), 989-93.

[36] Harris PJF, Liu Z, Suenaga K. Imaging the atomic structure of activated carbon. Journal of Physics-Condensed Matter. 2008; **20**(36).

[37] Grimme S, Muck-Lichtenfeld C, Antony J. Noncovalent interactions between graphene sheets and in multishell (Hyper)Fullerenes. Journal of Physical Chemistry C. 2007; **111**(30), 11199-207.

[38] Behler K, Osswald S, Ye H, Dimovski S, Gogotsi Y. Effect of thermal treatment on the structure of multi-walled carbon nanotubes. Journal of Nanoparticle Research. 2006; **8**(5), 615-25.

[39] Chen J, Kuno A, Matsuo M, Tsukada T, Tamura T, Osato K, et al. Removal of entrapped iron compounds from isothermally treated catalytic chemical vapor deposition derived multi-walled carbon nanotubes. Carbon. 2008; **46**(3), 391-6.

[40] Kalaitzidou K, Fukushima H, Drzal LT. Multifunctional polypropylene composites produced by incorporation of exfoliated graphite nanoplatelets. Carbon. 2007; **45**(7), 1446-52.

[41] Fukushima H. Graphite nanoreinforcements in polymer nanocomposites. East Lansing, MI, USA: Michigan State University; 2003.

[42] Aladekomo JB, Bragg RH. Structural Transformations Induced in Graphite by Grinding - Analysis of 002-X-Ray Diffraction Line-Profiles. Carbon. 1990; **28**(6), 897-906.

[43] Salver-Disma F, Tarascon JM, Clinard C, Rouzaud JN. Transmission electron microscopy studies on carbon materials prepared by mechanical milling. Carbon. 1999; **37**(12), 1941-59.

[44] Conway BE. Electrochemical Supercapacitors: Scientific Fundamentals and Technological Applications: Springer 1999.

[45] Pandolfo AG, Hollenkamp AF. Carbon properties and their role in supercapacitors. Journal of Power Sources. 2006; **157**(1), 11-27.

[46] Cheng PZ, Teng HS. Electrochemical responses from surface oxides present on HNO3-treated carbons. Carbon. 2003; **41**(11), 2057-63.

[47] Kinoshita K, Bett JAS. Potentiodynamic Analysis of Surface Oxides on Carbon-Blacks. Carbon. 1973; **11**(4), 403-11.

[48] Binder H, Kohling A, Richter K, Sandstede G. Ueber Die Anodische Oxydation Von Aktivkohlen In Wässrigen Elektrolyten. Electrochimica Acta. 1964; **9**, 255-74.

[49] Dhar HP, Christner LG, Kush AK. On the Effect of the Fe-2+/Fe-3+ Redox Couple on Oxidation of Carbon in Hot H3po4. Journal of Electroanalytical Chemistry. 1986; **213**(1), 161-7.

[50] K. Koziol MSAW. Three-Dimensional Internal Order in Multiwalled Carbon Nanotubes Grown by Chemical Vapor Deposition (Adv. Mater. 6/2005). Advanced Materials. 2005; **17**(6), NA.

[51] Dresselhaus MS, Endo M. Relation of carbon nanotubes to other carbon materials. *Carbon Nanotubes* 2001:11-28.

[52] Gruver GA. Corrosion of Carbon-Black in Phosphoric-Acid. Journal of the Electrochemical Society. 1978; **125**(10), 1719-20.

[53] Liu ZY, Brady BK, Carter RN, Litteer B, Budinski M, Hyun JK, et al. Characterization of carbon corrosion-induced structural damage of PEM fuel cell cathode electrodes caused by local fuel starvation. Journal of the Electrochemical Society. 2008; **155**(10), B979-B84.

[54] Yu PT, Gu W, Zhang J, Makharia R, Wagner FT, Gasteiger HA. Carbon-Support Requirements for Highly Durable Fuel Cell Operation. *Polymer Electrolyte Fuel Cell Durability* 2009:29-53.

[55] Burg P, Cagniant D. Characterization of Carbon Surface Chemistry. *Chemistry and Physics of Carbon, Vol 30* 2008:129-75.

[56] Bleda-Martinez MJ, Lozano-Castello D, Morallon E, Cazorla-Amoros D, Linares-Solano A. Chemical and electrochemical characterization of porous carbon materials. Carbon. 2006; **44**(13), 2642-51.

[57] Choo HS, Kinumoto T, Nose M, Miyazaki K, Abe T, Ogumi Z. Electrochemical oxidation of highly oriented pyrolytic graphite during potential cycling in sulfuric acid solution. Journal of Power Sources. 2008; **185**(2), 740-6.

[58] Siroma Z, Tanaka M, Yasuda K, Tanimoto K, Inaba M, Tasaka A. Electrochemical corrosion of carbon materials in an aqueous acid solution. Electrochemistry. 2007; **75**(2), 258-60.

CHAPTER 6

KINETIC MODEL OF THE ELECTROCHEMICAL OXIDATION OF GRAPHITIC CARBON IN ACIDIC ENVIRONMENTS

6.1. INTRODUCTION

Carbon is an essential material for aqueous electrochemical energy devices such as low-temperature fuel cells (LTFCs), redox-flow batteries, and supercapacitors [1-4]. Graphene based carbons, such as carbon black, used in the electrodes of these devices are susceptible to electrochemical oxidation resulting in mass loss and surface oxide growth [3]. Increasing levels of oxidation correlate with a decrease in performance reducing the useable life of the electrochemical system [3, 5-8]. Predicting the rate of electrochemical oxidation, and thus the lifespan of the electrochemical system, has proven to be challenging for the industrial and scientific communities alike [9, 10]. To date, a kinetic model based on an electrochemical mechanism has not been published. Available models either completely neglect the complex behavior observed or use empirical equations correlated with mass loss of the electrode [5, 9, 11, 12]. These approaches provide no physical insight into the observed behavior and therefore do not advance the basic understanding of the electrochemical oxidation mechanism. Furthermore, an empirical approach is inherently poor at predicting mass loss and surface oxide concentrations under oxidation conditions differing from those used to derive the model.

LTFCs include phosphoric acid fuel cells and proton exchange membrane fuel cells (PEMFC) where carbon is used as a catalyst support for metal nanoparticles.

Electrochemical oxidation occurs during both normal and abnormal operating conditions of a PEMFC. However, oxidation during abnormal conditions, such as the start or stop of the fuel cell stack, is typically more severe than normal operating conditions [7, 9, 13, 14]. In PEMFCs, this phenomenon is commonly referred to as carbon corrosion. Abnormal conditions are transient in nature and are likely to occur thousands of times. Therefore a numerical model capable of tracking the oxidation of the carbon during cyclic potential exposures is necessary to accurately predict the lifespan of the fuel cell stack. The purpose of this work is to present a model capable of meeting the needs outlined above.

The electrochemical mechanism for CO_2 formation is presently unknown with only a modest quantity of kinetic data available in the published literature. The lack of kinetic data is a result of the difficulties in treating a transient, nonlinear, and competing parallel reaction pathway coupled with the challenging quantification of reaction and product concentrations with time. The existing knowledge is summarized as follows. First, CO_2 formation in moderate to dilute acids has been shown to be first order in the partial pressure of water vapor [10, 15]. Second, the current efficiency for CO_2 formation is near 80 % at long times [16, 17]. Third, the rate of reaction during a potentiostatic hold slows with time and is commonly approximated with a power law, $i = kt^{-n}$ [3]. This empirical equation, or some variation of it, is the most common rate expression assumed for the electrochemical oxidation of carbon. Fourth, the decay of current has a moderate degree of reversibility after a reducing potential is applied to the carbon [18, 19]. The reversibility is a function of the severity of the previous oxidation and reducing

conditions. Lastly, CO has been detected but measured to be lower than a factor of 10 compared to CO_2 and is thus neglected here [10, 20, 21].

The quantity and speciation of surface oxides on graphitic carbons has been investigated with a large number of experimental techniques. These techniques include, but are not limited to, X-ray photoelectron spectroscopy, temperature programmed desorption, Boehm titration, and Fourier-transform infrared spectroscopy [3, 22]. Due to the well documented limitations of each technique, only a qualitative understanding of the surface chemistry exists. Lactone, anhydride, carboxylic, quinone, and phenol functional groups have been detected as well as others [3, 22, 23]. The role of these oxides in the electrochemical oxidation of carbon remains to be discovered. Evidence does exist to support general conclusions on some aspects of the mechanism. The surface coverage of oxides increases with exposure to oxidative potentials [3, 18, 23-25]. Various oxides are formed with differing electrochemical behavior. Some species are completely reversible and may be removed through electrochemical reduction [26]. Other chemistries display pseudo-capacitance [3, 18, 23]. Still other surface oxides appear to catalyze the formation of CO_2 [17, 27]. Correlating a specific behavior to the chemistry of the surface oxide species is unknown except for two instances discussed further in section 2.1.

High surface area disordered carbons are heat treated to promote graphitization resulting in a catalyst support with greater resistance to electrochemical oxidation [3, 6, 28, 29]. Although the graphitization process increases the stability, it also results in a

lower surface area. A minimum required surface area of 100 m^2/g has been suggested to achieve adequate dispersion of the metal nanoparticles such as platinum [30]. Recently, we reported an in-depth study of various carbons with and without heat treatment [17]. Much of this and other work focuses on Vulcan XC-72 (Cabot Corporation), a commonly used catalyst support in PEMFC. After heat treatment of XC-72 for two hours at 1900 °C under Argon, the carbon displayed substantially improved resistance to electrochemical oxidation and a Brunauer-Emmett-Teller (BET) [31] specific surface area of 100 m^2/g. Therefore, we choose this material to be the basis for our parameter estimation.

Based upon the published literature and work within our laboratory, we present a kinetic model to describe the behavior of carbon oxidation as a function of time, temperature, and potential. Due to deficient published kinetic data, some phenomenological aspects are necessary. For example, the specific chemistries of oxide species are assumed based upon some general observations in literature but without rigorous determination. Nonetheless, this proposed model presents the first attempt to use mechanistic details to understand and predict the complicated and poorly understood behavior of the electrochemical oxidation of carbon.

6.2. MODEL

6.2.1 Electrochemistry

This proposed mechanism assumes the existence of two types of sites on the carbon surface, # and *. The # sites are the active sites for the rate determining step of CO_2 formation. Here water is reversibly adsorbed and initial oxides are formed. The * sites are the location of both CO_2 loss and simultaneous oxide formation. The two site assumption is necessary to allow for the production of an oxide that does not consume sites involved in the rate determining step. No other physical formulation of the mechanism was found to give acceptable results. A two site model has also been proposed for the gas phase oxidation of carbon [32]. However, the physical role of the sites most likely differs for electrochemical oxidation and gas phase as the oxidant is water and not molecular oxygen. The first reaction, Equation 6.1, is the growth of a catalytic oxide necessary to represent the CO_2 behavior observed in graphitized carbons [17, 27]. Colmenares *et al*. term this oxide a nucleation site or active center [27]. We adopt the term catalytic in reference to the constancy of the oxide during CO_2 formation. To model non-graphitized carbons, the equilibrium surface concentration of this oxide may be assumed initially present. This assumption may or may not be physically correct but allows for a semi-empirical approach to modeling the observed reaction.

$$C^{\#} + H_2O \rightarrow C^{\#}OH + H^+ + e^- \qquad (6.1)$$

The first step in our proposed CO_2 mechanism is the reversible adsorption of water onto the reaction site, #, Equation 6.2a. This step is assumed to be fast and at equilibrium. The second step is assumed to be the slowest and thus the rate determining step (RDS), Equation 6.2b. The RDS is proposed based upon the previously mentioned first order reaction dependence on water partial pressure. The elementary steps after the RDS are unknown and perhaps unimportant for this model. We present the necessary equations to match the stoichiometry requirements but are careful to state no irrefutable experimental evidence exits to support any of the reaction intermediates postulated here or elsewhere in the published literature, Equation 6.2c-e. Our stoichiometry generally follows that suggested by Binder *et al*. and results in an 80 % current efficiency [3, 16, 17]. The concentrations of reactant intermediates are assumed to be negligible in the site balance.

$$C^{\#} + H_2O \leftrightarrow C^{\#}(H_2O)_{ads} \tag{6.2a}$$

$$C^{\#}(H_2O)_{ads} + C^{\#}OH \rightarrow C^{\#}OC^{\#}OH + 2H^{+} + 2e^{-} \tag{6.2b}$$

$$2C^{\#}OC^{\#}OH + 3C^{*} + 3H_2O \rightarrow C^{*}O(C^{*}OOH)_2 + 2C^{\#} + 2C^{\#}OH + 4H^{+} + 4e^{-} \tag{6.2c}$$

$$C^{*}O(C^{*}OOH)_2 \rightarrow C^{*}OOH + C^{*}O + * + CO_2 + H^{+} + e^{-} \tag{6.2d}$$

$$C^{*}OOH \rightarrow * + CO_2 + H^{+} + e^{-} \tag{6.2e}$$

The carbon oxidation current generally diminishes during electrochemical oxidation. As no physical model has been published in literature, no consensus exists on the source(s) of current decay. We advocate three physical reasons for this decay in order to explain the complicated behavior observed. The first source of time decay is from the mass loss suffered during the gasification to CO_2. As shown later, we express the observed rate to be proportional to the total sites available. We define a site in relation to the specific surface area of the carbon. Thus, a decrease in mass results in a proportionate decrease in total sites available for carbon oxidation. This assumes the specific surface area and concentration of sites does not change with time. BET measurements have not shown a significant change in specific surface area after prolonged oxidation [23]. Mass loss induced irreversible decay is only significant under conditions of elevated potential and temperature for long times or many cycles.

The second source of time decay is the reversible formation of a passive surface oxide as described in Equation 6.3. This oxide is responsible for the characteristic power law decay observed and often approximated by $i = kt^{-n}$. The stoichiometry, x, is the parameter that controls the slope of the total current. Here, we find $x = 3$ to be the best fit. A value of $x = 3$ is shown in section 6.6 to translate to a CO_2 current decaying at $n = 1/2$. The result in the supporting information is based upon an ideal system where no other transients are occurring. The oxidation current from the growth of this oxide typically dominates the total current at short times. A two electron transfer was chosen based upon the electrochemical reduction of chemically produced oxides on carbon [26]. The authors found 2.6 electrons were required per oxygen atom removed in their system [26].

$$xC^{\#} + H_2O \leftrightarrow C^{\#}_xO + 2H^+ + 2e^- \quad (6.3)$$

The third and final source of time decay is irreversible and results from reduction of the oxidized carbon surface. Equations 6.4–6.6 describe the chemistry chosen to physically represent the observed behavior. Equation 6.4 is a consumption of the catalytic oxide to establish an equilibrium concentration on the # sites. This equilibrium is suggested to be affected by the production of other surface oxides. Exposure to potentials greater than 1 V produce the oxides C^*O and $C^{\#}_xO$ on the carbon surface. We propose that a reduction of the C^*O oxide, Equation 6.5, results in the formation of a species that further reduces the equilibrium concentration of the catalytic oxide, $C^{\#}OH$. Equation 6.6 is a representation of the acceleration of Equation 6.4 with increasing quinone coverage, $C^{\#}_xO_2$.

$$2C^{\#}OH + (x–2)C^{\#} + H_2O \rightarrow C^{\#}_xO_3 + 4H^+ + 4e^- \quad (6.4)$$

$$C^{\#}_xO + C^*O \rightarrow C^{\#}_xO_2 + C^* \quad (6.5)$$

$$2C^{\#}OH + (x\text{-}2)C^{\#} + H_2O + C^{\#}_xO_2 \rightarrow C^{\#}_xO_3 + C^{\#}_xO_2 + 4H^+ + 4e^- \quad (6.6)$$

The final electrochemical equation is the redox couple of the quinone/hydroquinone group (Q/HQ). This oxidation reduction reaction is prominent in the cyclic voltammetry studies of oxidized graphene based carbons [18, 23, 25, 33].

$$C^{\#}_{x}(OH)_2 \leftrightarrow C^{\#}_{x}O_2 + 2H^+ + 2e^- \quad (6.7)$$

6.2.2 Rate Equations

The kinetic expressions chosen to model the electrochemical Equations 6.1–6.7 are displayed in the Table 6.1. The rate expressions are numbered to correspond to the relevant electrochemical equation. For example, r_1 is the rate equation used to describe Equation 6.1. The dependence of oxidation on the partial pressure of water has only been reported for CO_2 generation and is thus considered solely in r_2. To minimize the number of unknown parameters, the rate constant k_2 in r_2 is assumed to include the equilibrium coefficient for the adsorption of water, $K_{C\#(H2O)}$, from Equation 6.2a. All rate constants, k_j, are in mol/cm^2 s based on the surface area measured with the BET method. A Frumkin factor, g, is included in some rate equations to describe the change in energy as the surface coverage increases [34, 35]. Increasing coverage is assumed to have a repulsive effect on the addition of subsequent species. A value of $g = 3$ is used for all reactions that include the parameter and improves the overall fit of the model. The reference conditions for the equilibrium potentials, U_j, are assumed to be 100 kPa and 1 mol/L concentrations. The derivation of r_3 is included in the supporting information but all reactions generally assume the first electron transfer to be rate limiting in both oxidation and reduction unless stated otherwise. Although the concentration of protons, c_+, is included in r_3, no experimental data on the effect of pH in carbon oxidation have been reported. The inclusion of the c_+ in r_7 is based on substantial evidence of the dependence of the Q/HQ

reaction on pH [3, 33]. The rate equation r_6 has taken the dependence on quinone coverage to be 0.25. This fractional dependence is necessary to accurately represent the cyclic decay discussed later in section 2.4. The electrode potential, V, is the difference between the metal potential and a hypothetical standard hydrogen electrode (SHE) with p_{H2} = 100 kPa and c_+ = 1 mol/L. Experimental data collected against a reversible hydrogen electrode are corrected within the model to the hypothetical SHE.

Table 6.1. Rate equations used to model the proposed mechanism.

$$r_1 = k_1 \theta_{vac}^{\#} \exp\left[\frac{\alpha_{a,1} F}{RT}\left(V - U_1\right) - g\theta_{\text{cov}}^{\#}\right]$$

$$r_2 = k_2 \theta_{vac}^{\#} \theta_{COH}^{\#} \left(\frac{p_o}{p_o^{ref}}\right) \exp\left[\frac{\alpha_{a,2} F}{RT}\left(V - U_2\right)\right]$$

$$r_3 = k_3 \left\{\left(\theta_{vac}^{\#}\right)^3 \exp\left[\frac{\alpha_{a,3} F}{RT}\left(V - U_3\right) - g\theta_{\text{cov}}^{\#}\right] - \theta_{CxO}^{\#} \left(\frac{c_+}{c_+^{ref}}\right) \exp\left[-\frac{\alpha_{c,3} F}{RT}\left(V - U_3\right) + g\theta_{\text{cov}}^{\#}\right]\right\}$$

$$r_4 = k_4 \theta_{vac}^{\#} \theta_{COH}^{\#} \exp\left[\frac{\alpha_{a,4} F}{RT}\left(V - U_4\right) - g\theta_{\text{cov}}^{\#}\right]$$

$$r_5 = -k_5 \theta_{CxO}^{\#} \theta_{CO}^{*} \exp\left[-\frac{\alpha_{c,5} F}{RT}\left(V - U_5\right)\right]$$

$$r_6 = k_6 \theta_{vac}^{\#} \theta_{COH}^{\#} \left(\theta_{CxO2}^{\#}\right)^{0.25} \exp\left[\frac{\alpha_{a,6} F}{RT}\left(V - U_6\right) - g\theta_{\text{cov}}^{\#}\right]$$

$$r_7 = k_7 \left\{\theta_{Cx(OH)2}^{\#} \exp\left[\frac{\alpha_{a,7} F}{RT}\left(V - U_7\right)\right] - \theta_{CxO2}^{\#} \left(\frac{c_+}{c_+^{ref}}\right) \exp\left[-\frac{\alpha_{c,7} F}{RT}\left(V - U_7\right)\right]\right\}$$

6.2.3 Material Balances

The material balance on the moles of carbon, N_c, is expressed in Equation 6.8. Here S is the specific surface area in cm^2/g and M is the molecular weight of carbon. The material balances for the surface oxide species are located in Table 6.2.

$$\frac{\partial N_c}{\partial t} = -r_2 S N_c M \tag{6.8}$$

The total current, i_{total}, is the summation of rates multiplied by Faraday's constant and the available carbon area, Equation 6.9. If N_c is taken to be on a geometric area basis, i_j has units of A/cm^2.

$$i_{total} = \sum_j i_j = S N_c M F \sum_j r_j n_j \tag{6.9}$$

6.2.4 Fitting Parameters

Only a few parameters may be calculated or are available in the literature. The remaining values have been fit to experimental data. As detailed previously, the literature instructs the rate of CO_2 formation is first order in the partial pressure of water vapor. Therefore, we assume the equilibrium potential for CO_2 formation is the standard potential calculated for water vapor reacting with carbon. The temperature dependence of

this value was calculated from tabulated thermodynamic data [36] and is shown below in Equation 6.10. U_2 is equal to 0.15 V at 80 °C.

$$U_2 = -0.00023T + 0.2326 \tag{6.10}$$

Table 6.2. Material balances for kinetic model

$$[*] = [*]_{vac} + [C^{*}O]$$

$$[\#] = [\#]_{vac} + [C^{\#}OH] + x([C^{\#}{}_xO] + [C^{\#}{}_x(OH)_2] + [C^{\#}{}_xO_2] + [C^{\#}{}_xO_3])$$

$$\theta_l^s = \frac{[l]}{[s]};\ \theta_{vac}^{*} = \frac{[*]_{vac}}{[*]};$$

$$\theta_{\text{cov}}^{\#} = 1 - \theta_{vac}^{\#} = \theta_{COH}^{\#} + x\left(\theta_{CxO}^{\#} - \theta_{CxO2}^{\#} - \theta_{CxO3}^{\#}\right)$$

$$\frac{\partial \theta_{COH}^{\#}}{\partial t} = \frac{r_1 - 2\left(r_4 + r_6\right)}{[\#]}$$

$$\frac{\partial \theta_{CxO}^{\#}}{\partial t} = \frac{r_3 + r_5}{[\#]}$$

$$\frac{\partial \theta_{CO}^{*}}{\partial t} = \frac{\left(\frac{1}{2}r_2\right) + r_5}{[*]}$$

$$\frac{\partial \theta_{CxO3}^{\#}}{\partial t} = \frac{r_4 + r_6}{[\#]}$$

$$\frac{\partial \theta_{CxO2}^{\#}}{\partial t} = \frac{r_7 - r_5}{[\#]}$$

$$\frac{\partial \theta_{Cx(OH)2}^{\#}}{\partial t} = \frac{-r_7}{[\#]}$$

The model was first fit to the total and CO_2 currents from a 1.3 V hold at 80 °C in a Nafion® membrane electrode assembly (MEA) based on previously published work [17]. All experimental data were collected at 100 % relative humidity (RH) under flowing nitrogen gas. A completely vacant surface is assumed for the initial conditions of the numerical model. Experimental measurements suggest a small surface concentration of oxygen is initially present on heat treated carbon ~1 x 10^{-6} mol/m^2 [17]. This oxygen concentration is either persistent during heat treatment or chemisorbed from the atmosphere after heat treatment [22]. The effect of these oxides on the electrochemical oxidation mechanism is unknown and thus neglected here. The electrodes are electrochemically reduced at 0.04 V to minimize the role of any minor oxides already present on the surface. Simulations assuming a nonzero initial concentration of oxides produced a fit of equal or poorer quality than those with an initially vacant surface. The system of differential equations was solved with BAND [37] using Crank-Nicholson time stepping. A Levenberg-Marquardt algorithm was used to find the best fit for the 1.3 V hold [38]. The transfer coefficients were fit to data from the potentiostatic holds at 1.4 V and 1.2 V at the same experimental conditions. The fitted parameters were then used to simulate a cyclic voltammogram (CV). The fitting process was iterated to reach a compromise between fitting peak locations in the CV and potential dependence observed in the potentiostatic holds.

The surface concentration of each site, [*] and [#], is determined during the fitting process. An initial assumption for the maximum number of sites may be calculated assuming a hexagonally bonded graphite structure. Calculations from literature and our

own suggest 1.7 – 6.6 x 10^{-5} mol sites / m^2 [23, 24]. A simple calculation shows that at 80 % current efficiency, 1 monolayer (ML) would be reached after 5-16 % weight loss has occurred for a specific surface area of 100 m^2/g. As the literature has shown CO_2 evolution does not stop at these levels of weight loss [6, 18], the reaction should not be limited by 1 ML of surface oxide formation. It is not clear whether a film is formed or more sites are made available. We have observed a passivity type behavior under severe, oxidative potentiostatic holds for non-heat-treated carbons. For example, an as-received XC-72 carbon in ½ M H_2SO_4 will display passivity around 300 minutes at 1.3 V and 80 °C and also at 1.4 V and 60 °C. This behavior occurs near 11 % weight loss for the 250 m^2/g carbon. We also note that Nafion® based MEAs of as-received XC-72 did not display this passivity type behavior [17]. Without more information, especially in regards to heat treated carbons, we take the [*] = 10^{-4} mol sites/m^2 and limit simulations to a maximum of 20 % weight loss. 5-10 % weight loss has been suggested to result in unacceptable performance degradation for state of the art electrodes [6, 30]. The surface concentration of # sites is determined by fitting the total current at short times with the passive oxide formation, Equation 6.3. [#] is fit to be 0.045 times smaller than [*].

All rate constants are assumed to have an Arrhenius dependence on temperature, Equation 6.11. The activation energy, E_a, was fit to 60 °C data from Nafion® bonded porous electrodes in ½ M H_2SO_4 as currents from crossover hydrogen begin to dominate at lower temperature studies in the MEAs. Although some differences exist between these two electrolytic environments, Nafion® bonded carbon in ½ M H_2SO_4 provides a reasonable means for evaluating the temperature dependence.

$$k_i = k_i^o \exp\left(\frac{-E_a}{RT}\right) \tag{6.11}$$

The final fitting process is to establish the change in equilibrium concentration of the catalytic oxide during repeated cycling. Experimental results show a 15 % decrease in total and CO_2 current after each 1 hour oxidation hold followed by a reduction at 0.04 V [17]. This decay is large compared to the 1-2 % mass loss during each exposure. The effect of the quinone species on the catalytic oxide, Equations 6.5 and 6.6, is fit to match the 15 % decay. If we take the same potential dependence for reactions 1, 4, and 6, the equilibrium concentration of the catalytic oxide may be represented by the following expression.

$$K_{COH}^{\#} = \frac{k_1}{k_4} = \theta_{COH}^{\#}\left(1 + \frac{k_6}{k_4}\left(\theta_{CxO2}^{\#}\right)^{0.25}\right) \tag{6.12}$$

The fitted parameters and their source are detailed in Table 6.3. Parameters are lumped whenever possible to minimize the number of unknowns. The inclusion of $K_{C\#(H2O)}$ in k_2, is an example previously discussed in section 2.2. The treatment of the catalytic oxide is simplified by assuming the same kinetic dependencies for r_4 and r_6. Only the rate constants have differing values. Some general comments may be made regarding the uniqueness of the parameters. Due to the dearth of published kinetic data, many of the parameters have assumed or fitted values. One example is the coupling of the passive oxide and carbon dioxide formation reactions, r_2 and r_3. The CO_2 current depends

directly on the rate constant and the vacant sites available. We are unable to separate the two contributions, and thus a different combination of the activation energies for r_2 and r_3 may provide a similar solution. Acknowledging these introduced uncertainties, we maintain that a well defined physical model maintains a strong advantage over those that are empirically formulated.

6.3. EXPERIMENTAL

6.3.1 Materials and Testing

The experimental results were obtained using the materials and methods detailed previously [17]. Briefly, Vulcan XC-72 (Cabot Corporation) carbon black batches were separately heat treated under Argon for two hours at 1600, 1900, 2200, and 2400 °C. The carbon treated at 1900 °C is the basis for the parameter estimation using the kinetic model. Nafion® ionomer, produced by the DuPont Co., was used as the binding electrolyte. The 1100 g/mol equivalent weight (EW) Nafion ionomer was purchased as 20 wt% alcohol based solution from Ion-power, Inc. Nafion® polymer electrolyte is based on a per(fluorosulfonic acid) chemistry and is the standard electrolyte for PEMFCs. A 0.8 to 1.0 weight ratio of ionomer to carbon was maintained in the electrodes. Nafion® bonded electrodes were tested in ½ M H_2SO_4 under temperature and potential control. Humidified nitrogen gas protected the three electrode cell from oxygen intrusion. MEAs were fabricated in-house and tested in the usual way [17, 18, 39]. A fuel cell test station maintained operating temperature, dewpoint, and mass flowrates. All MEA experimental

data were collected at 100 % RH under flowing nitrogen gas. The condensing water was removed from the exit gas of the carbon electrode. The CO_2 concentration of the dry gas stream was analyzed with a model 600 series nondispersive infrared detector (NDIR) from California Analytical Instruments, Inc. A platinum based reversible hydrogen electrode was used for all tests.

6.4. RESULTS AND DISCUSSION

6.4.1 Potentiostatic Holds

A comparison between experiment and simulation for total and CO_2 currents during potentiostatic holds for an 1100 EW Nafion® based MEA at 80 °C and 100 % RH are shown in Figure 6.1 on a log-log scale. The experimentally measured CO_2 is transformed into a current using Faraday's law and 4 electrons per molecule. The fit is excellent for 1.3 and 1.4 V particularly at times greater than 10 minutes. The fit for 1.2 V is satisfactory although less impressive than that for 1.3 and 1.4 V. The largest discrepancy exits for the steep current decline at times less than 10 minutes. This current is from the formation of the reversible passive oxide, Equation 6.3. The shape of the simulated passive oxide current appears to be different from that measured experimentally. However, the same order of magnitude is represented. Contributions from double layer capacitance have been calculated and found to be negligible at times greater than 0.01 minutes. As performance decay of PEMFC is correlated with weight loss, we have placed a greater emphasis to match the CO_2 formation.

Table 6.3. Parameters for kinetic model and their source: [a] calculated; [b] Levenberg-Marquardt algorithm; [c] manual fitting; [d] assumed.

parameter	**units**	r_1	r_2	r_3	r_4	r_5	r_6	r_7
k^o	mol/cm^2 s	2.35E-16 [b]	9.50E-03 [b]	2.19E-07 [b]	1.18E-12 [c]	4.22E-18 [c]	2.35E-11 [c]	6.00E-8 [d]
U (80 °C)	V vs SHE	1.00 [d]	0.15 [a]	0.95 [c]	1.00 [d]	1.00 [d]	1.00 [d]	0.57 [c]
α_a	N/A	0.35 [c]	0.65 [c]	0.48 [c]	0.5 [d]	N/A	0.5 [d]	0.5 [d]
α_c	N/A	N/A	N/A	0.65 [c]	N/A	1.0 [c]	N/A	0.5 [d]
E_a	kJ/mol K	10 [c]	110 [c]	50 [c]	10 [c]	10 [c]	10 [c]	20 [d]

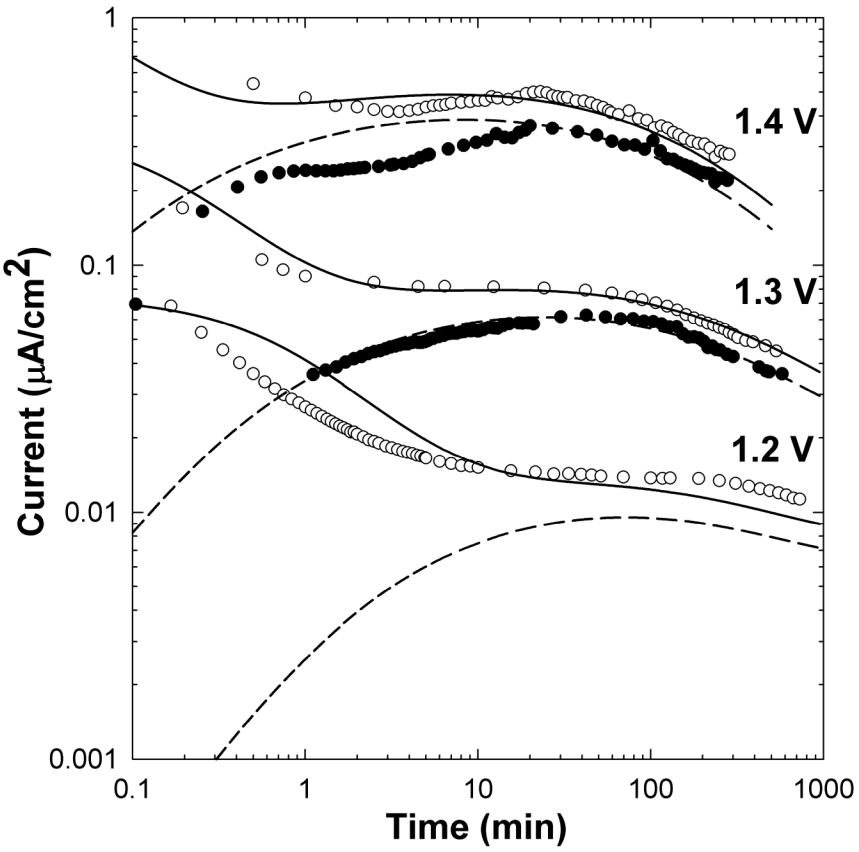

Figure 6.1. Simulation and experimental results for 1.2, 1.3, and 1.4 V potentiostatic holds at 80 °C and 100 % RH. Simulated total (solid line) and CO_2 current (dashed line) are compared to measured total current (open circles) and CO_2 (closed circles). CO_2 evolution at 1.2 V was too small to be accurately monitored with our experimental approach.

The kinetic model allows for an examination of the mechanism for time decay during potentiostatic oxidation. Figure 6.2 displays the oxide coverage and remaining fraction of initial carbon as a function of time during a 1.3 V hold at 80 °C. The transient behavior of CO_2 formation is most significantly affected by the growth of the catalytic oxide and the reduction of vacant # sites by the passive oxide. Only at times near 1000 minutes for 1.3 V and 100 minutes for 1.4 V does the weight loss contribute to a substantial reduction in the current. The interplay between the growth of the catalytic

oxide and the consumption of vacant sites by the passive oxide leads to a power law decay less severe than expected from the calculations in the supporting information. For the 1.3 V hold, the empirical time decay exponent for the experimental data between 100 and 500 minutes is $n = 0.3$. Even though we have used $x = 3$ for the stoichiometry of the passive oxide in r_3, the simulation has excellent agreement with experimental data.

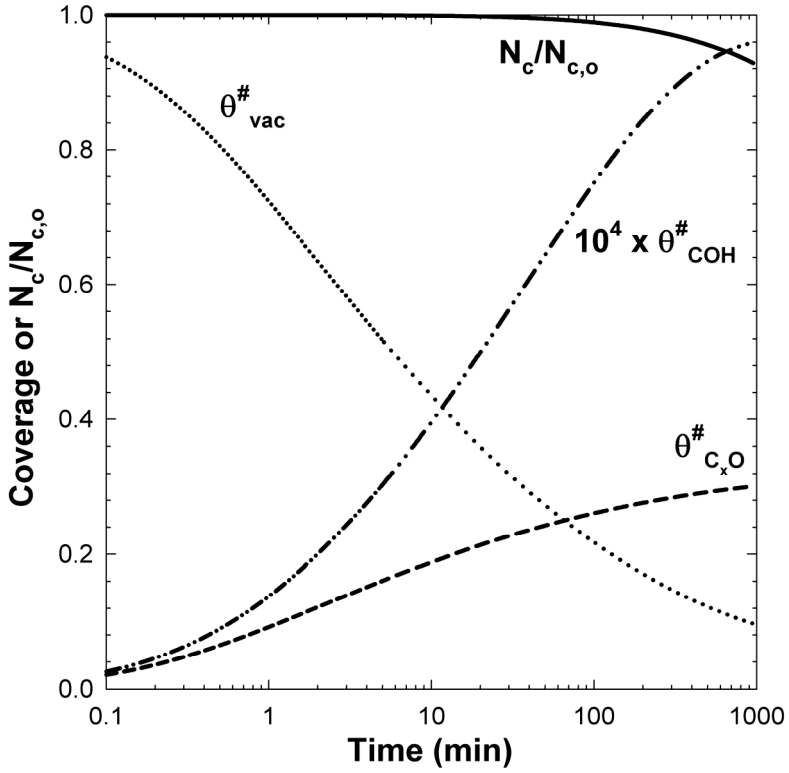

Figure 6.2. Simulated oxide coverage and remaining fraction of initial carbon for a MEA held at 1.3 V at 80 °C and 100 % RH.

Activation energies for the proposed reactions were determined to ensure a wide range of applicability of the model. The simulation and comparison of potentiostatic holds measured at 60 °C is presented in Figure 6.3. The values of activation energies used can be found in Table 6.3. The model is most successful in the prediction at long

times and for 1.3V. This result is similar to the comparison of the model at 80 °C. Conversely, here the fit for the 1.2 V hold is more satisfactory than that for 1.4 V. The poor prediction of the model at short times results from the treatment of the passive oxide formation. As these experimental data originates from Nafion® bonded electrodes in ½ M H_2SO_4, we expect differences in the electrolytic environment to affect the double layer. Comparison between these electrodes at 80 °C with MEA data display strong similarities with modest discrepancies. Two groups have reported activation energies for CO_2 formation for carbon black supporting platinum nanoparticles. Mathias *et al*. report a lumped activation energy of 67 kJ/mol for 100 % RH under potentiostatic conditions [5, 30]. Maass *et al*. report an activation energy of 58 kJ/mol during cyclic voltammetry while controlling for water vapor concentration changes with temperature [10]. The cyclic voltammetry study is interesting but may be affected by the presence of platinum as discussed by Roen *et al*. [40]. Our fitted activation energy for CO_2 formation differs from these values. The separate treatment of the different reactions, Equations 6.1-6.3, results in three activation energies that all contribute to the rate of CO_2 formation. We obtain an observed E_a of 65 kJ/mol in agreement with Mathias *et al*. if we use a single lumped activation energy for all temperature effects. However, the treatment of reactions separately allows an examination of how each contribution may depend on temperature. For example, the growth of the catalytic oxide is fit with an activation energy of 10 kJ/mol. This temperature dependence is necessary to accurately model the small change in the location of maximum rate of CO_2 formation.

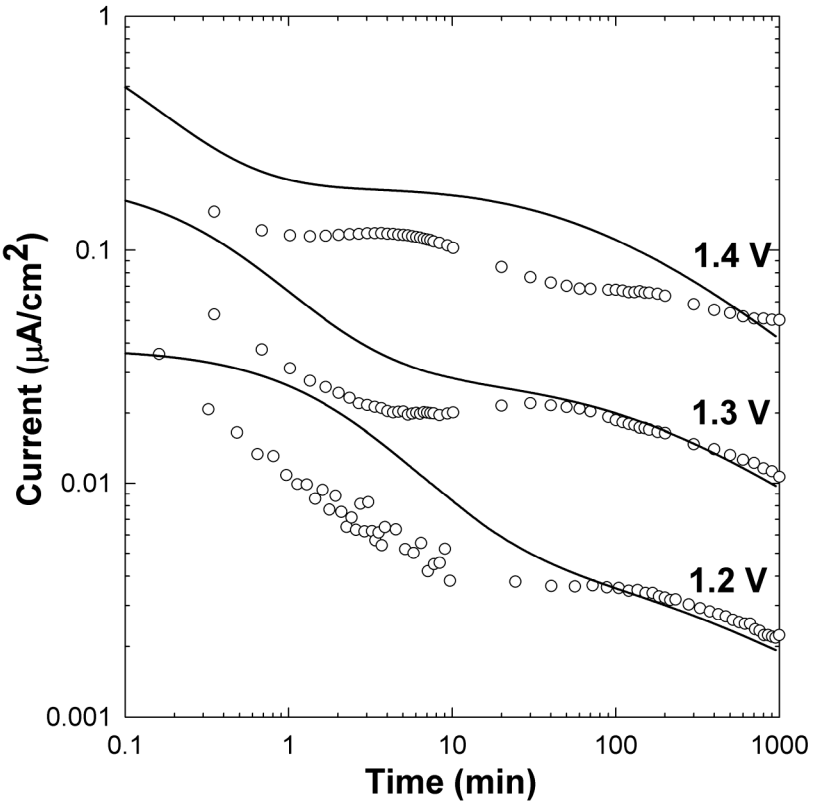

Figure 6.3. Simulation and experimental results for 1.2, 1.3, and 1.4 V potentiostatic holds at 60 °C and 100 % RH. Simulated total current (solid line) is compared to measured total current (open circles).

6.4.2 Transient Potential Exposure

A comparison between simulated and experimentally measured CVs at 10 mV/s and 30 °C is displayed in Figure 6.4. The capacitance was empirically fit to the measured CV. The CV display the same general behavior with the poorest fit being the position of the cathodic peak. The prediction of the cathodic peak location becomes worse with increasing temperature. Experimental data show a positive shift in the cathodic peak potential as temperature is increased. Our model does not predict this behavior. The

empirical potential dependent capacitance is provided in Equation 6.13 and 6.14. For XC-72 heat treated at 1900 °C, C_o is equal to 2.2 μF/cm^2.

$$C_{dl} = C_o(0.65 + 0.67V) \qquad \text{positive sweep} \qquad (6.13)$$

$$C_{dl} = C_o(1.10 + 0.32V) \qquad \text{negative sweep} \qquad (6.14)$$

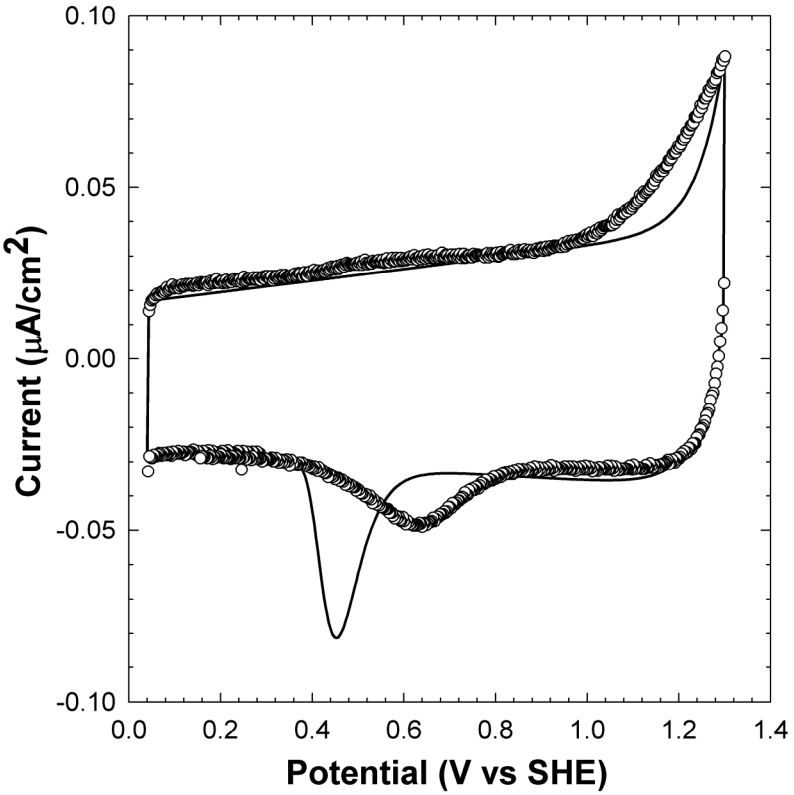

Figure 6.4. Cyclic voltammogram experimentally measured (open circles) and simulated (solid line) at 10 mV/s and 30 °C.

The irreversible decay observed after potential cycling is perhaps the most relevant decay mechanism for fuel-cell stack operation. A simulated oxidation reduction

cycle is used to evaluate this decay mechanism. We hold the carbon at 1.3 V for 60 minutes and then conduct a CV sweep at 50 mV/s with a lower potential of 0.04 V before holding at the high potential again. The model captures the decrease in CO_2 and total current after an initial build up of the catalytic oxide Figure 6.5a. Figure 6.5b clearly shows the decrease in the concentration of the catalytic oxide after each reduction. As the $C^{\#}_xO_2$ and C^*O concentrations rise, the equilibrium concentration for $C^{\#}OH$ is reduced.

The electrochemical behavior of an oxidized carbon is further investigated by examining the contribution to the current from different sources during the second oxidation cycle. The total current, CO_2 current, and currents that produce the C^*O and $C^{\#}_xO$ oxides are displayed in Figure 6.6. At short times, the current is dominated by the formation of the passive oxide, $C^{\#}_xO$. At longer times, the CO_2 current represents 80 % of the total with the simultaneous production of C^*O contributing the remaining 20 %. This current behavior is similar to those observed for disordered graphene-based carbons and may provide clues to the mechanistic differences [17].

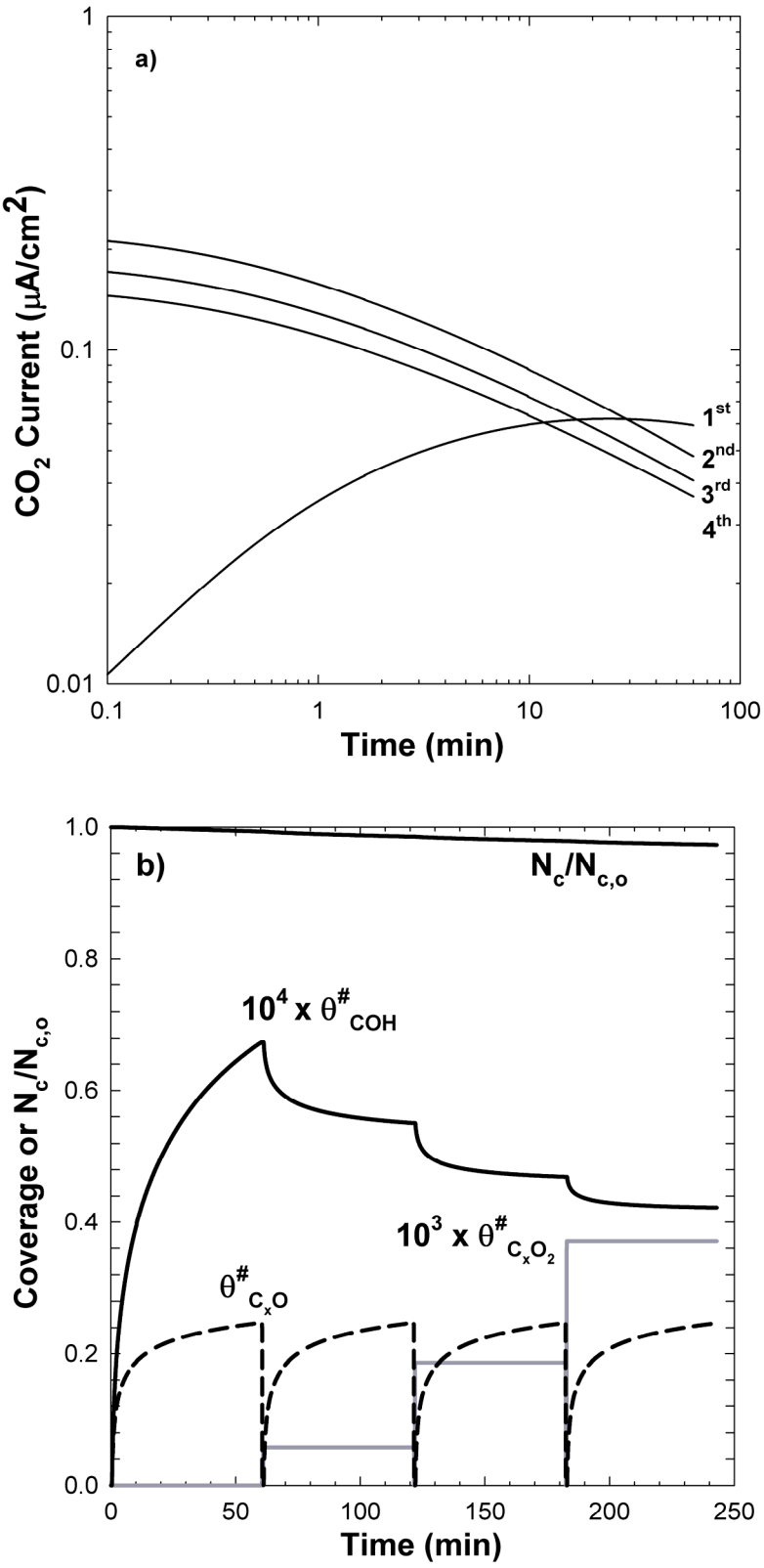

Figure 6.5: Simulated CO_2 current (a) and oxide coverage (b) during repeated cycles of a 60 minute 1.3 V potentiostatic hold and a CV with lower potential of 0.04 V at 80 °C.

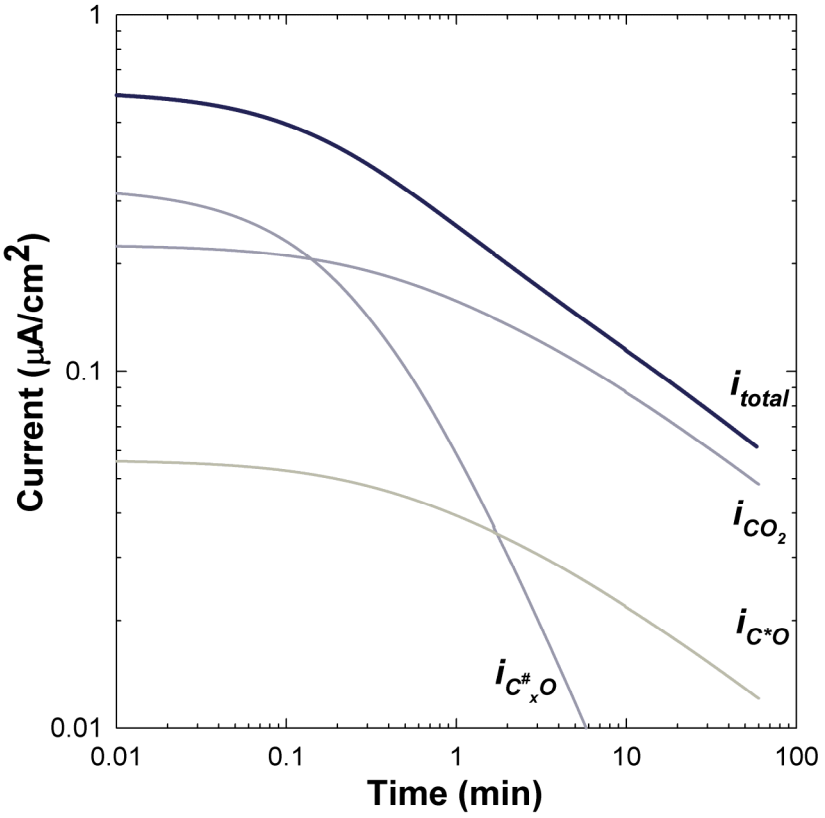

Figure 6.6. Simulated total current and its constituents for the second oxidation cycle of a 60 minute 1.3 V potentiostatic hold after a CV with lower potential of 0.04 V at 80 °C.

We investigated the effect of transient potential exposure on the rate of carbon oxidation using square wave potential cycling (SQWV). Here, we maintained the high potential at 1.3 V and varied the lower potential for different simulations. The potential is held for a 30 second period before sweeping at 0.5 V/s to the next potential limit. A sweep instead of an immediate step is used to provide a more realistic comparison to both actual fuel cell operation and potential controlled experiments. This results in less than 2 seconds of delay before the next potential hold and is likely insignificant. Each simulation reached 1000 total minutes at the potential of 1.3 V and the data have been normalized to this time in the Figure. The simulation conditions are 80 °C and 100 %

RH. A lower potential limit of 0.7 V is found to be the most severe potential exposure tested, Figure 6.7a. This SQWV potential exposure results in more than twice the mass loss compared to the potentiostatic hold. The potential cycle with a lower limit of 0.4 V is the least severe of cycles tested and similar to that of the potentiostatic hold. The surface coverage of the catalytic oxide, $\theta^{\#}_{COH}$, is much lower for all SQWV exposures than in the potentiostatic hold, Figure 6.7b. The potential cycling maintains a higher concentration of vacant # sites through the reduction of the passive oxide. The larger concentration of vacant sites overcomes the reduced catalytic oxide coverage leading to a greater rate of CO_2 formation and thus greater weight loss, Equation 6.2. The species coverage for the different potential exposures is compared in Table 6.4. The values listed are for the last reducing cycle after a total of 1000 minutes at the high potential. This equates to 2000 cycles with a 30 second step time at the high potential. The behavior at short times is highlighted in the inset of both Figures 6.7a and 6.7b. The rate of CO_2 formation at short times is somewhat different of that observed over longer time intervals. One of the largest potential cycle, 1.3 – 0.5 V, suffers the largest weight loss between 0 and 10 minutes. The higher weight loss initially observed results from the catalytic oxide concentration increasing faster than compared to the 1.3 – 0.7 V cycle.

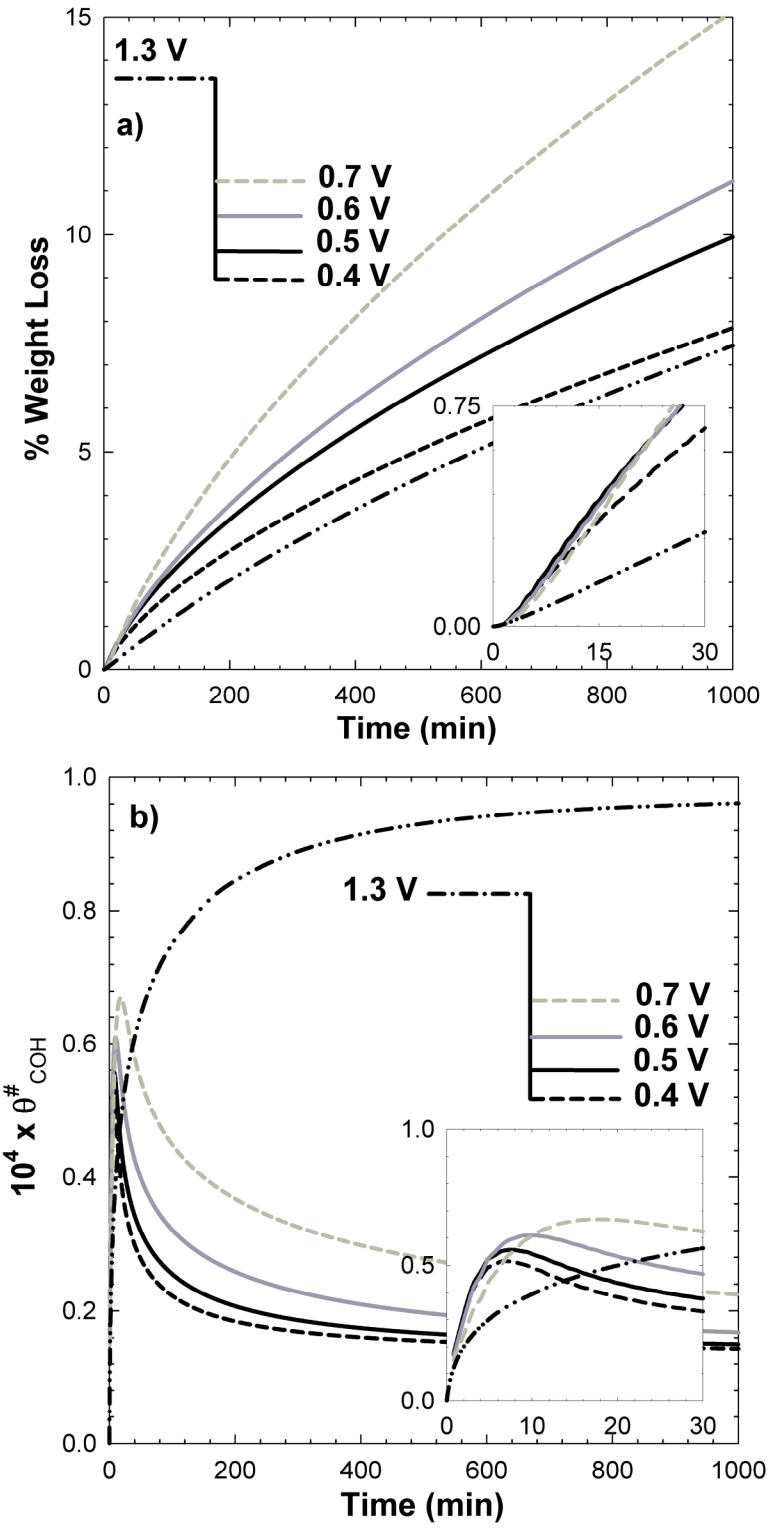

Figure 6.7. Simulations of square wave cycling with different lower potential limits and 30 seconds at each potential. The cumulative % weight loss a) and coverage of $C^{\#}OH$ oxide b) is shown as a function of time at high potential for both cycled and potentiostatic conditions. Inset highlights behavior at short times.

Table 6.4. Coverage of surface species at the end of 2000 SQWV cycles or 1000 minute potentiostatic hold at 80 °C and 100 % RH.

Potential		Covergages							
Upper	**Lower**	**#,vac**	**$C^{\#}OH$**	**$C^{\#}_xO$**	**$C^{\#}_xO_2$**	**$C^{\#}_x(OH)_2$**	**$C^{\#}_xO_3$**	**$C^{*}O$**	**% wt loss**
1.3	0.40	0.59	1.4E-05	0.000	0.0003	0.1262	0.009	0.33	7.8
1.3	0.50	0.66	1.5E-05	0.000	0.0070	0.0955	0.011	0.43	9.9
1.3	0.60	0.78	1.7E-05	0.002	0.0399	0.0205	0.012	0.49	11.2
1.3	0.70	0.73	2.2E-05	0.066	0.0140	0.0003	0.009	0.68	15.1
1.3	N/A	0.10	9.6E-05	0.301	0.0000	0.0000	1.5E-04	0.31	4.0

The cycling simulation results warrant further discussion. Several reduction processes occur during the lower potential of a SQWV cycle. The equilibrium coverage of $C^{\#}OH$ is lowered due to the reduction of the $C^{*}O$ and formation of quinone $C^{\#}_{x}O_2$. This reaction, Equation 6.5, requires the presence of $C^{*}O$ but also the passive oxide, $C^{\#}_{x}O$. Depending on the value of the reducing potential, the passive oxide may be reduced and removed from the carbon surface. One might hypothesize the existence of a potential range that would maximize the reduction in $C^{\#}OH$ equilibrium and allow for continued $C^{\#}_{x}O$ growth. This would result in a temporary passivity of the carbon surface as suggested by some experimental results [18]. However, the kinetic model does not support this hypothesis. Instead the most stable potential exposure is that which cycles to the lowest potential. An increase in quinone coverage both reduces the concentrations of the vacant sites and the catalytic oxide. SQWV cycling with a step length of 15 seconds was also simulated showing similar behavior with marginally more carbon loss.

6.4.3 Effect of Heat Treatment

The differences between XC-72 carbons exposed to various levels of high temperature heat treatment may be evaluated with the proposed model. Here we change only the BET surface area and concentration of # sites, [#], to fit the experimental results reported previously [17]. The concentration of # sites is shown in Figure 6.8 as a function of heat treatment temperature (HTT). The specific surface area, *S*, as measured by the BET method is also shown. At higher HTT, the concentration of active sites is reduced. This reduction of active sites and thus reactivity is expected and also observed in the published literature on gas phase oxidation of carbon blacks [32]. The [#] may be

accurately represented with an exponential fit, Equation 6.15. The active sites decrease with temperature significantly faster than the BET surface area. This explains the greater intrinsic stability of heat treated carbons. We note that the assumed total concentration of sites is $1x10^{-4}$ mol/m^2. It is interesting that the lowest HTT carbon tested is approaching this value. Based upon the increasing [#] with lower HTT, we hypothesize as-received carbons may no longer have two separate sites and thus differ mechanistically. This is also supported by the difference in CO_2 behavior exhibited [17].

$$[\#] = 70.3\exp\left(-0.0075T_{HTT}\right) \tag{6.15}$$

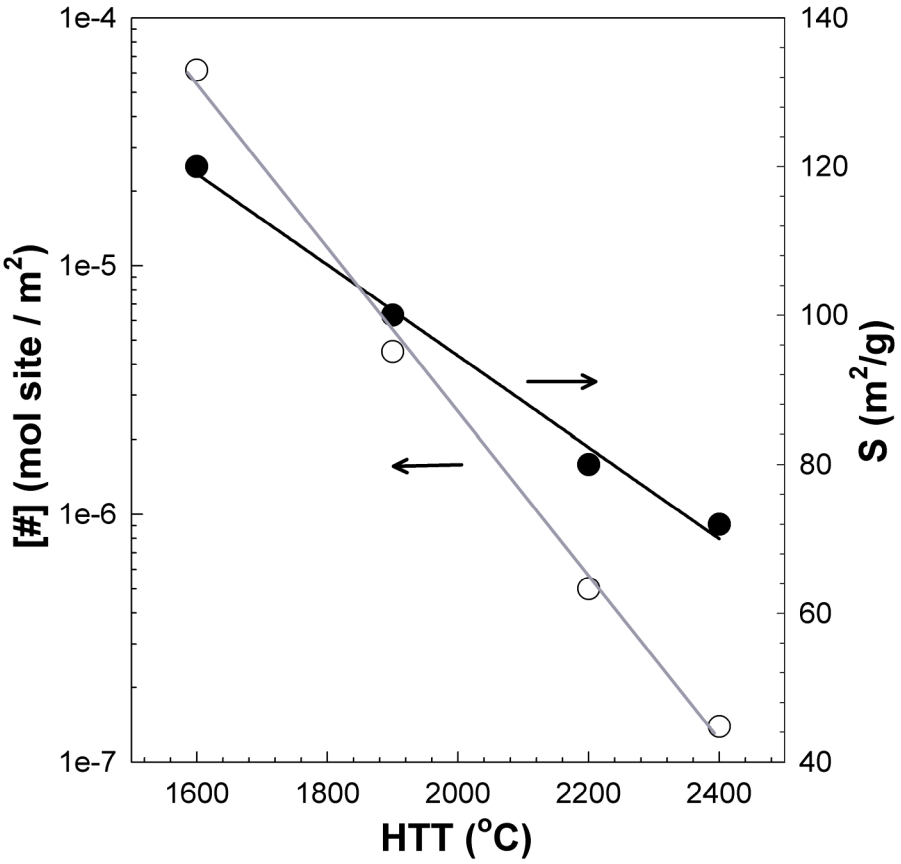

Figure 6.8. The concentration of active sites decreases exponentially and the BET surface area decreases linearly with increasing HTT.

6.4.4 Limitations and Assumptions of the Model

The most significant limitation of this model is the treatment of the passive oxide, Equation 6.3. Experimental results show broad, poorly defined reduction peaks after prolonged electrochemical oxidation [17, 27]. Our model is unable to represent this behavior. This has direct consequences for the simulation of a fuel cell stack. Our model will be most successful when the reducing potential used during potential cycling is near 0.0 V to ensure complete reduction of reversible species. Lower potential limits of 0.7 or 0.5 V may not capture the correct cycling behavior. This limitation may not hinder the simulations of start and stop cycling as the cathode of the PEMFC typically reaches hydrogen potentials at some point. The poor fit at short times during a potentiostatic hold is also related to the passive oxide formation. Clearly, a more robust treatment of this electrochemistry would improve the model. Nonetheless, the mechanism is unknown at this time and the approach presented here is a significant advancement over past treatments. The passive oxide does provide a successful means of treating the CO_2 decay observed during potentiostatic exposures.

The kinetic expression chosen to represent the passive oxide, r_3, presents a significant challenge when fitting the current during short times of a potentiostatic hold and during the reduction cycle of a CV. This kinetic expression inherently assumes the existence of an equilibrium passive oxide surface concentration. One approach to matching the steep current decline at short times in Figure 6.1 is to increase the rate constant, k_3. However, the equilibrium coverage is then quickly reached and the CO_2 current no longer decay in a power-law manner. Interestingly, the equilibrium nature of

this rate expression does appear to match the experimental data for XC-72 heat treated at 2200 and 2400 °C. These carbons display decay similar to the power-law expression until reaching a constant rate of CO_2 formation [5, 17]. This would suggest an equilibrium surface concentration of the passive oxide does exist. A more accurate fit might be obtained by treating each of the three proposed elementary steps individually, Equations 6.22–6.24. We choose the kinetic expression in r_3 to minimize the number of rate parameters determined during the fitting procedure. Experiments are proposed in section 4.5 to enable the specific determination of rate parameters for Equations 6.22–6.44 or perhaps the existence of a different reaction mechanism.

The dependence of the reaction kinetics on the oxidant, water, should be discussed further. An attempt to include the partial pressure of water in the rate expressions of r_1 and r_3 resulted in poor predictions compared to experiment. For catalytic oxide formation, r_1, the temperature dependence of the saturation pressure of water is larger than the activation energy fit to experimental data. For the passive oxide growth, r_3, inclusion of the water partial pressure induced a significant temperature dependence on the equilibrium coverage. This behavior is not observed in the experimental data. Two possible treatments explain these differences. First, the kinetic expression for r_1 and r_3 may follow the elementary steps suggested by Equations 6.22 and 6.23. The first and slowest step is the oxidation of the carbon surface followed by hydrolysis. This approach was first suggested by Binder *et al*. and has since been repeated often in the literature [3, 16, 23]. The second treatment would be to postulate the rates to be dependant on the concentration of the condensed phase rather than that of the

vapor phase. This treatment would lead to the unsatisfying conclusion of water vapor and liquid reacting with different manners on the carbon surface. We have used water vapor as the sole reactant following the only available experimental evidence [10, 15]. The use of the partial pressure of water vapor also allows for the natural treatment of fuel-cell operation at lower than 100 % RH, which is common in automotive applications.

Other limitations of the model are detailed here. The (pseudo-) capacitance of carbon increases after electrochemical oxidation and is the most dominate feature of the CV [3, 4, 17, 18, 23, 25]. We have not attempted to quantify this behavior as we have focused on tracking mass loss and oxide growth. This model does not consider the effect of adsorption of CO_2, which has been shown to desorb from the carbon surface during a reducing potential [18, 27]. Our measurements show this amount to be around 5% of the total carbon dioxide formed and thus neglected here. We do not consider any interactions of the carbon with the metal catalyst it supports in PEMFCs. Studies have suggested Platinum serves to catalyze a surface oxide to CO_2 during potential cycling [10, 21, 40]. This model could be coupled with a platinum oxidation model to explore this behavior [39, 41-43]. However, improvements in the treatment of the carbon surface oxide reduction may be necessary. When modeling a catalyzed carbon, some initial surface oxides are likely to be present. Carbon supports are often chemically oxidized to enable a well dispersed catalyst systems. Perhaps more important is the mixed potential present when a platinum-carbon system is exposed to oxygen. At the mixed potential of oxygen reduction and carbon oxidation, the carbon is exposed to potentials near 1.1 V and is thus

oxidized to some degree [5, 11, 13]. This oxidation may be included in any simulation by changing the initial conditions of the numerical model.

6.4.5 Recommendations

The current from the formation of the passive oxide matched poorly with experimental results even though CO_2 formation was an excellent fit. More work on the stoichiometry and formation of this oxide is the opportunity for greatest advancement in the kinetic model. Temperature programmed desorption (TPD) studies appear to be the most robust technique for the analysis of carbon surface chemistry. While TPD analysis of electrochemically oxidized carbon black has been published [23], the researchers typically look at surface oxides over long periods of electrochemical oxidation. The analyses suggested here should be conducted at short oxidation times and possibly low temperatures (20 – 40 °C) as the CO_2 formation has been shown to simultaneously produce surface oxides [16, 17]. Short oxidation times should limit the C^*O oxide growth while highlighting the passive oxide and catalytic oxide. The comparison of oxide concentrations between this short oxidation time and the initial concentration should reveal some important features of the chemistry and stoichiometry. The sample must not be reduced before TPD is performed and oxygen chemisorption from the atmosphere must be controlled or accounted for in the oxygen balance. These experiments would be complimented by a symmetrical set where the samples are electrochemically reduced after oxidation. This comparison should confirm what portion of the oxide is completely removed after reduction [26]. The mechanism of current decay in cyclic operation must also be examined. Our kinetic mechanism advocates that a reduction reaction affects the

concentration of the catalytic oxide. This assumption needs verification and refinement with further studies of the carbon surface chemistry.

6.5. CONCLUSIONS

A mechanism and numerical model for the electrochemical oxidation of graphitic carbon in aqueous and acidic environments has been presented. The model represents a significant step in understanding the complicated behavior of this electrochemical process. At a fundamental level, the mechanistic approach allows the investigation of previous assumptions for the basic reaction steps and physical reasons for transient phenomena. Furthermore, the use of physical species and driving forces allows for robust analysis of the electrochemical oxidation of carbon under more realistic conditions such as potential cycling. Implementation of the model into fuel-cell decay models will greatly improve lifetime predictions. On the basis of this work, continued experimental studies will refine the proposed mechanism to improve the treatment of the surface oxides. The stoichiometry and kinetics of the initial passive oxide growth is the subject in most need of greater investigation.

6.6. SUPPORTING INFORMATION

We consider reactions 2 and 3 in an attempt to explain the role of a passive oxide in the time dependent current decay. A simplified version of the r_2 and r_3 with the appropriate material balances may be expressed as the following.

$$\frac{\partial \theta_{vac}^{\#}}{\partial t} = -\frac{k_3}{[\#]}\left\{\left(\theta_{vac}^{\#}\right)^{x} \exp\left[\frac{\alpha_{a,3}F}{RT}\left(V-U_3\right)\right] - \theta_{CxO}^{\#} \exp\left[-\frac{\alpha_{c,3}F}{RT}\left(V-U_3\right)\right]\right\} \quad (6.16)$$

$$\frac{\partial N_c}{\partial t} = -k_2 \theta_{vac}^{\#} \exp\left[\frac{\alpha_{a,2}F}{RT}\left(V-U_2\right)\right] SN_cM \quad (6.17)$$

If we take the limit of high overpotentials and create a lumped rate parameter A', we may ignore the cathodic term in Equation 6.16, resulting in Equations 6.18– 6.21.

$$\frac{\partial \theta_{vac}^{\#}}{\partial t} = A'\left(\theta_{vac}^{\#}\right)^{x} \quad (6.18)$$

$$\theta_{vac}^{\#} = \left[(1-x)(A't)\right]^{\frac{1}{1-x}} \quad (6.19)$$

$$\frac{\partial N_c}{\partial t} = -k_2 A'' t^{-n} \exp\left[\frac{\alpha_{a,2}F}{RT}\left(V-U_2\right)\right] SN_cM \quad (6.20)$$

$$-n = \frac{1}{1-x} \quad (6.21)$$

The empirical power law decay equation is now approximated by a simplified reaction sequence with the power n being related to the stoichiometry of the passive oxide.

The rate expression chosen to represent the passive oxide growth, r_3, is based upon the following postulated elementary steps. First, the carbon lattice is oxidized.

$$x[\#] \leftrightarrow [\#]_x^+ + e^- \tag{6.22}$$

This step is slow in the anodic direction and taken to be the RDS for oxidation. The consumption of multiple carbon atoms has bee previously suggested by Binder *et al.* and Choo *et al.* for example [16, 44]. Binder *et al.* also assumed oxidation and hydrolysis as separate steps. This results in a kinetic expression independent of water concentration. Next, the oxidized carbon site reacts with water. Both the anodic and cathodic directions of this reaction step occur quickly compared to the others.

$$[\#]_x^+ + H_2O \leftrightarrow [\#]_x OH + H^+ \tag{6.23}$$

The final step in the oxidation process is deprotonation of the oxide. This step is taken to be slow in the cathodic direction and the RDS for the reduction process. Thus a simplified rate expression, r_3, for reactions 6.21–6.23 includes the anodic portion of 6.21 and cathodic portion of 6.23 assuming the same equilibrium potential, U_3, and rate constant, k_3.

$$[\#]_x OH \leftrightarrow [\#]_x O + H^+ + e^- \quad (6.24)$$

REFERENCES

[1] Conway BE. Electrochemical Supercapacitors: Scientific Fundamentals and Technological Applications: Springer 1999.

[2] Dicks AL. The role of carbon in fuel cells. Journal of Power Sources. 2006; **156**(2), 128-41.

[3] Kinoshita K. Carbon: Electrochemical and Physicochemical Properties. New York: Wiley 1988.

[4] Pandolfo AG, Hollenkamp AF. Carbon properties and their role in supercapacitors. Journal of Power Sources. 2006; **157**(1), 11-27.

[5] Makharia R, Kocha SS, Yu PT, Sweikart MA, Gu W, Wagner FT, et al. Durable PEM Fuel Cell Electrode Materials: Requirements and Benchmarking Methodologies. ECS Transaction. 2006; **1**(8), 3-18.

[6] Yu PT, Gu W, Makharia R, Wagner FT, Gasteiger HA. The Impact of Carbon Stability on PEM Fuel Cell Startup and Shutdown Voltage Degradation. ECS Transaction. 2006; **3**(1), 797-809.

[7] Yu PT, Gu W, Zhang J, Makharia R, Wagner FT, Gasteiger HA. Carbon-Support Requirements for Highly Durable Fuel Cell Operation. *Polymer Electrolyte Fuel Cell Durability* 2009:29-53.

[8] Borup R, Meyers J, Pivovar B, Kim YS, Mukundan R, Garland N, et al. Scientific aspects of polymer electrolyte fuel cell durability and degradation. Chemical Reviews. 2007; **107**(10), 3904-51.

[9] Gallagher KG, Darling RM, Fuller TF. Carbon-support corrosion mechanisms and models. In: Vielstich W, Yokokawa H, Gasteiger HA, eds. *Handbook of Fuel Cells: Advances in Electrocatalysis, Materials, Diagnostics and Durability, Volumes 5 & 6*. Chichester, UK: John Wiley & Sons, Ltd 2009:819-282.

[10] Maass S, Finsterwalder F, Frank G, Hartmann R, Merten C. Carbon support oxidation in PEM fuel cell cathodes. Journal of Power Sources. 2008; **176**(2), 444-51.

[11] Meyers JP, Darling RM. Model of carbon corrosion in PEM fuel cells. Journal of the Electrochemical Society. 2006; **153**(8), A1432-A42.

[12] Takeuchi N, Fuller TF. Modeling and investigation of design factors and their impact on carbon corrosion of PEMFC electrodes. Journal of the Electrochemical Society. 2008; **155**(7), B770-B5.

[13] Perry ML, Darling RM, Kandoi S, Patterson TW, Reiser C. Operating Requirements for Durable Polymer-Electrolyte Fuel Cell Stacks. *Polymer Electrolyte Fuel Cell Durability* 2009:399-417.

[14] Reiser CA, Bregoli L, Patterson TW, Yi JS, Yang JDL, Perry ML, et al. A reverse-current decay mechanism for fuel cells. Electrochem Solid State Lett. 2005; **8**(6), A273-A6.

[15] Appleby AJ. Corrosion in Low and High Temperature Fuel Cells - An Overview. Corrosion. 1987; **43**(7), 398-408.

[16] Binder H, Kohling A, Richter K, Sandstede G. Ueber Die Anodische Oxydation Von Aktivkohlen In Waessrigen Elektrolyten. Electrochimica Acta. 1964; **9**, 255-74.

[17] Gallagher KG, Yushin G, Fuller TF. The Role of Nanostructure in the Electrochemical Oxidation of Model-Carbon Materials in Acidic Environments. Carbon. 2009, Submited.

[18] Gallagher KG, Wong DT, Fuller TF. The effect of transient potential exposure on the electrochemical oxidation of carbon black in low-temperature fuel cells. Journal of the Electrochemical Society. 2008; **155**(5), B488-B93.

[19] Siroma Z, Tanaka M, Yasuda K, Tanimoto K, Inaba M, Tasaka A. Electrochemical corrosion of carbon materials in an aqueous acid solution. Electrochemistry. 2007; **75**(2), 258-60.

[20] Chaparro AM, Mueller N, Atienza C, Daza L. Study of electrochemical instabilities of PEMFC electrodes in aqueous solution by means of membrane inlet mass spectrometry. Journal of Electroanalytical Chemistry. 2006; **591**(1), 69-73.

[21] Willsau J, Heitbaum J. The Influence of Pt-Activation on the Corrosion of Carbon in Gas-Diffusion Electrodes - a Dems Study. Journal of Electroanalytical Chemistry. 1984; **161**(1), 93-101.

[22] Burg P, Cagniant D. Characterization of Carbon Surface Chemistry. *Chemistry and Physics of Carbon, Vol 30* 2008:129-75.

[23] Kangasniemi KH, Condit DA, Jarvi TD. Characterization of vulcan electrochemically oxidized under simulated PEM fuel cell conditions. Journal of the Electrochemical Society. 2004; **151**(4), E125-E32.

[24] Kinoshita K, Bett J. Electrochemical Oxidation of Carbon-Black in Concentrated Phosphoric-Acid at 135 Degrees C. Carbon. 1973; **11**(3), 237-47.

[25] Kinoshita K, Bett JAS. Potentiodynamic Analysis of Surface Oxides on Carbon-Blacks. Carbon. 1973; **11**(4), 403-11.

[26] Cheng PZ, Teng HS. Electrochemical responses from surface oxides present on HNO3-treated carbons. Carbon. 2003; **41**(11), 2057-63.

[27] Colmenares LC, Wurth A, Jusys Z, Behm RJ. Model study on the stability of carbon support materials under polymer electrolyte fuel cell cathode operation conditions. Journal of Power Sources. 2009; **190**(1), 14-24.

[28] Kinoshita K. Influence of Heat-Treatment and Physicochemical Properties on the Electrochemical Oxidation of Carbon Blacks In Phosphoric Acid. In: Sarangapani S, Akridge JR, Schumm B, editors. The Electrochemistry of Carbon; 1983 August 17-19; Cleveland, OH: The Electrochemical Society, Inc; 1983. p. 273-90.

[29] Kinoshita K, Bett JAS. Effects of Graphitization on the Corrosion of Carbon Blacks. In: Tedmon CS, editor. Proceedings of the Symposium on Corrosion Problems in Energy Conversion and Generation; 1974; 1974. p. 43-55.

[30] Mathias MF, R. M, H.A. G, Conley JJ, Fuller TJ, Gittleman CJ, et al. Two Fuel Cells In Every Garage? The Electrochemical Society Interface. 2005; **14**(3), 24-35.

[31] Brunauer S, Emmett PH, Teller E. Adsorption of gases in multimolecular layers. Journal of the American Chemical Society. 1938; **60**, 309-19.

[32] Arenillas A, Rubiera F, Pevida C, Ania CO, Pis JJ. Relationship between structure and reactivity of carbonaceous materials. J Therm Anal Calorim. 2004; **76**(2), 593-602.

[33] Leon C, Radovic LR. Interfacial Chemistry and Electrochemistry of Carbon Surfaces. *Chemistry and Physics of Carbon, Vol 24* 1994:213-310.

[34] Delahay P. Double Layer and Electrode Kinetics. New York: John Wiley & Sons 1965.

[35] Noel M, Vasu KI. Cyclic Voltammetry and the Frontiers of Electrochemistry. London: Aspect 1990.

[36] Chopey NP. Handbook of Chemical Engineering Calculations. New York, NY: McGraw-Hill 2003.

[37] Newman J, Thomas-Alyea KE. Electrochemical Systems. 3rd ed. Hoboken, New Jersey: John Wiley & Sons, Inc. 2004.

[38] Press WH, Teukolsky SA, Vetterling WT, Flannery BP. Numerical Recipes in FORTRAN: The Art of Scientific Computing. 2nd ed. Cambridge, UK: Cambridge University Press 1986.

[39] Bi W, Fuller TF. Temperature effects on PEM fuel cells Pt/C catalyst degradation. Journal of the Electrochemical Society. 2008; **155**(2), B215-B21.

[40] Roen LM, Paik CH, Jarvic TD. Electrocatalytic corrosion of carbon support in PEMFC cathodes. Electrochem Solid State Lett. 2004; **7**(1), A19-A22.

[41] Bi W, Fuller TF. Modeling of PEM fuel cell Pt/C catalyst degradation. Journal of Power Sources. 2008; **178**(1), 188-96.

[42] Darling RM, Meyers JP. Kinetic model of platinum dissolution in PEMFCs. Journal of the Electrochemical Society. 2003; **150**(11), A1523-A7.

[43] Darling RM, Meyers JP. Mathematical model of platinum movement in PEM fuel cells. Journal of the Electrochemical Society. 2005; **152**(1), A242-A7.

[44] Choo HS, Kinumoto T, Jeong SK, Iriyama Y, Abe T, Ogumi Z. Mechanism for electrochemical oxidation of highly oriented pyrolytic graphite in sulfuric acid solution. Journal of the Electrochemical Society. 2007; **154**(10), B1017-B23.

PART 2

CHAPTER 7

WATER MANAGEMENT IN PEM FUEL CELLS

A critical aspect of proton exchange membrane fuel cells (PEMFC) operation is the management of water within individual cells and the system as a whole [1, 2]. Water is the product of the oxygen reduction reaction (ORR) occurring at the cathode of the fuel cell. The polymer electrolytes presently used in PEMFCs require humidification to achieve adequate proton conductivities and minimize degradation. The humidification of the membrane is achieved through interaction with the ORR product water and through additional saturation of the gaseous reactant streams. Although high water content is desired within the membrane, open porosity in the electrode and gas diffusion layer is necessary to allow rapid transport of reactants to the catalytic sites. The performance of the cell, particularly at higher current densities, is hindered by any reduction in reactant transport due to the filling of pores with water [3]. Thus, an optimum system and cell design is necessary to allow for operation near 100 % relative humidity (RH) while maintaining low liquid saturation levels in the porous media [1, 2]. Chapter 9 presents work on capillary-pressure saturation relationships for PEMFC porous media. The hysteresis observed during filling and draining of the pores from various saturation levels is measured and implications discussed. Several other complicating factors for water management also exist.

The dynamics of water in a PEMFC is illustrated in Figure 7.1. A concentration profile of water may exist in the membrane even if both reactant streams, H_2 and Air/O_2,

are at 100 % RH before entering the cell [4]. During the passage of current, water is dragged from the anode to the cathode with each proton that is transported. This phenomenon is referred to as electro-osmotic drag and is discussed in greater detail in Chapter 8. Conversely, water is transported from the cathode to the anode by a chemical potential gradient that results from the drag of water by protons. This opposing action is referred to as the back diffusion of water. Capillary pressure differences have also been suggested to drive water from the cathode to the anode. Indeed, polymer electrolytes have been suggested to exhibit properties of both a concentrated solution and a porous media [5, 6]. Generally, competing water transport mechanisms within the membrane create a concentration gradient with lower water content on the anode side. This lower water content raises the overall resistance of the membrane and may result in a proton transport limiting current similar to the limiting current observed for oxygen transport [7, 8].

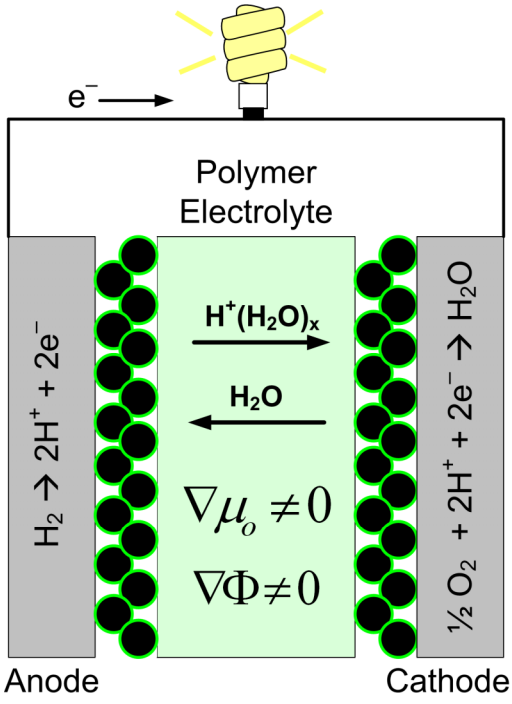

Figure 7.1. Water dynamics in a PEMFC.

PEMFCs must be able to complete an unassisted start from far below 0 °C if they are to be the power source in personal automobiles [9]. These fuel cells must operate under all environmental conditions including those in which the thermodynamically stable phase of water is a solid. Clearly, the presence of ice has implications for a system that requires hydration and produces water as a product. Chapter 8 focuses on some of the scientific challenges to understanding material and transport properties of the water-polymer-electrolyte system below 0 °C. The measured properties are used in a numerical model to investigate their affect on the start of a PEMFC from temperatures significantly below 0 °C.

REFERENCES

[1] Larminie J, Dicks A. Fuel Cell Systems Explained. 2nd ed. Hoboken, New Jersey: John Wiley & Sons 2003.

[2] Perry ML, Darling RM, Kandoi S, Patterson TW, Reiser C. Operating Requirements for Durable Polymer-Electrolyte Fuel Cell Stacks. *Polymer Electrolyte Fuel Cell Durability* 2009:399-417.

[3] Li H, Tang Y, Wang Z, Shi Z, Wu S, Song D, et al. A review of water flooding issues in the proton exchange membrane fuel cell. Journal of Power Sources. 2008; **178**(1), 103-17.

[4] Fuller TF, Newman J. Water and Thermal Management in Solid-Polymer-Electrolyte Fuel-Cells. Journal of the Electrochemical Society. 1993; **140**(5), 1218-25.

[5] Weber AZ, Darling RM, Newman J. Modeling two-phase behavior in PEFCs. Journal of the Electrochemical Society. 2004; **151**(10), A1715-A27.

[6] Weber AZ, Newman J. Modeling transport in polymer-electrolyte fuel cells. Chemical Reviews. 2004; **104**(10), 4679-726.

[7] Eames DJ, Newman J. Electrochemical Conversion of Anhydrous Hcl to Cl-2 Using a Solid-Polymer-Electrolyte Electrolysis Cell. Journal of the Electrochemical Society. 1995; **142**(11), 3619-25.

[8] Perry ML, Newman J, Cairns EJ. Mass transport in gas-diffusion electrodes: A diagnostic tool for fuel-cell cathodes. Journal of the Electrochemical Society. 1998; **145**(1), 5-15.

[9] Borup R, Meyers J, Pivovar B, Kim YS, Mukundan R, Garland N, et al. Scientific aspects of polymer electrolyte fuel cell durability and degradation. Chemical Reviews. 2007; **107**(10), 3904-51.

CHAPTER 8

ELECTRO-OSMOSIS AND WATER UPTAKE IN POLYMER ELECTROLYTES IN EQUILIBRIUM WITH WATER VAPOR AT LOW TEMPERATURES

8.1. INTRODUCTION

Proton-exchange membrane fuel cells (PEMFCs) have increasingly been touted as a possible alternate power source to the internal combustion engine in the transportation sector. Cost and durability are large barriers to commercialization in automobiles. Furthermore, a PEMFC must be able to start in environmental conditions below 0 °C [1]. Since water is produced at the cathode of PEMFCs and is also required to humidify the polymer electrolyte, these lower temperatures complicate operation of the power-plant due to the thermodynamically favored phase being a solid.

During the start of a PEMFC from temperatures below 0 °C, the management of the product water is critical and challenging [1]. Whereas the existence of supercooled (liquid) water has been shown in PEMFCs [2], transport of this thermodynamically metastable phase is poorly understood. Furthermore, the low saturation pressure of water at these temperatures minimizes vapor transport. Due to the diminished ability to remove product water, the water must be stored without excessively restricting the flow of reactants until the system temperature rises above the freezing point. The porosity of the catalyst layer and the water holding capacity of the polymer electrolyte have been identified as the most significant storage volumes for water [3-6]. Researchers have

demonstrated a greater amount of water may be stored in the membrane when the polymer electrolyte is equilibrated at low relative humidity before start [3-6]. The maximum water the membrane can store is suggested to be the difference between the water content at unit water activity and the initial water content prior to a start. However, an attempt to double membrane storage capacity by doubling the thickness of the membrane resulted in less capacity than predicted [4].

Changes in the hydration isotherm below 0 °C can directly affect the capacity for water storage during freeze starts. Moreover, membrane transport properties such as the conductivity and the water diffusion coefficient are dependent upon the hydration isotherm. In current published cold start models, isotherms relating the membrane water content to the partial pressure of water in the vapor phase are assumed to be the same as those measured at room temperature [3-6]. Significant temperature effects have been published between 25 and 80 °C [7-10]; therefore, the isotherm is expected to change below 25 °C as well.

Treating the water-ionomer system as a binary electrolyte, concentrated solution theory defines three independent transport parameters to model transport within the membrane of a PEMFC: the ionic conductivity, the diffusion coefficient of water and the electro-osmotic drag coefficient [11]. The conductivity and the diffusion coefficient have both been the subject of numerous investigations. Electro-osmotic drag measurements have been reported, albeit to a lesser extent [12]. Fundamental transport and material properties measured at low temperatures, those below 0 °C, remain absent from the

literature. A few results have been reported for the conductivity, and one report exists for the liquid equilibrated diffusion coefficient [13-15]. The goal of this work is to describe our findings regarding the temperature dependence of the electro-osmotic drag coefficient and the water sorption isotherm of some common and promising membrane chemistries. The experimental results obtained are applied using numerical modeling that probes the importance of water related phenomenon as they impact cold-start and sub-freezing operation of fuel cells.

Below 0 °C, the feasibility of experimental methods involving liquid water for the determination of electro-osmotic drag is unclear. Furthermore, whether or not a membrane is liquid equilibrated below 0 °C also remains to be shown. In contrast, the interaction of the membrane with water vapor is straightforward. Therefore, our experimentation will utilize vapor equilibrated methods. At the time of this publication, only the activity gradient and electrophoretic nuclear magnetic resonance (ENMR) methods are able to determine the vapor equilibrated drag coefficient [12]. Use of the activity gradient method is advantageous as only minimal assumptions are required to analyze the results [16, 17]. The significant assumption in the activity gradient method is that the membrane is accurately represented by a binary electrolyte, macroscopically isotropic and at thermal equilibrium with the environment. Drag coefficients determined from ENMR measurements require a hydrodynamic physical model, whose validity has been questioned for hydrations levels found in vapor equilibrated membranes [18].

Nafion® membranes are the standard polymer electrolyte chemistry for PEMFCs. Nafion® is based on a per(fluorosulfonic acid) (PFSA) chemistry, which involves a poly(tetrafluoroethylene) (PTFE) backbone with perfluorinated ether side chains terminating in sulfonic acid end groups [19], Figure 8.1a. Although the PFSA chemistry has excellent durability and conductivity, existing membranes perform poorly at low relative humidity and/or high temperatures (> 100 °C), have limitations in terms of mechanical properties and chemical modification, and are relatively expensive. A class of membranes based on sulfonated poly(arylene ether sulfone), often referred to as BPSH, provide a framework for studying the limitations and possible advantages of hydrocarbon based membranes. By changing the equivalent weight and the sequence and number of repeat units, physical and transport properties of the water-polymer system are optimized and mechanisms elucidated [20]. The structure of BPSH is presented in Figure 8.1b. Random co-polymers of BPSH are typically defined by the relative percentage of sulfonated repeat units to unsulfonated. Multi-block co-polymers are defined by the length of sulfonated and unsulfonated blocks. Block and random BPSH copolymers provide distinct polymer electrolyte systems to further evaluate electro-osmosis in PEMFCs.

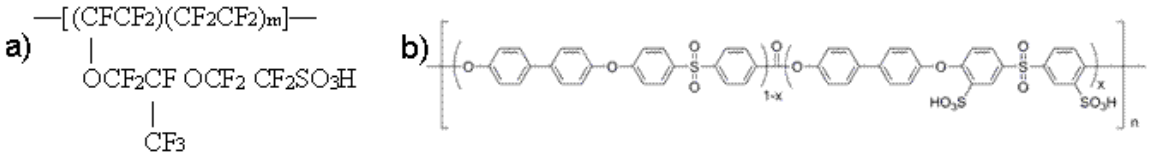

Figure 8.1. Structure of a) Nafion and b) BPSH-XX

8.2. THEORY

8.2.1 Water Vapor Sorption Isotherm

The sorption isotherm is a relationship between the concentration and the activity of water in the polymer. For this work, water activity, a_o, is defined as the ratio of the partial pressure of water, p_o, to the saturation pressure of liquid water at the system temperature, $p_{o,l}^*$. Two temperature effects are expected to influence the isotherm for water sorption in polymer electrolyte membranes. First, the sorption of water in the polymer electrolyte is an exothermic process and becomes less favorable as temperature increases. Simply stated, the membrane absorbs more water at constant activity as system temperature decreases. This increase in water content has previously been predicted by chemical thermodynamics for data collected above 0 °C [21].

The second temperature effect is a consequence of the lower vapor pressure of ice when compared to liquid water at the same temperature [22]. Water in polymer electrolyte membranes is found in a liquid state below the activity that corresponds to the freezing point of pure water. This activity is equivalent to the ratio of saturation pressures of ice, $p_{o,s}^*$, to supercooled liquid water, $p_{o,l}^*$. Since supercooled water freezes into ice over the timescales needed to equilibrate the polymer with the system water activity in our isopiestic measurements, the sorption isotherms measured below 0 °C are bounded to activities equal to or less than that of ice, Equation 8.1. This behavior has been observed

in NMR measurements of unfrozen water in polymer electrolytes and for water sorption in wood at temperatures below 0 °C [23-25].

$$a_o = \left(\frac{p_o}{p_{o,l}^*} \right) \leq \left(\frac{p_{o,s}^*}{p_{o,l}^*} \right) = f(\lambda) \tag{8.1}$$

Differential scanning calorimetry (DSC) measurements have shown the existence of different states of water in polymer electrolytes [14, 15, 26]. These studies have classified water into different states, such as freezable and non-freezable; or bulk, bound-freezable and bound-non-freezable. While these specific classifications are useful for describing the variable nature of the water environment, water inside the membrane more accurately represents a continuum of states rather than discrete states. The local environment that dictates the nature of water is determined by factors such as the size and nature of the water domains and their interface with the charged polymer electrolytes. These aspects are particularly relevant when considering studies like those presented here that focus on membrane properties at sub-freezing temperatures.

8.2.2 Electro-osmosis

The electro-osmotic drag coefficient, ξ, is the ratio of the flux of water to that of protons in the absence of a concentration gradient [16],

$$\xi = \frac{N_o}{N_+}. \tag{8.2}$$

The drag coefficient may be determined as a function of water activity using an activity-gradient cell. In this cell, the two ends of a membrane are exposed to two separate compartments. In each compartment, the membrane is in contact with a platinized platinum mesh electrode, hydrogen gas and water vapor. By controlling the partial pressure of water vapor in each compartment, one may establish a gradient in the chemical potential of water in the membrane. This activity difference may be measured by determining the electrostatic potential difference between the two platinum electrodes. The experimental apparatus is depicted in Figure 8.2.

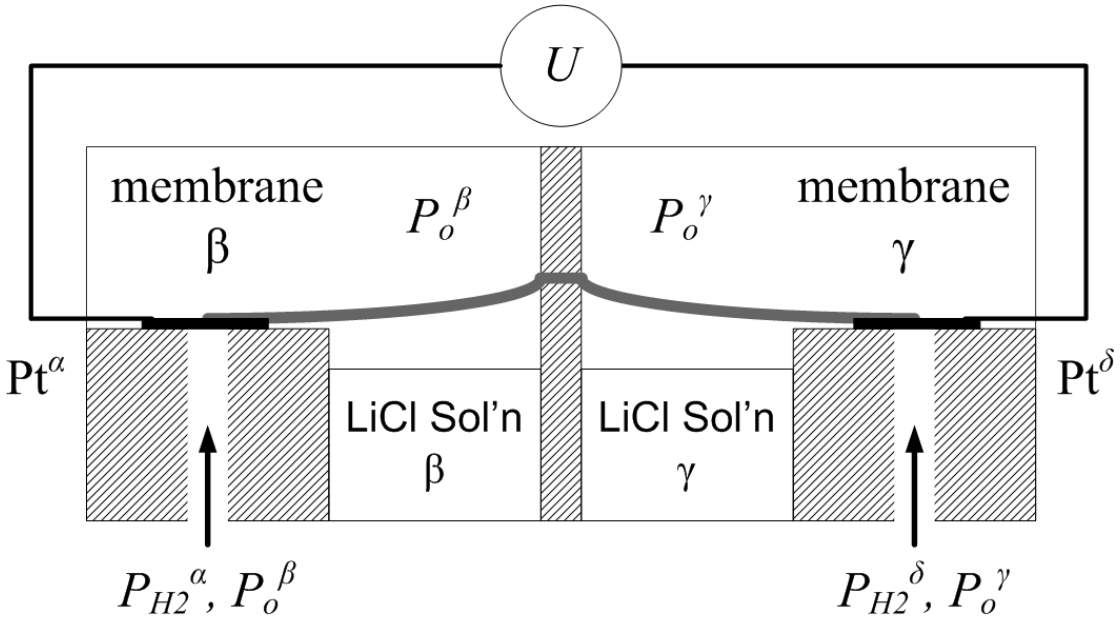

Figure 8.2. Water vapor activity-gradient cell for determining the electro-osmotic drag coefficient in a polymer electrolyte membrane.

Fuller and Newman provide a derivation of the mathematical equations used to treat this activity-gradient cell [16]. Briefly, the cell potential, U, is

$$FU = F\left(\Phi_1^{\alpha} - \Phi_1^{\delta}\right) = \left(\mu_{e^-}^{\delta} - \mu_{e^-}^{\alpha}\right) = \frac{1}{2} RT \ln \frac{p_{H_2}^{\delta}}{p_{H_2}^{\alpha}} + \int_{y_\gamma}^{y_\beta} \nabla \mu_+ dy \tag{8.3}$$

Using concentrated solution theory, the gradient in the electrochemical potential of the hydrogen ion can be shown to be equivalent to the product of ξ and the negative gradient of the electrochemical potential of water,

$$\nabla \mu_+ = -\xi \nabla \mu_o \tag{8.4}$$

Assuming the fugacity of hydrogen in the two chambers is equivalent due to the low vapor pressure of water < 0 °C, the expression for the cell potential reduces to

$$FU = -\int_{y_\gamma}^{y_\beta} \xi \frac{d\mu_o}{dy} dy \tag{8.5}$$

The cell potential may be corrected for the difference in fugacity at higher temperatures. By defining the activity of water, a_o, as the deviation from the reference state, μ^*_o, which is taken to be pure water at the specified temperature and 101.325 kPa and reasonably assuming ideal gas behavior

$$\mu_o^{\beta} = \mu_o^* + RT \ln\left(a_o^{\beta}\right) = \mu_o^* + RT \ln\left(\frac{p_o^{\beta}}{p_o^*}\right) \tag{8.6}$$

Differentiation of Equation 8.6 and manipulating the expression to reach the variables of interest results in an expression that may be used to determine ξ at equilibrium

$$\xi\left(a_o^\beta\right) = -F\frac{dU}{d\mu_o^\beta} = -F\frac{dU}{d\mu_o^\beta}\frac{d\ln\left(p_o^\beta / p_o^\gamma\right)}{d\ln\left(p_o^\beta / p_o^\gamma\right)} = -\frac{F}{RT}\left[\frac{dU}{d\ln\left(p_o^\beta / p_o^\gamma\right)}\right] \tag{8.7}$$

By holding the partial pressure of water in right compartment, γ, constant and varying the partial pressure in the left compartment, β, the data may be fit with an empirical relation. Then the derivative of this relation with respect to chemical potential of water in the left compartment is equivalent to the drag coefficient at this chemical potential.

8.2.3 Temperature Dependence of the LiCl Osmotic Coefficient

Both the measurement of ξ and of water uptake involves equilibrium with LiCl solutions to impose a specific water vapor activity setting the activity of water in the membrane. To accurately control water content in the membrane, it is important to understand how the activity of water in the electrolyte solution changes with salt concentration and system temperature. The osmotic coefficient is typically used to relate the concentration to activity as it represents the departure from an ideal solution more intuitively than activity coefficients [27]. The osmotic coefficient, ϕ, is related to water activity by the molality, m, molecular weight, M_o, and the number of moles of ions into which a mole of electrolyte dissociates, ν, [28]

$$\ln\left(a_o\right) = -\frac{\nu m M_o \phi}{1000}. \tag{8.8}$$

No comprehensive measurements of the activity of water in LiCl solutions below 0 °C have been reported in the open literature. We have chosen to linearly extrapolate the temperature dependence of the osmotic coefficient from measured values between 25 and 100 °C, which show a linear dependence of the osmotic coefficient on temperature [29], Figure 8.3. A linear extrapolation is most likely incorrect but without guidance from other measurement, we accept the resulting uncertainty with the view that only minor deviations will result. Published experimental results have shown a continuation of this seemingly linear trend to 250 °C [30, 31].

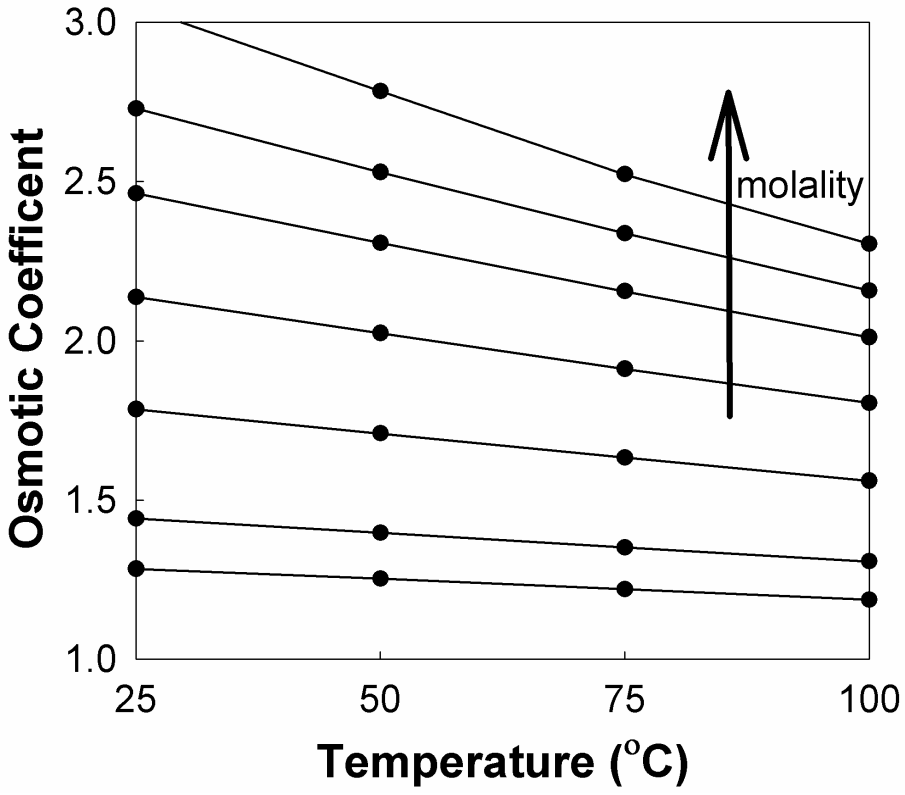

Figure 8.3. LiCl osmotic coefficient as a function of temperature at molalities of 3, 4, 6, 8, 12, and 18 mol/kg. Results from Gibbard and Scatchard are shown for 25, 50, 75 and 100 °C

8.3. EXPERIMENTAL

8.3.1 Material

Anhydrous LiCl of 99% minimum purity was purchased from Alfa Aesar. 18 m solutions were obtained by mixing the solid LiCl with de-ionized water. Less concentrated solutions were achieved by diluting the 18 m stock mixture. Nafion® membranes were provided by the E. I. du Pont de Nemours and Company. Nafion® 112 and 117 membranes were properly pretreated by boiling in the following solutions for one hour: 1% H_2O_2, de-ionized water, ½ M H_2SO_4, and de-ionized water. BPSH-35, a random copolymer of 4,4'-biphenol, 4,4'-dichlorodiphenylsulfone, and 3,3'-disulfonated-4,4'-dichlorodiphenylsulfone, where 35 refers to the mole percentage of disulfonated repeat units, was synthesized by a polycondensation reaction as described in the literature [32]. A multi-block copolymer containing a hydrophilic, disulfonated poly(arylene ether sulfone) block and a hydrophobic, unsulfonated block (BPSH-20-BPS-15, where 20 and 15 refer to the molecular weight in kg/mol of the disulfonated and unsulfonated segments, respectively) was synthesized as previously reported [33]. Both BPSH membranes were synthesized by the research group of Prof. James E. McGrath. BPSH membranes were pretreated by boiling in de-ionized water before being placed in the activity-gradient cell. The dry masses of all membranes were found by first drying for 24 hours at 110 °C under vacuum. The membranes were then quickly removed, hermetically sealed and weighed.

8.3.2 Temperature control

An Espec ESX-3CA environmental chamber was utilized to control system temperature ± 0.3 °C. A plastic sheet was used as barrier to prevent large temperature rises when the chamber door was open. Openings in the sheet allowed the apparatus to be manipulated while maintaining temperature.

8.3.3 Activity-gradient cell

To determine the drag coefficient, we used a variation of the apparatus discussed in Reference [17]. Modifications were made to allow for the measurement of four separate membranes during the same experimental run. The design and construction of this cell occurred at Los Alamos National Laboratory (Los Alamos, New Mexico USA) by Thomas A. Zawodzinski and John Davey and was kindly loaned to us for the experimental runs presented here-in. A specialty gas mixture of 4% H_2 in N_2 of ultra high purity grade (Airgas, Inc) was used to avoid a flammable mixture inside of the environmental chamber. The gas was humidified before entering the activity-gradient cell to prevent a change in water partial pressure. The saturators were filled with a LiCl solution of the same concentration as the corresponding side of the drag cell. Low flow rates resulting in a few bubbles per second ensured the concentration of the LiCl solutions remained constant over the course of the experiment. The molality of the reference solution was changed depending on the temperature of the experiment to prevent solidification. 3 m LiCl solution was used at –10 °C and 5 m was used at –25 °C.

Condensation of water onto the membrane or the freezing of water in the gas tubing and fittings are significant issues in performing these experiments. To ensure a successful run, the saturator bottles used to humidify the gas are first brought to system temperature. Next the activity-gradient cell is lowered to system temperature with the membranes isolated from the wells containing the electrolyte solution and the gas flowing to the cell. The isolation of the electrolyte solutions prevents evaporation and condensation onto the membrane during the drop in the cell's temperature. Unless stated otherwise, all membranes were initially equilibrated with ~30 % relative humidity before testing. Finally, when all temperatures are equal, the membranes are exposed to the electrolyte solutions. The potential of the membranes was measured with a 6 ½ digit multimeter with an input resistance greater than 10 GΩ.

8.4. RESULTS AND DISCUSSION

8.4.1 Water Uptake at Low Temperatures

We measured the equilibrium water uptake for Nafion® at –10 and –25 °C. The LiCl solutions were first cooled to the required temperature before a membrane equilibrated at approximately 30 % relative humidity was placed in the sealed vessel. Membranes were exposed to water vapor above the LiCl solution for at least ten days before being removed, sealed in a container and weighed. One measurement taken after seven days produced similar results as that measured after ten days, which supports our assertion that equilibrium was obtained. The membranes were also exposed to water

vapor from pure ice. The results are shown in Figure 8.4 as a function of the water activity in the membrane, with the reported results by Springer *et al*. at 30 °C for comparison [34]. The data show similar qualitative trends below 0 °C as the previously reported data above 0 °C when using the activity scale based on the saturation pressure for liquid water, $p_{o,l}^{*}$. This suggests water behaves as a liquid over the range of water activities measured below 0 °C. If the activity scale is based upon the saturation pressure of ice, the measured curves deviate significantly from each other.

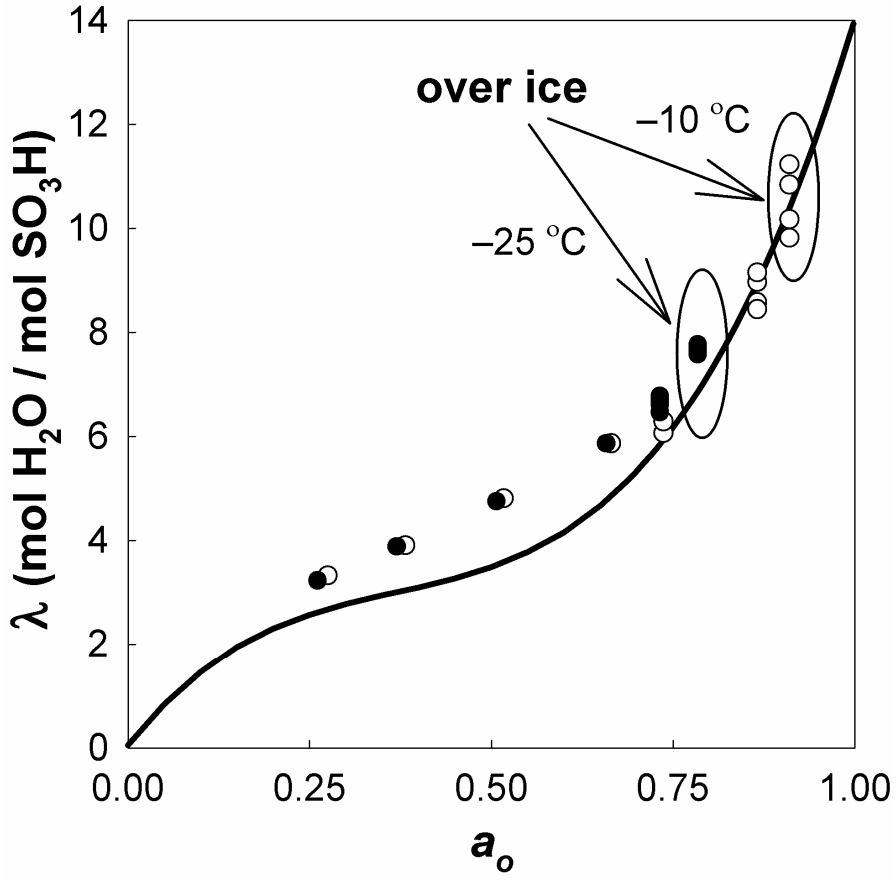

Figure 8.4. Measured water uptake at –25 °C (solid circles) and –10 °C (open circles) as a function of the liquid water activity in the membrane. Measured isotherm at 30 °C (solid line) from Springer *et al*. is also shown for comparison.

The maximum water content occurs at the saturation pressure for ice, which is denoted in the figure as the highest measured water activity below 0 °C. This equates to a continually decreasing maximum water content, λ_{max}, with temperature. Only considering the effect on uptake due to differences of saturation pressure, we may consider the maximum uptake as a function of temperature. In Figure 8.5, lines of constant λ are displayed as a function of temperature using the empirical fit of Springer *et al*. [34]. The partial pressure of water which corresponds to a specific λ at a specified temperature is calculated by knowing the saturation pressure of liquid water as a function of temperature and specifying the desired water content. The vapor pressure corresponding to ice is shown representing the maximum thermodynamically stable water partial pressure at a specified temperature. The intersection of the ice vapor pressure and the constant λ represents the maximum λ in equilibrium with vapor at that temperature. The maximum λ in equilibrium with water vapor is 14 at 0 °C and ~8 at –20 °C. The inset in Figure 8.5 compares this prediction to our experimentally measured λ_{max} at –10 and –25 °C with good agreement.

The indirect effect of having lower water content in the membrane during a cold start is that of a decreased diffusion coefficient and lower conductivity. Both transport properties are a function of the water content in the membrane and have an Arrhenius dependence on temperature. The lower water content and lower temperatures are predicted to significantly decrease fuel-cell performance.

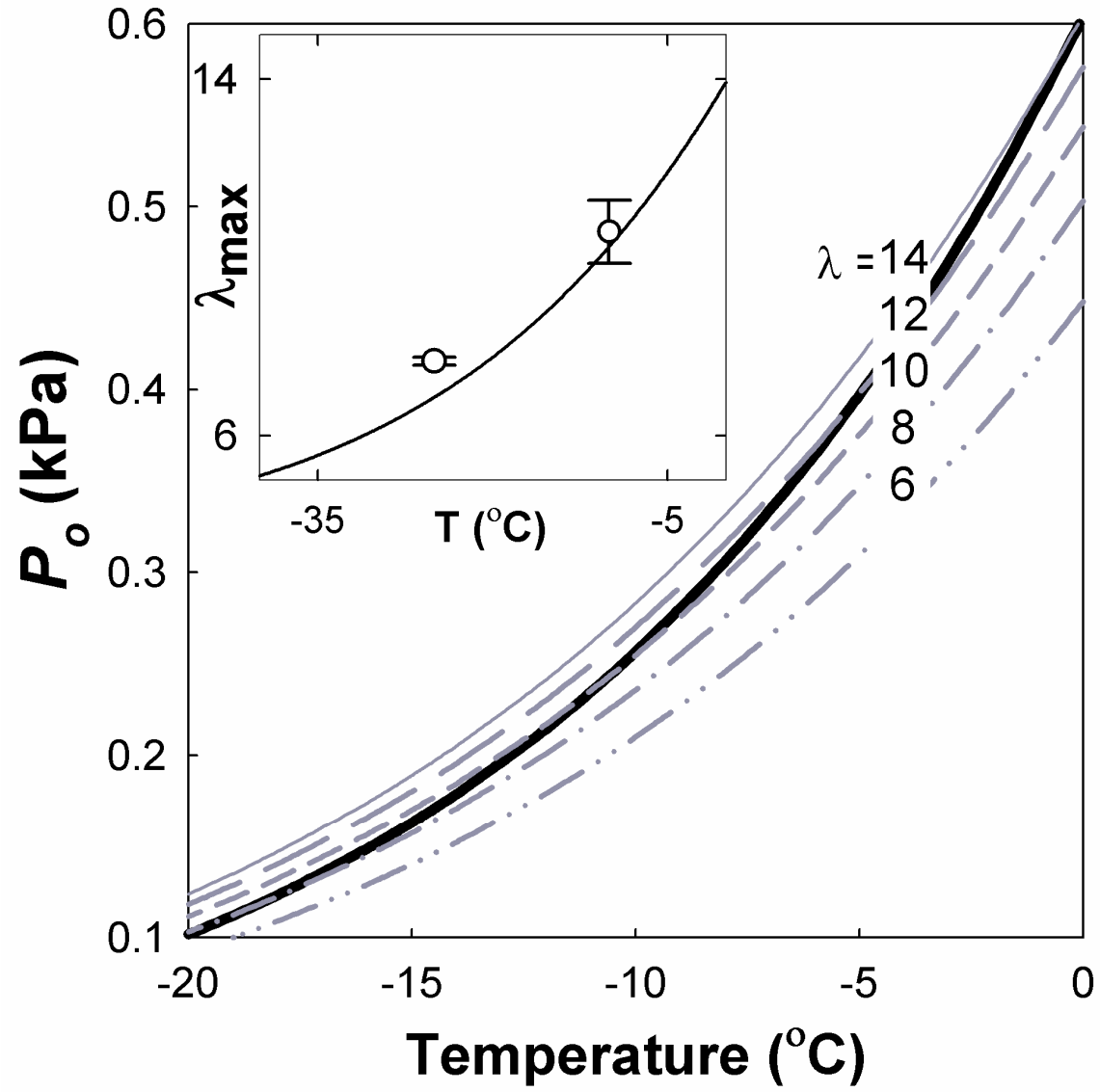

Figure 8.5. Maximum uptake as a function of temperature is found at the intersection of lines of constant water content (grey lines) and saturation pressure of ice (solid black line). Inset: λ equilibrated with water vapor over ice. Experimentally measured data from Figure 8.4 is included as a comparison.

8.4.2 Electro-osmotic Drag Coefficient

The electric potential measured during the equilibration process was monitored on at least an hourly basis until quasi-equilibrium was established. The potentials were recorded after two to three days of equilibration time. The dimensionless potential for Nafion® 112 membranes are shown as a function of the ratio of partial pressures of water in the two chambers of the activity-gradient cell in Figure 8.6. The data presented in Figure 8.6 is fit with a linear trend which clearly shows the drag coefficient is constant over the water contents probed.

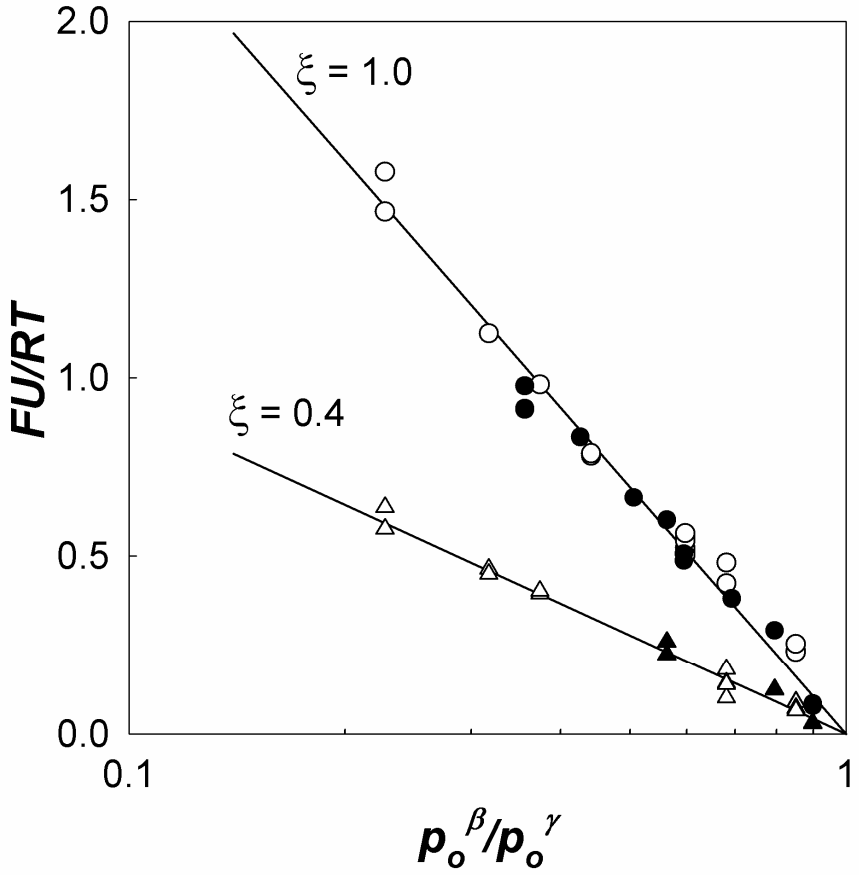

Figure 8.6. FU/RT vs p^{β}_o/p^{γ}_o for Nafion® 112 at –25 °C (solid circles) and –10 °C (open circles); BPSH at –25 °C (solid triangles) and –10 °C (open triangles)

No significant temperature dependence of ξ was observed at –10 and –25 °C within experimental reproducibility. Furthermore, the drag coefficient of Nafion appears to be equal to that reported by Zawodzinski *et al*., $\xi \approx 1$, over a range of activities at 30 °C [17]. An important observation is that this technique measures the drag coefficient over a moderate portion of the hydration isotherm below 0 °C. High water contents that result in larger hydrophilic domains are inaccessible as a result of being bounded by the vapor pressure of ice at high activities. Low water contents are also unavailable as LiCl solutions are bounded by solubility and the precipitation of salts at low water activities [35]. Our measurements at 30 °C for 1100 EW Nafion® resulted in values between those reported in the literature, $1.0 < \xi < 1.5$ [16, 17]. However, run to run deviation prevent us from presenting a statistically significant result at these higher temperatures. The cell design used in our experiments failed to provide seal consistency between compartments at above freezing temperatures. At the low water partial pressures below 0 °C, the relaxation of the cell was unnoticeable. At elevated temperatures, a cell potential decay on the order of 40 - 100 μV/hr was measured. We are unsure if the most significant temperature effect driving cell potential decay is a change in the mechanical aspects of the seal material or the reduction in mass transport properties and driving forces. Still, the results presented here provide sufficient evidence that the vapor equilibrated drag coefficient is within the range as that measured at temperatures above 0 °C.

The dimensionless potential for both the block and random co-polymer BPSH membranes are shown in Figure 8.6. No difference is found between the two polymer structures. We believe this to be a result of the limited portion of hydration isotherm

available below 0 °C. Hydration isotherms show the block BPSH has much larger hydrophilic domains at high water activities, Figure 8.7. At water activities near unity, we would expect the drag coefficient of the block co-polymer would be higher than that of the random copolymer. The lower value of the drag coefficient, $\xi \approx 0.4$, for the BPSH membranes (compared to ~1 for Nafion®) reflects electro-osmotic drag differences in these two materials for liquid equilibrated membranes (1.4 for BPSH to 3.6 for Nafion at 80 °C) although much smaller in magnitude [36]. Drag coefficients smaller than unity have also been measured in poly(etherketone) (PEEKK) chemistries using ENMR [18] and in liquid equilibrated BPSH-30 and sulfonated poly(imide) (sPI) using the direct methanol fuel cell method [36, 37]. Measurements in this study at 30 °C for the BPSH membranes resulted in values in the range of $0.4 < \xi < 0.6$ but suffer from the same variability from the cell relaxation discussed in regards to Nafion®.

The difference in drag coefficients between Nafion® and the BPSH chemistries is due to the size and structure of the hydrophilic domains. Nafion® has been described as having large and relatively open channels while BPSH has a less segregated domain structure attributed to a stiffer backbone and decreased driving force for phase separation [20]. Similar behavior has been shown for PEEKK, another hydrocarbon membrane chemistry [38]. As a result, water in BPSH membranes has a much higher interaction with the polymer. The consequence of increased interaction of water with the polymer is a lower drag coefficient as well as other transport properties.

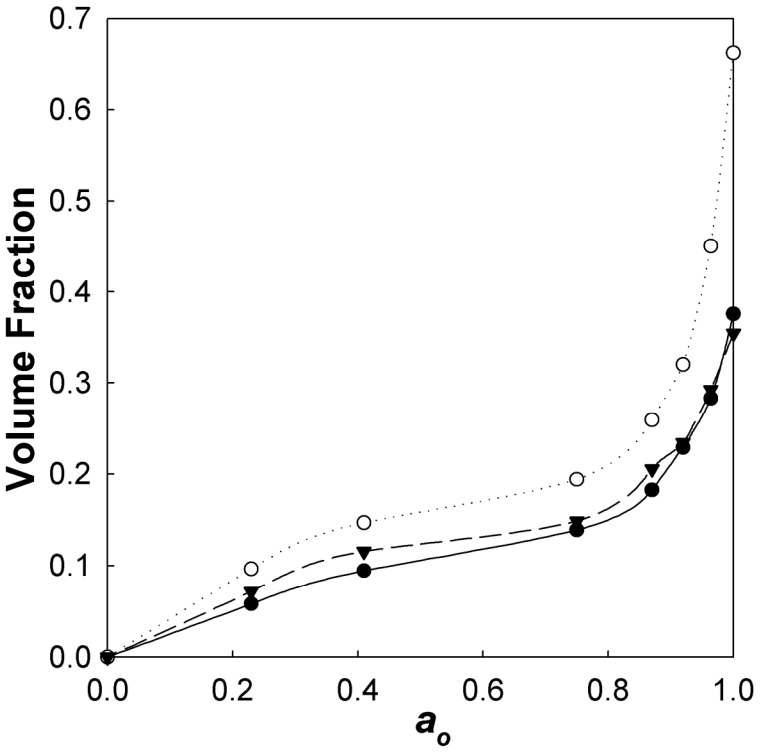

Figure 8.7. Sorption isotherms at 22 °C for Nafion® 112 (solid circles), BPSH-35 (solid triangles), and BPSH-20-BPS-15 (open circles)

Electro-osmosis in fuel cell membranes can be attributed to the movement of the solvated proton (when transported via vehicle mechanism) and hydrodynamic pumping that results from this movement. The observed electro-osmotic drag coefficient reflects a combination of the extent of vehicle versus hopping mechanism (structure diffusion) responsible for proton conduction and the susceptibility of the local environment to hydrodynamic pumping [12]. Figure 8.8 displays a depiction of these two transport mechanisms. We discuss our data here in terms of conduction mechanism, due to the presence of drag coefficients in polymer electrolytes less than unity.

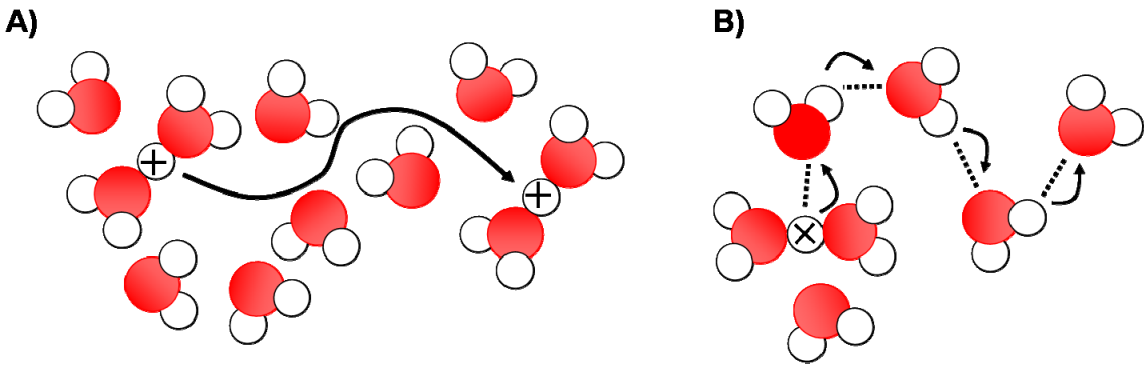

Figure 8.8. Depiction of a) the vechicle mechanism and b) the hopping or Grotthuss mechanism for proton transport.

One must always be careful postulating atomistic mechanisms from macroscopic measurements. However, macroscopic measurements can aid in establishing limiting cases in the mechanisms. Here we conclusively present the measurement of a drag coefficient less than unity in an aqueous polymer-electrolyte system. Taking the hydronium ion as the sole charge transport species, the drag coefficient for vehicular transport has a lower limit of 1. However, this value would only be obtained if no additional water transport occurred due to hydrodynamic pumping or drag of other waters in the solvation shell. Quantum mechanical calculations predict protons (in aqueous phases) are always strongly solvated by multiple water molecules forming Eigen ($H_9O_4^+$) and Zundel ($H_5O_2^+$) ions in order to lower free energy [39-41]. Additionally, hydrodynamic pumping of water can only further increase drag, strongly suggesting meaningful drag coefficients are greater than 1 for vehicular transport. While we cannot ascertain the relative importance of proton transport by vehicle or hopping mechanism from drag measurements because drag coefficients do not independently probe proton hydration and hydrodynamic pumping; we are able to make at least one basic conclusion.

Namely, the measured drag coefficient in BPSH membranes, being less than unity, demands a significant participation of a proton hopping mechanism even at low water contents.

There are at least three separate experimental observations that have led to suggestions that the minimum electro-osmotic drag coefficient in polymer electrolytes is unity and/or that proton transport under specific conditions occurs extensively through vehicular transport of the hydronium ion. These studies have been based upon NMR, quasielastic neutron scattering measurements (QENS), and measurements of electro-osmotic drag. The mechanism of transport is particularly important as development of membranes that maintain adequate conductivity at low water contents is a key research goal for polymer electrolytes. Efficient conduction through a hopping mechanism is a potential pathway toward such materials.

NMR studies have compared the self diffusion coefficients of water with measured conductivity to compare the mobility of conducted protons to water molecules in polymer electrolytes (primarily Nafion®) [17, 42]. In Nafion®, these NMR studies showed that at low water contents the mobility of conducting protons and water was nearly equal, leading to the suggestion that proton transport was occurring exclusively by a vehicular transport mechanism associated with movement of the water molecules. These studies also showed that at high water contents proton transport occurred much faster than water diffusion. These data were presented as evidence of a significant contribution to conduction by proton hopping [17, 42].

QENS measurements suggest that proton transport occurs by the diffusion of H_3O^+ over the full range of hydration in Nafion® [43, 44]. These studies have shown that the fraction of non-diffusing protons is equal to three across the full hydration range of Nafion®, highly suggestive of the hydronium ion as the active species of transport. The work of Pivovar and Pivovar [44] warns that the correlation to H_3O^+ may be the result of a serendipitous coincidence due to complex and possibly competing proton transport mechanisms [41]. Whereas Perrin [43] proposed three hypotheses to explain this observation, the first two of which were discussed as improbable. The third hypothesis was that of a nondiffusing hydronium ion that ruled out the Grotthuss mechanism at all levels of hydration. The authors presented arguments based on confinement effects and high acidity as potential reasons for discrepancies with the behavior of bulk water. These results contradict the NMR findings discussed in the previous paragraph at high water contents and also are clearly not supported by the data obtained here for BPSH nor other data reported for liquid equilibrated membranes for similar hydrocarbon ionomers [12]. Furthermore, BPSH and similar hydrocarbon polymers show similarly high acidity, lower amounts of bulk-like water, and smaller water domain sizes suggesting even stronger confinement effects [20].

Measurements of drag coefficients of Nafion®, also in agreement with those reported here, show a tendency toward unity at low water contents [17, 42]. This trend toward unity could also suggest conduction as occurring by vehicular transport of hydronium ions, as it is the most straightforward explanation of the observed

phenomenon. However, this may also be a serendipitous coincidence, perhaps related to the fraction of non-diffusion protons observed in the QENS studies, due to the competition of different proton conduction mechanisms and rates, as they also cannot be used to explain the values less than one observed here.

The existence of Grotthuss mechanism proton transport at low water contents within a polymer electrolyte necessitates further probing of assertions of proton conduction mechanisms at low water contents. Beyond the previously mentioned trends of decreasing drag with decreasing water uptake and qualitative differences in drag coefficients between BPSH and Nafion® persisting under liquid and vapor equilibrated states, other trends of drag coefficients of BPSH and Nafion® are worthy of discussion. Temperature dependence of these systems show a clear trend under liquid equilibrated condition for increasing drag with increasing temperature for both BPSH and Nafion® approximately doubling between room temperature and 80 °C [36, 45]. The simplest explanation for this behavior is different activation energies for different proton conducting mechanisms, although this trend does not seem to hold true for Nafion® at the low temperatures and vapor equilibrated conditions we have probed in this study. Another trend has been shown within the family of BPSH polymers for increasing electro-osmotic drag with increasing sulfonation level (doubling from 1.5 for BSPH-40 to 3.0 for BPSH-60 for the conditions probed) [36, 46]. As sulfonation level increases, water uptake and the number of waters per sulfonic acid group increase significantly, and these phenomenon as well as others have been attributed to changes in local water domain structure [20]. While changes in the extent of Grotthuss mechanism and vehicular

conduction (or the vehicular transport species) are certainly possible between these samples, hydrodynamic pumping in response to vehicular transport is almost certainly a major factor in these observed differences. As the observed drag coefficients of Nafion® and BPSH qualitatively show similar trends under low water content conditions as they do at high water content conditions, one could conclude that the difference in the measured drag coefficients between BPSH and Nafion® is most likely a result of the susceptibility of the hydrophilic domains to hydrodynamic pumping. Thus we are suggesting the relative proton transport mechanisms, hopping compared to vehicle, in the two membrane chemistries could be very similar in magnitude. Additionally, the species of vehicular transport (whether they be Eigen ($H_9O_4^+$), Zundel ($H_5O_2^+$), or hydronium (H_3O^+) ions) might also be very similar at similar water activities. These claims need further probing such as QENS measurements either investigating BPSH and comparing the results with those reported for Nafion® or probing Nafion® with other counterions incapable of hopping conduction and/or computational studies, which allow for Grotthuss shuttling.

Ice formation within polymer electrolytes is another possible complicating factor for cold temperature membrane properties. To explore the effect of the presence of ice within the membrane, we attempted to measure the drag coefficient with a Nafion® membrane that was pre-saturated with liquid water and quickly frozen between metal plates at –25 °C. After the experimental apparatus and membrane were both equilibrated with the chamber temperature, the frozen membrane was placed into the apparatus. The measured potential as a function of equilibration time is shown in Figure 8.9. The

potential rise is delayed until the ice sublimates or melts and evaporates from the membrane. After the ice is removed, the potential rises to a value that is in good agreement with a membrane that was pre-dried before testing.

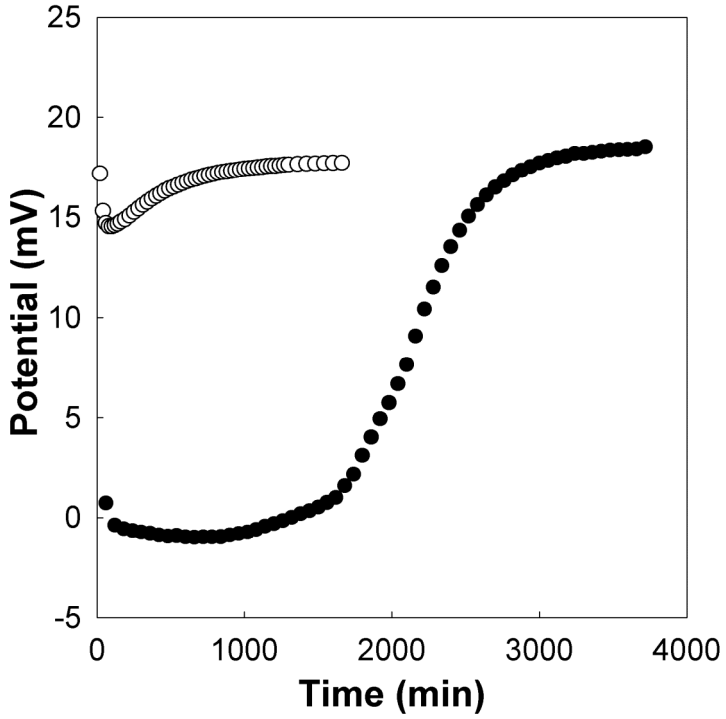

Figure 8.9. Measured potential of a pre-dried (open circles) and pre-frozen (solid circles) membrane as a function of time in the activity-gradient cell at –25 °C.

All published work that provide evidence of ice inside of the hydrophilic domains of the membrane have been with membranes that were rapidly frozen [13-15, 26]. Although this has experimental benefits, it is dissimilar to the cooling profile of a fuel-cell stack that would be used in an automobile. The time for a typical automotive stack to reach subzero temperatures after operation is on the order of 20 hours. This slow process will most likely result in different membrane water contents than if the membrane were quickly frozen.

As a thought experiment, one may consider the water content of a polymer electrolyte membrane after a slow freezing process in a PEMFC stack. At temperatures above freezing, the membrane is most likely equilibrated to some extent with liquid water as a result of water condensing with decreasing system temperature. At temperatures just below 0 °C, bulk water in the gas-diffusion layer or flow field will freeze. At this point a gradient in the partial pressure of water now exists. The water in the membrane is in a liquid state and in equilibrium with the partial pressure of supercooled water. The water that is now frozen has a lower partial pressure, the vapor pressure of ice. Water will begin to evaporate out of the membrane and deposit as ice external of the membrane. The drop in system temperature dries out the membrane to a point where it is in equilibrium with the vapor pressure of ice at the system temperature. The thin membranes, ~18-25 μm, and high surface area electrodes used in current membrane electrode assemblies promote this drying out process. Ice formation external of the membrane could potentially be the source of reductions in gas transport or damage from frost heave [47, 48].

8.4.3 Ohmically Limited Current

As current is passed between electrodes, each proton drags water from the anode to the cathode through electro-osmosis. This process creates a gradient in water activity resulting in the diffusion of water from the cathode back to the anode. Under a steady-state condition, a concentration profile exists that is the result of these two competing processes. As the conductivity of the membrane is a function of water content, low water concentrations result in large ionic resistances. As the voltage drop across the electrolyte

is increased, the PEMFC approaches a pseudo-limiting current caused by large ionic resistance at the anode. In contrast to typical limiting currents where the concentration of a reactant goes to zero, the electro-osmotic drag coefficient decreases with water content, and therefore a true limiting current is not reached. Nonetheless, in one respect it is no different than an oxygen limiting current in that the power output from the PEMFC will drop to zero.

Weber and Newman proposed an updated and expanded PEMFC model based upon concentrated solution theory that includes liquid and vapor equilibrated membrane models [49]. Since the behavior of supercooled water in the components of PEMFCs is uncertain, we employ the Weber and Newman model below 0 °C with some modifications, the most significant being the lack of treatment of a liquid equilibrated membrane. Here, we treat only the membrane phase in a 1-D steady-state isothermal numerical model. Although transient and nonisothermal phenomena have significant effects on PEMFC operation below 0 °C, we use this model to probe the interaction of the three transport parameters defined by concentrated solution theory. Using our measurements and others reported in the literature, we compare current-potential behavior for PFSA and BPSH chemistries during a cold start. The conductivity, water diffusion coefficient, and electro-osmotic drag coefficient of BPSH-35 are lower than those of Nafion. The lower valued transport parameters of BPSH-35 compared to Nafion has been attributed to the structure of the hydrophilic domains as discussed early [20].

8.4.3.1 Membrane Model Governing Equations.

The membrane is modeled with concentrated solution for multi-component diffusion. In this work, the chemical potential is assumed the sole driving force and related to the difference in the velocity of species j and i. A more general and rigorous discussion is presented by Newman [28]

$$c_i \nabla \mu_i = \sum_j K_{ij} \left(v_j - v_i \right). \tag{8.9}$$

The phenomenological interaction coefficients, K_{ij}, through the Onsager reciprocal relations, may be related to ½n(n–1) transport properties where n is the number of species. For the binary electrolyte considered here, the pertinent properties are the transport coefficient, α, the ionic conductivity, κ, and the transport number of water, ξ. The conductivity of the electrolyte may be related to the current, $\boldsymbol{i}$, passed in the absence of a gradient in the chemical potential of water, μ_o,

$$i = -\kappa \nabla \Phi_2 . \tag{8.10}$$

Where the solution potential, Φ_2, is defined from the chemical potential of a proton, μ_+, and Faraday's constant, F,

$$\Phi_2 = \frac{\mu_+}{F}. \tag{8.11}$$

The electro-osmotic drag coefficient is defined above in Equation 8.2. Concentrated solution theory simplifies the ratio of fluxes to the ratio of transport numbers, where the transference of species i, t_i^m, is referenced to the membrane and not the solvent, water. The charge, z_+, and the transference number of a proton are both unity in a binary electrolyte with stationary anions. Thus the electro-osmotic drag coefficient is equivalent to the transport number of water [16],

$$\xi = \frac{N_o}{N_+} = \frac{t_o^m z_+}{z_o t_+^m} = \frac{t_o^m}{z_o} \tag{8.12}$$

which is not necessarily zero for a neutral species. The final independent transport property relates the flux of water to a gradient in its chemical potential in the absence of current,

$$N_o = -\alpha \nabla \mu_o \tag{8.13}$$

The gradient in the chemical potential of water may be related to the water activity, a_0, by

$$\nabla \mu_o = RT \nabla \ln a_o \tag{8.14}$$

The transport coefficient, α, may be related to a measurable diffusion coefficient. Equation 8.15 provides this relation assuming the membrane is stationary. Here D_{μ_0} is

the diffusion coefficient of water, c_o is the concentration of water, and x_0 is the mole fraction of water

$$\alpha = \frac{c_o D_{\mu_o}}{RT(1-x_o)} \tag{8.15}$$

Substituting these definitions into the flux equations defined by concentrated solution theory results in the comprehensive flux equations for water and protons [11], Equations 8.16 and 8.17. The flux of water, $\boldsymbol{N_o}$, and of protons, $\boldsymbol{N}_+$, are found to be

$$N_o = -\frac{\kappa\xi}{F}\nabla\Phi_2 - \left(\alpha + \frac{\kappa\xi^2}{F^2}\right)\nabla\mu_o \tag{8.16}$$

and

$$FN_+ = i = -\kappa\nabla\Phi_2 - \frac{\kappa\xi}{F}\nabla\mu_o\,. \tag{8.17}$$

Within the membrane under steady state, the divergence of ionic current and flux of water is equal to zero,

$$\nabla\cdot i = 0 \tag{8.18}$$

And

$$\nabla \cdot N_o = 0 \tag{8.19}$$

8.4.3.2 Membrane and Transport Properties

We adopt the same dependence on water volume fraction and temperature for the conductivity and the water diffusion coefficient as reported by Weber and Newman [49]. The water volume fraction, f, is related to the molar volumes of the membrane, V_m, and water, V_o, and by the number of water molecules per acid group, λ.

$$f = \frac{\lambda V_o}{V_m + \lambda V_o} \tag{8.20}$$

The conductivity is modeled using a percolation relation with an Arrhenius dependence on temperature and a prefactor κ_o. Here T_{ref} is 303.15 K.

$$\kappa = \kappa_0 \left(f - 0.06\right)^{1.5} \exp\left[\frac{15000}{R}\left(\frac{1}{T_{ref}} - \frac{1}{T}\right)\right] \tag{8.21}$$

The diffusion coefficient of water is considered to be proportional to the water volume fraction and also maintains an Arrhenius dependence on temperature with prefactor $D_{\mu 0,o}$.

$$D_{\mu_o} = D_{\mu_o,0} f \exp\left[\frac{20000}{R}\left(\frac{1}{T_{ref}} - \frac{1}{T}\right)\right] \tag{8.22}$$

Although multiple membrane hydration models exist in the literature, none adequately fit the reported low temperature measurements. An empirical fit of the hydration isotherm and water activity at –10 and –25 °C is used .

$$\lambda = C_1 a_o^{\,3} + C_2 a_o^{\,2} + C_3 a_o \tag{8.23}$$

The prefactors used in this simulation for the conductivity and the diffusion coefficient of water in 1100 EW PFSA membrane (i.e. Nafion 112) are the same as those presented by Weber and Newman [49]. These prefactors, the electro-osmotic drag coefficient, and the constants used for the hydration isotherm below 0 °C are listed in Table 8.1. The hydrocarbon based membrane, BPSH, has been studied at various equivalent weights and random or multi-block copolymer configurations. However, only the random copolymer BPSH-35 (35 mol % disulfonated) has reported values for the diffusion coefficient [50], conductivity [50], hydration isotherm, and vapor equilibrated electro-osmotic drag coefficient. The hydration isotherm for BPSH-35 at room temperature is nearly identical to 1100 EW Nafion membrane, Figure 8.7. Therefore, the same isotherm is used for both membrane chemistries below 0 °C. The dry densities, ρ_m, and equivalent weights of the two polymers are also reported in Table 8.1 for calculation of the water volume fraction [49, 51].

Table 8.1. Membrane Properties

Parameter	Nafion	BPSH-35	Reference (Nafion); (BPSH)
κ_0 (S/cm)	0.50	0.27	[49]; [50]
$D_{\mu o,0}$ (cm^2/s)	1.8×10^{-5}	1.2×10^{-5}	[49]; [50]
ξ (-10 and -25 °C)	1.0	0.4	(this work)
c_1, c_2, c_3 (n_0/n_{-SO3})	35.12, –43.49, 21.96		(this work)
$\rho_{m,\,dry}$ (g/cm^3)	2.0	1.3	[49]; [51]
EW (g/mol $-SO_3$)	1100	666	N/A

8.4.3.2 Simulation of the ohmically limited current

The current-potential behavior is found by raising the potential drop across the electrolyte and calculating ***i***. The solution potential at the anode is arbitrarily set to zero. The boundary conditions for the flux of water are specific to the problem we are addressing.

We have shown the maximum water content in the membrane at temperatures below 0 °C to be a function of the ratio of the saturation pressures of ice and liquid water, Equation 8.1. Therefore, the temperature we are investigating will have significant effects on the hydration of the membrane and thus the transport properties. At the cathode, we set the water content equal to the maximum value in equilibration with water vapor at the temperature of interest. This value is found at the activity in Equation 8.24 and decreases as the temperature is lowered. At the anode boundary, the flux of water is assumed to be negligible due to the low vapor pressure of water below 0 °C. Alternatively, a parameter could be defined to compare cases with a positive or negative flux across the anode boundary [52]. In order to focus on the differences between transport properties of specific membrane chemistries, we restrict this discussion to a no flux condition at the anode boundary.

$$\lambda_{\max}(T) = f\left[a_o(T)\right] = f\left[\frac{p^*_{o,s}(T)}{p^*_{o,l}(T)}\right] \tag{8.24}$$

In an effort to validate transport properties used at lower temperatures, the resistance of Nafion 112 was simulated and compared to reported data from Thompson *et al*. [6] , Figure 8.10. The calculated and measured values are in good agreement over a range of hydration levels. Figure 8.9 also demonstrates the resistance approaches infinity as the water content drops to a low limiting value. This is a result of the percolation model, Equation 8.21, used to model the conductivity. Without other published measurements, validation of the transport coefficient, α, is not attempted. The predicted current-potential responses are shown in Figure 8.11. With a membrane 50 microns in thickness, the ohmically limited current is only approached at large potential drops of nearly 1 V. From this calculation, the start of a fuel cell below 0 °C will be limited by the transfer of protons to cathode for the oxygen reduction reaction if high current densities are sought. Lower temperatures exacerbate this limitation. Nafion shows better performance than the BPSH membrane at reasonable potential drops.

BPSH reaches a higher current than Nafion as a result of a lower electro-osmotic drag coefficient. The performance benefit of the lower electro-osmotic drag coefficient is delayed until large potentials are reached and therefore only provide minimal gain during the operation or start of a PEMFC below 0 °C. At higher current densities (*e.g* > 200 mA/cm^2), heat generated from the oxygen reduction reaction is no longer negligible and may result in greater water transport toward the anode [53]. Therefore, simulated results

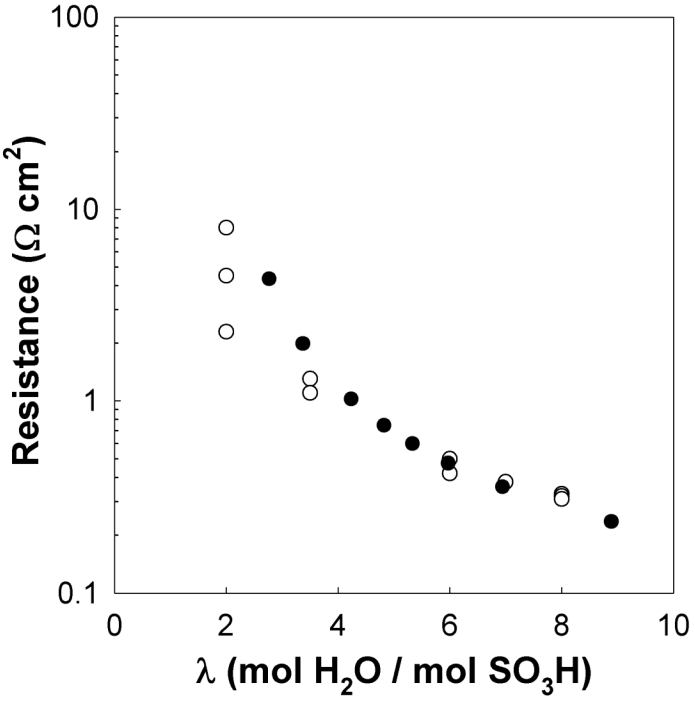

Figure 8.10. Simulated membrane through plane resistance (solid circles) compared to the measured values reported in Reference [6] for Nafion 112 at –20 °C over a range of water contents (open circles.)

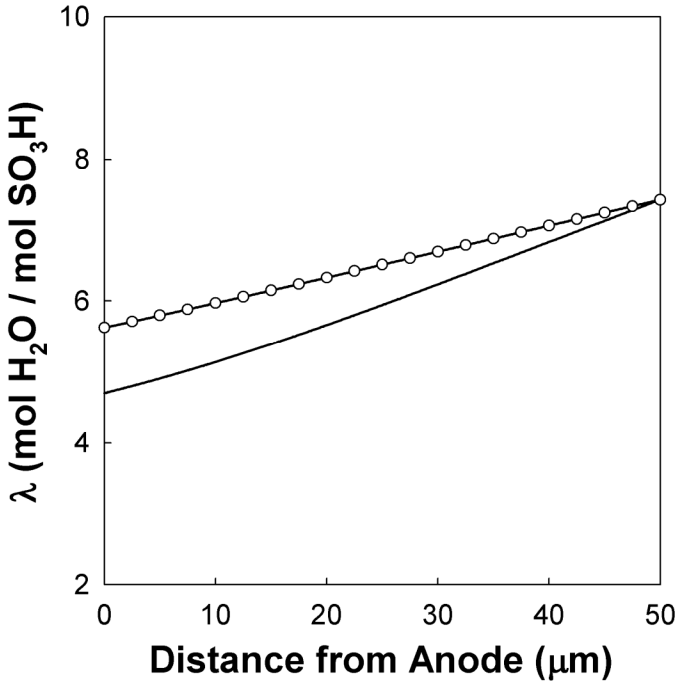

Figure 8.11. Simulated current potential behavior for Nafion 112 (—) and BPSH-35 (○) for membranes of 50 microns at –10 and –25 °C.

at higher current densities should be used only as a source of discussion of the interplay between the transport coefficient and the electro-osmotic drag coefficient.

Figure 8.12 displays the water content as a function of position for both membranes at –25 °C and a current density of 200 mA/cm^2. The transport properties of Nafion result in a lower average water content when compared to BPSH. This lower average water content only slightly diminishes the storage capacity of the membrane, ~7%, but increases the resistance of the electrolyte. However, the conductivity of Nafion is nearly twice the value of BPSH under fully hydrated conditions resulting in a lower membrane resistance even at lower average water content.

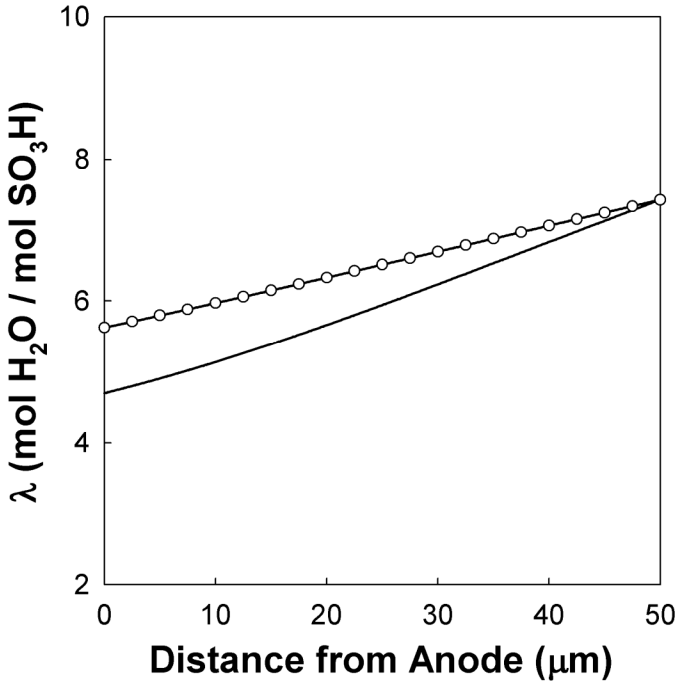

Figure 8.12. Simulated membrane water content at 200 mA/cm^2 and a system temperature of –25 °C for BPSH-35 (–○–) and Nafion 112 (—).The left side of the membrane is adjacent to the anode.

8.4.3.2 Summary of simulation of results

The findings presented here-in have important implications for material selection and operation of a PEMFC below 0 °C. Membranes with lower drag coefficients provide only marginal improvement at steady state as they also have lowered conductivity and water back diffusion. Moreover, attempts to increase water storage capabilities for cold start operation should be based upon sorption behavior up to the saturation pressure of ice and not supercooled liquid water. Finally, high current densities are without value during operation below 0 °C if power output is required to drive external loads. Alternatively, this high overpotential may serve as an internal heat source to bring the system temperature above 0 °C.

8.5. CONCLUSIONS

Physical and transport properties of PFSA and BPSH membrane chemistries have been presented with particular emphasis on values measured at –10 and –25 °C. The electro-osmotic drag coefficient remains relatively constant over the range of temperatures and water contents investigated in this study. However, significant differences exist between the vapor equilibrated drag coefficient for PFSA and BPSH membranes. The electro-osmotic drag coefficient of BPSH membranes was found to be approximately 0.4, below that of Nafion® which is approximately 1. A drag coefficient less than unity suggests that a significant fraction of the proton transport mechanism involves the hopping of protons. Understanding the contributions of the Grotthuss

mechanism at low hydration levels will have important implications for high temperature, low humidity polymer electrolyte development.

The hydration isotherm for Nafion® is presented for temperatures below 0 °C. At equilibrium, the maximum vapor uptake will decrease with temperature as a result of the lower saturation pressure for ice than that for supercooled liquid water. This diminution of the maximum water content lowers the water storage capability during a cold start. Moreover, significant reduction in the performance of a PEMFC is found in the numerical simulation of the ohmically limited current. The reduction of water content at lower temperatures results in additional lowering of the transport properties, κ and $D_{\mu o}$, which depend on water volume fraction as well as temperature.

REFERENCES

[1] Borup R, Meyers J, Pivovar B, Kim YS, Mukundan R, Garland N, et al. Scientific aspects of polymer electrolyte fuel cell durability and degradation. Chemical Reviews. 2007; **107**(10), 3904-51.

[2] Ishikawa Y, Morita T, Nakata K, Yoshida K, Shiozawa M. Behavior of water below the freezing point in PEFCs. Journal of Power Sources. 2007; **163**(2), 708-12.

[3] Mao L, Wang CY. Analysis of cold start in polymer electrolyte fuel cells. Journal of the Electrochemical Society. 2007; **154**(2), B139-B46.

[4] Tajiri K, Tabuchi Y, Kagami F, Takahashi S, Yoshizawa K, Wang CY. Effects of operating and design parameters on PEFC cold start. Journal of Power Sources. 2007; **165**(1), 279-86.

[5] Tajiri K, Tabuchi Y, Wang CY. Isothermal cold start of polymer electrolyte fuel cells. Journal of the Electrochemical Society. 2007; **154**(2), B147-B52.

[6] Thompson EL, Jorne J, Gu WB, Gasteiger HA. PEM fuel cell operation at -20 degrees C. I. Electrode and membrane water (charge) storage. Journal of the Electrochemical Society. 2008; **155**(6), B625-B34.

[7] Gates CM, Newman J. Equilibrium and diffusion of methanol and water in a Nafion 117 membrane. Aiche Journal. 2000; **46**(10), 2076-85.

[8] Hinatsu JT, Mizuhata M, Takenaka H. Water-Uptake of Perfluorosulfonic Acid Membranes from Liquid Water and Water-Vapor. Journal of the Electrochemical Society. 1994; **141**(6), 1493-8.

[9] Rieke PC, Vanderborgh NE. Temperature-Dependence of Water-Content and Proton Conductivity in Polyperfluorosulfonic Acid Membranes. Journal of Membrane Science. 1987; **32**(2-3), 313-28.

[10] Thampan T, Malhotra S, Tang H, Datta R. Modeling of conductive transport in proton-exchange membranes for fuel cells. Journal of the Electrochemical Society. 2000; **147**(9), 3242-50.

[11] Fuller TF, Newman J. Water and Thermal Management in Solid-Polymer-Electrolyte Fuel-Cells. Journal of the Electrochemical Society. 1993; **140**(5), 1218-25.

[12] Pivovar BS. An overview of electro-osmosis in fuel cell polymer electrolytes. Polymer. 2006; **47**(11), 4194-202.

[13] Cappadonia M, Erning JW, Stimming U. Proton Conduction of Nafion((R))-117 Membrane between 140 K and Room-Temperature. Journal of Electroanalytical Chemistry. 1994; **376**(1-2), 189-93.

[14] Saito M, Hayamizu K, Okada T. Temperature dependence of ion and water transport in perfluorinated ionomer membranes for fuel cells. Journal of Physical Chemistry B. 2005; **109**(8), 3112-9.

[15] Thompson EL, Capehart TW, Fuller TJ, Jorne J. Investigation of low-temperature proton transport in Nafion using direct current conductivity and differential scanning calorimetry. Journal of the Electrochemical Society. 2006; **153**(12), A2351-A62.

[16] Fuller TF, Newman J. Experimental-Determination of the Transport Number of Water in Nafion-117 Membrane. Journal of the Electrochemical Society. 1992; **139**(5), 1332-7.

[17] Zawodzinski TA, Davey J, Valerio J, Gottesfeld S. The Water-Content Dependence of Electroosmotic Drag in Proton-Conducting Polymer Electrolytes. Electrochimica Acta. 1995; **40**(3), 297-302.

[18] Ise M, Kreuer KD, Maier J. Electroosmotic drag in polymer electrolyte membranes: an electrophoretic NMR study. Solid State Ionics. 1999; **125**(1-4), 213-23.

[19] Mauritz KA, Moore RB. State of understanding of Nafion. Chemical Reviews. 2004; **104**(10), 4535-85.

[20] Hickner MA, Pivovar BS. The chemical and structural nature of proton exchange membrane fuel cell properties Fuel Cells. 2005; **5**(2), 213-29.

[21] Meyers JP, Newman J. Simulation of the direct methanol fuel cell - I. Thermodynamic framework for a multicomponent membrane. Journal of the Electrochemical Society. 2002; **149**(6), A710-A7.

[22] Murphy DM, Koop T. Review of the vapour pressures of ice and supercooled water for atmospheric applications. Quarterly Journal of the Royal Meteorological Society. 2005; **131**(608), 1539-65.

[23] Hedlin CP. Sorption isotherms of twelve woods at subfreezing temperatures. Forest Products Journal. 1968; **17**(12), 43-8.

[24] Koiwai A, Kamiya A, Kawasumi M. Study on Water Content of Perfluorosulfonic Acid Ionomer Membranes Below Water Freezing Point. ECS Transactions. 2007; **11**(1), 587.

[25] Tarkow H. Reinterpretation of Anomalous Moisture Adsorption Isobars Below Odegrees C. Tappi. 1971; **54**(4), 593-&.

[26] Kim YS, Dong LM, Hickner MA, Glass TE, Webb V, McGrath JE. State of water in disulfonated poly(arylene ether sulfone) copolymers and a perfluorosulfonic acid copolymer (nafion) and its effect on physical and electrochemical properties. Macromolecules. 2003; **36**(17), 6281-5.

[27] Robinson RA, Stokes RH. Electrolyte Solutions. 2nd ed. Mineola, NY: Dover Publication 2002.

[28] Newman J, Thomas-Alyea KE. Electrochemical Systems. 3rd ed. Hoboken, New Jersey: John Wiley & Sons, Inc. 2004.

[29] Gibbard HF, Scatchar.G. Liquid-Vapor Equilibrium of Aqueous Lithium-Chloride, Form 25degrees to 100degreesc and from 1.0 to 18.5 Molal, and Related Properties. Journal of Chemical and Engineering Data. 1973; **18**(3), 293-8.

[30] Holmes HF, Mesmer RE. Isopiestic Studies of Aqueous-Solutions at Elevated-Temperatures .6. Licl and Cscl. Journal of Chemical Thermodynamics. 1981; **13**(11), 1035-46.

[31] Holmes HF, Mesmer RE. Thermodynamic Properties of Aqueous-Solutions of the Alkali-Metal Chlorides to 250-Degrees-C. Journal of Physical Chemistry. 1983; **87**(7), 1242-55.

[32] Wang F, Hickner M, Kim YS, Zawodzinski TA, McGrath JE. Direct polymerization of sulfonated poly(arylene ether sulfone) random (statistical) copolymers: candidates for new proton exchange membranes. Journal of Membrane Science. 2002; **197**(1-2), 231-42.

[33] Lee H-S, Roy A, Lane O, Dunn S, McGrath JE. Hydrophilic-hydrophobic multiblock copolymers based on poly(arylene ether sulfone) via low-temperature coupling reactions for proton exchange membrane fuel cells Polymer. 2008; **49**(3), 715-23.

[34] Springer TE, Zawodzinski TA, Gottesfeld S. Polymer Electrolyte Fuel-Cell Model. Journal of the Electrochemical Society. 1991; **138**(8), 2334-42.

[35] Monnin C, Dubois M, Papaiconomou N, Simonin JP. Thermodynamics of the LiCl+H2O system. Journal of Chemical and Engineering Data. 2002; **47**(6), 1331-6.

[36] Hickner MA. Structure and Transport in Fuel Cell Proton Exchange Membranes. Blacksburg, VA: Virginia Polytechnic Institute and State University; 2003.

[37] Ren XM, Henderson W, Gottesfeld S. Electro-osmotic drag of water in ionomeric membranes - New measurements employing a direct methanol fuel cell. Journal of the Electrochemical Society. 1997; **144**(9), L267-L70.

[38] Kreuer KD. On the development of proton conducting polymer membranes for hydrogen and methanol fuel cells. Journal of Membrane Science. 2001; **185**(1), 29-39.

[39] Elliott JA, Paddison SJ. Modelling of morphology and proton transport in PFSA membranes. Physical Chemistry Chemical Physics. 2007; **9**(21), 2602-18.

[40] Marx D. Proton transfer 200 years after von Grotthuss: Insights from ab initio simulations. Chemphyschem. 2006; **7**(9), 1848-70.

[41] Petersen MK, Voth GA. Characterization of the solvation and transport of the hydrated proton in the perfluorosulfonic acid membrane nafion. Journal of Physical Chemistry B. 2006; **110**(37), 18594-600.

[42] Kreuer KD, Paddison SJ, Spohr E, Schuster M. Transport in proton conductors for fuel-cell applications: Simulations, elementary reactions, and phenomenology. Chemical Reviews. 2004; **104**(10), 4637-78.

[43] Perrin JC, Lyonnard S, Volino F. Quasielastic neutron scattering study of water dynamics in hydrated nafion membranes. Journal of Physical Chemistry C. 2007; **111**(8), 3393-404.

[44] Pivovar AA, Pivovar BS. Dynamic behavior of water within a polymer electrolyte fuel cell membrane at low hydration levels. Journal of Physical Chemistry B. 2005; **109**(2), 785-93.

[45] Ren XM, Gottesfeld S. Electro-osmotic drag of water in poly(perfluorosulfonic acid) membranes. Journal of the Electrochemical Society. 2001; **148**(1), A87-A93.

[46] Pivovar BS, Hickner MA, Wang F, McGrath JE, Zelenay P, Zawodzinski TA. AIChE Topical Conference Proceedings; 2002 Spring Meeting; New Orleans, LA; 2002. p. 535.

[47] Kim S, Ahn BK, Mench MM. Physical degradation of membrane electrode assemblies undergoing freeze/thaw cycling: Diffusion media effects. Journal of Power Sources. 2008; **179**(1), 140-6.

[48] Kim S, Mench MM. Physical degradation of membrane electrode assemblies undergoing freeze/thaw cycling: Micro-structure effects. Journal of Power Sources. 2007; **174**(1), 206-20.

[49] Weber AZ, Newman J. Transport in polymer-electrolyte membranes - II. Mathematical model. Journal of the Electrochemical Society. 2004; **151**(2), A311-A25.

[50] Harrison WL, Hickner MA, Kim YS, McGrath JE. Poly(arylene ether sulfone) copolymers and related systems from disulfonated monomer building blocks: Synthesis, characterization, and performance - A topical review. Fuel Cells. 2005; **5**(2), 201-12.

[51] Kim YS, Einsla B, Sankir M, Harrison W, Pivovar BS. Structure-property-performance relationships of sulfonated poly(arylene ether sulfone)s as a polymer electrolyte for fuel cell applications. Polymer. 2006; **47**(11), 4026-35.

[52] Eames DJ, Newman J. Electrochemical Conversion of Anhydrous Hcl to Cl-2 Using a Solid-Polymer-Electrolyte Electrolysis Cell. Journal of the Electrochemical Society. 1995; **142**(11), 3619-25.

[53] Zaffou R, Yi JS, Kunz HR, Fenton JM. Temperature-driven water transport through membrane electrode assembly of proton exchange membrane fuel cells. Electrochem Solid State Lett. 2006; **9**(9), A418-A22.

CHAPTER 9

CAPILLARY PRESSURE SATURATION RELATIONS FOR PEM FUEL CELL GAS-DIFFUSION LAYERS

9.1. INTRODUCTION

Water management is a critical aspect of the operation of proton-exchange membrane fuel cells (PEMFCs) [1]. Typical membranes utilized in PEMFCs require high relative humidity to maintain adequate conductivity. However, this requirement must be balanced by the need to remove product water generated at the catalyst layer. In the membrane phase, water is dragged with each proton that is conducted due to electro-osmosis and diffusion occurs due to the ensuing activity gradient. In the porous diffusion media or gas-diffusion layer (GDL), reactant gases must be transported to the catalyst layer, while water vapor and/or liquid transport is also occurring. The GDL is typically composed of carbon fiber paper or cloth which meets the mechanical, thermal, electronic and mass transport requirements of PEMFCs [2]. A significant body of work exists in the published literature on the measurement and modeling of these transport properties in PEMFCs [3, 4].

Transport in the GDL may be treated with the physics of two-phase immiscible flow used in the field of porous media [3, 4]. The pores are often idealized as cylindrical capillaries allowing analysis with the Young-Laplace equation (Y-LE) [5].

$$P_c = P_{nw} - P_w = \frac{2\gamma\cos(\theta)}{r} \tag{9.1}$$

The capillary pressure, P_c, is related to the surface tension of the liquid, γ, the resulting contact angle, θ, and the capillary radius, r. The capillary pressure is the difference in pressure between the nonwetting fluid, P_{nw}, and the wetting fluid, P_w. For the purposes of this work, we take the gas phase to be the nonwetting phase and the liquid phase to be the wetting phase.

Although the Y-LE is indispensable for ascribing physical insight into the behavior in porous media, a more meaningful discussion of PEMFC GDLs involves a discussion of the relationship between the capillary pressure and saturation level (CPSR). The saturation or fill level of the GDL is required to determine the permeability of the liquid phase and the open porosity for gaseous diffusion. At high saturations, the PEMFC is said to be flooding and the limiting current is significantly reduced from restricted oxygen flux [6, 7]. The saturation is defined as the fraction of pore volume filled with liquid.

$$S_w = \frac{V_w}{V_p} \tag{9.2}$$

Where V_w is the volume of water in the GDL and V_p is the volume of the pores.

The saturation and capillary pressure are typically related with a modified form of the Y-LE, an entirely empirical function, or semi-empirical function, such as the Leverett function. Using the method of standard porosimetry [8], Kumbur *et al.* correlate the octane drainage curves of PEMFC GDLs with a modified form of the Leverett function for changes in wettability, compression and temperature [9-11]. In an effort to specifically account for the geometry of the porous media, pore network models of GDLs have also been used to create CPSRs [12-14]. Another approach is the statistical calculation of a bundle of capillaries [7]. This calculation allows the direct manipulation of pore radii or interfacial tension distributions which may result in an improved understanding of the limiting factors in PEMFC performance.

Although a large number of models exist for PEMFCs, the modeling of hysteresis in CPSR has not been included in published fuel cell models. The lack of experimental measurements of GDL CPSRs is most likely the cause of this omission. Using MSP, drainage curves with octane and imbibition curves with water have been presented [9-11, 15]. Fairweather *et al*. have shown the difference in the boundary imbibition and drainage curves for water in PEMFC GDLs [16]. Other researchers have found no hysteresis evident in the CPSR [17]. Further work is needed to understand the cause, size and effect of hysteresis in GDLs.

9.2. EXPERIMENTAL

9.2.1 Materials

A number of different carbon papers are commercially available and used in PEMFC design. We have chosen to present two samples with different properties as representative of some of the possible GDLs currently used. TGP-H-060 was purchased from Toray Industries, Inc. and will be referred to simply as Toray. Carbon fiber paper was also purchased from Mitsubishi Rayon Corporation and will be referred to as MRC. The measured uncompressed thicknesses of Toray and MRC are 0.19 and 0.12 mm respectively. GDLs were evaluated both as-received (AR) and after a wet-treating process (WT). The WT-GDLs are rendered hydrophilic with an in-house proprietary process. This process modifies the surfaces of the individual fibers which make up the GDL. The resulting hydrophilic chemistry remains stable for more than ten thousand hours under fuel cell operating conditions. Further details on wet-treating processes may be found in the patent literature [18-20].

Scanning electron micrographs (SEM) of both as-received materials are presented in Figure 9.1. Both GDLs are constructed of carbon fibers and resin. However, AR-Toray is composed almost entirely of fibers 7 μm in diameter while AR-MRC has both 7 and 4 μm diameter fibers. Backscattered SEM images, not shown here, highlight the role of phenolic resin at the junction of fibers in AR-Toray. Regions of resin can be observed with diameters as large as 500 μm in AR-Toray samples but are not evident in the backscattered images of AR-MRC.

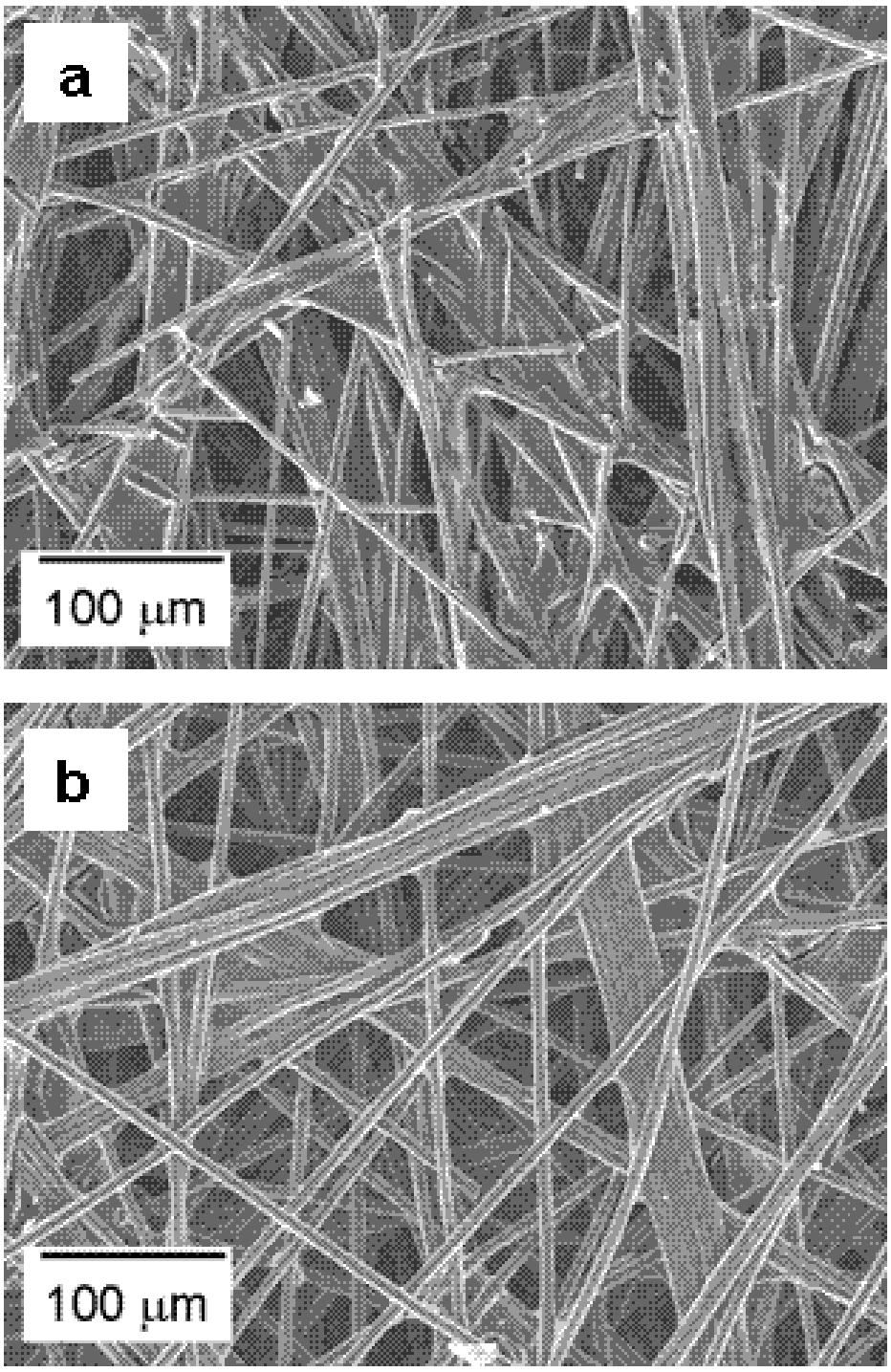

Figure 9.1. SEM of GDLs: a) AR-MRC b) AR-Toray

9.2.2 Mercury Intrusion Porosimetry

Mercury Intrusion Porosimetry (MIP) was performed on both samples by Micromeritics Instrument Corporation. A mercury-GDL contact angle of 130° was used for the analysis. Volumes attributed to pore diameters greater than half of the GDL sample width are considered experimental artifact and discarded. The technique of MIP has been used extensively in the soil science community where the pores are often formed by spherically shaped particles. In this environment, MIP with the Y-LE determines the characteristic cylindrical pore size. Narrow pore throats shield larger openings incorrectly attributing pore volume to smaller characteristic radii [21]. From Figure 9.1, the geometry of the GDLs is clearly different than the pore throat and openings observed in soil science. At the porosities of the GDLs used, ~75%, shielding is most likely less of a concern. Although uncertainties exist as a result of differences in pore openings, estimation of contact angles, large pressures, and mixed wettability, MIP provides a valuable source of comparison for the CPSRs reported within [15].

9.2.3 Saturation Measurements

In order to measure the CPSR, we employ the use of water transport plate (WTP) technology. A WTP is a finely porous hydrophilic carbon plate. The WTP technology, as practiced by UTC Power, is discussed by Yi *et al*. and evaluated with a numerical model by Weber and Darling [22, 23]. For our experimental purposes, we place a 3.8 cm x 5 cm GDL between two of the WTPs. The experimental apparatus is illustrated in Figure 9.2. In the bottom WTP, water flows through the internal coolant channels below atmospheric pressure; hence the WTP is maintained at positive capillary pressures. This water may

flow to and from the GDL through the porous WTP if the capillary pressure in the GDL is different than capillary pressure in the WTP and should equalize the capillary pressures at long times. Since the WTP has a small pore radius and contact angle, the WTP remains completely saturated, to a good approximation, over a large range of capillary pressures. This plate also has channels adjacent to the GDL that are open to ambient air ensuring a constant gas pressure of 101.3 kPa. A separate WTP without channels is placed on top of the GDL to prevent evaporation and provide a small force to ensure contact between the GDL and the base WTP. Although the role of compression on CPSRs has been shown, we neglect the effect during this discussion [11]. The top WTP results in a pressure of 70 Pa on the GDL. The top WTP is first allowed to equilibrate with the capillary pressure of the base WTP before the GDL is placed in between. The liquid pressure is controlled by a valve and pump on the coolant flow line which circulates between the WTP and a small reservoir which is open to the atmosphere. Saturation levels in GDLs are measured at capillary pressures from 0 to 25 kPa. GDL samples are from the same respective supplier manufacturing run. Run to run variability is not expected to change the conclusions found in this work.

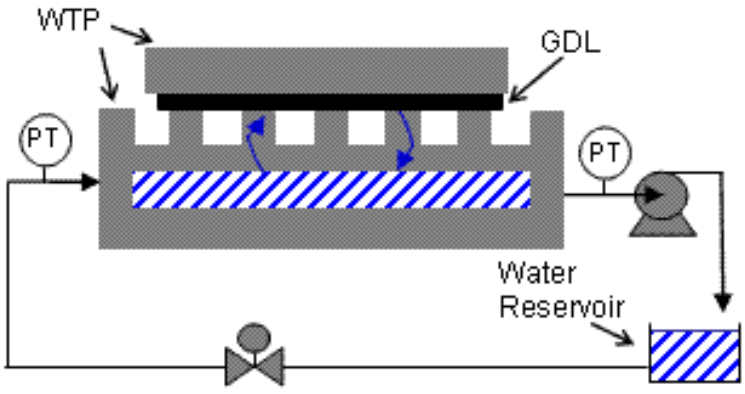

Figure 9.2. Experimental apparatus for measuring CPSRs. PT: pressure transducer.

The time constant for equilibration may be estimated using a time dependent material balance equation.

$$\varepsilon_o \frac{\partial \rho S_w}{\partial t} = -\nabla \cdot \rho v_0 \tag{9.3}$$

The wetting fluid may be considered incompressible and thus density of water, ρ, is considered constant. Darcy's law provides the volumetric flux of the wetting fluid.

$$v_0 = -K_w \frac{k}{\mu_w} \nabla P_w \tag{9.4}$$

The absolute permeability for Toray is 9 x 10^{-12} m^2 [24]. The relative permeability of the wetting phase is expressed as the following.

$$K_w = S_w^n \tag{9.5}$$

The value of n has been reported as a range of values, typically 3 to 9. Here, we conservatively chose n = 5. Substituting Equation 9.4 into 9.3 and assuming an isotropic permeability results in Equation 9.6.

$$\varepsilon_o \frac{\partial S_w}{\partial t} = K_w \frac{k}{\mu_w} \nabla^2 P_w \tag{9.6}$$

To reach the characteristic time constant, $t^* = t/\Theta$, we assume transport occurs only in the x dimension and scaling with the largest characteristic dimension, L, we have $X = x/L$. Here Θ is the dimensionless time and X is the dimensionless length. Furthermore, using the chain rule

$$\frac{\partial S_w}{\partial t} = \frac{\partial S_w}{\partial P_w}\frac{\partial P_w}{\partial t} \tag{9.7}$$

We arrive at the characteristic time

$$t^* = \frac{\varepsilon_o \mu_w L^2}{K_w k_w}\frac{\partial S_w}{\partial P_w} \tag{9.8}$$

The characteristic time, t^*, is shown in Equation 9.8 where all fluid properties are that of water. Here, ε_o is the bulk porosity of the GDL and μ is the viscosity of water. L is half the width of a gas channel in the WTP, the largest characteristic dimension. The product of the saturated permeability, k, and the relative permeability K_w, is equivalent to the permeability at the saturation of interest. The slope of the CPSR, $\partial S_w/\partial P_w$, was first approximated and later compared with the measured results.

The largest characteristic time over the CPSR is on the order of seconds. To ensure equilibrium, we wait at least ten minutes before removing the sample. After, the samples are removed from the WTP and sealed in a polyethylene bag to avoid evaporation. The bag is then weighed on an analytical balance. This procedure is repeated

at the next capillary pressure. The minimum change in capillary pressure between data points is 1.5 kPa to prevent significant effects as a result of internal GDL water movement after removal from the WTP. Multiple boundary drainage and imbibition curves are measured to present a continuous and complete set of data. At conditions near fully saturated, a small amount of water is left in the bag during the weighing and transfer processes. This mass was never found to be greater than 6 mg or 0.5 % of the total water mass in the GDL.

Each point at a presented capillary pressure is the average of three GDLs at three slightly different pressures with a total separation of 0.6 kPa. The liquid pressure drops along the WTP due to the pressure drop in the interior flow channels. The inlet and exit pressures are monitored. The pressure for each GDL sample is found by assuming laminar flow which is reasonable at the low flow rates used, 50 to 80 cm^3/min. The largest difference in measured saturation between the samples occurs at the steepest point in the CPSR and after a vacuum fill.

To determine the saturation, we must first determine the pore volume. This is accomplished by utilizing a liquid with a low surface tension, isopropyl alcohol (IPA) or octane, which is wicked into the pores of the GDL. Due to the low surface tension, it is reasonable to assume complete saturation. By measuring the increase in weight or mass of fluid in the pores, m_f, and using the known fluid density, ρ_f, the pore volume is simply

$$V_p = \frac{m_f}{\rho_f} \tag{9.9}$$

The skeletal density of the GDL, ρ_{sk}, which is related to the porosity,[2] may be determined from Equation 9.10, the dry sample mass, m_s, and the geometric sample volume, V_s,

$$\rho_{sk} = \frac{m_s}{V_s - V_p} \tag{9.10}$$

The skeletal densities of Toray and MRC were found to 1.91 and 1.67 g/cm^3 respectively. These values correspond to a bulk porosity of 73 % for Toray and 81 % for MRC.

9.2.4 Vacuum Fill

To achieve a saturated GDL, $S_w > 0.9$, the pores of the GDL were vacuum filled with water. The GDL is submerged in de-ionized water and weighted to prevent the sample from floating. Then the vessel is sealed in a chamber which is repeatedly brought under vacuum. The expansion of gas in the low pressure environment causes bubbles to exit the GDL and rise out of the liquid bath. When the system pressure is returned to atmospheric, water fills the pores that once held the gas that has since escaped. Since the GDL is submerged, there is no pathway for gas to re-enter the pores. After multiple repetitions, a high saturation level is achieved which compares closely with that achieved with IPA. The vibrations from the connected vacuum pump most likely assisted with the removal of gases while the sample was submerged.

9.3. RESULTS

The drainage and imbibition curve for AR-Toray are presented in Figure 9.3. The drainage curve from a vacuum filled sample undergoes the steepest drop in saturation near a capillary pressure of 5 kPa. For capillary pressures greater than 9 kPa only a slow decline of saturation occurs. This behavior is a result of the majority of pore volume in Toray being distributed near a single pore radius. The remaining saturation at capillary pressures greater than 20 kPa corresponds to small hydrophilic pores and trapped water that will be removed upon further cycling. The residuals of the drainage curve fit, measured – fitted, are shown in the inset of Figure 9.3. These values are taken from the individually measured samples to determine the goodness of fit. The scatter is reasonably even with some deviation at low capillary pressures. All of the residuals, ΔS_w, are ≤ 0.08 units of saturation. The majority of scatter is attributed to slightly different states of initial saturation. As we will discuss throughout this work, the wetting history of the sample determines the drainage or imbibition path it will follow.

The imbibition from a dry AR-Toray sample is delayed until capillary pressures approach zero. The imbibition for a vacuumed filled sample that was drained to 20 kPa exhibits a similar shape to the dry sample. An increase in saturation only occurs at capillary pressures near zero. The saturation at zero capillary pressure for the initially dry sample is half of the value for the sample that was vacuum filled and subsequently drained. This hysteresis as well as the difference in imbibition and drainage curves is commonly found in porous media. The cause of hysteresis has been attributed to a

number of mechanisms. On rough or heterogeneous media like the GDLs used here, the contact angle is larger for an advancing fluid when compared to a receding fluid [5, 25, 26]. In situations such as this one, where the receding contact angle appears to be less than 90° and the advancing angle is greater than 90°, the decision to arbitrarily define one phase as the wetting phase is justified. Geometrical factors such as pore shape also result in preferential filling or drainage resulting in a different capillary pressure for the same saturation [5].

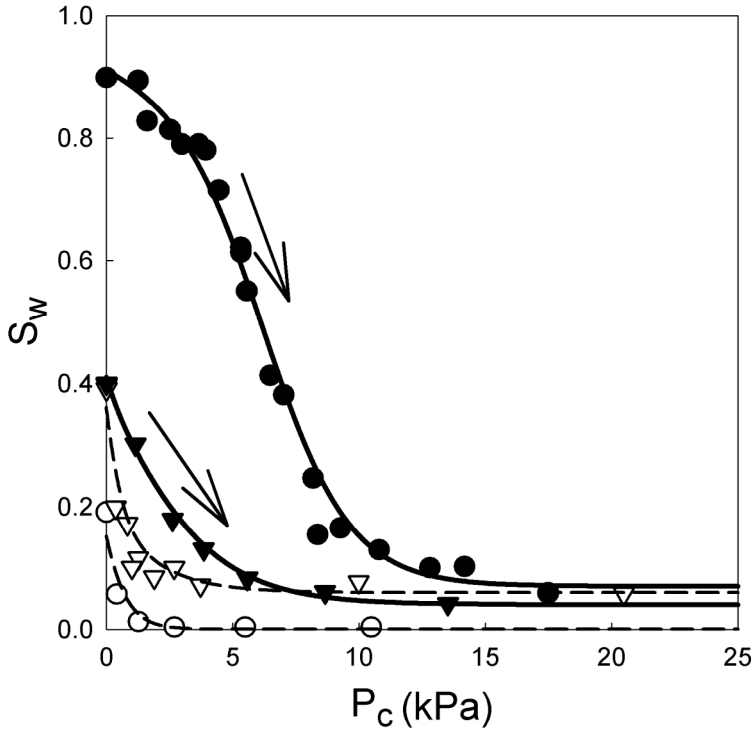

Figure 9.3. Drainage and imbibition curves for AR-Toray. Solid circles are experimentally measured drainage saturations initiated after a vacuum fill. Open circles are measured imbibition saturations starting from a dry sample. Open triangles is imbibition starting from a sample that was initially vacuum filled and drained to 20 kPa. The solid triangle curve is the drainage from the open triangle imbibition. Inset figure presents the residuals of individually measured S_w from that predicted by the fit for the drainage after a vacuum fill.

This behavior of water in the GDL pores is further investigated by draining the sample from various levels of saturation. After filling the sample to 0 kPa, a draining scanning curve is traced by raising the capillary pressure. This draining curve crosses over the imbibition curve the sample had previously traced, resulting in a lower saturation at the same capillary pressure. AR-Toray appear to have only a small irreducible wetting saturation, $S_w^0 = 0.01$.

The role of hysteresis may be studied more completely in this apparatus with a sample that has a greater hydrophilic nature. The CPSR for a WT-Toray sample is presented in Figure 9.4. The drainage curve is almost identical to that of the AR-Toray. However, the residuals for the WT-Toray displayed in the inset of Figure 9.4 are less on average and more evenly distributed when compared to AR-Toray. The wet-treatment process may provide for a consistent and more uniform surface chemistry than what is found in as-received samples. All residuals for the WT-Toray are ≤ 0.05 units of saturation. The lower run to run variability of the WT-Toray will also enable a more precise analysis of hysteresis in GDLs. During imbibition from a dry sample, the saturation reaches 0.85 at 0 kPa, which is four times higher than the AR-Toray. The wet-treating process significantly decreases the contact angle between water and the GDL. This decrease in contact angle allows a greater fraction of the pores to be filled at a higher capillary pressure. The wetting treatment also significantly reduces the differences between the imbibition and drainage curves. Since the drainage curve is not shifted from the AR-Toray sample, we may conclude the advancing contact angle undergoes a greater

change than the receding angle. The nature of the advancing contact angle changes from being larger than 90° and hydrophobic to less than 90° and hydrophilic. However, the existence of some hysteresis is still evident.

Several drainage curves from different saturations are displayed in Figure 9.4. As the saturation decreases, the drainage curve asymptotically approaches the main drainage curve or boundary curve. The drainage curves starting from saturations other than fully wetted are commonly referred to as drying scanning curves. The imbibition from a saturation other than the irreducible wetting saturation are termed wetting scanning curves [5]. Clearly, the wetting and dewetting history of the sample is of great importance.

The CPSR for AR-MRC is not significantly dissimilar from AR-Toray over the range of capillary pressures measured, Figure 9.5. The shape of the drainage shows a different slope suggesting a moderately different pore distribution. However, the WT-MRC drainage curve is significantly different when compared to the other drainage curves. At high capillary pressures, the saturation level is twice the value of the AR-MRC. By wet-treating the GDL, we have observed behavior about the pore structure of the hydrophobic components which would be inaccessible without large negative capillary pressures. These results suggest that the moderate saturation at high capillary pressures is a result of small pores which are normally of a hydrophobic nature.

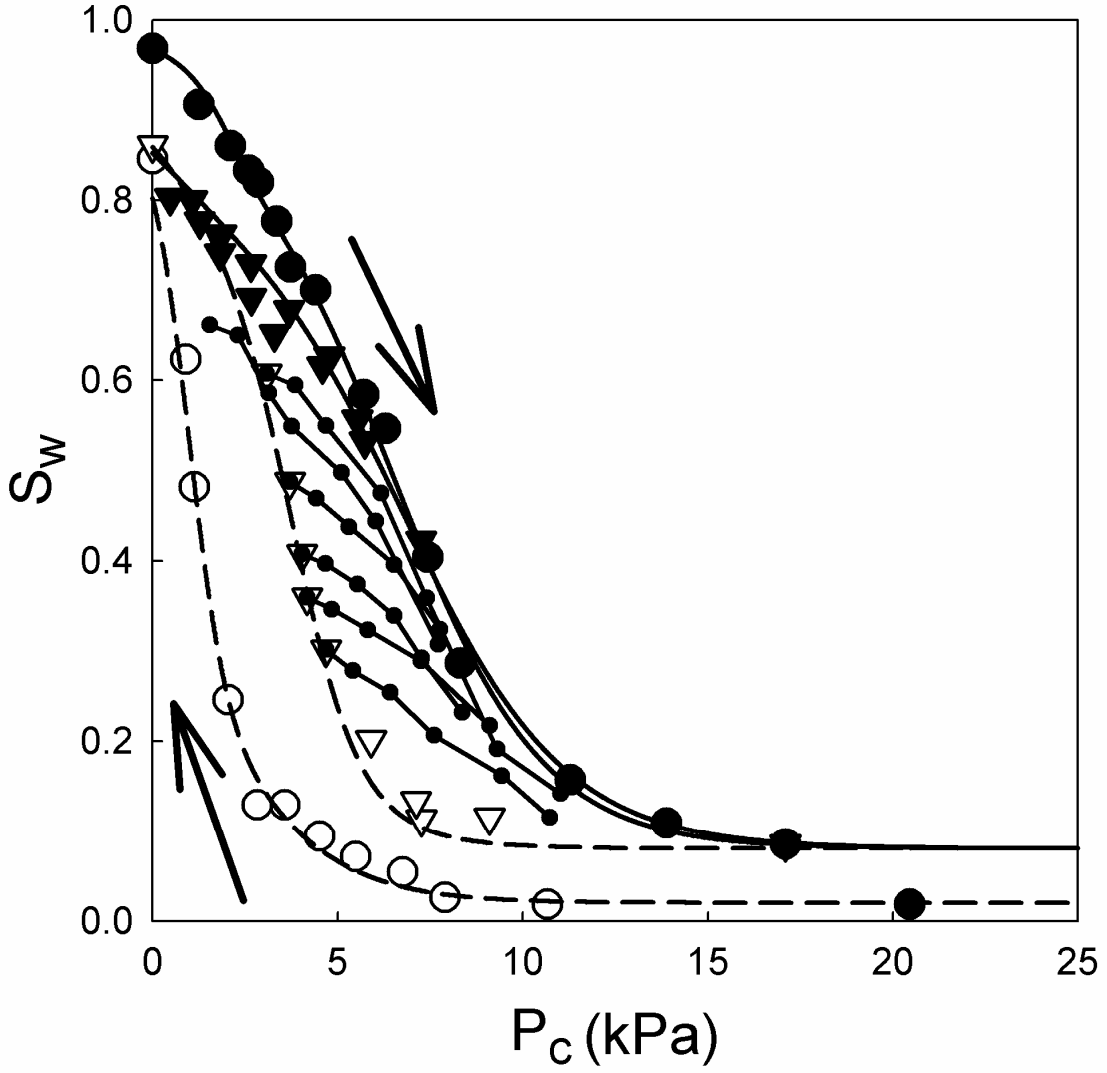

Figure 9.4. Drainage and imbibition curves for WT-Toray. Solid circles are experimentally measured drainage saturations. Open circles are measured saturations for imbibition from a dry GDL. Open triangles are measured saturations for imbibition from a vacuum filled and subsequently drained GDL. Inset figure presents the residuals of individually measured S_w from that predicted by the fit for the drainage after a vacuum fill.

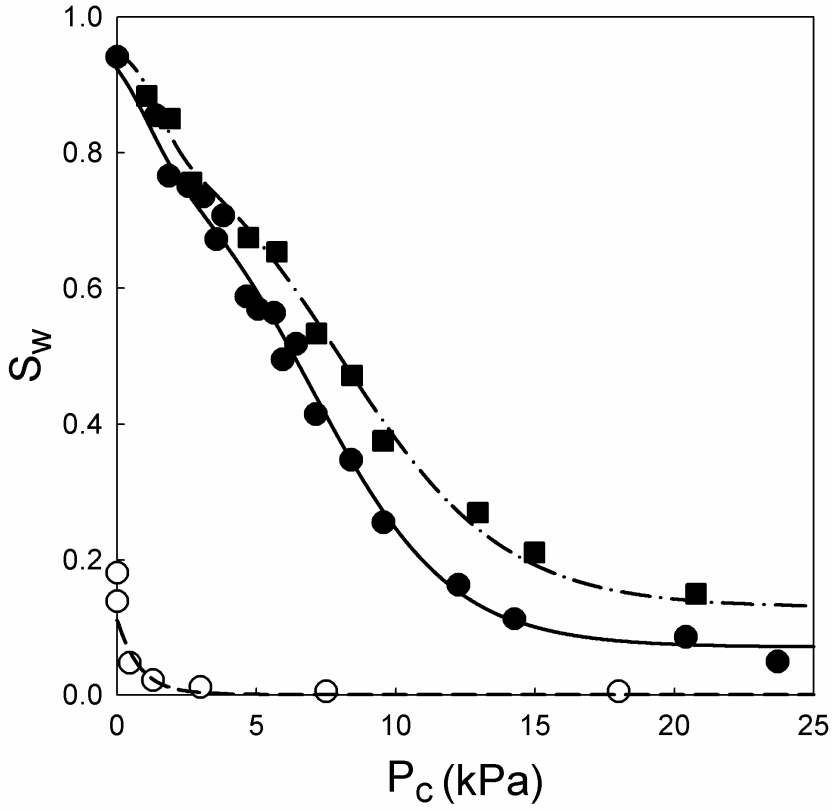

Figure 9.5. Drainage and imbibition curves for MRC. AR-MRC: Solid circles are experimentally measured drainage saturations, open circles are measured imbibition saturations. WT-MRC Drainage curve is solid squares.

9.4. DISCUSSION

9.4.1 Distribution of Pore Sizes and Surface Energy

We can make some determinations about the pore distribution as a function of capillary pressure by analyzing the CPSR for the as-received as compared to the wet-treated samples. The pore radii may be approximately determined by using a liquid with a known contact angle such as mercury or wetting solvents such as octane. This approach requires the use of the Y-LE and the assumption the pores are adequately modeled by

capillaries. From Figure 9.1, the pores do not appear to be cylindrical; therefore, we acknowledge an unquantifiable error is introduced into the discussion. The pore distribution as determined by MIP is displayed in Figure 9.6. Toray appears to have symmetric distribution of pores with an average characteristic radius of 15 μm, which is within the range of reported values of 9 to 20 μm [2, 15]. MRC appears to have a broader micron pore distribution of similar radius to Toray. However, MRC also has a distribution of smaller pores. Since the WT-MRC sample had a greater saturation at higher capillary pressures than the AR-MRC sample, we suggest the smaller pore radii displayed in MIP are of hydrophobic nature in the AR-MRC.

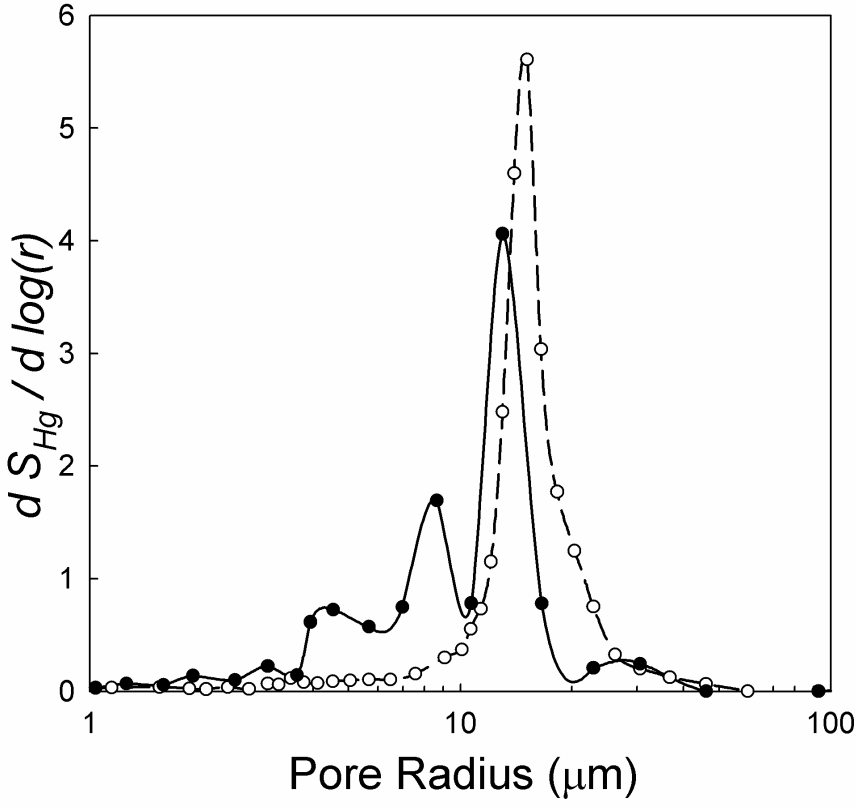

Figure 9.6. Characteristic pore radius as determined by MIP.

In the discussion of porous media, it is common to assign a distribution of pores as hydrophobic, $\theta > 90$, or as hydrophilic, $\theta < 90$. This simplification allows for a physical model with the following conclusions. Small hydrophilic pores fill at high positive capillary pressures with larger hydrophilic pores also filling at low positive capillary pressures. For hydrophobic contact angles, large pores fill at small negative capillary pressures followed by small pores being filled at large negative capillary pressures. Thus at high negative capillary pressures, all pores will be filled. In this model, a capillary pressure of zero equates to all of the hydrophilic pores being filled and all of the hydrophobic pores being drained. However, we have shown the majority of the pore volume in the AR-GDLs behaves as a hydrophobic pore during imbibition and as a hydrophilic pore during drainage. Thus, broad classifications of pores and their surface energies should only be made under well defined circumstances.

9.4.2 Empirical CPSR Fit

To assist with the use of the experimentally measured CPSRs, we have fit the data with the use of a hyperbolic tangent function. No physical meaning is strictly ascribed to the variables except for the capillary pressure, P_c, and wetting saturation, S_w. The following equations are used as an empirical representation of the CSPRs we have measured

$$S_{-} = \frac{1}{2}\left[1 + \tanh\left(-A_{-}\left[P_c + B_{-}\right]\right)\right] \tag{9.11}$$

$$S_{+} = \frac{1}{2}\left[1 + \tanh\left(-A_{+}\left[P_c + B_{+}\right]\right)\right] \tag{9.12}$$

$$S_w = S_{+}^{0} + \left(1 - S_{+}^{0} - S_{-}^{0}\right)\left[f_{+}S_{+} + \left(1 - f_{+}\right)S_{-}\right] \tag{9.13}$$

All saturations at negative capillary pressures are our predictions based upon the measured CPSRs from the wet-treated samples and MIP. Nonetheless, the Toray predictions compare favorably with those reported by Faiweather *et al*. who used a technique that enabled measurements of saturation at negative capillary pressures [16]. The researchers found that the imbibition and drainage curves for AR-Toray are of nearly identical shape, but offset from each other. Table 9.1 summarizes the parameter values for MRC and Toray. A comparison for the full drainage and imbibition curves for AR-Toray and AR-MRC is shown in Figure 9.7.

Table 9.1. Parameters for curve fits to CPSRs; AR: as-received; WT: wet-treated; D: drainage; I: imbibition; VF: vacuum fill

GDL	Curve	Initial Condition	A_{-}	B_{-}	A_{+}	B_{+}	S_{+}^{0}	S_{-}^{0}	f_{+}
AR-Toray	D	VF	0.3	–1.5	0.29	–6.2	0.07	0.0	0.9
	I	VF, D to 20 kPa	0.31	0.5	1.1	0.38	0.06	0.05	0.7
	I	Dry	0.6	–3.0	0.8	0.8	0.0	0.05	0.7
WT-Toray	D	VF	1.0	–2.0	0.25	–6.5	0.08	0.0	0.9
	D	I to 0 kPa	0.4	0.05	0.23	–6.8	0.08	0.05	0.85
	I	Dry	1.0	–1.0	0.3	–2.0	0.02	0.05	0.35
	I	D 20 kPa	0.3	–2.0	0.6	–3.9	0.08	0.05	0.57
AR-MRC	D	VF	0.7	–1.0	0.2	–7.0	0.07	0.0	0.82
	I	Dry	0.2	9.0	0.7	1.3	0.0	0.05	0.8
WT-MRC	D	VF	1.0	–1.5	0.17	–8.0	0.13	0.0	0.85

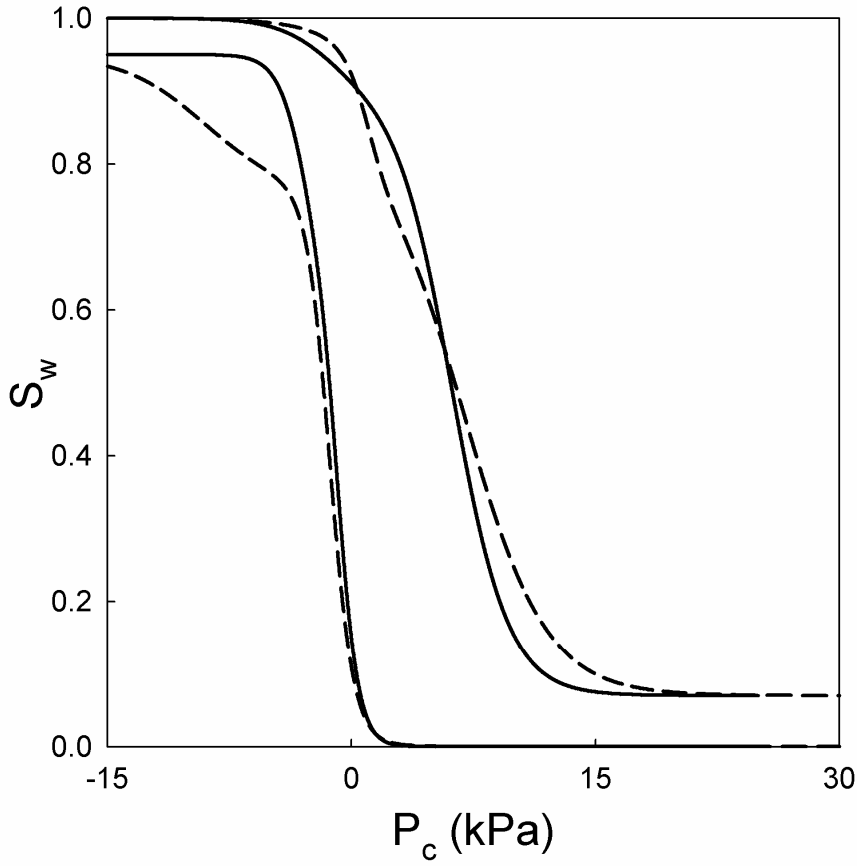

Figure 9.7. Comparison of CPSRs for AR-Toray (solid line) and AR-MRC (dashed line).

9.4.3 Contact Angle Hysteresis

Using the Y-LE and the measured CPSR, the contact angle for imbibition and drainage may be estimated for AR-Toray. The results are shown in Table 9.2 using a pore radius of 15 μm estimated from MIP porosimetry and a radius of 12 μm reported from capillary flow porometry [2], the capillary pressure at the steepest point in the CPSR and the surface tension of water, 0.072 N/m. The use of pore radii determined from two separate techniques demonstrates the order of uncertainty. The values for a graphite fiber and poly(tetrafluoroethylene) (PTFE) from Penn and Miller and the values for two polyacrylonitrile (PAN) based carbon fibers from Bismarck *et al*. as measured with the Wilhelmy balance principle are also displayed [27, 28]. Toray and the graphite fiber have

similar contact angles and hysteresis between advancing and receding. Some uncertainty exists in the use of the Y-LE and in the exact contact angle measurements for graphite fiber made by Penn and Miller [28]. Furthermore, differences in the surface chemistry of the fibers has a direct impact on the surface energy and resulting contact angles [27]. However, the majority of hysteresis observed in the CPSR may be reasonably attributed to this difference in advancing and receding contact angle.

Using the sessile drop method on the surface of Toray, researchers have reported an effective contact angle of 112 ° for water on Toray [15]. This effective contact angle is a value corrected for the roughness and porosity of the GDL [29]. The applicability of an external contact angle measurement is unclear when compared to the values in Table 9.2. The contact angle which controls the imbibition and draining process is more appropriately measured between two fibers. In this scenario, the angle of the fiber intersection and the advancing and receding nature of the contact angle are important [30]. However, this measurement is challenging at the length scales of GDL pores. The values obtained from a single fiber appear to be more significant than that of an external contact angle.

Table 9.2. Advancing (θ_a) and receding (θ_r) contact angles

Material	θ_a (°)	θ_r (°)	$\theta_a - \theta_r$ (°)	Source
Toray (15 μm)	98	51	47	This work
Toray (12 μm)	96	59	37	This work
PAN fiber	80	48	32	Ref [27]
PAN fiber	83	56	27	Ref [27]
Graphite fiber	94	45	49	Ref [28]
PTFE	112	92	21	Ref [28]

In order to maintain sufficient porosity for gaseous diffusion, GDLs are often wet-proofed with materials such as PTFE. This treatment increases the contact angle as a result of the low surface energy of the PTFE. The process of wet-proofing GDLs typically results in an anisotropic coating producing a bimodal pore network [9, 15]. One pore network resembles that of the as-received sample due to a minimal or nonexistent PTFE content. The other pore network may have a changed porosity and certainly lower surface energy from the PTFE coating [9]. The increase in advancing and receding contact angle should shift the CPSR to more negative capillary pressures. A close inspection of the wet-proofed results of Fairweather *et al*. reveals an offset in the CPSR where saturation moves from one pore network to the other during imbibition [16]. The hysteresis demonstrated in this paper is directly applicable to wet-proofed GDLs. Even on a smooth and well defined PTFE surface, contact angle hysteresis is still observed (see Table 9.2) [28]. The averaging of two CPSRs, one for the as-received network and another shifted slightly to more negative capillary pressures, will prove an adequate approximation of the dual pore network of wet-proofed GDLs.

9.4.4 Effect on Limiting Current

The effect of saturation and wetting history on the limiting current in a PEMFC may be considered. If we consider an isothermal situation where the limiting current is controlled by diffusion of oxygen through the GDL, the ratio of the flux of oxygen in the GDL with a specified saturation to flux of oxygen in a dry GDL is equivalent to the ratio of limiting currents under the same conditions. Assuming Fickian diffusion of dilute

oxygen or the diffusion of oxygen through a stagnant mixture, Equation 9.14 describes the molar flux.

$$N_{O_2} = -\frac{\varepsilon_o (1 - S_w) D_{O_2} P}{\tau R T} \nabla y_{O_2} \tag{9.14}$$

P and T are the system pressure and temperature. R is the ideal gas constant and D_{O2} is the diffusion coefficient of oxygen. The porosity, ε, is equivalent to the product of the bulk porosity, ε_o, and the nonwetting saturation, $(1–S_w)$. The tortuosity, τ, is that considered by Bruggeman to be equal to $\varepsilon^{-0.5}$. The use of Fickian diffusion and the Bruggeman correlation is an oversimplification of actual transport through the GDL. The goal of this empirical analysis is to present a basic demonstration of the effect of hysteresis on the limiting current as might be observed during the measurement of a polarization curve. The ratio of fluxes simplifies to

$$\frac{I_{\lim}^{S=S_w}}{I_{\lim}^{S=0}} = \frac{N_{O_2}^{S=S_w}}{N_{O_2}^{S=0}} = (1 - S_w)^{1.5} \tag{9.15}$$

The ratio of limiting currents is plotted in Figure 9.8 for both the drainage and imbibition curves for WT-Toray. A ratio of limiting currents near unity represents a low saturation level while a ratio near zero is indicative of a flooded GDL. Depending on whether the GDL is being filled or drained, the dependence of the limiting current with saturation and thus time will change.

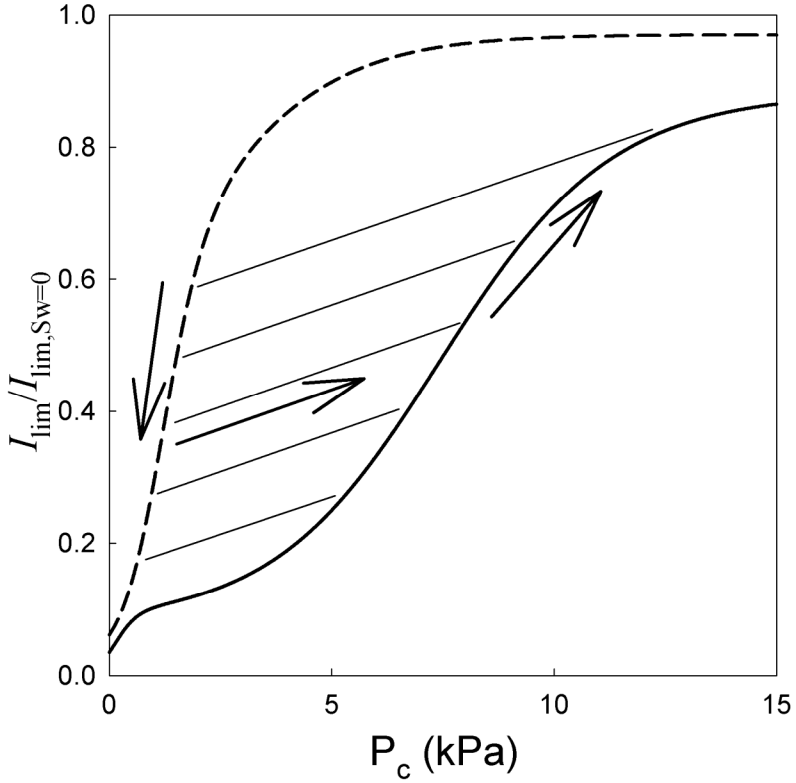

Figure 9.8. Change in WT-Toray dimensionless limiting current based upon history of wetting. Imbibition is the dotted line and drainage is the solid line. Arrows demonstrate the filling and subsequent draining path of hypothetical PEMFC operation.

9.4.5 Water Management

An alternative approach to water management in PEMFCs is to actively control the capillary pressure at the boundary of the WTP and the GDL. By holding the WTP at sufficiently high capillary pressures, the GDL saturation is maintained near the irreducible saturation. Furthermore, WTPs create a 100 % relative humidity environment while also controlling liquid water transport [22].

9.5. CONCLUSIONS

Measured hysteresis in CPSRs for PEMFC GDLs produced by Toray and Mitsubishi Rayon is presented. The hysteresis is primarily a result of the difference in the advancing and receding contact angle of water on the carbon fibers which compose the GDL. This hysteresis is shown to have a direct impact on the limiting current of PEMFCs.

If the wetting history of sample is accounted for, modeling the saturation level becomes substantially more difficult. To avoid an almost infinite set of boundary conditions, a closed form relation that predicts both static and dynamic capillary hysteresis such as that presented by Beliaev and Hassanizadeh may be necessary [31]. If PEMFC models continue to neglect the effect of wetting history, the order of error involved needs to be quantified. Future work involving CPSRs should focus on understanding phenomena which results in effects on the same order of the hysteresis presented within this work or on the presence of hysteresis itself.

REFERENCES

[1] Fuller TF, Newman J. Water and Thermal Management in Solid-Polymer-Electrolyte Fuel-Cells. Journal of the Electrochemical Society. 1993; **140**(5), 1218-25.

[2] Mathias M, Roth J, Fleming J, Lehnert W. Diffusion Media Materials and Characteristics. In: Vielstich W, Yokokawa H, Gasteiger HA, eds. *Handbook of Fuel Cells: Fuel Cell Technology and Applications, Volumes 3 & 4*. Chichester, UK: John Wiley & Sons, Ltd 2003.

[3] Wang CY. Fundamental models for fuel cell engineering. Chemical Reviews. 2004; **104**(10), 4727-65.

[4] Weber AZ, Newman J. Modeling transport in polymer-electrolyte fuel cells. Chemical Reviews. 2004; **104**(10), 4679-726.

[5] Bear J. Dynamics of Fluids in Porous Media. Mineola, NY: Dover Publication 1988.

[6] Li H, Tang Y, Wang Z, Shi Z, Wu S, Song D, et al. A review of water flooding issues in the proton exchange membrane fuel cell. Journal of Power Sources. 2008; **178**(1), 103-17.

[7] Weber AZ, Darling RM, Newman J. Modeling two-phase behavior in PEFCs. Journal of the Electrochemical Society. 2004; **151**(10), A1715-A27.

[8] Volfkovich YM, Bagotzky VS, Sosenkin VE, Blinov IA. The standard contact porosimetry. Colloids and Surfaces a-Physicochemical and Engineering Aspects. 2001; **187**, 349-65.

[9] Kumbur EC, Sharp KV, Mench MM. Validated leverett approach for multiphase flow in PEFC diffusion media. Journal of the Electrochemical Society. 2007; **154**(12), B1295-B304.

[10] Kumbur EC, Sharp KV, Mench MM. Validated leverett approach for multiphase flow in PEFC diffusion media - III. Temperature effect and unified approach. Journal of the Electrochemical Society. 2007; **154**(12), B1315-B24.

[11] Kumbur EC, Sharp KV, Mench MM. Validated leverett approach for multiphase flow in PEFC diffusion media - II. Journal of the Electrochemical Society. 2007; **154**(12), B1305-B14.

[12] Gostick JT, Ioannidis MA, Fowler MW, Pritzker MD. Pore network modeling of fibrous gas diffusion layers for polymer electrolyte membrane fuel cells. Journal of Power Sources. 2007; **173**(1), 277-90.

[13] Nam JH, Kaviany M. Effective diffusivity and water-saturation distribution in single- and two-layer PEMFC diffusion medium. International Journal of Heat and Mass Transfer. 2003; **46**(24), 4595-611.

[14] Sinha PK, Wang CY. Pore-network modeling of liquid water transport in gas diffusion layer of a polymer electrolyte fuel cell. Electrochimica Acta. 2007; **52**(28), 7936-45.

[15] Gostick JT, Fowler MW, Ioannidis MA, Pritzker MD, Volfkovich YM, Sakars A. Capillary pressure and hydrophilic porosity in gas diffusion layers for polymer electrolyte fuel cells. Journal of Power Sources. 2006; **156**(2), 375-87.

[16] Fairweather JD, Cheung P, St-Pierre J, Schwartz DT. A microfluidic approach for measuring capillary pressure in PEMFC gas diffusion layers. Electrochemistry Communications. 2007; **9**(9), 2340-5.

[17] Nguyen TV, Lin G, Ohn H, Wang X. Measurement of capillary pressure property of gas diffusion media used in proton exchange membrane fuel cells. Electrochem Solid State Lett. 2008; **11**(8), B127-B31.

[18] Bett JAS, Wheeler DJ, Bushnell C, inventors; 5,840,414. United States. 1998.

[19] Cipollini NE, inventor 6,258,476. United States. 2001.

[20] Frisk JW, Boand WM. 6,733,841. 2004.

[21] Ioannidis MA, Chatzis I. Network Modeling of Pore Structure and Transport-Properties of Porous-Media. Chemical Engineering Science. 1993; **48**(5), 951-72.

[22] Weber AZ, Darling RM. Understanding porous water-transport plates in polymer-electrolyte fuel cells. Journal of Power Sources. 2007; **168**(1), 191-9.

[23] Yi JS, Yang JDL, King C. Water management along the flow channels of PEM fuel cells. Aiche Journal. 2004; **50**(10), 2594-603.

[24] Gostick JT, Fowler MW, Pritzker MD, Ioannidis MA, Behra LM. In-plane and through-plane gas permeability of carbon fiber electrode backing layers. Journal of Power Sources. 2006; **162**(1), 228-38.

[25] Extrand CW, Kumagai Y. An experimental study of contact angle hysteresis. Journal of Colloid and Interface Science. 1997; **191**(2), 378-83.

[26] Good RJ. Journal of Adhesion Science and Technology. 1992; **6**, 1269.

[27] Bismarck A, Tahhan R, Springer J, Schulz A, Klapotke TM, Zell H. Influence of fluorination on the properties of carbon fibres. Journal of Fluorine Chemistry. 1997; **84**(2), 127-34.

[28] Penn LS, Miller B. A Study of the Primary Cause of Contact-Angle Hysteresis on Some Polymeric Solids. Journal of Colloid and Interface Science. 1980; **78**(1), 238-41.

[29] Cassie ABD, Baxter S. Wettability of porous surfaces. Transactions of the Faraday Society. 1944; **40**, 0546-50.

[30] Ma SX, Mason G, Morrow NR. Effect of contact angle on drainage and imbibition in regular polygonal tubes. Colloids and Surfaces a-Physicochemical and Engineering Aspects. 1996; **117**(3), 273-91.

[31] Beliaev AY, Hassanizadeh SM. A theoretical model of hysteresis and dynamic effects in the capillary relation for two-phase flow in porous media. Transport in Porous Media. 2001; **43**(3), 487-510.

PART 3

CHAPTER 10

RECOMMENDATIONS

This dissertation represents a significant advance in the fundamental understanding of multiple challenges facing low temperature fuel cells (LTFC). However, even more remains to be done within the same subsets addressed in this document. The recommendations presented within this chapter are restricted to those in the area of the electrochemical oxidation of carbon.

The mechanism of the electrochemical oxidation of carbon is complex and poorly understood. The work presented in Chapters 4-6 culminated in the development of a physical model. This model attempted to explain the electrochemical responses observed in our laboratory and reported in the literature. The proposed mechanism captures many aspects of oxidation, but is hindered by assumptions regarding the surface chemistry of the multiple oxidation reactions occurring on the carbon surface. Both fundamental science and engineering approaches are possible for future work and they should proceed concurrently. As understanding of the fundamental science behind the mechanism is improved, models attempting to represent this process may be refined.

The current from the formation of the passive oxide matched poorly with experimental results even though CO_2 formation was an excellent fit. More work on the stoichiometry and formation of this oxide is the opportunity for greatest advancement in the kinetic model. Temperature programmed desorption (TPD) studies appear to be the

most robust technique for the analysis of carbon surface chemistry. The analyses suggested here should be conducted at short oxidation times and possibly low temperatures (20 – 40 °C) as the CO_2 formation has been shown to simultaneously produce surface oxides in Chapter 5. Short oxidation times should limit the C*O oxide growth while highlighting the passive oxide and catalytic oxide. The comparison of oxide concentrations between this short oxidation time and the initial concentration should reveal some important features of the chemistry and stoichiometry. The sample must not be reduced before TPD is performed and oxygen chemisorption from the atmosphere must be controlled or accounted for in the oxygen balance. These experiments would be complimented by a symmetrical set where the samples are electrochemically reduced after oxidation. This comparison should confirm what portion of the oxide is completely removed after reduction. The mechanism of current decay in cyclic operation must also be elucidated. Our kinetic mechanism advocates that a reduction reaction affects the concentration of the catalytic oxide. Verification and refinement of this mechanism requires further studies of the carbon surface chemistry.

A deeper understanding is required of the chemical and electrochemical interactions of carbon with platinum and, to a lesser extent, carbon with molecular oxygen. Platinum catalysts have been shown to produce CO_2 during potential cycling as discussed in Chapter 2. Carbon oxidation from potential cycling in normal operating conditions may result solely from the interaction of platinum with carbon. The numerical model presented in Chapter 6 may be coupled with a platinum oxidation model and an interactive reaction proposed. A common hypothesis in the literature is that platinum

oxidizes a carbon surface oxide to CO_2. Coupling the carbon and platinum models will allow researches to select the appropriate oxide interaction mechanism with platinum or one of platinum's oxides.

The stability of carbon will always be challenged by the environment of acidic LTFCs as demonstrated by the Pourbaix diagram in Chapter 2. Systems mitigation strategies coupled with high temperature heat treatment may be successful in reducing performance losses due to carbon oxidation. In addition, two other approaches are possible. First, new materials such as metal oxides may replace carbon as the catalyst support. Conductivity, solubility, ion contamination, and wetting characteristics make this approach unlikely to succeed. Second, the role of carbon in the electrode may be redefined. In this approach, carbon is no longer a catalyst support in the traditional sense. A nanostructured catalyst such as a platinum nanotube or whisker could be embedded within a porous carbon electrode [1-4]. The carbon serves as the porous electrode and electron conductor [4]. However, the need to support nanoparticles no longer exists, allowing the possibility of using a more graphitic structure with larger resistance oxidation. Moreover, any catalytic effect platinum may have on the oxidation process is minimized by the lower degree of contact. This second approach would also be conducive to the non-carbon supports discussed in Chapter 2. Whether durability goals are achieved through these approaches or others, carbon will likely be a primary component of future generations of LTFCs and other electrochemical systems.

REFERENCES

[1] Chen ZW, Waje M, Li WZ, Yan YS. Supportless Pt and PtPd nanotubes as electrocatalysts for oxygen-reduction reactions. Angewandte Chemie-International Edition. 2007; **46**(22), 4060-3.

[2] Debe M. Novel catalysts, catalysts supports, and catalyst coated membrane methods. In: Vielstich W, Yokokawa H, Gasteiger HA, eds. *Handbook of Fuel Cells: Fuel Cell Technology and Applications, Volumes 3 & 4*. Chichester, UK: John Wiley & Sons, Ltd 2003.

[3] Tang JM, Jensen K, Waje M, Li W, Larsen P, Pauley K, et al. High performance hydrogen fuel cells with ultralow Pt loading carbon nanotube thin film catalysts. Journal of Physical Chemistry C. 2007; **111**(48), 17901-4.

[4] Pivovar BS. Low loadings of platinum in PEM Fuel Cell Electrodes. Golden, CO 2009.

APPENDIX

FORTRAN CODE FOR KINETIC MODEL OF ELECTROCHEMICAL OXIDATION OF GRAPHITIC CARBONS

1. INTRODUCTION

The following section contains an example input file and exact code used to simulate the proposed kinetic model presented in Chapter 6. Absoft Pro Fortran for Windows v9.0 was used to compile and execute the code. The simulation results are stored in a text file titled “output.txt” after execution of the program.

2. EXAMPLE INPUT FILE

```
900      ! Zweiten modeling approach
901      ! Good except for not steep short times
60.0     ! tc, Cell temperature, C
1.0      ! proton concentration
0.3      ! eps, Electrode porosity
6.0e-6   ! .6 mg/cm2 Carbon
100.0    ! BET m2/g Carbon
1.0e-4   ! mol * sites/m2 Irrev oxide formation
4.5d-6   ! mol # sites/m2 where the action is 4.5d-6
1.0      ! water activity
902      ! Kinetic variables
7.8e-18  ! rk(1), Rate constant for CcOH mol/(s cm2-C)
5.1e-19  ! rk(2), Rate constant for CO2 mol/(s cm2-C)
8.8e-15  ! rk(5), Rate constant for CpO mol/(s cm2-C)
1.4e-19  ! rk(6), Rate constant for CsO mol/(s cm2-C)
6.0e-11  ! rk(8), Rate constant for CHQ mol/(s cm2-C)
10000.0  ! Ea1 (J/mol K) Activation energy for CcOH
110000.0 ! Ea2 (J/mol K) Activation energy for CO2
```

```
50000.0  ! Ea5 (J/mol K) Activation energy for CpO
10000.0  ! Ea6 (J/mol K) Activation energy for CsO
20000.0  ! Ea8 (J/mol K) Activation energy for CHQ
0.35     ! alfa for CcOH
0.65     ! alfa for CO2
0.48     ! alfa for CpO
0.65     ! alfc for CpO
0.50     ! alfa for CsO
1.00     ! alfc for CsO
0.50     ! alfa for CHQ
0.50     ! alfc for CHQ
1.00     ! stoich for CcOH consumption
3.00     ! stoich for CpO formation
3.000    ! g1, Frumkin parameter
3.000    ! g5, Frumkin parameter
1.000    ! U1, CcOH Standard Potential
0.950    ! U5, CpO Standard Potential
2.5      ! cap, Double-layer capacitance, F/g
0.000    ! init Coverage CcOH
5000.d0          ! keq1
1.0e5    ! keq2
0.25d0   ! Cq stoich
```

3. FORTRAN CODE

```
      program eqnsolve
          implicit real*8 (a-h,o-z)

c***** ACKNOWLEDGEMENT ********************************
c***** This code is based on a numerical model programmed by ******
c***** Rob Darling, UTC Power, South Windsor, CT ***************


c         print *,"Square waves, 300 s"
c         call square(50,30.d0,30.d0)

c         print *,"Triangular waves"
c         call triang(800.d0)

c         print *,"Oxidation Reduction"
c         call oxred(19300.d0)
```

```
c       print *,"Short Oxidation Reduction"
c       call shortoxred(129601.0d0)

        print *,"Potentiostatic Hold"
        call hold(60000.d0)

        print *,"a la fin"
        end


c*************************************************************************
c******* PHYSICAL MODEL  ******************************************
c*************************************************************************



c*************************************************
c********  CYCLIC VOLTAMMETRY  *****************
c*************************************************

      subroutine triang(tplace)
        implicit real*8 (a-h,o-z)
        common /var/ w(20),wp(20)
        common /pot/ volt,charge,curdens
        common /tstep/ time1,ht,runtime,sweep,tpfreq
        common /fitpar/ fit_param(20)
        common /param/ a1,a2,a3,a4,a5,a6
        dimension eq(20)

c***** Store fitting parameters
c       a1 = fit_param(1)
c       a2 = fit_param(2)
c       a3 = fit_param(3)
c       a4 = gparam
        rt = tplace

c***** Initialize the equations
        call eqn(1,n,eq,1,0.d0)

        runtime=rt
         ht=1.0d-2
         phold = 0.d0
         time1=0.d0
        cvsweep=1d-2 ! 10 mV/s
        sweep=cvsweep
        vmin=0.04d0
```

```
      vmax=1.2d0
      tpfreq=runtime/2000.d0
      volt=vmin
      voltlim=vmax

      k=0
 10   k=k+1

      call algebra(n,iter,iflag)
       if(iflag .eq. 1) stop

c***** Output results
      if(time1 .ge. tprint) then
      call eqn(2,n,eq,1,0.d0)
      call eqn(3,n,eq,1,0.d0)
      tprint=tprint + tpfreq
      endif

      do i=1,n
        wp(i)=w(i)
      enddo

      time1=time1+ht
       volt=volt + sweep*ht

    if(time1.lt.runtime) then
      if((voltlim.eq.vmax).and.(volt.lt.vmax)) goto 10
      if((voltlim.eq.vmin).and.(volt.gt.vmin)) goto 10
         if(voltlim .eq. vmax) then
           voltlim=vmin
           vmax=vmax+0.1d0
           sweep=-cvsweep
         else
           voltlim=vmax
           sweep=cvsweep
           ncycle=ncycle+1
         end if



         goto 10
      else
         return
      endif
      return
      end
```

```
c*************************************************
c********  Oxidation Reduction  ***********************
c*************************************************
c*** minimal ouput compared to oxred
      subroutine shortoxred(tplace)
            implicit real*8 (a-h,o-z)
            common /var/ w(20),wp(20)
            common /pot/ volt,charge,curdens
            common /tstep/ time1,ht,runtime,sweep,tpfreq
            common /fitpar/ fit_param(20)
            common /param/ a1,a2,a3,a4,a5,a6
            dimension eq(20)

c***** Store fitting parameters
c           a1 = fit_param(1)
c           a2 = fit_param(2)
c           a3 = fit_param(3)
c           a4 = gparam
            rt = tplace
            ptime= 0.d0

c***** Initialize the equations
             call eqn(1,n,eq,1,0.d0)

            runtime=rt
            htinitial=1.0d-2
            ht=htinitial
            phold = 30.d0
            time1=0.d0
            cvsweep=5d-1
            sweep = cvsweep ! 100 mV/s
            vmin=0.70
            vmax=1.3d0

            tpfreq=100.0
            tprint=tpfreq
            volt=vmin
            voltlim=vmax

            k=0
 10         k=k+1

            call algebra(n,iter,iflag)
             if(iflag .eq. 1) stop
```

```
c***** Output results
          if(time1 .ge. tprint) then
         call eqn(2,n,eq,1,0.d0)
         call eqn(3,n,eq,1,0.d0)
         tprint=tprint + tpfreq
         endif

         do i=1,n
           wp(i)=w(i)
         enddo

         time1=time1+ht
         volt=volt + sweep*ht

         if(time1.lt.runtime) then
           if((voltlim.eq.vmax).and.(volt.lt.vmax)) goto 10
           if((voltlim.eq.vmin).and.(volt.gt.vmin)) goto 10

           if(voltlim .eq. vmax) then
                 if(ptime.lt.phold) then
                 sweep = 0.d0
                 if (ptime.gt.5.d0) ht = 1.0d-2
                 if (ptime.gt.100.d0) ht = 1.0d0
                 if (ptime.gt.600.d0) ht = 10.0d0
           ptime = ptime + ht
           goto 10
           elseif(ptime.gt.phold) then
           ptime= 0.d0
           ht = htinitial
           voltlim=vmin
           vmax=vmax !+ 0.1d0
           sweep=-cvsweep
           end if
         else
            if(ptime.lt.phold) then
           sweep = 0.d0
              if (ptime.gt.5.d0) ht = 1.0d-2
              if (ptime.gt.100.d0) ht = 1.0d0
              if (ptime.gt.600.d0) ht = 10.0d0
           ptime = ptime + ht
           goto 10
           elseif(ptime.gt.phold) then
           ptime= 0.d0
           ht = htinitial
           voltlim=vmax
           vmax=vmax !+ 0.1d0
```

```
            sweep=cvsweep
          end if
          end if

          goto 10
          else
          return
          endif
          return
          end

        subroutine oxred(tplace)
          implicit real*8 (a-h,o-z)
          common /var/ w(20),wp(20)
          common /pot/ volt,charge,curdens
          common /tstep/ time1,ht,runtime,sweep,tpfreq
          common /fitpar/ fit_param(20)
          common /param/ a1,a2,a3,a4,a5,a6
          dimension eq(20)

c***** Store fitting parameters
c       a1 = fit_param(1)
c       a2 = fit_param(2)
c       a3 = fit_param(3)
c       a4 = gparam
        rt = tplace
        ptime= 0.d0

c***** Initialize the equations
       call eqn(1,n,eq,1,0.d0)

          runtime=rt
          htinitial=1.0d-2
          ht=htinitial
          phold = 3600.d0
          time1=0.d0
          cvsweep=1d-2
          sweep = cvsweep ! 10 mV/s
          vmin=0.04d0
           vmax=1.3d0

          tpfreq=htinitial*50.d0
          tprint=tpfreq
          volt=vmin
          voltlim=vmax
```

```
      k=0
 10   k=k+1

      call algebra(n,iter,iflag)
      if(iflag .eq. 1) stop

c***** Output results
      if(time1 .ge. tprint) then
      call eqn(2,n,eq,1,0.d0)
      call eqn(3,n,eq,1,0.d0)
      tprint=tprint + tpfreq
      endif

      do i=1,n
        wp(i)=w(i)
      enddo

      time1=time1+ht
      volt=volt + sweep*ht

    if(time1.lt.runtime) then
      if((voltlim.eq.vmax).and.(volt.lt.vmax)) goto 10
      if((voltlim.eq.vmin).and.(volt.gt.vmin)) goto 10

        if(voltlim .eq. vmax) then
          if(ptime.lt.phold) then
       sweep = 0.d0
          if (ptime.gt.5.d0) ht = 1.0d-2
          if (ptime.gt.100.d0) ht = 1.0d0
          if (ptime.gt.600.d0) ht = 10.0d0
       ptime = ptime + ht
       tpfreq = ht
       if (ptime.gt.5.d0) tpfreq = ht*10.0d0
       goto 10
       elseif(ptime.gt.phold) then
       ptime= 0.d0
       ht = htinitial
       tpfreq=htinitial*50.d0
       voltlim=vmin
       vmax=vmax !+ 0.1d0
       sweep=-cvsweep
       end if
     else
          voltlim=vmax
          sweep=cvsweep
          tpfreq=htinitial*50.d0
```

```
          end if


           goto 10
          else
           return
          endif
          return
          end

c*************************************************
c******** POTENTIOSTATIC HOLD ******************
c*************************************************

      subroutine hold(tplace)
          implicit real*8 (a-h,o-z)
          common /var/ w(20),wp(20)
          common /pot/ volt,charge
          common /tstep/ time1,ht,runtime,sweep,tpfreq
          dimension eq(20)
c***** Initialize the equations
          call eqn(1,n,eq,1,0.d0)

          rt = tplace
          ht=10.0*1d-4
          time1=0.0
          tprint=0.0
          runtime= rt
          tpfreq=0.1d0+time1/runtime
          volt= 1.3
          sweep=0.0
c         print *,"runtime=",runtime
          k=0
10        k=k+1


          call algebra(n,iter,iflag)
          if(iflag .eq. 1) stop

c***** Output results
          if(time1 .ge. tprint) then

          call eqn(2,n,eq,1,0.d0)
          call eqn(3,n,eq,1,0.d0)
          tprint=tprint + tpfreq
c         print *,"okay"
```

```
        endif

        do i=1,n
          wp(i)=w(i)
        enddo

         time1=time1+ht
        volt=volt + sweep*ht

        if (time1.gt.5.d0) ht = 10.0*1.d-2
        if (time1.gt.100.d0) ht = 10.0*1.d-1
        if (time1.gt.1000.d0) ht = 10.0d0
        if (time1.gt.300.d0) tpfreq=300.d0
        if (time1.gt.6000.d0) tpfreq=3000.d0
        if (time1.le.runtime) then
           go to 10
        else
          return
        end if

        return
        end

c*****************************************************
c********  SQUARE WAVE CYCLING  ***********************
c*****************************************************

  subroutine square(nmax,ttop,tbot)
        implicit real*8 (a-h,o-z)
        common /var/ x(20),xp(20)
        common /pot/ volt,charge
        common /tstep/ time1,ht,runtime,sweep,tpfreq
        dimension eq(20)
c***** Initialize the equations
        call eqn(1,n,eq,1,0.d0)

        ht=1d-3
        time1=0.d0
        tprint=0.0
        tswitch=ttop
        runtime=2.0*nmax*tswitch
        tpfreq=1.d-1*runtime/dble(nmax)

        tswap=tswitch
        volt=0.d0
        vmin= 0.70
```

```
          vmax= 1.30
          volt=vmax

          k=0
 10       k=k+1

          if (time1.gt.tswap) then
             tswap=time1+tswitch
          if (volt.ge.vmax) then
              volt=vmin
                    tswitch=ttop
                   else if (volt.eq.vmin) then
                    volt=vmax
              tswitch=tbot
              ncycle=ncycle+1
          end if
          end if

        call algebra(n,iter,iflag)
        if(iflag .eq. 1) stop

c***** Output results
        if(time1 .ge. tprint) then
        call eqn(2,n,eq,1,0.d0)
        call eqn(3,n,eq,1,0.d0)
              tprint=tprint + tpfreq
              endif

          do i=1,n
            xp(i)=x(i)
          enddo

           time1=time1+ht

        if (time1.le.runtime) then
          go to 10
          else
            return
          end if

          return
          end

c*************************************************

      subroutine algebra(n,iter,iflag)
```

```
      implicit real*8 (a-h,o-z)
      common /mat/ b(20,20),d(20,41)
      common /var/ w(20),wp(20)
      dimension eq(20),dc(20)
      parameter (itmax= 1000,rtol=1d-6,atol=1d-10)

      iflag=0
      iter =0
100   iter=iter+1


c***** Get the d's
      call eqn(2,n,eq,1,0.d0)
      do i=1,n
      d(i,1)=eq(i)
      enddo

c***** Get the b's by numerical differentiation

      do k=1,n
      dc(k)=1d-6
      call eqn(2,n,eq,k,dc(k))
      do i=1,n
      b(i,k)=-(eq(i)-d(i,1))/dc(k)
      enddo
      enddo

c***** Solve the linear equations

      call matinv(n,1,determ)

c***** Check for convergence and update the variables

      kerrg=0
      do i=1,n
      if(kerrg .eq. 0) then
      if(dabs(d(i,1)) .gt. rtol*dabs(w(i))) kerrg=1
      if((kerrg.eq.1).and.(dabs(d(i,1)).lt.atol)) kerrg=0
      if(iter .eq. itmax) then
      write(*,*) i,d(i,1),w(i)
      end if
      end if

      wnew=w(i)+d(i,1)
      if(wnew .lt. 0.d0) then
      wnew=0.01*w(i)
```

```
          end if
          w(i)=wnew
          enddo

          if((iter.le.itmax).and.(kerrg.eq.1)) goto 100
          if(iter.gt.itmax) write(*,*) "Maximum iterations reached."
          if(iter.gt.itmax) then
           iflag=1
           else
          call eqn(2,n,eq,1,0.d0)
          call eqn(4,n,eq,1,0.d0)
          end if

          return
          end



      subroutine eqn(mode,n,eq,k,dw)
          implicit real*8 (a-h,o-z)
          common /mat/ b(20,20),d(20,41)
          common /var/ w(20),wp(20),wa(20)
          common /tstep/ time1,ht,runtime,sweep,tpfreq
          dimension eq(20),dwdt(20)
          common /fitpar/ fit_param(20)
          common /param/ a1,a2,a3,a4,a5,a6

c       Problem specific parameters
          parameter(fc=96487.d0,rgas=8.314d0)
          common /pot/ volt,charge,curdens
          dimension rk(10)
          dimension rate(3,3),ratec(3,3),ratep(3,3)
          dimension alfa(10),alfc(10)
c*********************************************************
       if(mode .eq. 1) then  !  Initial guesses
c*********************************************************

 101   format(25(1h ,e12.6))
 110   format(25(a8,3x))
          open(unit=1,file="output.txt",status="unknown")
          write(1,110) "Time","Pot","C_gr","VacX","VacY","CovCcOH",
     & "CovCsO","CovCsOH","CovCQ","CovCHQ","CovC2O3","cdCcOH","cdCsO",
     & "cdCpO","cdCO2","mcdCcor","cdCQ"

c***** Variable names
          n=10              !  Number of variables solved for
```

```
      iV=1            !  Voltage
      iC=2            !  Initial carbon moles mol/cm2
      iCx=3           ! Vacant Site #
      iCy=4           !  Vacant Site *
      iCcOH=5         !  Catalytic oxide
      iCsO=6          !  Simultaneous e- tx
      iCpO=7          !  Passive Oxide
      iCQ=8           !  Quinone
      iCHQ=9          !  Hydroquinone
      iCO3=10         !  Anhydride
      iCH=11          !  Proton concentration (Auxillary)


c***** Physical constants
      pi=4.d0*datan(1.d0)

c     Input parameters
      open(unit=2,file="input.txt",status="unknown")
      read(2,*) dummy
      read(2,*) dummy
      read(2,*) tc       !  Temperature, C
      read(2,*) concprot  !  Proton concentration
      read(2,*) eps      !  Ionomer volume fraction in electrode
      read(2,*) gC       !  Mass of carbon g
      read(2,*) BET      !  BET surface area of carbon m2/g
      read(2,*) cSiteA   !  mol * sites/m2 Irrev oxide formation
      read(2,*) cSiteB   !  mol # sites/m2 where the action is
      read(2,*) aW       !  Water activity

      siteratio = cSiteB/cSiteA !To avoid having a "stiff" set of equations

c*****  Rate constants
       read(2,*) dummy
       read(2,*) rk(1)
       read(2,*) rk(2)
       read(2,*) rk(5)
       read(2,*) rk(6)
       read(2,*) rk(8)
       read(2,*) Ea1
       read(2,*) Ea2
       read(2,*) Ea5
       read(2,*) Ea6
       read(2,*) Ea8
       read(2,*) alfa(1)
       read(2,*) alfa(2)
       read(2,*) alfa(5)
```

```
          read(2,*) alfc(5)
          read(2,*) alfa(6)
          read(2,*) alfc(6)
          read(2,*) alfa(8)
          read(2,*) alfc(8)
          read(2,*) sCovY
          read(2,*) sCovX
          read(2,*) g1
          read(2,*) g5
          read(2,*) U1
          read(2,*) U5
          read(2,*) cap
          read(2,*) covinit
          read(2,*) rkeq1
          read(2,*) rkeq2
          read(2,*) sCQ


c***** Initial conditions
        wmC = 12.01d0
        Cinit = gC/wmC
        w(iC)= Cinit            ! Moles carbon
        w(iCcOH)= 0.0d0         ! Initial CcOH coverage
        w(iCsO) = 0.0d0         !  Initial CsO coverge
        w(iCpO)=  0.1d0         ! Initial CpO coverage
        w(iCQ) =  0.0d0         ! Initial CQ coverage
        w(iCHQ) = 0.0d0         ! Initial CHQ coverage
        w(iCO3) = 0.0d0         ! Initial CO3 coverage
        w(iCx)= 1.d0-sCovX*(w(iCpO)+w(iCcOH)+w(iCHQ)+w(iCQ)+w(iCO3))
        !  Init Vacant site #

        w(iCy)= 1.d0-w(iCsO)  !  Init Vacant site *
        w(iCH)= concprot              !  Proton concentration / 1 M
        w(iV) = volt              !  Initial electrode potential


c***** Fitting parameters

        tk=tc+273.15d0
        frt=fc/rgas/tk
        U2 = -0.00023d0*tk +0.2326d0

        psat = 611.21d0*dexp(17.502*(tk-273.15)/(240.97+tk-273.15))
        po = psat*aW
        prel = po/101325.d0  !ref pressure 101.325 kPa
c***** Murphy and Koop, Q. J. R. Meteorol. Soc. (2005), 131, p1539
```

```
      RHE = -dlog((101325.d0/(101325.d0-po))
     &                  *(w(iCH)/1.d0)**2.d0)/(2.d0*frt)


      areaC=BET*100.d0*100.d0              !  cm2/g
      sitepermol = cSiteA*BET*wmC
      spcfmole = cSiteA*0.0001   !  mol sites/cm2-C



      exT1 = dexp(Ea1/rgas*(1/353.15d0-1/tk))
      exT2 = dexp(Ea2/rgas*(1/353.15d0-1/tk))
      exT5 = dexp(Ea5/rgas*(1/353.15d0-1/tk))
      exT6 = dexp(Ea6/rgas*(1/353.15d0-1/tk))
      exT8 = dexp(Ea8/rgas*(1/353.15d0-1/tk))


      rk(1)=rk(1)*exT1
      rk(2)=rk(2)*exT2
      rk(5)=rk(5)*exT5
      rk(6)=rk(6)*exT6
      rk(8)=rk(8)*exT8

      rewind(2)
      close(2)

      do i=1,n
         wp(i)=w(i)
      enddo

c*********************************************************
      elseif(mode .eq. 2) then  !  Governing equations
c*********************************************************

      wsave=w(k)
      w(k)=w(k)+dw
      call derv(n,ht,dwdt)

c*************************************************************
c****** Reaction kinetic expressions
c*************************************************************


c***** Catalytic Oxide growth: C* + H2O -->C*OH
```

```
      CvacY = w(iCy)
      if (CvacY.lt.0.d0) CvacY=0.1d-5

      CvacX = w(iCx)
      if (CvacX.lt.0.d0) CvacX=0.1d-5
      covCpO = w(iCpO)
      if (covCpO.gt.1.d0) covCpO=1.d0
      CcovX = 1.d0 - CvacX

      ex1a = dexp( alfa(1)*frt*(w(iV)-U1)-g1*CcovX)
      ratec(1,1)=rk(1)/siteratio*(CvacX*ex1a)



c***** Primary Carbon Dioxide Formation: C + 2H2O --> CO2 + 4H+ + 4e-

      ex2a = dexp( alfa(2)*frt*(w(iV)-U2))
      ratec(2,1)=rk(2)*prel*w(iCcOH)**sCovY*CvacX*ex2a !sCovY=1
      ratec(2,2)=ratec(2,1)*areaC*w(iC)*wmC   !mol CO2/cm2-geom

c***** Passive Oxide formation: xC# + H2O = C#xOH + H+ + e-

      ex5a = dexp( alfa(5)*frt*(w(iV)-U5)-g5*CcovX)
      ex5c = dexp(-alfc(5)*frt*(w(iV)-U5)+g5*CcovX)

      ratec(1,2)=rk(5)/siteratio*(1-fracIrr)*(CvacX**sCovX*ex5a
     &            -covCpO*w(iCH)*ex5c)


c***** CHQ Couple:  Cx(OH)2 = CxO2 + 2e- + 2H+


      covCQ = w(iCQ)
      covCHQ = w(iCHQ)
      covQuin = covCQ + covCHQ
      ex8a = dexp( alfa(8)*frt*(w(iV)-0.57))
      ex8c = dexp(-alfc(8)*frt*(w(iV)-0.57))
      ratec(3,2)=rk(8)/siteratio*(covCHQ*ex8a-
     &            covCQ*w(iCH)*ex8c)

      ex6c = dexp(-alfc(6)*frt*(w(iV)-U1))
      ratec(2,3) = -rk(6)/siteratio*covCpO*w(iCsO)*ex6c   ! CQ formation

      ratec(3,1) = w(iCcOH)*ratec(1,1)*rkeq1
      ratec(3,3) = w(iCcOH)*ratec(1,1)*covCQ**sCQ*rkeq2
```

```
c***** Anhydride formation: C#xO + CsO + H2O --> CxO3 + * + 2H+ + 2e-


c***** Averaging

          do ii=1,3
          do jj=1,3
            rate(ii,jj)=(ratec(ii,jj) +ratep(ii,jj))/2.d0
            enddo
          enddo

c*************************************************************
c****** Differential equations
c*************************************************************

c***** EQUATION iCx:  Vacant sites
       eq(iCx)= w(iCx)-(1.0d0-w(iCcOH)-sCovX*(w(iCpO)
     &    +w(iCQ)+w(iCHQ)+w(iCO3)))

c***** EQUATION iCy:  Vacant sites
          eq(iCy)= w(iCy)-(1.d0-w(iCsO))


c***** EQUATION iC:  Moles of carbon lost
       eq(iC)= dwdt(iC)
     &          + (rate(2,2))

c***** EQUATION iCcOH:  Fractional CcOH ox cov
       eq(iCcOH)= dwdt(iCcOH)
     &           + (2.d0*rate(3,1)+rate(3,3)-rate(1,1))/spcfmole

c***** EQUATION iCsO:  Fractional CsO ox cov
      eq(iCsO)= dwdt(iCsO)
     &           + (-0.5d0*rate(2,1)-rate(2,3)*siteratio)/spcfmole

c***** EQUATION iCpO:  Fractional CpO ox cov
       eq(iCpO)= dwdt(iCpO)
     &           + (-rate(2,3)-rate(1,2))/spcfmole

c***** EQUATION iCQ:  Fractional CQ ox cov
       eq(iCQ)= dwdt(iCQ)
     &           + (-rate(3,2)+rate(2,3))/spcfmole !+rate(3,3)

c***** EQUATION iCHQ:  Fractional CHQ ox cov
       eq(iCHQ)= dwdt(iCHQ)
     &           + (rate(3,2))/spcfmole
```

```
c***** EQUATION iCO3:  Fractional CO3 ox cov
      eq(iCO3)= dwdt(iCO3)
     &          + (-rate(3,1)-rate(3,3))/spcfmole

c***** EQUATION iV:  Set voltage

c          eq(iV)= cd + cdorr + cdcor ! set mixed potential

      eq(iV) = volt - (w(iV) - RHE)


c***** Return unperturbed variable
      w(k)=wsave

c*******************************************************
     elseif(mode .eq. 4) then  !  Save converged auxillary variables
c*******************************************************
      do ii=1,3
        do jj=1,3
          ratep(ii,jj)=ratec(ii,jj)
          enddo
         enddo

c*******************************************************
     elseif(mode .eq. 3) then  !  Output
c*******************************************************
         if (sweep.gt.0) then
          capV = cap*(0.65d0 + w(iV)*0.667d0)
          else
          capV = cap*(1.1d0 + w(iV)*0.32d0)
         endif

          cdCcOH= rate(1,1)*1.d0*Fc*areaC*w(iC)*wmC*siteratio !mol CO2/cm2-geom
          cdCO2 = rate(2,2)*4.d0*Fc
          cdCsO = rate(2,1)*1.d0*Fc*areaC*w(iC)*wmC !2e-/2co2 = 1
          cdCpO = rate(1,2)*2.d0*Fc*areaC*w(iC)*wmC*siteratio  !mol CO2/cm2-geom
          cdCQ = (rate(3,2)*2.d0 + rate(2,3)*0.d0)
     &                              *Fc*areaC*w(iC)*wmC*siteratio !mol CO2/cm2-geom
          cdCO3 = (rate(3,1)*4.d0+rate(3,3)*4.d0)*Fc*areaC*w(iC)*wmC*siteratio
          cdcor = cdCcOH + cdCO2 + cdCsO + cdCpO + cdCQ + sweep*capV*gC

        curdens = cdcor/gC

      write(1,101) time1,(w(i),i=1,n),cdCcOH/gC,cdCsO/gC,
```

```
    &   cdCpO/gC, cdCO2/gC, curdens, cdCQ/gC
          print *,"write",time1
c*******************************************************
          endif
c*******************************************************
          return
          end


      subroutine derv(n,ht,dwdt)
          implicit real*8 (a-h,o-z)
          dimension dwdt(20)
          common /var/ w(20),wp(20),wa(20)

          do i=1,n
            dwdt(i)=(w(i)-wp(i))/ht
            wa(i)=(w(i)+wp(i))/2.d0
          enddo

          return
          end


    subroutine matinv(n,m,determ)

c***** Matrix inversion
          implicit real*8 (a-h,o-z)
           common /mat/ b(20,20),d(20,41)
          dimension id(20)
          determ=1.0
          do 1 i=1,n
 1        id(i)=0
          do 18 nn=1,n
           bmax=1.1
           do 6 i=1,n
            if(id(i).ne.0) goto 6
            bnext=0.0
            btry=0.0
            do 5 j=1,n
             if(id(j).ne.0) goto 5
             if(dabs(b(i,j)) .le. bnext) goto 5
             bnext=dabs(b(i,j))
             if(bnext .le. btry) goto 5
             bnext = btry
             btry = dabs(b(i,j))
             jc=j
```

```
5      continue
     if( bnext .ge. bmax*btry) goto 6
          bmax = bnext/btry
          irow = i
          jcol = jc
6      continue
    if(id(jc) .eq. 0) goto 8
         determ = 0.0
         return
8   id(jcol)=1
    if(jcol .eq. irow) goto 12
         do 10 j=1,n
          save=b(irow,j)
          b(irow,j)=b(jcol,j)
10    b(jcol,j)=save
    do 11 k=1,m
          save=d(irow,k)
          d(irow,k)=d(jcol,k)
11    d(jcol,k)=save
12    f=1.0/b(jcol,jcol)
         do 13 j=1,n
13    b(jcol,j)=b(jcol,j)*f
    do 14 k=1,m
14        d(jcol,k)=d(jcol,k)*f
    do 18 i=1,n
          if(i .eq. jcol) goto 18
          f=b(i,jcol)
    do 16 j=1,n
16     b(i,j)=b(i,j)-f*b(jcol,j)
    do 17 k=1,m
17     d(i,k)=d(i,k)-f*d(jcol,k)
18   continue
         return
         end
```